Lehrstuhl für Leichtbau
der Technischen Universität München

Active Trim Panel Attachments for Control of Sound Transmission through Aircraft Structures

Stephan Tewes

Vollständiger Abdruck der von der Fakultät für Maschinenwesen der Technischen Universität München zur Erlangung des akademischen Grades eines

Doktor-Ingenieurs

genehmigten Dissertation.

Vorsitzender: Univ.-Prof. Dr.-Ing. habil. H. Ulbrich

Prüfer der Dissertation:

1. Univ.-Prof. Dr.-Ing. H. Baier
2. Univ.-Prof. Dr.-Ing. H.P. Wölfel,
   Technische Universität Darmstadt

Die Dissertation wurde am 18.07.2005 bei der Technischen Universität München eingereicht und durch die Fakultät für Maschinenwesen am 03.07.2006 angenommen.

Vorwort

Die vorliegende Arbeit entstand während meiner Tätigkeit als Doktorand in der Abteilung LG-MD am Corporate Research Centre der Firma EADS in Ottobrunn.

Bedanken möchte ich mich daher bei allen Mitarbeitern der Abteilung LG-MD, die durch ihre Hilfe und mit Rat und Tat zum Gelingen dieser Arbeit beigetragen haben. Insbesondere danken möchte ich Herrn Dr.-Ing. R. Maier, da er diese Arbeit ermöglicht und die gesamte Zeit aktiv betreut hat. Ebenso gilt mein besonderer Dank den Herren Dr. rer. nat. M. Grünewald und Dr.-Ing. A. Peiffer für die vielen fachlichen Ratschläge und Anregungen.

Mein herzlicher Dank gilt außerdem Herrn Prof. Dr.-Ing. H. Baier, Inhaber des Lehrstuhls für Leichtbau der Technischen Universität München, für seine Unterstützung und Interesse an dieser Arbeit sowie für die Übernahme des Hauptreferats. Auch danken möchte ich Herrn Prof. Dr.-Ing. H.P. Wölfel für die Übernahme des Korreferats und Herrn Prof. Dr.-Ing. habil. H. Ulbrich für die Übernahme des Prüfungsvorsitzes.

Abstract

Typical aircraft structures usually show an unsatisfactory transmission loss behaviour at low audible frequencies and it is expected that this problem will become even worse for future composite fuselage structures. Exterior perturbations on the fuselage skin and the airframe, such as engine noise or the turbulent flow along the fuselage skin, are transmitted as airborne and structure-borne noise on the trim panel and in the cabin interior. Passive measures for noise control, such as sound absorbing materials placed in the cavity between the fuselage and the trim panel, generally work well above 1 kHz, but to be effective at low frequencies, conventional noise reduction methods would require a substantial increase in mass and volume, which is typically not available in aircraft structures. Therefore, active noise and structural control concepts appear quite attractive to improve the acoustic passenger comfort in commercial aircraft.

In this thesis a new active structural acoustic control (ASAC) concept based on an active trim panel suspension is investigated. The control concept is developed by means of a comprehensive, vibro-acoustic simulation model representing a typical, generic aircraft sidewall section and consists of active trim panel attachment elements with integrated piezoelectric actuators. They are designed to replace the passive shock mounts, which are normally used as connection elements between the trim panel and the fuselage structure. The particular actuator design permits to control three independent components of structure-borne sound transmitted from the fuselage into the trim panel. Amongst different sensor concepts, structural accelerations have proved to provide an efficient error signal for the control system. Thus, the dynamic response of the attachment elements and the trim panel can be controlled with the actuators. By reducing the local vibration levels at the sensor positions a significant reduction of transmitted sound power is obtained.

A prototype control system is tested on a 1 by 1 m plane sidewall section consisting of a stiffened CFRP-fuselage panel and a honeycomb core trim panel. The whole system comprises four active attachment elements used to connect the trim panel to the fuselage frames, and is mounted in a transmission loss test suite between a reverberation and an anechoic chamber. The reverberation room is used for the excitation with a pair of loudspeakers or a shaker mounted directly on the fuselage skin panel. In the anechoic chamber the sound power radiated by the trim panel is determined by intensity measurements. The ASAC system is tested against various tonal excitations at frequencies where the transmission loss of the passive system exhibits some minima as well as for third octave band random noise. For tonal noise up to 20 dB reduction of radiated sound power and for third octave band noise attenuations of up to 10 dB were achieved demonstrating that such a system provides a new possibility to reduce cabin interior noise and consequently improve passenger comfort.

Contents

Nomenclature

Roman Letters

a	Length; source diameter
A	Matrix of in-plane stiffness; surface area; system matrix
b	Width
B	Input matrix; matrix of coupling stiffness; number of fan blades
B_A	Bulk reacting coefficient
c	Damping coefficient; element of damping matrix C; speed of sound
C	Damping matrix; electric capacity; influence matrix; matrix of plant responses; output matrix
d	External signal; perturbation signal vector; piezoelectric charge coefficient; distance; piezoelectric coupling matrix
D	Bending stiffness; electric flux density; feedthrough matrix; matrix of rotational stiffness
e	Error signal
E	Electric field strength; expectation operator; Young's modulus
f	Frequency
F	Force
g	Transfer function
G	Cross correlation; Green's function; shear modulus; transfer matrix
h	Element of controller matrix H; filter impulse response; thickness
H	Controller matrix
I	Electric current; identity matrix; integer variable; sound intensity
j	Imaginary unit
J	Cost function
k	Element of stiffness matrix K; stiffness; wavenumber
K	Integer variable; stiffness matrix
l	Length
L	Actuation effort power ratio; coupling matrix; integer variable
L_W	Sound power level
m	Element of mass matrix M; integer variable; mass per unit area
M	Actuation effort transformation matrix; integer variable; mass matrix; moment
n	Integer variable; normal unit vector; rotational speed
N	Force; integer variable; interpolation matrix
p	Fluid pressure
P	Fluid pressure; matrix relating structural load to input signal; power

P_0	Reference sound power
Q	Electric charge; reduced stiffness matrix; volume flow
r	Filtered-reference signal; position vector; reflection coefficient
R	Distance; electric resistance; filtered-reference signal vector; load vector; sound transmission index, also denoted as transmission loss
s	Laplace operator; length
S	Mechanical compliance matrix; surface area
t	Thickness; time
T	Measurement time; sampling time; temperature; transformation matrix
u	Control signal vector; input signal
u, v, w	Displacements; velocities
U	Electric voltage; input vector
w	FIR-filter coefficient
x	Input signal
x, y, z	Cartesian coordinates; displacements
X	Displacement; state vector
y	Output signal
Y	Error signal vector; output signal vector
Z	Impedance

Greek Letters

α	Convergence factor; modal displacement amplitude; random phase; thermal expansion coefficient
β	Modal pressure amplitude; weighting parameter
δ	Dirac pulse; Kronecker delta function; ratio of mechanical to acoustic stiffness
δ_m, δ_p	Relative magnitude mismatch; relative phase mismatch
Δa, Δl, Δs	Displacements
ΔT	Temperature load
ϵ	Strain
ε	Dielectric permittivity
ϕ	Eigenvector; incidence angle
φ	Principle direction of an orthotropic material
Φ	Eigenvectors matrix
γ	Leakage factor; shear angle
η	Loss factor
κ	Curvature; discrete frequency
λ	Mass ratio; wavelength
Λ	Piezoelectric induced strain
μ	Convergence factor
ν	Poisson's ratio
θ	Incidence angle
ρ	Density
σ	Stress

τ	Shear stress; sound transmission coefficient
ω	Angular frequency; eigenfrequency
Ω	Eigenfrequency diagonal matrix
ψ	Modal amplitude of Ψ
Ψ	Antiderivative of pressure P
ζ	Modal damping parameter

Indices

a	Actuator
act	Actuator
b	Bending; boundary
eq	Equivalent
f	Fluid
h	Half space
hs	Host structure
i	Incident
n	Normal direction
p	Primary
r	Radiation; reflected; resonance
s	Structure
t	Total; transmitted
tot	Total
wp	Plate wave impedance

Abbreviations

AAE	Active attachment element
ANC	Active noise control
ANVC	Active noise and vibration control
ASAC	Active structural acoustic control
ATVA	Adaptive tunable vibration absorbers
AVC	Active vibration control
BEM	Boundary element method
BPF	Blade-passing frequency
CAD	Computer-aided-design
CFRP	Carbon fibre reinforced plastic
DSP	Digital signal processor
FEM	Finite element method
FIR	Finite impulse response
GA	Genetic algorithms
LMS	Least-mean-square
MIMO	Multiple input, multiple output
MSC	MacNeal-Schwendler Corporation

NASA	National Aeronautics and Space Administration
PR	Power ratio
PVDF	Polyvinylidene fluoride polymer
PZT	Lead zirconate titanate
SEA	Statistical energy analysis
SISO	Single input, single output
SPL	Sound pressure level
TBL	Turbulent boundary layer
TL	Transmission loss

Miscellaneous

∇^2	Differential operator
$\Re(x)$	Real part of x
$\Im(x)$	Imaginary part of x
$\mathbb{C}$	Complex number
$\mathbb{R}$	Real number
$\overline{x}$	Average of x
x^*	Complex conjugate of x
x^H	Hermitian of x
$\dot{x}$	Time derivate of x
x^T	Transpose of x

Chapter 1

Introduction

Interior noise levels inside modern subsonic aircraft are nowadays much improved in comparison to the past because the noise emission of the engines, constituting the primary source of external and internal noise components in flight, has been continuously reduced over the last decades. In general, aircraft sidewalls are also optimised with respect to their sound transmission behaviour and, by applying additional sound proofing materials to the fuselage, satisfactory sound pressure levels in the cabin are usually obtained.

Yet, typical aircraft sidewalls have the least efficiency in reducing the sound transmission at frequencies below 500 Hz. Depending on the flight condition, various tonal and broadband noise components in this frequency range, especially due to buzz-saw noise and jet noise emitted by the engines and the turbulent boundary layer along the fuselage, are still perceived as very annoying by passengers. Thus, passenger comfort could be further improved by decreasing the structural sound transmission into the cabin at lower audible frequencies. However, the low-frequency sound transmission is mainly controlled by the area weight of the structure and a substantial decrease in sound transmission would require an important increase in mass, hence representing a non-viable option for aircraft interior noise control.

An alternative solution for this particular problem is provided by so-called *active control* systems. With an active system the dynamic structural response to an external perturbation, and consequently the sound radiation into the cabin, can be influenced and controlled. In the present study this principle is applied to the control of sound transmission through aircraft sidewall structures at low audible frequencies and is addressed by means of a numerical model and experimental investigations.

1.1 State-of-the-Art

Since the late 1940s aircraft interior noise control has become a more and more important issue in aircraft design. A brief overview covering the most important aspects of aircraft interior noise is presented in Chapter 2.2.

States-of-the-art in commercial aircraft are passive techniques used to reduce the sound transmission through the aircraft sidewall and the resulting sound pressure level in the cabin. Acceptable interior noise levels in combination with a low structural weight are usually obtained by employing several individual structural partitions that are separated by fluid gaps. The

airspace acts like a spring between the individual masses of the partitions and transmits the sound energy. Above a certain frequency, known as the mass-air-mass resonance, the fluid uncouples the mechanical behaviour of the structural partitions, thus resulting in a low sound transmission.

In aircraft design this principle is realised with double wall structures, which are composed of the primary fuselage and the cabin trim panels. In addition, the resulting fluid cavity is filled with porous sound absorbing materials such as fibreglass wool, which further enhances the transmission loss capabilities of the aircraft sidewall by dissipating acoustic energy into heat. Thus, a good transmission loss performance can be realized for a large part of the audible frequency range, while being compliant to a main priority in aircraft design, which is the requirement for a low structural weight.

A major drawback of those configurations is the poor performance in sound transmission reduction at frequencies below and close to the mass-air-mass resonance. This behaviour is inherent to such systems and essentially due to the following points:

- Below the mass-air-mass resonance frequency a coupling of the individual structural partitions through the cavity fluid occurs and the transmission loss behaviour is governed by the total mass of the complete sidewall partition. Thus, the requirement of low structural weight is opposed to noise control requirements.
- Close to the mass-air-mass resonance the sound transmission is even higher as a resonant coupling between the individual structures occurs through the airspace.
- The use of sound absorbing materials within the airspace can reduce the mechanical coupling through the cavity. However, the efficiency of sound absorbing materials in dissipating acoustic energy is limited at lower frequencies. Moreover, the available volume for such materials is restricted in aircraft sidewalls.
- In theory, the best transmission loss behaviour is obtained for double wall assemblies having no mechanical connections between the individual partitions. In an aircraft, the trim panel has to be mechanically attached to the primary fuselage, thus providing an additional structure-borne sound transmission path besides the airborne path through the cavity and increasing the sound transmission.

Alternative passive solutions to enhance the low-frequency sound transmission behaviour, for instance constrained layer damping applied to the fuselage, tuned vibration absorbers or an acoustically appropriate design of the fuselage, also require a substantial increase in mass and are therefore not convenient noise control techniques unless weight is not the overall governing design issue. Moreover, it is expected that, in comparison to conventional aluminium designs, future composite fuselage structures will have an even worse low-frequency transmission loss behaviour. In order to overcome the acoustic limitations of lightweight structures at low frequencies, active control systems are considered as a possible option for aircraft interior noise control.

An active control system is used to control and minimise certain physical quantities such as the cabin sound pressure level or the structural vibrations of the fuselage sidewall and consists of actuators required for the manipulation of the given physical quantity, error sensors to monitor

this quantity and a digital signal processor connecting the sensor response with the actuator excitation. The application of successful active control systems has been enabled by the rapid developments in microelectronics, adaptive signal processing and the progress made with smart materials and appropriate actuators.

Currently, active noise control systems are used in regional turboprop aircraft to reduce the interior sound pressure levels at low harmonics of the blade-passing frequency. In this case the sound field inside the cabin is controlled with a set of loudspeakers for the actuation and microphones for the error sensing of the sound field. However, to obtain a global attenuation in sound pressure, a high number of control channels are usually required because the primary noise source, the vibrating fuselage structure, is distributed over multiple surfaces.

For these reasons another active control approach has been proposed in literature. In general, interior noise is transmitted and radiated by the vibrating aircraft sidewall structure. Consequently the sound pressure level inside the cabin can be reduced by controlling the structural response of the sidewall with appropriate actuators and sensors. This type of control is known as *active structural acoustic control* and has been investigated in many studies published in literature. However, most of them are dealing with the control of flat, homogenous structures and only few publications are available where the application of an active structural acoustic control system has been explored and tested on realistic aircraft sidewalls.

1.2 Objectives of the Thesis

The purpose of the present study is the development of an active structural acoustic control system intended to reduce the low-frequency sound transmission into aircraft cabins through the sidewall structure. To attain this objective an appropriate actuator and sensor concept has to be determined. To prove this particular control concept, a prototype of the active system is to be demonstrated and tested on a generic fuselage sidewall section under laboratory conditions. In particular, the following requirements will have to be taken into account:

- The active system is to be developed for a typical aircraft sidewall section, consisting of a fuselage structure stiffened by frames and stringers and the trim panel representing the cabin lining. The trim panel is mechanically attached to the fuselage structure, thus permitting the sound transmission of structure-borne noise components besides the airborne path through the fluid enclosed by the fuselage structure and the trim panel. The cavity is partly filled with sound absorbing material to enhance the acoustic absorption properties and reduce the sound transmission.

- The utilised actuators and sensors should enable a straightforward integration within the aircraft sidewall section. Major design changes either to the fuselage structure or the trim panel are not possible. Further requirements are low weight and low volume of the active system.

- The target performance of the active system is a reduction in sound transmission ranging at least from 5 to 10 dB in order to obtain a clearly audible effect and have a benefit in comparison to classical, passive sound reducing treatments.

The development of such an active system is impeded by the complexity of the considered fluid-structural system and the high number of modes typically involved in its vibro-acoustic response to an external disturbance, even at low audible frequencies. Furthermore, standard tools for the efficient development of active control concepts for vibro-acoustic systems are currently not available. Thus, an appropriate model for the prediction of sound radiation from structures with incorporated active control systems has also to be developed within this study.

1.3 Organisation of the Thesis

The thesis is organised into five main parts. In the second chapter the basic principles concerning the sound transmission through single and double wall structures as well as the phenomenon of piezoelectricity are briefly discussed. A literature survey on aircraft interior noise and active control technologies is also given in Chapter 2.

A numerical model to describe the sound transmission through plane double wall sections is introduced in Chapter 3. The simulation procedure is based on an FEM-description of the structure. To obtain the sound power radiated by the structure a weak coupling between the structural behaviour and the surrounding air is assumed. Subsequently, the required acoustic quantities can be post-processed from structural vibration results. Furthermore, it is possible to incorporate piezoelectric actuators within the structural model, thus allowing investigations on the open- and closed-loop behaviour of various active structural control systems and their impact on the structural response and the sound radiation. The proposed simulation approach is validated at the end of Chapter 3 on a test case involving the sound transmission through a single and double wall aluminium panel.

In the fourth chapter this numerical approach is used to develop an appropriate active structural acoustic control system intended to reduce the low-frequency sound transmission through an aircraft sidewall. As basic simulation model a generic fuselage sidewall section, consisting of a 1 by 1 m stiffened fuselage panel furnished with a honeycomb core sandwich trim panel, is studied. Three different control concepts are investigated and numerically evaluated against each other for various excitations in order to determine the system having the best control performance on the sound radiation of the trim panel. The first control concept consists of piezoelectric actuators applied to the fuselage skin. Within the second concept the piezoelectric actuators are applied to the trim panel, whereas the third concept is based on active attachment elements, replacing the conventional shock mounts for the attachment of the trim panel to the fuselage frames, and thus allowing the excitation of additional control forces at the trim-panel mounting points.

A laboratory application of the structural acoustic control system based on the active attachment elements is demonstrated in Chapter 5. For this, a generic aircraft sidewall section with integrated active attachment elements is installed in a transmission loss test suite between a reverberation and anechoic chamber. The control performance of the active system is evaluated for various broadband and tonal excitations by measuring the sound intensity radiated by the trim panel with and without control respectively. The test setup, experimental methods, control loop implementation and experimental results are discussed in detail.

Finally, the conclusions obtained from this thesis and recommendations for future work are presented in Chapter 6.

Chapter 2

Scientific Background

Starting with a brief reminder of fluid and structural sound propagation the essential characteristics for understanding the phenomenon of structural sound transmission are briefly explained by means of an analytical model valid for infinite, plane single and double wall sections.

Aircraft interior noise is a typical example of structural sound transmission and is addressed in Chapter 2.2. Perturbations from external noise sources as the aircraft engines or the turbulent air flowing around the fuselage are transmitted as structural vibration through the fuselage sidewall and radiated into the cabin. In passenger aircraft the sidewall typically consists of the main structure, which is furnished in the cabin with additional trim panels. The state-of-the-art noise control concept are layers of fibreglass blankets, the so-called primary and secondary thermo-acoustic insulation[1], which are placed into the airborne transmission path between the main fuselage structure and the cabin trim panels.

Innovative materials such as piezoelectric ceramics in combination with modern control systems provide new alternatives for interior noise control. In literature such systems are referred to with the keywords *Active Noise Control* (ANC), *Active Vibration Control* (AVC) and *Active Structural Acoustic Control* (ASAC). Numerous studies about active control have been published in recent years, dealing with control applied to relatively simple structures up to systems designed for realistic airframes. A survey is given at the end of this chapter.

2.1 Structural Sound Transmission

In many technical applications it is required to minimize the sound transmission from one fluid region into another. This can be achieved, for example, by appropriate materials absorbing a part of the sound energy and dissipating it into heat [Ingard94]. Another widely used method is to introduce a suitable partition into the transmission path. The partition represents a change in acoustic impedance and leads to a partially reflection of the sound waves incident upon the partition.

The majority of engineering applications implies single and double wall partitions for which the basic physical principles describing the structural sound transmission are summarized in

[1]The primary insulation is attached to the main fuselage, whereas the secondary insulation is attached to the trim panels.

the following four chapters. Additional information can be found in the textbooks of Cremer and Heckl [Cremer96], Fahy [Fahy85] or Mechel [Mechel02].

2.1.1 Sound Propagation in Fluids

For most technical applications it is justified to describe the propagation of a sound wave through a homogeneous, compressible and non-viscous fluid as a small, dynamic pressure variation superimposed on the static equilibrium pressure. The pressure variation relative to the equilibrium state is the acoustic pressure and shall be denoted by p.

For a rectangular Cartesian coordinate system (x, y, z) the constitutive equation describing the propagation of a small pressure disturbance through an appropriate fluid is derived from the following linearised continuity equation:

$$\frac{\partial p}{\partial t} + \rho_0 \left(\frac{\partial u}{\partial x} + \frac{\partial v}{\partial y} + \frac{\partial w}{\partial z} \right) = 0 \ , \tag{2.1}$$

and the linearised momentum equations[2]:

$$\frac{\partial p}{\partial x} + \rho_0 \cdot \frac{\partial u}{\partial t} = 0 \ , \tag{2.2}$$

$$\frac{\partial p}{\partial y} + \rho_0 \cdot \frac{\partial v}{\partial t} = 0 \ , \tag{2.3}$$

$$\frac{\partial p}{\partial z} + \rho_0 \cdot \frac{\partial w}{\partial t} = 0 \ . \tag{2.4}$$

The mean static density of the fluid is denoted by ρ_0 and u, v, w are the acoustic particle velocities in x-, y- and z-directions superimposed on the static equilibrium state. Assuming an adiabatic process, synonymous with the relation $\partial p/\partial t = c_0^2 \cdot \partial \rho/\partial t$, the continuity and momentum equations can be combined to form the governing linear wave equation:

$$\frac{\partial^2 p}{\partial x^2} + \frac{\partial^2 p}{\partial y^2} + \frac{\partial^2 p}{\partial z^2} = \frac{1}{c_0^2} \cdot \frac{\partial^2 p}{\partial t^2} \ . \tag{2.5}$$

The propagation velocity of a small pressure disturbance in the fluid, the speed of sound, is abbreviated with the term c_0. With the assumption of a harmonic time dependence the wave equation might be rewritten in the frequency domain as:

$$\frac{\partial^2 p}{\partial x^2} + \frac{\partial^2 p}{\partial y^2} + \frac{\partial^2 p}{\partial z^2} = -\frac{\omega^2}{c_0^2} \cdot p \ , \tag{2.6}$$

which is also known as the Helmholtz differential equation. For technical problems as the interaction between plane structures and fluids, it is appropriate to study equation 2.6 in a two dimensional form involving only variations in two independent directions:

$$\frac{\partial^2 p}{\partial x^2} + \frac{\partial^2 p}{\partial y^2} = -\frac{\omega^2}{c_0^2} \cdot p = -k^2 \cdot p \ . \tag{2.7}$$

[2]Small quantities are neglected.

A general solution for the plane wave propagation is given by:

$$p(x, y, t) = \hat{p} \cdot e^{-jk_x x} \cdot e^{-jk_y y} \cdot e^{j\omega t} \ , \tag{2.8}$$

in which $\hat{p}$ is a complex pressure magnitude and k the wavenumber defined as $k = \omega/c_0$. The wavenumber represents the magnitude of a vector indicating the direction of propagation and also describes the phase change per unit increase of distance. Inserting the above expression in equation 2.7 yields in the following relation for the wavenumber k and its x- and y-components:

$$k^2 = k_x^2 + k_y^2 \ , \tag{2.9}$$

which must be satisfied for k_x and k_y at any given frequency to be a solution for the wave equation. The direction of the wave is given by the angle ϕ between the vector k and the x-axis. ϕ is determined by the relations:

$$\sin\phi = k_y/k \quad \text{and} \quad \cos\phi = k_x/k \ . \tag{2.10}$$

Furthermore, the momentum equations 2.2 to 2.4 relate the spatial pressure gradient in a given direction to the particle acceleration in that direction. Assuming a harmonic time dependence, the acceleration can be expressed by the velocity and the momentum equation becomes $\partial p/\partial n = -j\omega \cdot \rho_0 \cdot v_n$, where n denotes an arbitrary direction vector. The momentum relation is also appropriate to describe the boundary condition for the sound radiation and fluid loading on a vibrating fluid-structure interface. Thus, the normal velocity of a structure surface determines the normal pressure gradient of the fluid and vice versa. Assuming a surface lying in the y,z-plane and using the plane wave field from equation 2.8, the momentum equation $(\partial p/\partial x)_{x=0} = -j\omega \cdot \rho_0 \cdot u_{x=0}$ becomes:

$$k_x \cdot p_{x=0} = \omega \cdot \rho_0 \cdot u_{x=0} = k \cdot \rho_0 \cdot c_0 \cdot u_{x=0} = k \cdot Z_0 \cdot u_{x=0} \ , \tag{2.11}$$

since Z_0 is the acoustic impedance of a free plane wave given by the ratio of its acoustic pressure and particle velocity, $Z_0 = p/u = \rho_0 \cdot c_0$.

2.1.2 Bending Waves in Thin Plates

For an infinite and uniform thin plate of thickness h, subjected to a transversal excitation per unit area $\hat{p}$, the one dimensional bending equation is:

$$D \cdot (1 + j\eta) \cdot \frac{\partial^4 w}{\partial x^4} + m \cdot \frac{\partial^2 w}{\partial t^2} = \hat{p} \cdot e^{j(\omega t - kx)} \ , \tag{2.12}$$

with the bending stiffness D defined as $D = E \cdot h^3/12/(1 - \nu^2)$ and the mass per unit area $m = \rho \cdot h$. Damping is represented by the introduction of a complex Young's modulus[3]. A general solution to equation 2.12 can be expressed as:

$$w(x, t) = \hat{w} \cdot e^{j(\omega t - kx)} \ , \tag{2.13}$$

[3] $E' = E \cdot (1 + j\eta)$, with η being defined as loss factor.

where $\hat{w}$ is the complex amplitude of the transversal displacement w and k the wavenumber specified by the frequency ω and the phase speed c_b in the plate, $k = \omega/c_b$. Introducing the above expression for the flexural wave in equation 2.12 yields:

$$(D \cdot (1 + j\eta) \cdot k^4 - m \cdot \omega^2) \cdot \hat{w} = \hat{p} \ . \tag{2.14}$$

The ratio of the complex pressure magnitude to the complex velocity magnitude defines the structural wave impedance of the plate and takes the form:

$$Z_{wp} = \frac{\hat{p}}{j\omega \cdot \hat{w}} = -j \cdot (D \cdot k^4 - m \cdot \omega^2)/\omega + D \cdot k^4 \cdot \eta/\omega \ . \tag{2.15}$$

The solution of the homogeneous, undamped bending equation 2.14 yields the free-plate bending wavenumber $k_b = (\omega^2 \cdot m/D)^{1/4}$ and the phase speed $c_b = (\omega^2 \cdot D/m)^{1/4}$. For an excitation with $k = k_b$ an infinite small force per unit area causes an infinite large displacement and the wave impedance of the plate Z_{wp} becomes zero.

2.1.3 Sound Transmission through Infinite Single Wall Partitions

The sound transmission through an infinite partition separating two fluid domains can be regarded as a boundary value problem on the partition surface. Considering the system represented in Figure 2.1 the partition in the y,z-plane separates two acoustic domains characterized by impedances $Z_1 = \rho_1 \cdot c_1$ and $Z_2 = \rho_2 \cdot c_2$. An acoustic plane wave $\hat{P}_i$ is incident upon the partition from the left side with an angle of ϕ_1.

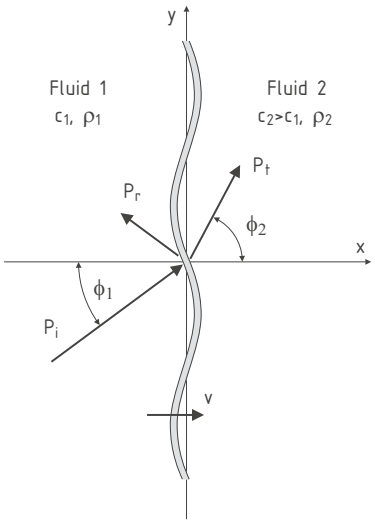

Figure 2.1: Transmission of oblique sound waves through an infinite single wall partition

The incident, reflected and transmitted pressure sound field may be written as[4]:

$$p_i(x, y) = \hat{P}_i \cdot e^{-jk_{1,x}x} \cdot e^{-jk_{1,y}y} \ , \tag{2.16}$$

[4]The term $e^{j\omega t}$ is omitted in the following.

$$p_r(x,y) = \hat{P}_r \cdot e^{jk_{1,x}x} \cdot e^{-jk_{1,y}y} = r \cdot \hat{P}_i \cdot e^{jk_{1,x}x} \cdot e^{-jk_{1,y}y} \ , \tag{2.17}$$

$$p_t(x,y) = \hat{P}_t \cdot e^{-jk_{2,x}x} \cdot e^{-jk_{2,y}y} \ . \tag{2.18}$$

In equation 2.17 the abbreviation r denotes the reflection coefficient defined as the ratio between the complex magnitude of the reflected wave to the complex magnitude of the incident wave. Furthermore, equation 2.9 and 2.10 must be satisfied for the wavenumber and its x- and y-components in both fluid domains. In addition, the trace wavenumber $k_{i,y}$ is the same on both sides and in the partition, hence $k_{1,y} = k_{2,y} = k_y$ or:

$$\sin\phi_2 / \sin\phi_1 = c_2/c_1 \ . \tag{2.19}$$

The transversal plate velocity is formulated as:

$$v(y) = \hat{V} \cdot e^{-jk_y y} \ . \tag{2.20}$$

The momentum equation 2.2 at $x = 0$ yields the boundary conditions for the particle velocity on the surface of the partition:

$$v(0,y) = (\hat{P}_i - \hat{P}_r) \cdot \cos\phi_1 \cdot e^{-jk_y y}/Z_1 = \hat{P}_i \cdot (1-r) \cdot \cos\phi_1 \cdot e^{-jk_y y}/Z_1 \ , \tag{2.21}$$

$$v(0,y) = \hat{P}_t \cdot \cos\phi_2 \cdot e^{-jk_y y}/Z_2 \ . \tag{2.22}$$

The effective load on the partition is equal to the pressure difference on both sides and from the bending wave equation 2.14 follows the relation:

$$Z_{wp} \cdot \hat{V} \cdot e^{-jk_y y} = (\hat{P}_i \cdot (1+r) - \hat{P}_t) \cdot e^{-jk_y y} \ . \tag{2.23}$$

Eliminating the reflection coefficient r and velocity magnitude $\hat{V}$ the complex pressure ratio $\hat{P}_t/\hat{P}_i$ is derived from equation 2.21 to 2.23:

$$\frac{\hat{P}_t}{\hat{P}_i} = \frac{2 \cdot Z_2 \cdot \cos\phi_1}{Z_2 \cdot \cos\phi_1 + Z_{wp} \cdot \cos\phi_1 \cdot \cos\phi_2 + Z_1 \cdot \cos\phi_2} \ . \tag{2.24}$$

The transmission coefficient τ relates the transmitted to the incident sound power:

$$\tau = \frac{\left|\hat{P}_t\right|^2 \cdot \cos\phi_2 / 2\rho_2 c_2}{\left|\hat{P}_i\right|^2 \cdot \cos\phi_1 / 2\rho_1 c_1} \ , \tag{2.25}$$

and the sound transmission index R is given by[5]:

$$R = 10 \cdot \log(\tau^{-1}) \ \ [dB] \ . \tag{2.26}$$

If the fluid on both sides of the partition is the same, equation 2.25 is reduced to:

[5] Also denoted as transmission loss TL in literature.

$$\tau = \frac{2 \cdot Z_0}{2 \cdot Z_0 + Z_{wp} \cdot \cos\phi} \ , \tag{2.27}$$

since $\phi_1 = \phi_2 = \phi$ and $Z_1 = Z_2 = Z_0$. Replacing the term Z_{wp} with the expression 2.15 for the wave impedance of the thin plate results in:

$$\tau = \frac{\left(2 \cdot Z_0/\cos\phi\right)^2}{\left(2 \cdot Z_0/\cos\phi + (D/\omega) \cdot \eta \cdot k^4 \cdot \sin^4\phi\right)^2 + \left(\omega \cdot m - (D/\omega) \cdot k^4 \cdot \sin^4\phi\right)^2} \ , \tag{2.28}$$

which can be further simplified by introducing the expression for the free flexural wavenumber k_b:

$$\tau = \frac{\left(2 \cdot Z_0/\omega m \cos\phi\right)^2}{\left(2 \cdot Z_0/\omega m \cos\phi + (k/k_b)^4 \cdot \eta \cdot \sin^4\phi\right)^2 + \left(1 - (k/k_b)^4 \cdot \sin^4\phi\right)^2} \ . \tag{2.29}$$

If the trace wavenumber k_y is equal to the wavenumber of the free bending wave in the plate, $k_y = k \cdot \sin\phi = k_b = (\omega^2 \cdot m/D)^{1/4}$, the reactive term of the wave impedance in equation 2.15 disappears and the transmission coefficient τ exhibits a local maximum. Therefore, with the assumption of an undamped structure, the incident sound wave will be totally transmitted into the second fluid domain and τ will be equal to one. This characteristic is referred to as *coincidence* and has a similar impact on the spatial periodicity as the resonance phenomenon for the temporal periodicity. For each angle of incidence the frequency connected with the coincidence phenomenon is given by the following relation:

$$\omega_{co} = (c_0/sin\phi)^2 \cdot (m/D)^{1/2} \ . \tag{2.30}$$

Since the term $sin\phi$ is always less than or equal to unity, the coincidence frequency ω_{co} cannot fall below a lower limit, which is designated as critical frequency or lowest coincidence frequency ω_c:

$$\omega_c = c_0^2 \cdot (m/D)^{1/2} \ . \tag{2.31}$$

The above equation shows that the critical frequency is proportional to term $(m/D)^{1/2}$. Thus, a stiff partition will have a lower critical frequency than a less stiff partition of similar weight.

It is now appropriate to analyse the sound transmission coefficient in dependence of the frequency ratio $\omega/\omega_c = (k/k_b)^2$. For $\omega \ll \omega_c$ the stiffness and damping terms, $(D/\omega) \cdot k^4 \cdot \sin^4\phi$ and $(D/\omega) \cdot \eta \cdot k^4 \cdot \sin^4\phi$ respectively, can be neglected in comparison to the inertia term $\omega \cdot m$ and the transmission coefficient τ is approximated by the relation:

$$\tau(\phi) \approx \left(1 + (\omega \cdot m \cdot \cos\phi/2Z_0)^2\right)^{-1} \ . \tag{2.32}$$

Assuming that $\omega \cdot m \cdot \cos\phi \gg 2 \cdot Z_0$, the sound reduction index may be written as:

$$R(\phi) = 20 \cdot \log\left(\omega \cdot m \cdot \cos\phi/2Z_0\right) \quad [dB] \ . \tag{2.33}$$

Equation 2.33, often referred to as *mass law* for oblique incident sound waves, illustrates that the sound reduction index depends mainly on the mass per unit area of the partition. The sound reduction index R increases with 6 dB per octave and 6 dB per doubling of mass.

With ω approaching ω_{co} for a given angle of incidence, the sound transmission is increased until it reaches a local maximum at $\omega = \omega_{co}$:

$$\tau(\phi) = (1 + \eta \cdot \omega_{co} \cdot m \cdot \cos\phi / 2Z_0)^{-2} \quad . \tag{2.34}$$

Relation 2.34 is controlled by the mechanical loss factor of the structure.

For frequencies well above the coincidence frequencies, $\omega \gg \omega_{co}$, the sound transmission is dominated by the stiffness term and τ becomes:

$$\tau(\phi) \approx \left(1 + \left(D \cdot k^4 \cdot \sin^4\phi \cdot \cos\phi / 2Z_0\omega\right)^2\right)^{-1} \quad . \tag{2.35}$$

As τ is proportional to the third power of ω, the sound reduction index increases with 18 dB per octave. A doubling of the bending stiffness would increase the sound reduction index by 6 dB.

The resulting transmission loss behaviour for various angles of incidence is exemplified in Figure 2.2 for an aluminium panel of 1 mm thickness. The sound reduction index given by equation 2.26 is plotted as a function of the frequency ratio ω/ω_c for incidence angles of 0°, 20°, 60° and 80°. The elastic modulus of aluminium is 74000 N/mm^2, the density 2,7 g/cm^3, the Poisson constant ν is 0,3 and the loss factor η equal to 0,1%. The fluid is assumed to be air with an acoustic impedance Z_0 of 416,5 kg/m^2, corresponding to a speed of sound of 340 m/s and a density of 1,225 kg/m^3. The resulting critical frequency from expression 2.31 is 11613 Hz.

Below the critical frequency, the sound reduction index is mass controlled. At a constant frequency the sound transmission is increased when the angle of incidence is augmented. Above the critical frequency the coincidence phenomenon occurs and for each single angle of incidence, except the normal incidence, a frequency can be found where the trace wavenumber of the fluid is coincident with the free flexural wavenumber of the partition, resulting in a minimal index of sound reduction. For frequencies much higher than the coincidence frequency the sound reduction index is dominated by the stiffness term and approximately increases with 18 dB per doubling of frequency.

In reality, sound waves may be incident from various angles simultaneously. For this case the sound reduction index may be determined by averaging expression 2.28 over the appropriate distribution of incidence angles. For a diffuse sound field, which is characterized by a statistical equal distribution of incidence angles, the following empirical relation, designated as *field incidence mass law*:

$$R_f = R(0°) - 5 \ \ [dB] \ , \tag{2.36}$$

yields a good approximation of experimental results at sub-critical frequencies. The field incidence mass law can also be approximated by averaging the transmission coefficient over an equal distribution of incidence angles from 0° to 78°.

The sound radiation from rectangular plates with finite dimensions is also of a great practical importance. For a flat plate mounted into an infinite baffle, the sound radiation can be

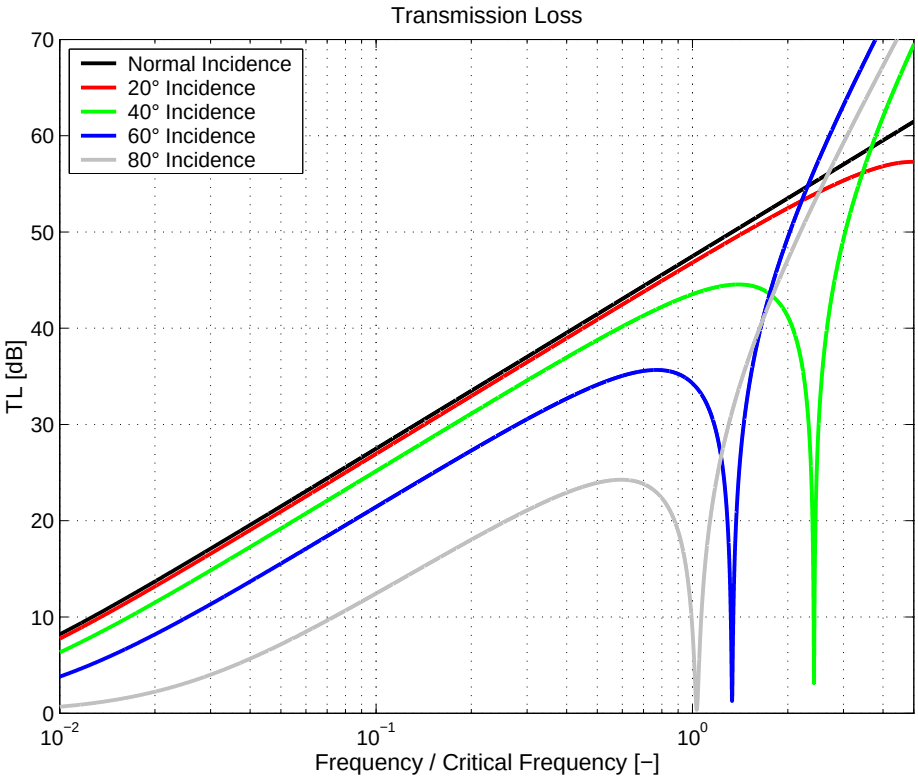

Figure 2.2: Transmission loss of an infinite single wall partition for various angles of incidence

calculated with the Rayleigh integral approach [Fahy85]. This requires the knowledge of the complex velocity distribution on the plate, which is composed of many superimposed modal contributions. Consequently, at low frequencies[6], the sound radiation is strongly governed by single vibrational eigenmodes. Each mode is associated with a certain radiation efficiency, which depends on the structural properties and boundary effects [Berry90, Wallace72]. In general odd modes are efficient radiators, resulting in a low transmission loss and even modes are less efficient radiators. Thus, at low frequencies, the TL behaviour of a finite partition is characterised by the succession of resonance and anti-resonance peaks. At high frequencies, where the structural response is governed by the superposition of multiple eigenmodes, the sound radiation from a finite partition is similar to the one from an infinite plate.

2.1.4 Sound Transmission through Infinite Double Wall Partitions

As it was shown in the previous chapter, for sub-critical frequencies, which in most cases cover a large part of the audible frequency range, the sound transmission of a single wall structure depends mainly on the mass per unit area of the employed partition. However, in practice it is often mandatory to have lightweight structures that provide a high sound reduction at the same time, two requirements being totally antipodal. A typical application would be an aircraft fuselage.

Nevertheless, it is possible to meet such requirements by employing partitions consisting of two

[6]The acoustical wavelength is large in comparison to a characteristic dimension of the plate.

or more walls being separated by fluid cavities. In a simple model for this configuration, the air in the cavity might be primarily seen as mechanical stiffness acting between the individual masses of the adjacent partitions. Depending on the excitation frequency, the cavity fluid leads to an effective decoupling of the structural behaviour of adjoining leaves and thus to a high transmission loss, but at resonance frequencies a strong coupling might occur, resulting in a sound reduction index that might be lower than the one given for a single leaf of the same total mass.

To demonstrate the behaviour of such systems a generic double wall partition, as depicted in Figure 2.3, is analysed theoretically. The setup consists of two infinite and homogeneous partitions separated by a distance d. It is assumed that the fluid on both sides as well as in the cavity has the same properties. The problem of sound transmission through the double wall system is solved in analogous manner as for the single wall partition.

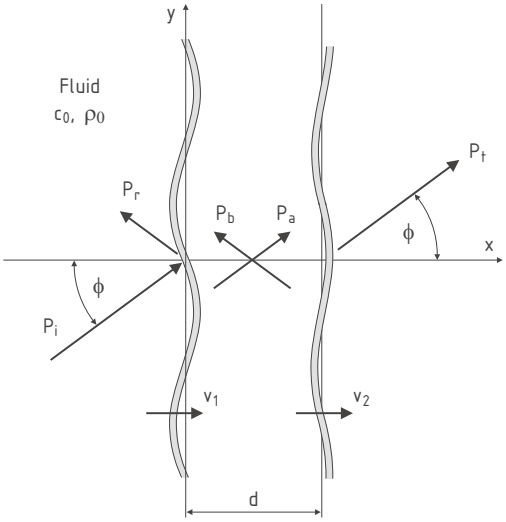

Figure 2.3: Transmission of oblique sound waves through an infinite double wall partition

The formulations for the incident, reflected and transmitted sound fields can be adopted from equation 2.16 to 2.18. In the cavity, the pressure results from the wave transmitted by the first partition as well as from a wave reflected by the second partition:

$$p_a(x,y) = \hat{P}_a \cdot e^{-jk_x x} \cdot e^{-jk_y y} \ , \tag{2.37}$$

$$p_b(x,y) = \hat{P}_b \cdot e^{jk_x x} \cdot e^{-jk_y y} \ . \tag{2.38}$$

With the plate velocities given by the following relations:

$$v_1(y) = \hat{V}_1 \cdot e^{-jk_y y} \ , \tag{2.39}$$

$$v_2(y) = \hat{V}_2 \cdot e^{-jk_y y} \ , \tag{2.40}$$

the boundary conditions obtained from the momentum equations applied to the first partition follow as:

$$v_1(0,y) = \hat{P}_i \cdot (1-r) \cdot \cos\phi \cdot e^{-jk_y y}/Z_0 \ , \tag{2.41}$$

$$v_1(0,y) = (\hat{P}_a - \hat{P}_b) \cdot \cos\phi \cdot e^{-jk_y y}/Z_0 \ , \tag{2.42}$$

and for the second partition as:

$$v_2(d,y) = (\hat{P}_a \cdot e^{-jk_x d} - \hat{P}_b \cdot e^{jk_x d}) \cdot \cos\phi \cdot e^{-jk_y y}/Z_0 \ , \tag{2.43}$$

$$v_2(d,y) = \hat{P}_t \cdot \cos\phi \cdot e^{-jk_x d} \cdot e^{-jk_y y}/Z_0 \ , \tag{2.44}$$

where $k_x = k \cdot \cos\phi$ and $k_y = k \cdot \sin\phi$ as defined in equation 2.10. The bending wave equation yields a further expression for each partition:

$$Z_{wp,1} \cdot \hat{V}_1 \cdot e^{-jk_y y} = \left(\hat{P}_i \cdot (1+r) - (\hat{P}_a + \hat{P}_b)\right) \cdot e^{-jk_y y} \ , \tag{2.45}$$

$$Z_{wp,2} \cdot \hat{V}_2 \cdot e^{-jk_y y} = \left(\hat{P}_a \cdot e^{-jk_x d} + \hat{P}_b \cdot e^{jk_x d} - \hat{P}_t \cdot e^{-jk_x d}\right) \cdot e^{-jk_y y} \ . \tag{2.46}$$

Resolving equations 2.16 to 2.18 and 2.37 to 2.46 for the pressure ratio of the transmitted to the incident sound field results in:

$$\frac{\hat{P}_t}{\hat{P}_i} = \frac{-2 \cdot j \cdot Z_0^2 \cdot \sin\left(kd \cdot cos\phi\right)/\cos^2\phi}{\tilde{Z}_1 \cdot \tilde{Z}_2 \cdot \sin^2\left(kd \cdot cos\phi\right) + Z_0^2/\cos^2\phi} \ , \tag{2.47}$$

with $\tilde{Z}_i$ used as an abbreviation for the term:

$$\tilde{Z}_i = Z_{wp,i} + Z_0 \cdot \left(1 - j \cdot \tan^{-1}\left(kd \cdot cos\phi\right)\right)/\cos\phi \ . \tag{2.48}$$

In the low-frequency range, when the acoustic wavelength is much greater than the partition separation distance, $kd \cdot cos\phi \ll 1$, equation 2.47 is simplified to:

$$\frac{\hat{P}_t}{\hat{P}_i} \approx \frac{-2 \cdot j \cdot Z_0^2/(kd \cdot cos\phi)}{\bar{Z}_1 \cdot \bar{Z}_2 + Z_0^2/(kd \cdot \cos\phi)^2} \ , \tag{2.49}$$

with $\bar{Z}_i = Z_{wp,i} \cdot cos\phi + Z_0 - j \cdot Z_0/(kd \cdot cos\phi)$. The term $\bar{Z}_i$ represents the combination of a structural wave impedance $Z_{wp,i}$ (defined by a stiffness, inertia and damping term as given in equation 2.15) with an acoustic damping term Z_0 and an acoustic stiffness term $Z_0/(kd \cdot cos\phi)$. The ratio of mechanical to acoustic stiffness can be expressed as:

$$\delta = \frac{D \cdot (k \cdot \sin\phi)^4/\omega}{Z_0/(kd \cdot cos\phi)} \ , \tag{2.50}$$

and is usually far less than unity for typical lightweight structures and air as fluid. Thus, the acoustical and mechanical damping as well as the mechanical stiffness can be neglected and the pressure transmission ratio $\hat{P}_t/\hat{P}_i$ is reduced to:

$$\frac{\hat{P}_t}{\hat{P}_i} \approx \frac{-2 \cdot j \cdot Z_0^2/(kd \cdot cos\phi)}{\omega \cdot Z_0 \cdot (m_1 + m_2)/kd - \omega^2 \cdot m_1 \cdot m_2 \cdot cos^2\phi} \ . \tag{2.51}$$

The above expression for the pressure ratio becomes infinite, when the denominator in equation 2.51 equals zero. This condition is fulfilled for the frequency ω_r:

$$\omega_r = \left(\frac{Z_0 \cdot c \cdot (m_1 + m_2)}{d \cdot m_1 \cdot m_2 \cdot cos^2\phi} \right)^{1/2} = \omega_0 \cdot cos^{-1}\phi \ . \tag{2.52}$$

The frequency ω_r is designated as the mass-air-mass resonance with ω_0 being the frequency of the fundamental mass-air-mass resonance for normal incidence. ω_r increases for decreasing values of partition separation distance d and is minimal when $m_1 = m_2$ for a total given mass $m_t = m_1 + m_2$.

For frequencies well below the mass-air-mass resonance the following conditions apply: $\omega \ll \omega_r$ and $\omega^2 \cdot m_1 \cdot m_2 \cdot cos^2\phi \ll (m_1 + m_2) \cdot Z_0 \cdot c/d$. Therefore, the term $\omega^2 \cdot m_1 \cdot m_2 \cdot cos^2\phi$ may be neglected in equation 2.51 and the pressure ratio becomes:

$$\frac{\hat{P}_t}{\hat{P}_i} \approx \frac{-2 \cdot j \cdot Z_0}{\omega \cdot (m_1 + m_2) \cdot \cos\phi} \ , \tag{2.53}$$

or equally expressed by the sound reduction index R:

$$R(\phi) \approx R(\phi, m_t) \ \ [dB] \ , \tag{2.54}$$

which is similar to the behaviour of a single-wall partition with the mass $m_t = m_1 + m_2$.

If the frequency is approaching the mass-air-mass resonance ω_r, the mechanical damping of the partitions may not be neglected anymore. At the frequency $\omega = \omega_r$ the pressure ratio is:

$$\frac{\hat{P}_t}{\hat{P}_i} = \frac{-2 \cdot j \cdot Z_0/cos\phi}{\omega \cdot (\eta_1 \cdot m_2 + \eta_2 \cdot m_1) + Z_0 \cdot (m_1^2 + m_2^2)/m_1 m_2 cos\phi} \ . \tag{2.55}$$

In the frequency range above the resonance, $\omega^2 \cdot m_1 \cdot m_2 \cdot cos^2\phi > (m_1 + m_2) \cdot Z_0 \cdot c/d$, the pressure ratio is inertia dominated and can be approximated as:

$$\frac{\hat{P}_t}{\hat{P}_i} \approx \frac{2 \cdot j \cdot Z_0 \cdot \omega_0^2}{\omega^3 \cdot \cos^3\phi \cdot (m_1 + m_2)} \ , \tag{2.56}$$

with the corresponding sound reduction index given by:

$$R(\phi) \approx R(\phi, m_t) + 40 \cdot \log((\omega/\omega_0) \cdot \cos\phi) \ \ [dB] \ . \tag{2.57}$$

As the pressure ratio is proportional to the third power of the frequency, a doubling of frequency is increasing the sound reduction index by 18 dB.

For the high-frequency range the variation of sound transmission with the frequency has to be analysed by using the exact solution of equation 2.47. In general, it can be said that the sound transmission behaviour is characterized by a succession of acoustic anti-resonances and resonances occurring in the cavity. The anti-resonance and resonance condition are $kd \cdot \cos\phi =$

$(2n-1)\cdot\pi/2$ and $kd\cdot\cos\phi = n\cdot\pi$ respectively, with n being any integer greater than zero. Neglecting the stiffness and damping terms in equation 2.47, the estimation for the pressure transmission ratio at anti-resonance frequencies becomes:

$$\frac{\hat{P}_t}{\hat{P}_i} \approx \frac{2\cdot j\cdot Z_0^2}{\omega^2\cdot m_1\cdot m_2\cdot\cos^2\phi}\ . \tag{2.58}$$

Hence, the sound reduction index takes the approximate form of:

$$R(\phi) \approx R(\phi, m_1) + R(\phi, m_2) + 6\ \ [dB]\ , \tag{2.59}$$

and increases with a rate of 12 dB per octave. Equation 2.59 represents the upper limit for the transmission loss behaviour in the high-frequency range.

At cavity resonance frequencies it is derived from equation 2.42 and 2.43 that the displacement of both partitions must be the same and the sound reduction index follows as:

$$\frac{\hat{P}_t}{\hat{P}_i} = \frac{2\cdot Z_0/\cos\phi}{Z_1 + Z_2 + 2\cdot Z_0/\cos\phi}\ . \tag{2.60}$$

With the assumption that the denominator in the above equation is dominated by the inertia term, the sound reduction index corresponds to the one given by a single leaf with the mass $m_t = m_1 + m_2$:

$$R(\phi) \approx R(\phi, m_t)\ \ [dB]\ . \tag{2.61}$$

The general variation of the sound reduction index with the frequency is shown in the following two figures considering as example a double wall partition made of 1 mm thick aluminium sheets. The same material properties as for the previous example are used. The separation distance of the leaves is 50 mm. Figure 2.4 shows the influence of various incidence angles (normal incidence, 20°, 40° and 60°) for frequencies ranging from 50 Hz to 20 kHz.

Below the fundamental mass-air-mass resonance, which occurs here at 231 Hz, the behaviour is that of a single leaf with $m_t = m_1 + m_2$. At the resonance frequencies the sound transmission behaviour is very much similar to the coincidence phenomenon. Above the fundamental mass-air-mass resonance and each cavity resonance for normal incidence (in the example occurring at multiples of 3,4 kHz) exists a frequency and an angle of incidence where a strong coupling between the cavity and the partition leaves occurs, resulting in a local TL minimum. Thus, for a diffuse field excitation, the sound transmission is controlled by resonant effects. Coincidence effects are also observed as for a single leave partition. They are particularly strong for systems consisting of identical panels. In the given example this is evident for the case with 60° incidence, where the coincidence occurs at a frequency of 15484 Hz.

Illustrated in Figure 2.5 is the dependency of the sound reduction index on the mass ratio $\lambda = m_1/m_2$. Using the same configuration as in the previous example and a normal incident sound field, the overall weight per unit area of the double wall partition is kept constant (5,4 kg/m^2), while varying the thickness ratio of the partitions. For identical partitions with $\lambda = 1$ the value of the sound reduction index at the mass-air-mass resonance ω_0 is minimized, whereas in the frequency range where cavity resonances occur, the upper limit of sound reduction is maximised by making $m_1 = m_2$. For values of m_1/m_2 or $m_2/m_1 \gg 1$ the transmission loss

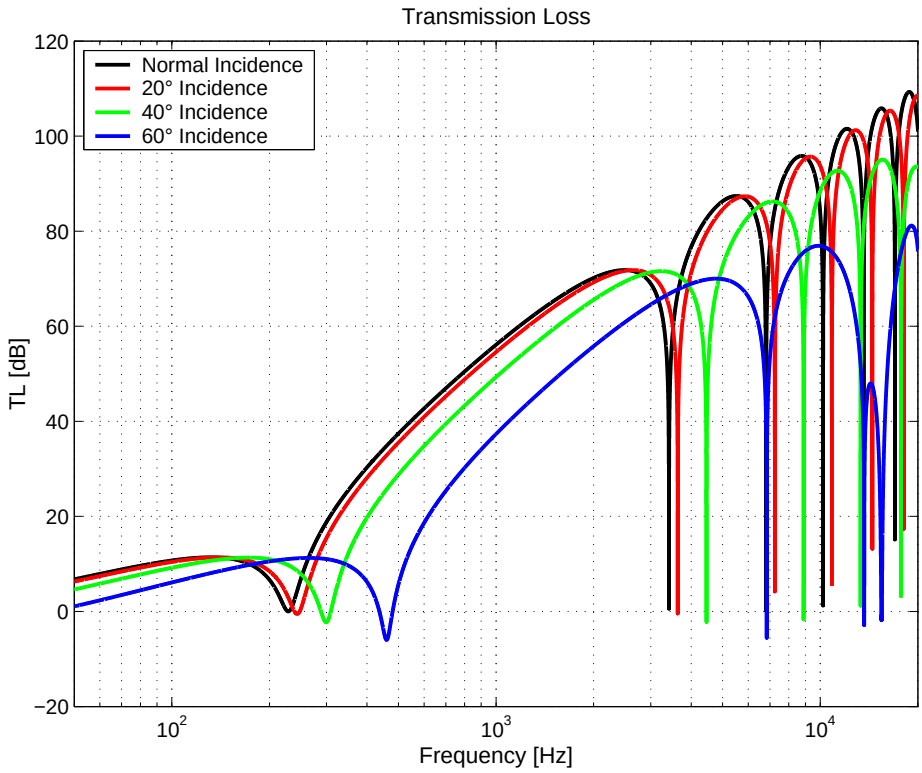

Figure 2.4: Transmission loss of an infinite double wall partition for various angles of incidence

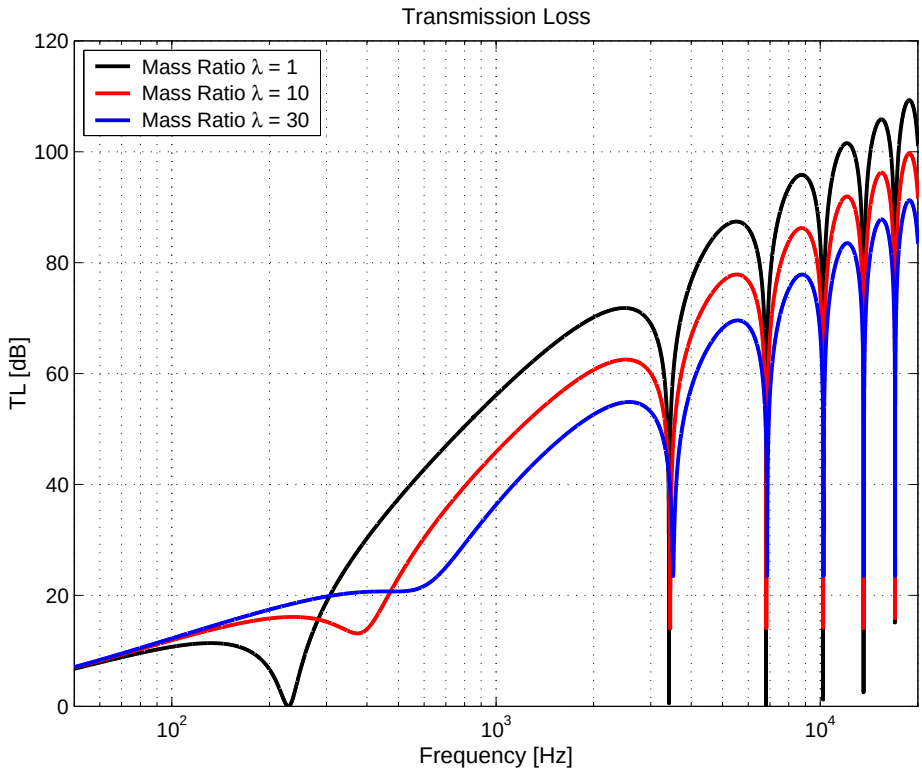

Figure 2.5: Transmission loss of an infinite double wall partition for various mass ratios

is increased at ω_0 but at the same time the maxima at cavity anti-resonances frequencies are lowered.

In addition, it should be noted that in practice layers of porous sound-absorbing materials are disposed into cavities to minimise resonant sound transmission. Depending on the material type and the frequency range the resonant coupling of the cavity to the partition leaves can be reduced to a large extent by the additional acoustic dissipation [Beranek49, Fahy85, Ingard94].

2.2 Aircraft Interior Noise

Aircraft interior noise represents an important point in the design process and operation of aircraft as intense interior noise levels may result in a feeling of discomfort for the passengers, increase the crew workload and fatigue, interfere with the internal crew communication and disturb the proper functioning of electronic equipment. Noise control measures are therefore required to assure an acceptable interior noise environment. However, they usually also result in penalties as increased structural weight or reduced cabin volume, which makes it difficult to determine the best compromise in efficient noise reduction and inevitable penalties.

2.2.1 Noise Sources

Main sources of interior noise are various contributions from the propulsion system such as the jet mixing and turbomachinery noise, the turbulent aerodynamic boundary flow around the vehicle and different aircraft systems such as hydraulics or air conditioning for instance. External noise sources as the engines or the turbulent flow around the fuselage impinge directly the fuselage skin and are propagated as airborne and structure-borne noise into the interior. Mechanical sources such as an unbalanced engine or structural, flow-induced vibrations are transmitted as structure-borne noise along the fuselage and radiated into the cabin. Each source has its own characteristics and local contributions are also dependant on the flight conditions. A short description of the main sources for modern subsonic civil aircraft fitted with high bypass-ratio turbofan jet engines is given in the following sections. A comprehensive summary can be found in the textbooks of [Bräunling04, Groeneweg95, Lilley95, Mixson95].

Jet Mixing Noise

A significant type of noise for any jet aircraft is the jet mixing noise. It is caused by the turbulent mixing process of the engine's exhaust stream with the ambient air. As indicated by *Lighthill's acoustic analogy* [Lilley95], the jet mixing noise is a strong function of jet exhaust velocity, namely depending on the sixth to eighth power of velocity. The development of engines with greater propulsive and fuel efficiency during the last decades led to increased bypass ratios, hence reducing the average exhaust velocity and jet noise levels. Even so, jet noise remains a main source of aircraft noise and its suppression is still subject of intensive studies.

The mixing process of the hot jet core and cold bypass exhausts with the atmosphere produces a broadband, haystack-shaped sound frequency spectrum. The shape of the spectrum reflects the fact that the turbulence structures that comprise the mixing process vary considerably,

increasing in size progressively downstream of the exhaust nozzle and decaying in intensity as the average exhaust velocity decreases and the mixing becomes complete. Due to convection and refraction effects the maximum sound intensity is radiated at oblique angles to the downstream direction of the jet. The sound perturbations impinging the fuselage structure may be considered with a spatially coherent excitation having a certain directivity pattern for a given flight condition. In comparison to a subsonic turbulent boundary layer noise excitation, jet noise is more efficient at exciting structural vibrations at lower frequencies and especially in the aircraft aft section interior noise may be dominated by jet noise components.

Turbomachinery Noise

In modern, high bypass ratio engines the major turbomachinery noise contribution is due to the fan. It contains three components: pure tones at the blade-passing frequency (BPF) and its harmonics, broadband noise and *buzz-saw noise*[7]. Turbomachinery noise represents the principle source of tonal noise in the cabin. Secondary sources such as the compressor and turbine stage typically produce only little contribution to the overall radiated turbomachinery noise.

The dominant sources of fan tone noise at the blade-passing frequency and its harmonics are usually excited by a rotor-stator interaction, where coherent parts of fan wakes interact with downstream stators and struts. Its fundamental frequency is given by the relation $f_{BPF} = n \cdot B$, where B is the number of fan blades and n the rotational speed of the fan shaft. The polar directivity pattern for discrete tones can be highly irregular depending on the actual source mechanism and frequency. Broadband noise is mainly due to turbulent flow inhomogeneities. The turbulence may result from the inflow in the engine, the inlet boundary layer, the blade wakes, or the blade tip vortices interacting with each other. To suppress fan and other internally generated turbomachinery noise the inlet and fan exhaust ducts of modern commercial transport aircraft are equipped with acoustic liners designed to absorb the sound generated by the various sources.

The third major component of turbomachinery noise is due to the fact that modern aero-engines use transonic fans. The fans are operated with supersonic relative speeds at the tips resulting in a further source known as buzz-saw noise [McAlpine01]. The flow approaching each blade passes through the shock waves associated with the adjacent blades and, as no two blades can be made absolutely uniform, the resultant shock pattern is unique to each blade and varies around the rotor due to the manufacturing tolerance. Hence, tonal sound is generated at a series of frequencies, which are multiples of the rotation speed. The dominant acoustic energy is concentrated at frequencies below and at the BPF. With higher local Mach numbers at the blade tips, low order harmonics tend to become the predominant source. The actual sound radiation is also strongly dependant on highly non-linear duct propagation phenomena as the rotating shock-wave pattern is spread in upstream direction through the inlet duct. Under certain conditions, mainly during take-off and climb, the buzz-saw noise mechanism can dominate the forward arc of the polar directivity radiation pattern as the main acoustic energy is radiated at angles of around 45° with respect to engine centreline [Léwy00]. Thus, buzz-saw noise can be clearly audible for the passengers, especially in the forward cabin.

[7] Also described as multiple pure tones or combination tones in literature.

Turbulent Boundary Layer Noise (TBL)

In cruise condition the turbulent boundary layer pressure field acting on the fuselage skin is in general the dominant source of noise in the forward and mid-cabin of high subsonic and supersonic commercial aircraft. For interior noise it represents the only non-engine related perturbation source. The structure of the turbulent pressure field depends on the Reynold and Mach numbers, the surface roughness, the pressure gradient and the velocity field outside the boundary layer. TBL noise is highly statistical in both space and time. Thus, depending on the flight condition and the location along the fuselage axis, its spectral density contains broadband components from below 100 Hz up to 2 kHz. To predict the sound transmission through a structure excited by a TBL pressure field one needs to know the local properties of the turbulent boundary layer, which is still the subject of intense research. A first semi-empirical description of the TBL field was derived with the Corcos formulation, which is based on the cross spectral densities of the pressure fluctuations [Corcos63]. For more approximate predictions less accurate empirical relations might be used [Ungar77].

Structure-Borne Noise

Structural vibrations, acting on distant regions of the airframe and being transmitted as vibration into the fuselage and the cabin, represent an additional source of interior noise. In contrast to the aforementioned components, which can be resumed under the term airborne noise, they are referred to as structure-borne noise. Known causes are, for instance, engine unbalance forces, especially on aircraft with aft engine-mount configurations and unsteady aerodynamic flows such as the wake of a propeller striking the wing or the tail. Further known sources are hydraulic pumps, air conditioning systems and other rotating equipment. Structure-borne noise is mainly associated with discrete perturbation frequencies.

2.2.2 Sound Transmission

The various airborne and structure-borne primary excitations impinging the fuselage are filtered by the structural response and then radiated into the cabin. Figure 2.6 shows an exemplary interior noise spectrum up to 600 Hz for a typical single aisle aircraft. It was measured in the forward cabin for two different flight conditions, climb and cruise. During the take off and climb phase tonal noise components due to a strong buzz-saw noise excitation are clearly audible in the broadband noise spectrum. The fundamental frequency is 79 Hz and corresponds to the shaft speed of the fan. In cruise condition all but one tonal component disappear, but the overall broadband noise caused by the jet and TBL noise primary perturbations is increased for frequencies above 200 Hz. The fundamental buzz-saw noise tone does not disappear, indicating a possible structure-borne sound transmission in this particular case and is reduced to 62 Hz as the engine thrust and speed is reduced for cruise. By cancelling the buzz-saw noise tones and reducing the broadband noise level the aircraft interior noise and the passenger comfort could be largely improved.

For airborne noise components, which are the major contributors to interior noise, the structural response characteristic may be described with the transmission loss behaviour of the aircraft sidewall [May85]. In passenger aircraft the sidewall represents a double wall multi-element system consisting of the fuselage structure, fibreglass blankets, impervious septa, an

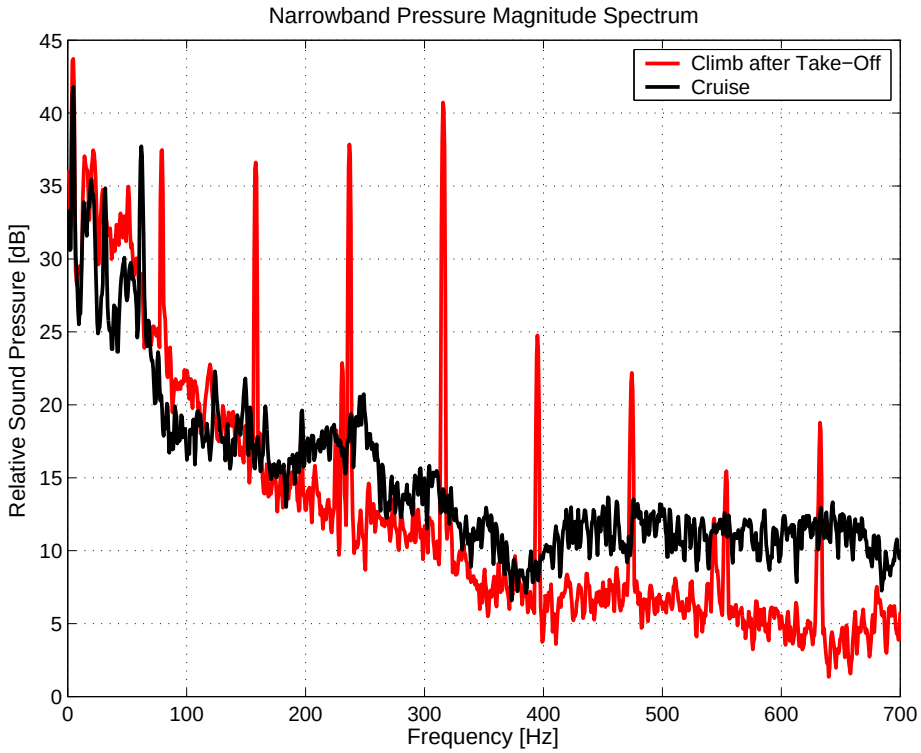

Figure 2.6: Single aisle interior noise spectrum

interior decorative trim panel and multi-pane windows. The fibreglass blankets are used for interior noise control issues and also provide the required heat insulation.

In contrast to the analytical mass law presented in Chapter 2.1.4 the sound transmission behaviour is more complex as a conventional aircraft structure consists of the fuselage skin, which is supported by longitudinal and circumferential stiffeners (stringers and frames). Detailed analytical models and measurements have shown that at low frequencies the skin and stiffeners vibrate in phase with the same magnitude. Thus, the mechanical properties can be smeared over a certain sidewall area and an equivalent orthotropic structural behaviour can be assumed. At high frequencies the structural wavelength becomes much shorter than the stiffener spacing and the stiffener motion can be neglected in comparison to the out-of-plane displacement of the skin. Hence, acoustic perturbations are mainly transmitted by vibrating, local skin patches. The validity of the simplifications is dependent on the actual mechanical properties of the considered fuselage structure. In the mid-frequency range in-between those behaviours both the skin and stiffener motions are strongly coupled and must be considered in detail for an analysis of sound transmission.

Some typical transmission loss curves for different aircraft sidewall structures available from literature [Tran95, Wilby73] are shown in Figure 2.7. Their common characteristic is the rather poor reduction of sound transmission in the low-frequency range up to 400 or 500 Hz. As passive treatments like fibreglass wool are not providing efficient absorption capabilities in this particular range of frequency [Thomas02], the transmission loss is mainly governed by the mass law with the structural mass of the aircraft sidewall being the main parameter. On the other hand, structural mass represents also a global variable in the overall aircraft design process

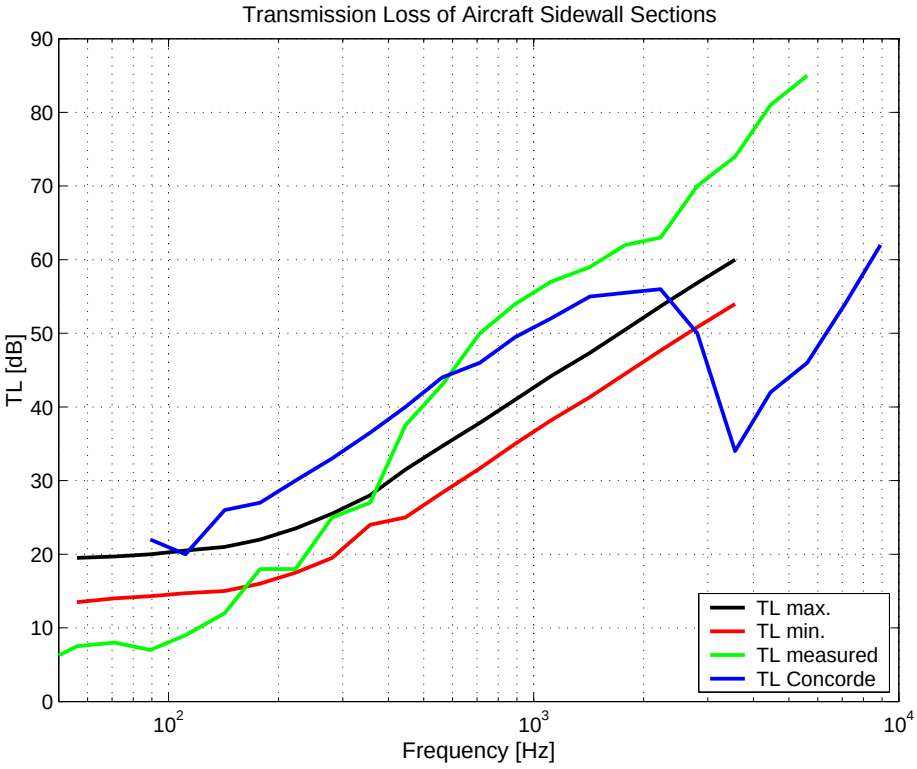

Figure 2.7: Transmission loss of various aircraft sidewall sections

and important requirements such as reduction of operating costs, fuel efficiency and decrease of environmental emissions can be directly achieved through a structural weight reduction. However, as a drawback to those benefits, a further reduction of structural weight will also lead to an increase of interior noise levels at low frequencies. It is expected that this problem will occur with future composite fuselages, thus necessitating a global design procedure taking into account the impact of novel structural concepts on the interior acoustics.

2.2.3 Noise Control

Interior noise control can be either achieved by reducing the perturbation strength directly at the source level or by attenuation during the sound transmission and in the cabin. As the first solution is extremely difficult to realise, conventional approaches are mostly based on passive treatments of the airframe, thus reducing the sound transmission through the fuselage structure. Active solutions, as on some turboprop aircraft[8], are still only used sporadically nowadays. In all cases however, the acoustic absorption properties of the cabin are also very important and are necessary to achieve reasonable interior sound levels. The trim panel, floor, ceiling and seats are designed to provide sufficient sound absorption characteristics.

The most common solution used for interior noise control is based on additional sidewall and fuselage treatments such as fibreglass insulation and constrained layer damping applied to the

[8]ANC systems to eliminate low-frequency propeller tones are, for instance, available on the Saab 340 [McKenna93] and 2000 [Lagö02] or the Bombardier Q Series Dash 8 and Raytheon Beech King Air 350.

fuselage skin [Mixson95] or the trim. The additional treatments have to satisfy numerous constraints such as thermal insulation, fireproofing, moisture-resistance and, above all, must have minimum weight and volume [May85]. Fibreglass blankets meet all the above requirements and are available in various densities from about 6 to 24 kg/m^3. Fibreglass is most efficient against broadband noise at frequencies greater than 500 Hz, where it provides a good additional noise reduction compared to the untreated double wall section. An improvement of the noise reduction at lower frequencies requires additional weight and can be achieved by introducing an impervious septa, such as lead-impregnated vinyl, between the layers of porous material.

In addition to the use of sidewall treatments, the noise transmission and acoustic radiation characteristics of fuselage structures can be modified by the addition of mass, damping or stiffness [Mixson95]. Damping is the most common method. The existing damping in fuselage skins is usually very small with values of about 1% and can be raised up to 5% by adding damping material (i.e. aluminium-backed tape) to the interior side of the skin, between the ring frames and stringers. This method is particularly adapted for resonant responses, for example the hydrodynamic coincidence between the turbulent boundary layer and local skin modes. The additional damping and mass change the dynamical behaviour of the structure, thus attenuating resonant excitations. However, appropriate materials have to be used as the fuselage skin temperature can decrease below -50°C during cruise. Measurements on large, modern jet aircraft have shown that interior sound pressure levels could thus be reduced by 3 to 8 dB above 800 Hz. Damping material can also be applied to other structural parts if their sound transmission and radiation behaviour is dominated by resonant components.

Further passive solutions are also utilised in aircraft applications. Dynamic vibration absorbers with tuned resonance frequencies are mainly used to reduce tonal noise components during cruise. Typical applications are the reduction of propeller noise in turboprop aircraft, where absorbers tuned to low harmonics of the propeller noise are installed on the ring frames and trim panels [Wright04]. In airplanes with rear-mounted turbofan engines control of structure-borne noise transmission can be achieved with absorbers mounted close to the engine pylon. Furthermore, in all kind of engine mounting systems vibration isolators made of elastomeric material or metal are used to attenuate structure-borne noise components excited by engine out-of-balance forces [Mixson95]. On trim panels vibration isolators are used to attach the panels on the ring frames and have been proved to provide a good reduction in sound transmission at higher frequencies.

Active noise and vibration control systems provide a novel approach to reduce the interior noise levels. In contrast to passive treatments better attenuations in sound transmission can be obtained with well designed active solutions. In addition, they may also require less supplementary weight and volume. An overview of various active systems described in literature is presented in Chapter 2.4. Many of those solutions are based on the piezoelectric principle, which is shortly described in the next chapter.

2.3 Piezoelectricity

In general the term *piezoelectricity* designates the physical relationship between a mechanical deformation and an electric charge that can be observed for some crystal materials. When such a material is deformed due to a mechanical loading, a relative shift of the positive and

negative ions in the crystal lattice occurs, producing an electric charge on the material's surface as shown by the scheme in Figure 2.8. This property is called the *direct piezoelectric effect* and was discovered in 1880 by Pierre and Jacques Curie on materials such as Rochelle salt, tourmaline or quartz. On the contrary, when an electric field is applied across the crystal lattice, the material deforms and becomes strained. The designation for this phenomenon is *converse piezoelectric effect*. The special ability of converting electrical into mechanical energy and vice versa, for static as well as highly dynamic processes, makes piezoelectric materials especially suited to be used as connection elements between the information processing and mechanical parts of control systems for open- or closed-loop operation. A more general overview of the piezoelectric phenomenon is given for instance in [Cady64, Rosen92], whereas the textbooks of Janocha and Preumont [Janocha92, Preumont97] are more focused on applications as actuator or sensor in active control systems.

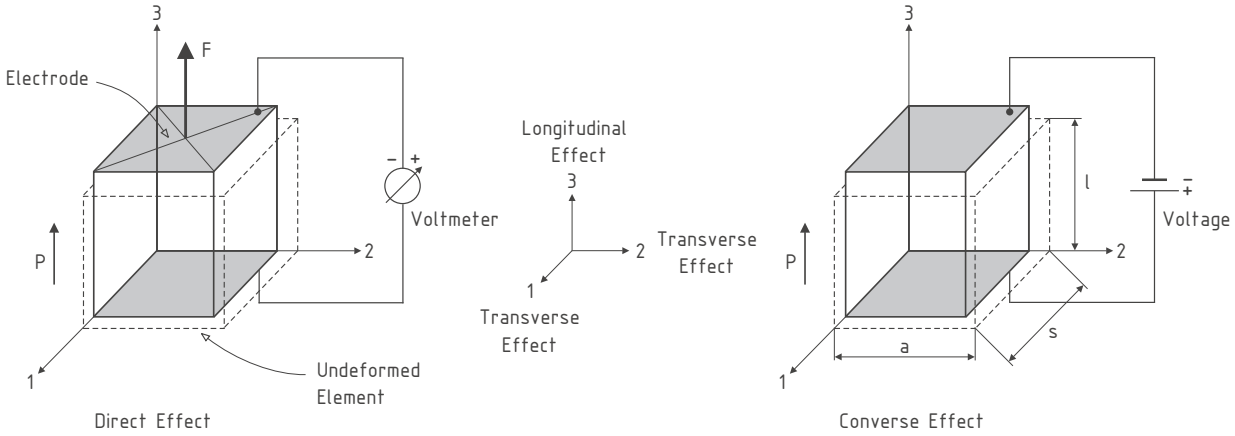

Figure 2.8: Direct and converse piezoelectric effect

Besides the natural crystals mentioned above, synthetic materials exhibiting a strong piezoelectric effect are lead zirconate titanate (PZT), barium titanate and polyvinylidene flouride polymer (PVDF) [Sessler81] among others. From this selection, PZT, a polycrystalline ceramic sintered from metallic oxide powders, is the most widely used piezoelectric material in industry.

On a nanoscopic scale the PZT crystal's unit cell, made up from negatively and positively charged ions, has, depending on the temperature, two distinctive states. Above the so-called Curie temperature[9] the unit cell possesses a geometrical centre of symmetry, which also corresponds to the centres of positive and negative electric charge. When the unit cell is deformed, no relative shift between the respective charges occurs. Thus, in this phase, the ceramic features a normal isotropic behaviour and the piezoelectric phenomenon does not appear.

Only below the Curie temperature, a mechanical deformation of the unit cell results in a shift of electric charges and vice versa. In this state the so-called spontaneous polarisation occurs. The structure of the crystal lattice is rearranged and the centro-symmetry of the unit cell is not maintained. The centres of the positive and negative charge are shifted relative to each other, resulting in an electric dipole with a polarisation direction pointing from the centre of the negative charge to that of the positive charge. Yet, due to the spatial random distribution of dipoles within the crystal, the net dipole of the ceramic on a macroscopic

[9]For PZT-ceramics the Curie temperature is around 165°C.

scale is still zero and the material does not show a piezoelectric behaviour. Therefore, during the manufacturing process, the dipoles are aligned by applying a strong electric field to the ceramic. This particular poling process leads to a remanent polarisation on a macroscopic scale and remains after the sintering process and removal of the poling field. As long as the ceramic is not exposed to extreme temperature, electric or mechanical loads, the material remains permanently piezoelectric and can be used to convert electric to mechanical energy or vice versa.

In a poled material like PZT, the piezoelectric behaviour is orthotropic with respect to the poling direction P (see Figure 2.8). Assuming that the material is poled in the direction of the 3-axis and a positive electric field is applied along the same axis, the material will expand in direction of the electric field by Δl and shorten in the plane normal to the field by Δs and Δa. The designations for these phenomena are longitudinal and transverse effect. Both will always appear conjointly and can be described by the following linear relations between the displacement and the voltage U applied across the electrodes in the poling direction:

$$\text{Longitudinal effect: } \Delta l \sim E_{el} \cdot l = U \ , \tag{2.62}$$

$$\text{Transverse effect: } \Delta s \sim E_{el} \cdot s = \frac{s}{l} \cdot U \ . \tag{2.63}$$

The transverse effect is also observed in the 2-direction, hence $\Delta a \sim E_{el} \cdot a = a \cdot U/l$. The term E_{el} denotes the resulting electric field strength and is defined as the ratio of voltage U to the ceramic thickness l in the 3-direction. This particular interaction between mechanical and electrical quantities has to be taken into account when examining the mechanical behaviour of the piezoelectric continuum. A number of assumptions are made to derive the basic governing equations:

- In principle, the behaviour of a piezo ceramic is non-linear due to hysteresis and saturation effects within the material. For the present application, it is assumed that non-linearities can be neglected. Depolarisation due to mechanical, thermal or electrical overloads must be prevented.
- Pyroelectric[10] and thermal effects are not taken into account, as it is assumed that the material is exposed only to small temperature variations.

The mechanical behaviour of a linear elastic material placed in a zero electric field is described by Hooke's law:

$$\epsilon = S \cdot \sigma \ , \tag{2.64}$$

where ϵ and σ are the vectors containing the strain and stress state of the elastic body. Strain and stress state are coupled through the compliance matrix S of the material.

In a stress-free dielectric medium the relation between the electric flux density D (electric charge per unit area) and the electric field strength E_{el} is given by:

[10] An electric charge resulting from a temperature variation and vice versa.

$$D = \varepsilon \cdot E_{el} \ . \tag{2.65}$$

Both quantities are coupled by the matrix ε, which is composed of the material's dielectric permittivity constants. The permittivity is often expressed in relation to the one of vacuum, which is $\varepsilon_0 = 8,85 \cdot 10^{-12}$ F/m.

For a piezoelectric material both types of behaviour are coupled according to the following relationship:

$$\epsilon = S \cdot \sigma + d^T \cdot E_{el} \ , \tag{2.66}$$

$$D = d \cdot \sigma + \varepsilon^\sigma \cdot E_{el} \ . \tag{2.67}$$

Equation 2.66 provides the basis to describe the application as actuator, whereas equation 2.67 represents the sensor configuration. In matrix notation, they can be rewritten as:

$$\begin{pmatrix} \epsilon \\ D \end{pmatrix} = \begin{bmatrix} S^E & d^T \\ d & \varepsilon^\sigma \end{bmatrix} \cdot \begin{pmatrix} \sigma \\ E_{el} \end{pmatrix} \ . \tag{2.68}$$

The matrix d contains the piezoelectric charge coefficients describing the amount of strain induced by an electric field in an unstressed material or the amount of electric flux density created by a mechanical stress in a zero electric field. ε^σ is the permittivity matrix for a constant stress state, whereas S^E denotes the mechanical compliance matrix for a constant electric field. In a Cartesian coordinate system, as illustrated in Figure 2.8, the strain and stress vector ϵ and σ, the electric flux density D and field strength E_{el} given in equation 2.68 are defined as:

$$\epsilon = \begin{pmatrix} \epsilon_{11} \\ \epsilon_{22} \\ \epsilon_{33} \\ 2 \cdot \epsilon_{23} \\ 2 \cdot \epsilon_{31} \\ 2 \cdot \epsilon_{12} \end{pmatrix} \ , \quad \sigma = \begin{pmatrix} \sigma_{11} \\ \sigma_{22} \\ \sigma_{33} \\ \sigma_{23} \\ \sigma_{31} \\ \sigma_{12} \end{pmatrix} \ , \quad D = \begin{pmatrix} D_1 \\ D_2 \\ D_3 \end{pmatrix} \ , \quad E_{el} = \begin{pmatrix} E_{el,1} \\ E_{el,2} \\ E_{el,3} \end{pmatrix} \ . \tag{2.69}$$

With the assumption of a poling along the 3-axis, the coupling matrix d and the dielectric matrix ε^σ for a constant stress state take the following forms:

$$d = \begin{bmatrix} 0 & 0 & 0 & 0 & d_{15} & 0 \\ 0 & 0 & 0 & d_{15} & 0 & 0 \\ d_{31} & d_{31} & d_{33} & 0 & 0 & 0 \end{bmatrix} \ , \tag{2.70}$$

and

$$\varepsilon^\sigma = \begin{bmatrix} \varepsilon^\sigma_{11} & 0 & 0 \\ 0 & \varepsilon^\sigma_{11} & 0 \\ 0 & 0 & \varepsilon^\sigma_{33} \end{bmatrix} \ . \tag{2.71}$$

The first index used for the components of the coupling matrix refers to the axis of the electric field and the second one to the considered mechanical degree of freedom. Thus, the term d_{31} corresponds to the transverse effect and d_{33} to the longitudinal effect. Similarly there exists a shear effect d_{15}, when an electric field is applied along the 1- or 2-axis of the piezo. For the matrix ε^{σ}, the first index denotes the direction of the electric flux density and the second one the direction of the applied electric field.

The components of the elastic compliance matrix S^E for a constant electric field can be expressed by the material properties in terms of Young's moduli E, shear moduli G and Poisson's ratios ν, resulting in the expression:

$$S^E = \begin{bmatrix} 1/E_{11} & -\nu_{12}/E_{11} & -\nu_{13}/E_{11} & 0 & 0 & 0 \\ -\nu_{12}/E_{11} & 1/E_{11} & -\nu_{13}/E_{11} & 0 & 0 & 0 \\ -\nu_{13}/E_{11} & -\nu_{13}/E_{11} & 1/E_{33} & 0 & 0 & 0 \\ 0 & 0 & 0 & 1/G_{23} & 0 & 0 \\ 0 & 0 & 0 & 0 & 1/G_{23} & 0 \\ 0 & 0 & 0 & 0 & 0 & 2\cdot(1+\nu_{12})/E_{11} \end{bmatrix} . \tag{2.72}$$

Nowadays, both the direct and converse piezoelectric effect are applied to a wide range of technical applications, ranging from audio buzzers as used in diverse electronic devices over quartz watches, microphones and accelerometers to ultrasonic transducers. For the purpose of active control the piezoelectric effect is either used in a sensor or actuator configuration. In this domain, PZT-ceramics and PVDF-foils are the most common piezoelectric materials. Some exemplary properties are listed in the table below. For comparison Barium Titanate and Quartz are also mentioned.

Table 2.1: Piezoelectric properties of PZT-5H, PVDF, Barium Titanate and Quartz

	PZT	**PVDF**	**Barium Titanate**	**Quartz**
Piezoelectric constant d_{31} [m/V]:	$-274\cdot10^{-12}$	$23\cdot10^{-12}$	$-35\cdot10^{-12}$	*
Piezoelectric constant d_{33} [m/V]:	$593\cdot10^{-12}$	$-33\cdot10^{-12}$	$86\cdot10^{-12}$	*
Relative permittivity $\varepsilon^{\sigma}_{11}/\varepsilon_0$ [-]:	3130	n/a	2920	4,52
Relative permittivity $\varepsilon^{\sigma}_{33}/\varepsilon_0$ [-]:	3400	12,4	168	4,68
Density [kg/m^3]:	7500	1800	6020	2650
Young's modulus [N/m^2]:	$6,0\cdot10^{10}$	$2,0\cdot10^{9}$	$1,2\cdot10^{11}$	$7,8\cdot10^{10}$
Max. tensile strain [%]:	0,13	≈ 50	n/a	$\approx 0{,}2$
Max. electric field [V/mm]:	1000	$3\cdot10^{4}$	n/a	n/a
Curie temperature [°C]:	195	100	≈ 120	583

* Piezoelectric coupling matrix d for Quartz: $d_{11} = -2,3\cdot10^{-12}$ m/V, $d_{14} = -0,67\cdot10^{-12}$ m/V, $d_{26} = 4,6\cdot10^{-12}$ m/V, $d_{12} = -d_{11}$ and $d_{25} = -d_{14}$. The remaining terms are equal to zero.

On closer examination of the material's relative properties, it becomes clear to what purpose each type is adapted. Compared to PZT, PVDF-foils exhibit relatively small piezoelectric constants as well as a low density and a low Young's modulus. For this reason, the efficiency of PVDF in converting electrical to mechanical energy is not very high and the use as an actuator on typical engineering structures is not very suitable. Nevertheless, the low stiffness,

low weight and high tensile strength particularly enables PVDF-foils to be used as sensor. Possible applications can be found in [Henrioulle03, Lee90, Lee91].

PZT ceramics are commonly used in commercially available actuators and sensors. The main actuator types are the stacked design and the laminar patch, which use the d_{33}- and the d_{31}-piezoelectric effect, respectively. Usually the longitudinal effect is twice as large as the transverse effect and is the preferred design, as a greater amount of force can be generated in this configuration. However, especially in the field of active structural acoustic control, the piezo patch configuration has some advantages and is often used. The basic principles for the stacked design and laminar arrangement are presented in the following sections. Alternative designs are hybrid and shear actuators. In hybrid actuators an integrated motion amplifier increases the limited actuator stroke in favour of the generated force [Janocha92, Rapp96]. The amplifying mechanism is mostly based on the leverage principle or on flexural devices taking advantage of the ratio between the longitudinal and lateral displacements in beam-like solid materials. An implementation of such a system has been realized for the actuation of higher harmonic control flaps in helicopter blades [Lorkowski01]. Designs using the shear deformation perpendicular to the electric field also reveal a great potential, since the shear effect d_{15} is approximately equal to $d_{15} \approx d_{33} + |d_{31}|$. Though, due to the complex manufacturing process, a commercial application is still challenging to implement and to realise [Rapp96].

Actuator Stack Design

Actuators in stack design make use of the d_{33}-effect. Since the maximum expansion in tension can only reach values in the order of 0,1 to 0,13% for typical PZT-ceramics, large actuator dimensions are required to achieve a reasonable stroke. However, this configuration would require high driving voltages to obtain an adequate electric field through the length of the actuator. For this reason stack actuators are made from a number of stacked, thin piezoceramic discs. The discs are separated by interjacent electrodes and paired in couples having an opposite poling direction P as illustrated by the scheme in Figure 2.9. With this particular arrangement, the displacement of each single element is additive and a relative low voltage is sufficient to generate the required electric field within each individual layer. To compensate the low tensile strength of PZT-ceramics, a compression preload is usually induced in the actuators.

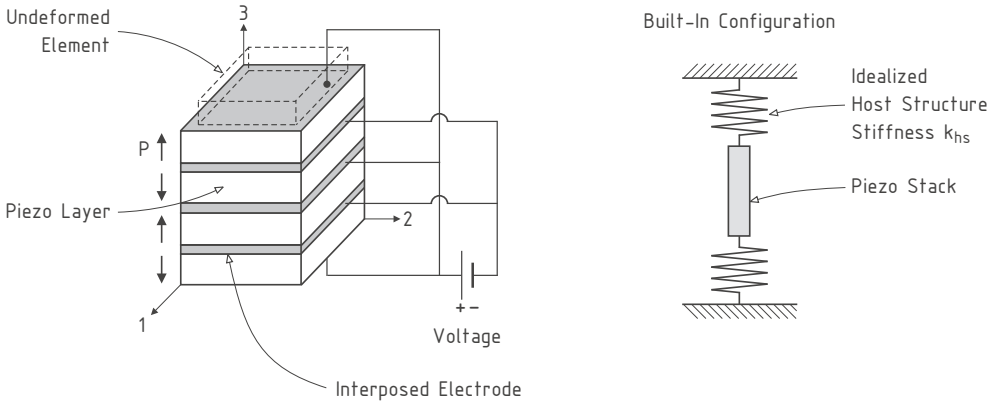

Figure 2.9: Piezoelectric stack actuator

The behaviour of a stack actuator can be described approximately with a simple static model.

When a static electric field is applied to the element, it responds with an elastic deformation along the 3-direction and simultaneously exerts a force on the supporting host structure as illustrated in Figure 2.9. The magnitude of displacement and exerted force depend on the actual stiffness k_{hs} of the host structure. The relation between the generated force F, displacement Δl and voltage U can be approximated by:

$$F = k \cdot d_{33} \cdot n \cdot U - k \cdot \Delta l \ , \tag{2.73}$$

where k is the actuator stiffness defined as $k = E_a \cdot S_a/l$. E_a is the elastic modulus of the actuator and S_a its cross sectional area. The number of ceramic layers in the actuator is abbreviated with n.

For an unconstrained actuator, the external load applied on the element is equal to zero, $F = 0$, and the maximum actuator displacement results in:

$$\Delta l_{max} = d_{33} \cdot n \cdot U_{max} \ . \tag{2.74}$$

If the actuator has to work against an infinite stiffness, Δl becomes zero and the maximum force is exerted on the host structure. This force is denoted as blocked force F_B:

$$F_B = k \cdot d_{33} \cdot n \cdot U_{max} = k \cdot \Delta l_{max} \ . \tag{2.75}$$

The resulting static behaviour in terms of force and displacement generated by a perfect stack actuator is shown in Figure 2.10 for different levels of driving voltage. From the intersection between the host structure's stiffness with the actuator behaviour, the common operating point can be derived. In the optimal operating point at $\Delta l_{max}/2$ the energy transmitted from the actuator into the structure, which is equal to the product of force and displacement, is at its maximum. Through the size of the cross sectional area, the stiffness of the actuator element can be optimized in regard to a given host structure.

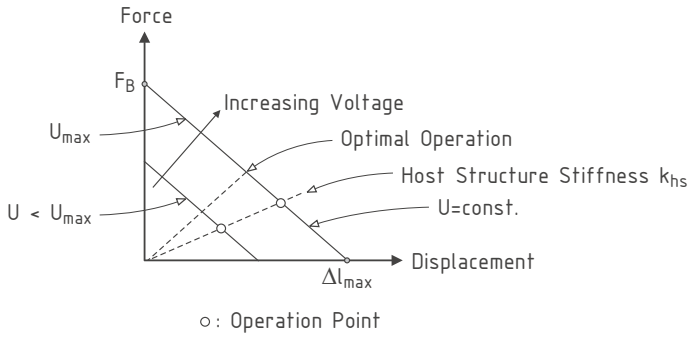

Figure 2.10: Operational behaviour of a perfect stack actuator

Compared with laminar patch actuators the degree of structural integration is lower, since the elements usually require an additional casing for the force transmission. Stack actuators are used in applications for position and vibration control, where only a small amount of displacement but large forces are required. Some examples are given in [Maier00, Maier02] for interior noise control in helicopters with active gearbox struts or in [Lorkowski01].

Laminar Patch Actuator

Laminar patch actuators are made from flat ceramic plates, which are bonded to the surface of the host structure or directly integrated into it. They are driven in the transverse mode and when an electric field is applied to the electrodes in 3-direction, the element responds with an expansion or contraction along the 1- and 2-axis due to the d_{31}-effect as shown in Figure 2.11. Because the displacement in this plane is partially constrained by the stiffness of the host structure, in-plane forces and moments are generated and introduced into the structure. Reciprocally, piezoelectric patches are also used in a sensor configuration, since a structural deformation inducing a strain in the plane of the elements can be measured through the resulting electric flux density D_3.

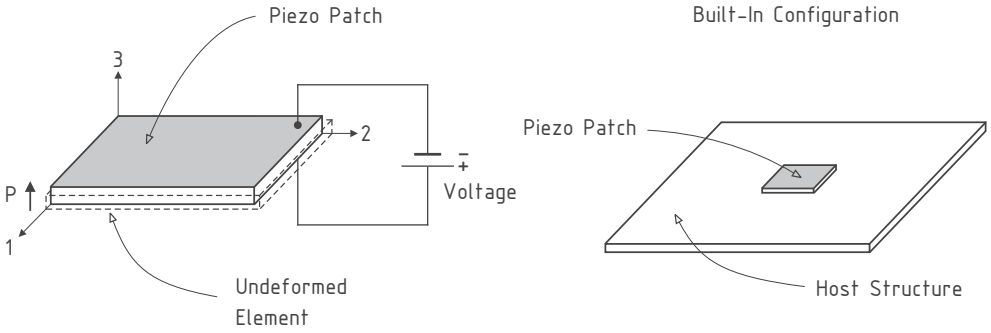

Figure 2.11: Piezoelectrical patch actuator

Applied to typical lightweight structures as thin plates, the bending moments induced by the actuator patch will generate an out-of-plane displacement of the plate. Since out-of-plane vibrations are also associated with the radiation of sound from plate-like structures, piezoelectric patches are especially suited to be used as actuators or sensors for active structural acoustic control of lightweight structures. This bending principle can be realized in a so-called bimorph or unimorph design. Both configurations are illustrated in Figure 2.12.

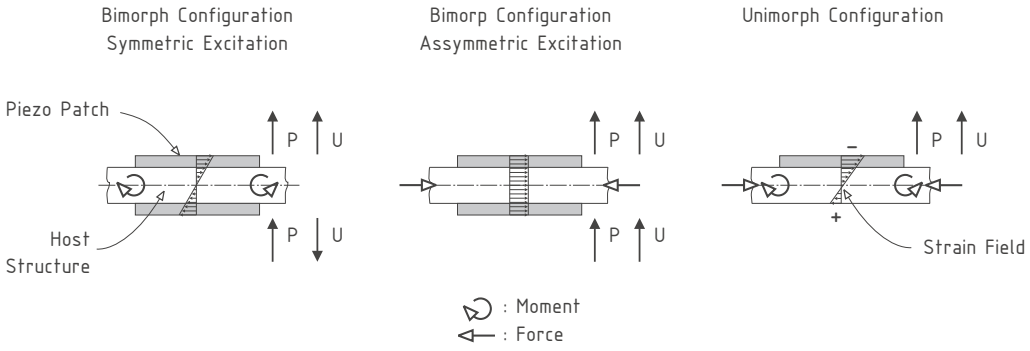

Figure 2.12: Configurations for surface bonded patch actuators

In the bimorph configuration the two opposed sides of the supporting plate are fitted with actuators patches, resulting in a symmetrical construction. If the actuators are poled in the same direction, an electric field, having opposite signs on both sides, will generate a pure

bending of the structure. The resulting extension in the neutral fibre is equal to zero because the opposed stresses generated by the upper and lower actuator are compensated by each other. On the contrary, if the electrical field has the same magnitude and direction in both actuators, a pure in-plane extension of the structure is obtained, as the strain field excited by the actuators is symmetrical with respect to the plate's neutral fibre.

In the unimorph configuration, only a single side of the structure is fitted with an actuator patch. Thus, simultaneously a bending moment and an in-plane force are induced into the host structure.

An analytical model for the description of multi-layer laminates with integrated patch actuators is presented in Chapter 3.2. If the patches are used in a sensor configuration, the measured electric charge Q is equal to the integral of the electric flux density D_3 over the electrode surface. For an elastic beam of width $b(x)$ and constant thickness h, on which is bonded a surface piezo sensor of negligible thickness and length l, the charge Q can be expressed with equation 2.67 for short-circuited electrodes, $E_{el} = 0$:

$$Q = \int_l D_3 \cdot b(x) \cdot dx = -E_a \cdot h/2 \cdot \int_l d_{31} \cdot w''(x) \cdot b(x) \cdot dx \ . \tag{2.76}$$

In this expression the strain has been replaced with the beam's curvature $w''(x)$, since for the thin piezo layer the strain can be approximated by $\epsilon_{11} = -h/2 \cdot w''(x)$. The resulting charge is proportional to a voltage U_{Sensor} and might be measured via a current or charge amplifier:

$$U_{Sensor} = -R \cdot I = -R \cdot \dot{Q} = -\frac{Q}{C} \ , \tag{2.77}$$

where R and C are the resistance and capacity of the current and charge amplifier respectively.

Compared with stack actuators, a higher stroke can be realized with the bending principle, but the stiffness and blocked force are usually considerably lower. As it is possible to bond the patches directly onto the structure, the degree of structural integration is higher.

2.3.1 Thunder Actuators

For the design of the active trim panel attachment system piezoelectric Thunder actuators[11] are used. Thunder actuators are small, adaptable and ready-made smart elements manufactured by Face International Corporation[12] and available in a wide variety of configurations and sizes. Through a special combination of materials and manufacturing process Thunder elements benefit from an exceptional ruggedness and can provide larger displacements than other available piezoelectric actuators.

The operational mode of such an element is based on the piezoelectric d_{31}-effect and the bending principle presented in the previous chapter. Two typical Thunder elements are shown on the left side of Figure 2.13. They are made from a composite laminate, consisting of a stainless steel substrate layer, a LaRC^{TM}-SI layer[13], a PZT piezoceramic wafer, another LaRC^{TM}-SI adhesive layer and a thin aluminium or copper top layer (see exploded view in Figure 2.13)

[11] *Thunder* is an acronym for *Th*in Layer *Un*imorph Ferroelectric *Driver*.

[12] Face International Corporation, Norfolk, VA USA 23508, http://www.faceco.com/

[13] LaRC^{TM}-SI is a NASA patented high temperature polyamide adhesive.

and are formed when the composite laminate is heated beyond the glass transition temperature of LaRC^{TM}-SI and cooled down to room temperature. During the cooling cycle, the material's different coefficients of thermal expansion induce a pre-stress in the individual layers leading to the characteristic domed shape of the Thunder element.

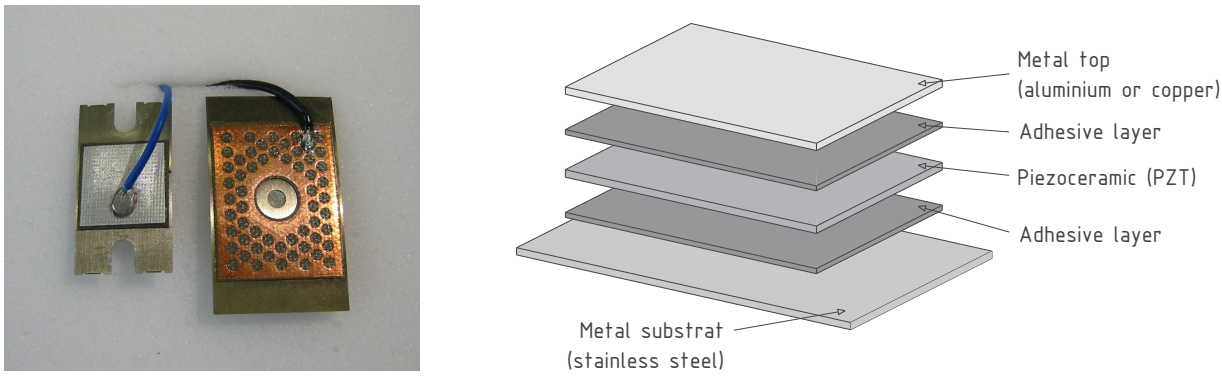

Figure 2.13: Thunder actuator and construction

As a result of the manufacturing process the internal stress state is such that the substrate is in tension and the ceramic in compression. This compression pre-stress for the PZT layer allows the element to be deflected far more than conventional piezoceramics without cracking. The metallic substrate layer and superstrate top layer also serve as electrodes for the electric power supply.

The following figure illustrates the principles of Thunder operation by showing the typical motion versus the applied voltage. When no voltage is present, the piezoceramic material remains in its pre-stressed compressive state while the steel substrate is in a tensile state as described above. This condition is depicted in the middle of Figure 2.14.

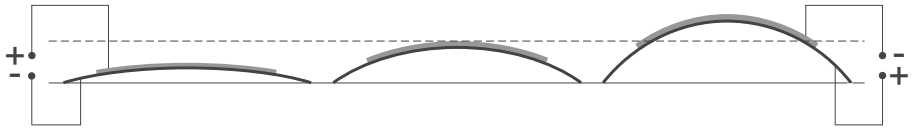

Figure 2.14: Thunder motion for a simply supported device

With a positive electric potential applied to the electrodes, the d_{31}-effect will try to shorten the piezoceramic geometrically. This causes the stainless steel substrate to flatten and move downward as illustrated on the left side of Figure 2.14. When a negative electric potential is applied across the electrodes of a Thunder element the piezoceramic material geometrically expands, causing the Thunder to move upwards in order to accommodate for the increased length of the ceramic material. The voltage limits in the down direction are twice as large as in the up direction (2360 V/mm instead of -1180 V/mm), whereas the peak-to-peak voltage during operation should not exceed 2360 V/mm. The operating temperature band ranges from -40 to 200°C. Typical dimensions for rectangular Thunder elements may vary approximately from 20 by 10 mm to 75 by 50 mm, while using 0,2 mm up to 0,5 mm thick ceramic layers. Typical bidirectional displacements, which are achieved in a cantilevered configuration with

the maximum allowable input voltage driven under 1 Hz, range from 0,1 mm to around 7 mm. The blocked force, measured for a simply supported device driven at maximum voltage, is ranging from several Newtons to more than 100 N.

For a good performance the actuator mounting and the force transmission are the most important points to consider when designing an active system with Thunder elements. In a cantilevered configuration large displacements may be achieved but, due to the low stiffness inherent to this arrangement, the ability to work against an external mass or stiffness is not very effective. Furthermore, besides the normal deflection, the actuator's end tip will also execute a small rotation due to the beam-like bending. Hence, the normal actuation force is always combined with a moment, which may make the active control impossible in certain cases.

To achieve a unidirectional translatory motion, it is possible to mount the Thunder elements in a clamshell configuration as reproduced in the drawing shown in Figure 2.15. Two elements are fastened symmetrically at their ends with an adequate clamping device. This design enables the actuator ends to move freely in the plane of the element, whereas at the centre points of each Thunder element the bending due to the piezoelectric d_{31}-effect causes an opposite normal deflection, which can be used as actuation force. The global behaviour of such an actuator unit is similar to the one of a stack actuator presented in the previous chapter.

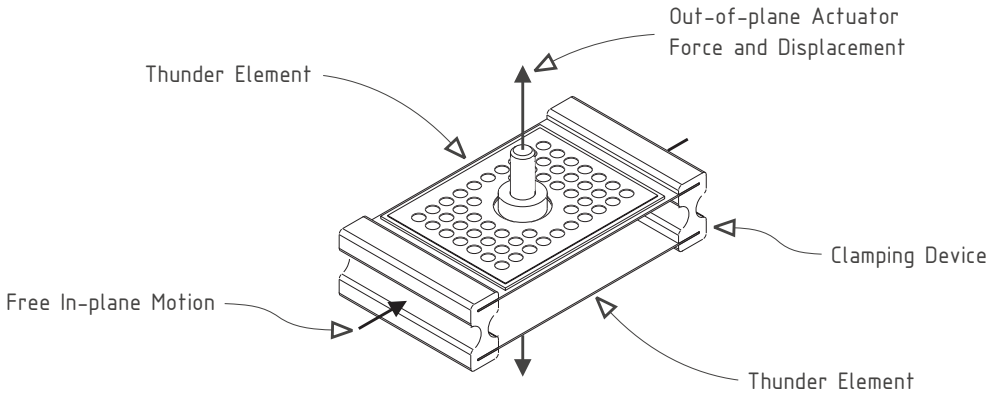

Figure 2.15: Thunder elements in a clamshell configuration

By using this symmetric configuration, the individual displacement of each element in the stack is additive, whereas for the force there is no change compared to a single actuator. An electric insulation between the devices is not required, because they will be contacting each other at the substrate layer only, thus sharing a common electric ground.

2.4 Active Control Technologies

Active technologies represent attractive solutions for various problems encountered in the control of noise and vibrations. Typically, as shown in Figure 2.16, active control systems consist of *actuators*, used to manipulate the particular waveform within the fluid or structure that is to be controlled, *sensors* to detect the primary excitations and a *control unit* generating the actuator driving signal from the error signal. From this follows an important characteristic of

active systems, which is the need of an external, additional energy supply. Another distinctive feature of active control systems, especially arising in vibro-acoustic applications, is that actuators and sensors are often distributed and highly integrated within the structure, thus requiring an integral modelling and development approach.

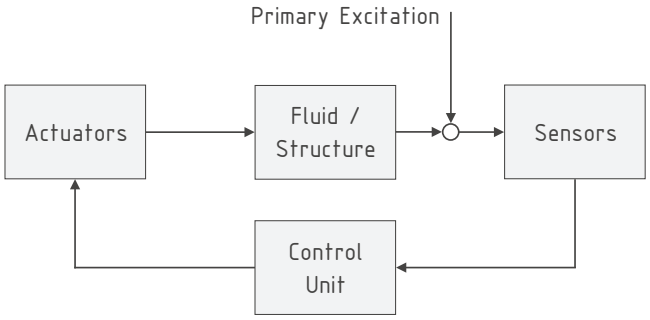

Figure 2.16: Active control system

The fundamental principle of active control is the destructive wave interference. By adding a second waveform to a primary perturbation a cancelling of the overall amplitude is obtained if the second waveform is of equal amplitude and opposite phase to the primary perturbation. In an active system this is done by monitoring the resulting waveform with appropriate error sensors and adapting the actuators and the second, artificially generated waveform with the controller in such way that a cancellation or at least a reduction of the residual amplitude at the sensor is achieved. The waveforms can either be structural displacements or variations in sound pressure.

First patent applications in the field of active noise control were made by Henri Coanda [Coanda30, Coanda32] and Paul Lueg [Lueg33] in the early 1930s (Coanda already mentioned a possible aircraft application), however the ideas were far in advance of the electronics technology required for practical noise control systems. Nearly twenty years later, Olson [Olson53a, Olson53b, Olson56] experimented with an *electronic sound absorber* to reduce the low-frequency noise in aircraft or automobiles in the vicinity of the occupant's head. His arrangement consisted of a microphone mounted in close proximity to the face of a loudspeaker cone. The loudspeaker was driven to null the sound pressure at the microphone, thus creating a quiet area around it. Further applications already described by Olson are electronic noise reducing headsets, active noise reduction in ducts and electronic vibration reducers. His experimental results were promising, but the electronics technology of his time was still not sufficiently advanced to enable implementation in useful applications. Conover's application of loudspeakers arranged around a noisy transformer was another early attempt at active noise control [Conover55].

The real breakthrough of active technologies came only in the 1980s, taking advantage of the fast advancing development of effective digital signal processors (DSP), along with progress in the field of control algorithms and the introduction of new smart materials like piezoelectric ceramics, magnetostrictive materials or shape memory alloys, allowing the design of new types of actuators and sensors. Nowadays, active control of noise and vibration is an intensive field of research and is, for instance, covered extensively in the textbooks of [Elliott01a, Fuller96, Hansen97, Kuo96, Preumont97]. An overview of various applications is given in the survey

articles of [Guicking03, Lagö02]. In regard to their respective application, active solutions may be classified into *active noise control*, *active vibration control* and *active structural acoustic control* systems, as described in the following chapters. The main emphasis is given to aircraft relevant applications. Further applications as in the field of flow control [Thomas02] are not considered here, as they are beyond the scope of this study. The basic control schemes used in active noise and vibration control are briefly addressed in Chapter 2.4.3.

2.4.1 Active Noise and Vibration Control

In active noise control applications a sound field cancellation is typically obtained with electro-acoustical actuators. Loudspeakers, used as actuators, cancel a sound pressure disturbance, which might be measured, for instance, with microphone sensors. As a result of this quite simple principle, a zone of quiet is created in the near field around the sensor, whereas elsewhere the sound pressure level might also be increased due to constructive interference effects. Even so, a more detailed analysis, as given for example in [Mangiante77, Nelson92], reveals that in theory it is possible to obtain a global attenuation inside a control volume without altering the sound pressure outside that volume by using a particular, continuous distribution of cancellation sources located on the surface of the controlled volume. However, a practical implementation would involve a very high system complexity, thus limiting its practical relevance.

For this reason practical ANC solutions are restricted to systems where the wavelength at the highest frequencies of interest is large with respect to the dimensions in which noise is to be cancelled. In this particular case the spatial sound pressure distribution is nearly constant and a loudspeaker placed near the primary source acts as sound absorber. The best known implementations of this technique are ANC headsets, which are manufactured for instance by trademarks such as Bose and Sennheiser for aircraft pilots. A further, commercial ANC solution is available from Ultra Electronics in England and is used for quietening cabins of turboprop aircraft with respect to low-frequency tonal noise components. It is fitted as a standard feature on the Bombardier Q Series Dash 8, Saab 2000, as well as Raytheon Beech King Air 350, and the system is optional on a certain number of other turboprop and even business-jet aircraft. The system components are concealed behind the aircraft trim. On the Saab 2000, for instance, 74 microphones are linked to a control unit, which in turn drives a total of 32 loudspeakers mounted on the trim panels [Lagö02]. Thus, a global noise reduction inside the passenger cabin is obtained on low-frequency, tonal propeller noise components. Active headrests with integrated microphones and loudspeakers, as already suggested by Olson and May, are another possibility to create a local attenuation around the head of a passenger. However, applications in cars and jet aircraft require the control of broadband perturbations. A possible design is reported in [Rafaely99]. Such a system is also offered by Ultra Electronics as *Ultra Quiet Seat* and is addressed to wide-bodied jet aircraft. It is reported to provide local broadband attenuations of up to 10 dB.

Further examples of ANC solutions can be found for instance in duct acoustics applications, where it is possible to attenuate the low-frequency sound radiation emanating from air conditioning ducts, pipes, chimneys or exhausts [Kuo96, Lagö02, Nelson92].

Vibration control is required on a wide variety of relevant engineering problems, either for structural safety reasons or to guarantee the proper functioning of technical equipment and provide isolation from a vibrating environment. This can be handled either by passive techniques or

by active vibration control. AVC differs from ANC that instead of sound pressure variations structural displacements, velocities or accelerations are controlled. To generate the necessary secondary signals, force transducer elements such as electrodynamic shakers or piezoceramic materials are required, whereas elements allowing a monitoring of structural deformations and vibrations are used as sensors.

Typical AVC applications are developed for the implementation in lightweight structures as encountered on aircraft and spacecraft. In helicopters vibrations are generated from the transient aerodynamic rotor forces at the blade-passing frequency and its harmonics. The vibrations are transmitted across the gearbox and the airframe to the pilot and the passengers. With active hydraulic actuators, replacing the conventional, elastomeric gearbox mounts, an average vibration reduction of up to 82% was demonstrated in flight tests [Fuller96]. For use in space applications various active systems have been designed to isolate antennas, payloads, technical equipment and experimental rigs from low-frequency structural vibrations. Some examples are given in [Bushnell97, Collins91, Henderson96, Hyde97, Thayer99]. Furthermore, AVC techniques are also used in civil engineering and machine tool applications. For instance active tuned mass dampers acting as resonance absorbers are used in high buildings to reduce wind-induced low-frequency vibrations. Active systems for the control of large cable structures (bridges, antennas) are currently under development [Achkire97, Bossens01, Kubo04]. In [Denkena04] a machine tool application to reduce chatter marks resulting from a relative motion between the cutting tool and the workpiece is presented. An active vibration control implementation for circular saws is reported in [Chen03].

2.4.2 Active Structural Acoustic Control

The principle of active structural acoustic control represents a combination of both the ANC and AVC principles. In many relevant technical applications, as for instance car or aircraft interiors, noise is primarily transmitted and radiated by the surrounding vibrating structure. Instead of controlling directly the sound pressure field and imposing a secondary, loudspeaker-generated sound field, the vibration characteristic of the structure itself is modified by the control, thereby altering its radiation efficiency and attenuating its sound radiation behaviour [Fuller92]. As in AVC applications, structural actuators and sensors related to the sound pressure are used (microphones, acceleration or strain sensors). However, the controlled frequency range is typically much higher than in AVC applications. Advantages of ASAC in comparison to ANC are that for some applications, involving for instance structural sound transmission, less control channels are required, thus reducing the system complexity. Furthermore, the actuator hardware implementation requires less weight and volume when strain-inducing actuators such as piezoceramic elements are used.

A considerable amount of studies involving active structural acoustic control were published during the last 15 years, documenting the advances made in the field of structural actuation, error sensing and control algorithms as well as the enormous interest of the research community and industry in this area. In practice most vibro-acoustic relevant structures, as encountered for instance in cars or aircraft, consist of more or less flat single and double wall partitions. For this reason many ASAC publications address various theoretical and experimental aspects in the control of sound transmission through general, flat homogeneous structures. The main results are summarized in the following two sections for single and double wall partitions.

Some examples of prototype ASAC applications developed for more realistic structures such as complete airframes are listed at the end of this chapter.

Control of Sound Transmission through Single Wall Partitions

The basic principles of active structural acoustic control are summarized in [Fuller96]. Considering as example a theoretical model (rectangular single wall structure excited by plane waves or local structural force inputs, a cost function related to the observed far field pressure is minimised with several independently controlled point forces or piezoelectric actuators), it is shown that, assuming certain conditions as proper size, number and placement of actuators, a reduction in sound transmission is achieved by two different control mechanisms: *modal suppression* (also referred to as *modal damping*) and *modal restructuring*. Modal suppression means that the excitation of structural modes having high radiation efficiencies is suppressed by the control, thus also attenuating the structural sound radiation. In contrast to this type of control, which effectively reduces the mean vibration level of the structure, the modal restructuring mechanism is based on the excitation of additional modes in such a way that the overall radiation behaviour of the structure becomes less efficient due to a destructive inference between the contributing radiation modes. However, with this type of control, the overall vibration level of the structure may not be attenuated significantly and sometimes even an increase is noticed.

In [Wang91] a comparison is made between point force and piezoelectric actuators. The analysis reveals that with a point force control slightly better results in sound transmission attenuation are obtained. However, due to their low cost and light weight, the use of piezoelectric actuators is regarded as more suitable for practical implementations. The use of a point force actuator for the control of structural sound transmission into a closed cavity is addressed in a series of articles by Pan and Hansen [Pan90, Pan91a, Pan91b]. An electromagnetic driver is used to minimise the sound pressure sensed by an error microphone in the cavity. Depending on the excitation frequency, modal suppression and modal restructuring are identified as control mechanisms. Furthermore, it is shown that the maximum noise reduction depends on the actuator location and that for an optimal system design additional constraints as the required actuation effort and resulting structural vibration level have be taken into account. A successful experimental application of piezoelectric actuators in the control of structural sound transmission, also using microphone error signals, is described in [Clark92a].

Particular emphasis in literature is given to the sensing approach. For the structural integration and from a practical point of view, it is desirable to have sensors located directly on the vibrating structure (acceleration and velocity sensors or strain-sensing elements as PVDF-foils or fibre optic sensors) instead of using microphones. To obtain a satisfactory reduction in sound transmission the physical quantities measured on the structure must provide a good estimate of the radiated sound power. As structural eigenmodes have different radiation efficiencies, this can be achieved either by designing distributed sensors, which respond only to certain structural vibrations having a high radiation efficiency or by weighting the outputs from an array of point sensors with an appropriate filter [Elliott93]. A control strategy, where the sound radiation is monitored with the strain field at discrete points on the structure, is proposed by Masson et al. [Masson97].

An active control of sound radiation using volume velocity cancellation is suggested by Johnson

and Elliott [Johnson95], as in particular at low frequencies the most efficiently radiating velocity distribution corresponds to the net volume displacement of the plate. This sensing strategy is compared in an analytical model to an optimal control where the radiated sound power is minimised. It is shown that at low frequencies similar sound power reductions in the far field are obtained with both types of control. However, volume velocity control is less prone to *control spill-over*[14] effects in terms of increased structural velocity and near-field pressure excitation, when a reciprocal actuator to the volume velocity sensor, generating a uniform force distribution over the whole panel surface, is used.

The feasibility of implementing PVDF-foils as distributed error sensors on the radiating structure is demonstrated with an experimental investigation in [Clark92b]. Two narrow PVDF-stripes are positioned perpendicular to each other on the supporting plate and thus measure odd plate-modes, which mainly contribute to the far-field sound radiation. Hence, the use of remote microphones in the control loop is not required. To detect the net volume velocity of the radiating plate specially tailored PVDF-sensors, measuring the bending response of the panel, are required. Experimental results obtained with such volumetric sensors are presented in [Charette97b, Gardonio01, Henrioulle01]. However, practical implementations are limited, as at higher frequencies the measured component related to an in-plane vibration of the panel dominates the sensor response and interferes with the detection of the bending components [Gardonio01]. An alternative approach to measure the volume velocity is its approximation by using the summed output from a number of discrete accelerations sensors [Elliott01b, Gardonio04a, Lee02].

In [Elliott01b, Gardonio04a] Elliott and Gardonio present a theoretical, comparative study comprising various kind of embedded structural actuators and sensors. The actuation is made either via a single uniform force actuator or an array of piezoelectric patches, whereas for the sensors a single volume velocity sensor or an array of point velocity sensors is used in combination with the actuators. The analysis is focused on systems based on single-channel feedback controllers, either in a global SISO configuration or in a local MIMO configuration. It is reported that in terms of radiated sound power similar results are obtained with the global SISO and local MIMO system. However, some practical advantages are seen in the MIMO system, as a relatively large number of low-frequency resonant modes and their sound radiation as well as residual vibrations and therefore the near-field sound pressure can be more efficiently controlled. The development and experimental testing of such a smart panel fitted with 16 uniformly distributed and collocated acceleration-sensor piezoceramic-actuator pairs is described in a series of three papers presented by Gardonio, Bianchi and Elliott [Bianchi04, Gardonio04b, Gardonio04c]. Each local actuator sensor pair is driven by an independent single velocity feedback control loop, thus increasing the damping in the vicinity of resonance frequencies. The experimental results prove that, provided an appropriate feedback gain is chosen, good reductions of the radiated sound power and the vibration energy of the panel can be obtained for random primary excitations. Depending on the excitation type, shaker or loudspeaker, and its frequency, third octave band reductions in radiated sound power ranging between 5 and 8 dB are reported.

In the numerical study by Baumann and others [Baumann92] a pure vibration controller is compared with a control system where the sound power, radiated from a beam and estimated

[14]The term spill-over designates the increased excitation with activated control on non-controlled quantities and frequencies.

from filtered structural measurements, is minimised. Simulation results show that the acoustic control yields better results in terms of total radiated sound power than the vibration controller. At some frequencies an increase of structural vibrations is noticed with the acoustic controller as vibration modes with low radiation efficiencies are excited. For broadband excitations at higher frequencies similar results are obtained with both sensing approaches. Baumann's theory is also investigated in [Thomas95], where a radiation filter matrix is used for the feedback control of sound radiation from a simply supported plate excited by TBL noise. The results indicate that a reduction of radiated sound power can be achieved on aircraft-like structures with an optimal feedback control.

A real-time sensing procedure, intended to estimate the radiated far-field sound pressure in a given direction, was demonstrated theoretically and experimentally by Maillard and Fuller [Maillard94a, Maillard94b, Maillard95]. The system consists of several structural point sensors, such as accelerometers for instance, whose signals are post-processed by digital filters. The filters are designed to model the Green's function between the sensors and a far-field location. The estimated far-field sound pressure is then used as an error signal in the ASAC system. The same authors present a numerical study [Maillard97] in which this sensing procedure is compared to a technique where the net structural volume velocity is estimated from structural point sensors. Using the same array of distributed acceleration sensors in both cases, the authors conclude that better control performances can be obtained with an error signal based on the estimated sound radiation.

Apart from the control strategy and type of actuators and sensors, the global control performance of ASAC systems is affected by additional parameters such as the number and size of actuators and sensors as well as their respective position on the structure. From a more practical point of view, weight, power consumption and cost are further design variables to be taken into account.

Some intuitive design rules are given for instance in [Jakob99]. It is demonstrated with a numerical model that with each independent control force input one structural eigenmode of the plate can be controlled. This criterion determines the controllable frequency range, depending on the number of actuators and sensors as well as the structural properties. Furthermore, a structural eigenmode cannot be controlled if the actuator or sensor is placed on a nodal line of this mode. It is shown that the optimal actuator location requiring the least actuation effort is in the antinodes of the associated eigenmode. Gardonio and Hansen [Gardonio04a] mention that, in general, the control performance in terms of sound power attenuation is increased by employing a greater number of actuators and sensors. However, from a certain number of actuators and sensors onwards, no major improvement is reached by a further increase in the number of control channels, which is explained by the physical spill-over effect introduced by piezoelectric patch actuators having finite dimensions.

Due to the complexity of ASAC systems and the multitude of involved design variables, numerical optimisation techniques are proposed in literature. A general procedure for the design of MIMO ASAC systems is suggested in [Clark92c]. Taking into account additional constraints as the actuation effort, structural vibration levels, number and size of actuators, the optimisation problem may become very complex. In such cases *genetic algorithms* (GA) prove to be a very efficient optimisation technique. Some ASAC GA applications are described for instance in [Li04, Nijhuis03]. Further possible optimisation approaches are discussed in a review report from Padula and Kincaid [Padula99].

Control of Sound Transmission through Double Wall Partitions

Due to the fluid-structure coupling, double wall partitions have the particularity of not being very efficient in reducing the sound transmission at low frequencies. However, since ASAC is most efficient in the lower frequency range, it is especially suited for reducing sound transmission through double wall partitions. Many aspects that hold for active control of sound transmission through single wall partitions (main control mechanism, actuation, sensing, etc.) can also be directly applied to double wall partitions. Furthermore, some additional aspects regarding the actuation and sensing approaches, which are unique to double wall sections, are discussed in literature. In terms of actuation concepts the investigations can be divided into two main groups using either *panel control* or *cavity control* [De Man03]. Panel control is based on structural actuators, whereas for cavity control acoustic sources located inside the double wall cavity are used, thus blocking the airborne sound transmission path. For the error signal either structural sensors or microphones located in the radiated sound field or in the cavity are used. However, similar to the literature available for single wall partitions, most authors treat only homogeneous, flat panel systems.

A comparative study between the panel and cavity control concept is presented in [Bao97, Pan98a]. The authors conclude that a cavity control approach in combination with cavity pressure sensors yields a better control performance in terms of sound radiation and vibration attenuation in comparison to a panel control approach. Similar results are obtained by De Fonseca et al. in a numerical and experimental study addressing the sound transmission through an aircraft sidewall consisting of a stiffened skin panel and a homogenous trim panel [De Fonseca98, De Fonseca99]. This behaviour can be explained by the fact that in the considered frequency range the modal density in the uncoupled cavity is usually much lower than on the uncoupled panels, which allows the use of less actuators and sensors with a cavity control concept [De Man03]. Concerning the active control of stiffened double wall cylinders, comparable results are obtained in a numerical study by Grosveld [Grosveld96]. It should be mentioned that these conclusion are only valid if, besides the airborne transmission path, no additional structure-borne paths are present within the structural system.

An analytical and experimental study of active control of sound transmission through a double wall system is presented by Carneal and Fuller [Carneal93, Carneal03]. The actuation is made via a set of piezoelectric patches either applied on the incident or the radiating panel. A set of microphones placed in the receiving chamber provide the error signal for the controller. From both analytical and experimental results the authors conclude that active control applied to the radiating panel is the more effective solution in terms of TL increase as this structural configuration exhibits a more efficient coupling to the radiated sound field. In addition, it is reported that the use of a stiff radiating panel increases the passive transmission loss performance as well as the control performance achieved with the active system. The panel control concept in combination with a volume velocity sensor is investigated in an article by Pan et al. [Pan98b]. The main finding is that in contrast to single panels, as investigated in [Johnson95], the control efficiency is limited to approximately half of the frequency range. This behaviour is explained by the modal participation of the first structural radiation mode, which is less dominant at higher frequencies in double wall systems than on a comparable single wall partition. To achieve a better active attenuation at higher frequencies the authors suggest the structural control of additional, low-order radiation modes.

A further comparative study of panel and cavity control is given in [Maury01]. The article addresses the control of flow-induced sound transmission through a generic aircraft sidewall (using flat, homogenous panels without structure-borne sound transmission). From a numerical model it is concluded that for a significant noise reduction in the low-frequency range the most efficient control strategy is the suppression of low-order skin panel modes. A less efficient control performance is obtained by suppressing structural trim-panel modes, whereas with a cavity control concept the least good sound attenuations are achieved.

Finally, a theoretical study concerning the active control of airborne and structure-borne sound transmissions through an aircraft sidewall is presented in a paper by Gardonio and Elliott [Gardonio98]. The structural model consists of a skin panel stiffened by stringers. In contrast to the aforementioned studies the trim panels are coupled to the skin panel by the cavity fluid and structural attachment elements allowing an additional structure-borne sound transmission. Three different control concepts are investigated by the authors: active mounts connecting both panels and driven in such a way as to cancel the out-of-plane velocity on the trim panel or minimise the total radiated sound power, cavity control with loudspeakers cancelling the cavity sound pressure or minimising the total radiated sound power and a combination of both systems. The control performance is evaluated for different cavity configurations (empty, partially or entirely filled with porous absorption material) and for transverse force and plane wave primary excitations. The results suggest that a cavity control with loudspeakers provides good attenuation in the mass-air-mass frequency range, whereas with active mounts no significant reduction of sound transmission is obtained, as in this frequency band the sound transmission is largely dominated by the airborne transmission path. Similar conclusions can be drawn from the experimental study of De Fonseca et al. [De Fonseca99].

ASAC Applications

The first full-scale, laboratory ASAC application was carried out on a fully trimmed Douglas DC-9 aft section [Fuller96]. A harmonic engine excitation as due to engine out-of-balance forces was simulated with a set of two shakers attached to the engine mounts and control was performed with two shakers, internally mounted to the engine pylon. Several combinations of up to seven microphones and five acceleration sensors were used for the error signal. With an acceleration control, local reductions in SPL of up to 9 dB were obtained at the excitation frequency of 170 Hz. However, on some microphones increased sound levels were also observed with activated control, thus highlighting the already mentioned aspect of ASAC control systems that a minimisation of vibration energy does not necessarily guarantee a noise attenuation. Also for a DC-9 engine mounting system a case study for active engine mounts based on hybrid electromagnetic-hydraulic actuators was carried out. The system is reported to significantly reduce the structure-borne noise transmitted from the engines into the airframe, thus attenuating the global cabin noise, while the engine's vibration level is not increased [Swanson93].

The reduction of propeller noise in turboprop aircraft by ASAC means is addressed in some studies. Sollo et al. investigated the application of ASAC systems to the ATR aircraft family [Sollo98]. This approach was demonstrated on a ATR42/72 fuselage mock-up, which was fitted with piezoceramics patches bonded to the fuselage skin and frames. The error signal was derived from microphones distributed inside the cabin at seated passenger height. The first

three propeller tones were controlled simultaneously and average noise reductions of around 10 dB were measured for the most significant test conditions. A flight test demonstration of an operational ASAC system was conducted on a Raytheon 1900D, a 19-seat twin turboprop aircraft [Palumbo99, Palumbo00]. The control system consisted of 21 inertial force actuators mounted on the fuselage frames and 32 microphones located near the passenger's head positions. Interior noise reductions of up 15 dB at the blade-passing frequency of 103 Hz were obtained during single-frequency control test, whereas on multi-frequency control tests at the BPF, its first and second harmonic, simultaneous reductions of 10 dB, 2,5 dB and 3 dB were obtained.

An ASAC application for helicopters is currently under development in Germany. In helicopters the gearbox represents a principle source of interior noise. Vibrations at the dominant gear-meshing frequency of about 1,9 kHz are transmitted as structure-borne sound through the gearbox struts into the airframe and radiated into the cabin. A prototype ASAC system based on smart gearbox struts with integrated piezoelectric actuators and acceleration control was successfully demonstrated in flight tests. Mean reductions of about 11 dB have been obtained for the cabin SPL on the dominant frequency [Maier00, Maier02].

Control of sound radiation with adaptive tunable vibration absorbers (ATVA) is another technique becoming increasingly popular for aircraft implementations [Carneal04, Charette97a, Franchek93, Wright04]. It is in fact a combination of passive and active methods. Basically, an ATVA works like a classical, passive vibration absorber, however the ATVA resonance frequency can be adjusted by active means in accordance with the operation conditions, thus increasing the bandwidth and performance of control. In contrast to an active solution with conventional transducers (piezoceramic patches, shakers, loudspeakers, etc.), a much lower control authority and system complexity is required and less electrical power is consumed.

2.4.3 Control Schemes

With respect to the utilised control laws, active control systems can be divided into feedforward and feedback control schemes. The main difference between a feedforward control scheme and feedback scheme is that with feedforward control a reference signal correlated to the actual primary disturbance is required in addition to the error sensors, whereas with feedback systems the requirement of additional reference sensors is eliminated.

Both control schemes can be used in principle with random and deterministic excitations. However, feedforward control of random excitations is only possible if the reference sensor is placed in a sufficient upstream direction with respect to the error sensors and the disturbance transmission. This limitation is due to the delay experienced with real-time control systems and is termed *causality constraint* [Burdisso93]. Thus, to guarantee a good control performance, the delay in the control path from the reference sensor to the error sensors must be smaller than the time required for the primary disturbance to travel from the reference sensor to the error sensors. Harmonic feedforward control requires only the detection of the fundamental driving frequency. Due to its ease of implementation and relatively good stability properties, the *filtered-X least-mean-square* (LMS) algorithm is a feedforward control scheme that is widely used in experimental applications for the control of harmonic disturbances (see for instance [Carneal93, De Fonseca98, De Fonseca99, Maier00, Palumbo99, Sollo98]). In numerical investigation LMS algorithms are also a very popular choice, as they give an upper-bound estimate

of the best possible control performance [De Fonseca98, De Man03, Gardonio98, Grosveld96, Nijhuis03].

However, the need for an additional reference signal represents a constraint for many practical applications and can be avoided by the use of appropriate feedback controllers. In model-based feedback control the control algorithm is reformulated internally as a feedforward problem by using an internal model of the plant [Baumann92]. Yet, as the implementation of such model-based controllers is difficult, non-model-based feedback controllers, being easier to implement in practice, are often preferred in literature [De Man03]. A shortcoming associated with this type of control is a limited control authority and performance since the system's stability must be guaranteed for various operating conditions. Nevertheless, by using collocated actuator and sensor pairs, as for instance point force actuators and velocity sensors, stability robustness is increased and as a result of the active control the damping in the structure is augmented [Preumont97].

In ASAC implementations this principle is frequently realized with collocated, uniform force actuators and sensors based on PVDF-foils or piezoelectric patches in combination with acceleration sensors. Thus, with a *direct velocity feedback* control the sound radiation from lightweight structures can be reduced, as the resonant components of the structural response to the primary excitation are more efficiently damped [Elliott01b, Gardonio01, Gardonio04b, Henrioulle01, Johnson95, Lee02, Nijhuis03]. As previously mentioned, in some studies the use of multiple actuator and sensor pairs connected by independent, local velocity feedback control loops is suggested in order to reduce structural sound radiation. This control configuration is referred to in literature as *decentralised velocity feedback* control [Gardonio04a, Gardonio04c].

2.5 Conclusions

From the available publications on active structural acoustic control one can conclude that it is possible to develop active control systems for reducing the sound transmission through single and double wall structures. However, the multitude of possible approaches and results also illustrate that the complexity of such systems remains on a very high level, especially when used in combination with double wall partitions. For these reasons it is important to consider all important factors affecting the control performance in the system design. These factors are, amongst others such as the power consumption or desired system complexity, the specific design of the structure to which the ASAC system is to be applied (stiffened structure, airborne and structure-borne transmission paths, cavity absorption), the type and positioning of the actuators, the sensor concept (structural or acoustic sensors), the type of primary excitation (harmonic or random, force or acoustic excitation) and the controller design (feedback or feedforward control scheme, narrow- or broadband excitation). In the present application the system development is based on a detailed numerical simulation model, which is presented in the next chapter.

Chapter 3

Numerical Simulation Model

An analytical model to predict the sound transmission through passive single and double wall partitions was presented in the previous chapter. The models are suited to provide fundamental understanding of the main physical effects underlying the phenomenon of structural sound transmission. Yet, the detailed behaviour of complex structures like aircraft sidewalls or the impact of active control systems cannot be taken into consideration.

Hence, a more sophisticated, numerical approach to predict the vibro-acoustic response of such systems for a frequency range up to 500 Hz is developed and presented in this chapter. The simulation model is based on the finite element method and is mainly used to design different ASAC systems and evaluate their efficiency in reducing the sound transmission. The structure is supposed to be mounted in an infinite, rigid baffle separating two semi-infinite acoustic domains. As the acoustic medium on the incident and radiating side is air, weak coupling between the structure and the surrounding fluid is assumed[1]. For this reason the analysis of the acoustic excitation, structural response and acoustic radiation can be made separately, as illustrated in the following diagram.

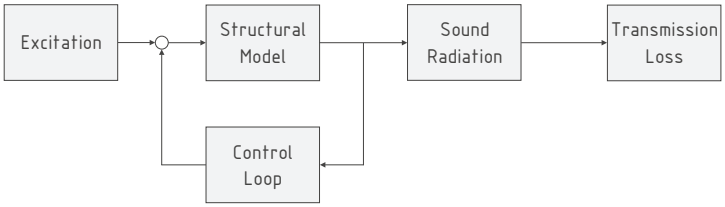

Figure 3.1: Vibro-acoustic simulation approach

The dynamic response of the system due to a certain pressure or mechanical perturbation on the incident side of the structure panel is calculated in a first step. It has been shown in the previous chapter that for double wall systems, connected by an enclosed fluid domain, the sound transmission is dominated by the fluid-structure coupling of the cavity and that the sound reduction index may even fall below the ideal value of the one for a single panel having the same total mass as the double partition [Fahy85]. The fluid-structure coupling of

[1]The coupling of the external fluid load to the structural response and vice versa is neglected. The validity of this assumption will be verified by comparing simulation results with measurements obtained for a generic structure.

the enclosed cavity must be consequently fully taken into account by the structural model. Once the dynamic behaviour on the radiating parts of the structure has been determined, the free field sound radiation is calculated with the Huygens-Rayleigh integral and the resulting transmission loss index is derived.

The ASAC system is incorporated by additional control loops for each individual actuator element. As the structure and the surrounding acoustic medium can both be considered to have a linear behaviour for small displacements, the superposition principle is used to compute the controlled system response, which will be a complex linear combination consisting of the primary response due to the initial perturbation and weighted secondary, controller-generated responses.

A validation of the numerical simulation model and the assumption of a weak fluid-structure coupling is presented at the end of this chapter. For a generic structure, consisting either of single or double wall aluminium panels, numerical and experimental results are compared and discussed for the structural and acoustic domain.

3.1 Modelling of Structural Sound Transmission

In recent years numerical modelling of miscellaneous vibro-acoustic problems has become a common subject in research and industry. The applications vary from diverse vehicle interior acoustic problems [Barisciano99, Kropp03, Marburg03, Papadopoulos03, Peiffer05] to the mechanical behaviour of complex structures (ships, satellites, etc.) coupled or excited by a circumjacent fluid [Cabos03, Moosrainer00, Witting99]. Depending on the type of analysis, the following numerical methods as well as suitable combinations are mainly used to solve vibro-acoustic problems:

- the finite element method (FEM),
- the boundary element method (BEM),
- and the statistical energy analysis (SEA).

The boundary element method is a numerical solution of the Kirchoff-Helmholtz wave equation and is used for radiation and scattering problems. In this formulation the sound field is related to the sound pressure and particle velocity on a closed boundary and additional sound sources. Closed and infinite fluid domains can be considered with this method. The SEA-method is based on the analysis of the mean energy equilibrium for a given system and on the breakdown of average power flows between complex subsystems as for instance structural and fluid domains. The subsystems are excited by frequency bands rather than single harmonic frequencies, which makes SEA especially suited to high-frequency problems with broadband excitation. Further information on the BEM- and SEA-methods are available for example in [Crighton92, Estorff00].

The present application involves the calculation of sound transmission through a generic sidewall partition consisting of several panels coupled by an enclosed fluid domain. As the frequency range is restricted to frequencies up to 500 Hz, and due to the additional requirement to incorporate the impact of piezoelectric actuators on the structural behaviour, an FEM-based simulation procedure is chosen to model the vibro-acoustic response of such a system.

The structural dynamic analysis is accomplished with the FEM-software *MSC/Nastran* and the numerical tool *Matlab* is used for pre- and post-processing of the acoustic results and the implementation of the control loop.

3.1.1 Structural Model

Real vibratory systems, having a continuous distribution of mass and stiffness, are characterized by the fact that they possess an infinite number of degrees of freedom. Mathematically this behaviour leads to a description with partial differential equations, which might be solved analytical for simple structures. But in general, for complex structures and boundary conditions, an analytical solution is not possible anymore.

With the method of finite elements a standard numeric tool is available that can be used to describe the static and dynamic behaviour of complex mechanical systems. The basic idea behind the FEM-procedure is that the structure can be discretised into small finite elements, which can be described by piecewise-continuous simple solutions. Each element is coupled in its respective behaviour to adjacent elements by several boundary constraints, thus leading to a global equation system combining the properties of the whole structure. By choosing an appropriate degree of discretisation and suitable types of finite elements, the structural behaviour can be predicted with an adequate accuracy. Formally this approach corresponds to a discretisation of the continuum and the partial differential equation is reduced to a system of standard differential equations [Bathe82, Cook89, Moosrainer00].

Assuming linear-elastic material behaviour and small deformations the governing equation of motion for a structural frequency-response FEM-analysis is derived from the Lagrange equation and Hamilton's Principle:

$$M_s \cdot \ddot{X}(t) + C_s \cdot \dot{X}(t) + K_s \cdot X(t) = R_s(t) \ , \tag{3.1}$$

in which X is the structural, nodal displacement vector with N_s degrees of freedom, R_s a structural excitation, M_s the mass matrix, K_s the structural stiffness matrix and C_s the damping matrix.

Starting with the weak formulation of the wave equation the governing equation of motion used in a fluid domain FEM-analysis is:

$$M_f \cdot \ddot{P}(t) + C_f \cdot \dot{P}(t) + K_f \cdot P(t) = R_f(t) \ , \tag{3.2}$$

where M_f is the acoustic mass matrix, C_f the acoustic damping matrix, K_f the acoustic stiffness matrix, R_f an acoustic load and P the acoustic, nodal pressure vector $\in \mathbb{R}^{N_f}$. Mathematically equation 3.1 and 3.2 represent each a linear system of second order differential equations.

Assuming a steady state solution of equation 3.1 the displacement vector can be written as:

$$X(t) = \hat{X}(\omega) \cdot e^{j\omega t} \ , \tag{3.3}$$

where $\hat{X}(\omega)$ denotes the complex amplitude at the angular frequency ω. Introducing equation 3.3 and its time derivatives in equation 3.1 yields:

$$\left[-\omega^2 \cdot M_s + j\omega \cdot C_s + K_s\right] \cdot \hat{X}(\omega) = \hat{R}_s(\omega) \ , \tag{3.4}$$

which is the governing equation of motion in the frequency domain. It can be solved by inverting the matrix term $[-\omega^2 \cdot M_s + j\omega \cdot C_s + K_s]$ for each forcing frequency, which is referred to as the direct approach. The fluid's equation of motion may be solved in a similar way.

For systems possessing a large number of degrees of freedom and forcing frequencies a direct solution of equation 3.4 may not be very efficient from a computational point of view [Blakely93]. An alternative solution is provided by a modal formulation, decoupling the equation of motion 3.4.

Using the homogenous equation of motion without considering the damping term C_s and by assuming that the displacement vector can be written as:

$$X(t) = \phi \cdot e^{j\omega t} \ , \tag{3.5}$$

the solution for a free, undamped vibration is obtained by solving the eigenvalue problem:

$$\left[K - \omega^2 \cdot M\right] \cdot \phi = 0 \ . \tag{3.6}$$

Equation 3.6 can be resolved with the theory of eigenvalues resulting in exactly N_s eigenpairs or eigenmodes (ω_1, ϕ_1), ..., $(\omega_{N_s}, \phi_{N_s})$, each satisfying the homogenous equation of motion for an undamped, free vibratory system. ϕ_i is the eigenvector or mode shape and ω_i the corresponding eigenfrequency. One can now define a matrix Φ_s, whose columns contain the orthogonal eigenvectors ϕ_i as well as a matrix Ω_s containing the eigenfrequencies on the diagonal entries. As the matrix of eigenvectors Φ_s defines a base of $\mathbb{R}^{N_s}$, the complex amplitude $\hat{X}(\omega)$ can be expressed as a weighted superposition of eigenvectors, a formulation also known as modal expansion in literature:

$$\hat{X}(\omega) = \Phi_s \cdot \alpha(\omega) \ . \tag{3.7}$$

The vector $\alpha(\omega)$ is the modal amplitude and describes the contribution of the different mode shapes to the structural displacement vector at a given forcing frequency ω. Multiplying the equation of motion with Φ^T from the left and replacing the displacement $\hat{X}$ with its modal expansion results in the following system of equation for the modal amplitude $\alpha(\omega)$:

$$\left[-\omega^2 \Phi_s^T M_s \Phi_s + j\omega \Phi_s^T C_s \Phi_s + \Phi_s^T K_s \Phi_s\right] \cdot \alpha(\omega) = \Phi_s^T \cdot \hat{R}_s(\omega) \ . \tag{3.8}$$

Φ_s can be mass-normalized such that $\Phi_s^T M_s \Phi_s = I$ and $\Phi_s^T K_s \Phi_s = \Omega^2$. A particular solution is obtained for undamped systems with $C_s = 0$. Due to the diagonal properties of $\left[-\omega^2 \Phi_s^T M_s \Phi_s + \Phi_s^T K_s \Phi_s\right]$ equation 3.8 is reduced to a system of N_s uncoupled equations, each representing a single mass oscillator. However, in general the matrix $\Phi_s^T C_s \Phi_s$ is full and an efficient solution of equation 3.8 is not possible anymore. But, with the presumption of a modal damping as given by the following relation, the term $\Phi_s^T C_s \Phi_s$ is reduced to a diagonal form and the benefits from the diagonal matrix properties in equation 3.8 are retained:

$$\Phi_s^T \cdot C_s \cdot \Phi_s = 2 \cdot diag(\omega_i \zeta_i) \ . \tag{3.9}$$

The variable ζ_i represents the modal damping parameter for the i-th eigenmode and is defined as ratio between the damping coefficient c_j to the critical damping $c_{cr,j}$ characterizing the aperiodic solution of a single mass oscillator (c_j, m_j, k_j being the damping coefficient, mass and stiffness of the single mass oscillator):

$$\zeta_i = \frac{c_j}{c_{cr,j}} = \frac{c_j}{2 \cdot \sqrt{k_j \cdot m_j}} \ . \tag{3.10}$$

The introduction of a modal damping matrix corresponds to the assumption that the complete energy dissipated during one vibratory cycle can be expressed as the sum of individual dissipation losses for each participating eigenmode. Typically, most engineering structures are weakly damped and the damping ratios that can be found in literature for various types of structures vary from $0,5$ up to 15% [Cook89, Cremer96]. The general solution of equation 3.8 is then obtained by:

$$\alpha_j(\omega) = \frac{\phi_{s,j}^T \cdot \hat{r}_{s,j}(\omega)}{\omega_j^2 + 2 \cdot j\omega \cdot \omega_j \cdot \zeta_j - \omega^2} \ , \quad j = 1 \ldots N_s \ . \tag{3.11}$$

For a harmonic excitation, modes with an eigenfrequency much higher than the forcing frequency contribute in general only to a neglectable extent to the displacement given in equation 3.7 and it is a common approach to truncate the modal expansion after the first M modes. Thus, the displacement vector is approximated by:

$$\hat{X}(\omega) \approx \widetilde{\Phi}_s \cdot \widetilde{\alpha}(\omega) \ , \tag{3.12}$$

with the reduced subspace $\widetilde{\Phi}_s \in \mathbb{R}^{N_s \times M}$ and $\widetilde{\alpha}(\omega) \in \mathbb{C}^M$. Typically $M \ll N_s$ and the computational effort in determining the modes and the modal amplitude is reduced to a great extent in comparison to the exact solution.

Applying the modal approach to the equation of motion valid for the fluid domain, results in a similar modal expansion for the complex pressure vector $\hat{P}(\omega)$:

$$\hat{P}(\omega) = \Phi_f \cdot \beta(\omega) \ . \tag{3.13}$$

Φ_f is the matrix of acoustic eigenvectors and $\beta(\omega)$ the modal amplitude vector of the fluid. Once the sound pressure has been computed, the particle velocity is derived from the Euler equation $\nabla p = -j\omega \cdot \rho_f \cdot v$.

When the structural behaviour is coupled to a fluid domain and vice versa the respective equations of motion 3.1 and 3.2 cannot be solved separately anymore. On the interface between the structure and the fluid the boundary condition is given by:

$$\frac{\partial p}{\partial n} = -\rho_f \cdot \frac{\partial^2 x_n}{\partial t^2} \ , \tag{3.14}$$

with n as normal unit vector pointing from the wetted surface to the structure and ρ_f as fluid density. For the structure and the fluid equation 3.14 corresponds to additional exterior loads applied on the interface surface S_{sf}. The pressure load on the structure is:

$$R_s = \int_{S_{sf}} (N_X^T \cdot n) \cdot p \cdot dS = \int_{S_{sf}} (N_X^T \cdot n) \cdot N_P \cdot dS \cdot P = L \cdot P \ , \tag{3.15}$$

and the acoustic load due to the vibrating structure equals:

$$R_f = -\int_{S_{sf}} N_P^T \cdot \ddot{x}_n \cdot dS = -\int_{S_{sf}} N_P^T \cdot (n \cdot N_X) \cdot dS \cdot \ddot{X} = -L^T \cdot \ddot{X} \ , \tag{3.16}$$

since L is the coupling matrix defined by:

$$L = \int_{S_{sf}} (N_X^T \cdot n) \cdot N_P \cdot dS \ . \tag{3.17}$$

N_X and N_P denote the interpolation matrices relating the discrete, nodal displacement and pressure vectors to the displacement and pressure distribution within one element.

Including the additional exterior loads on the left-hand side of equations 3.1 and 3.2 results in the governing equation of motion for the coupled fluid-structure problem:

$$\begin{bmatrix} M_s & 0 \\ L^T & M_f \end{bmatrix} \begin{pmatrix} \ddot{X}(t) \\ \ddot{P}(t) \end{pmatrix} + \begin{bmatrix} C_s & 0 \\ 0 & C_f \end{bmatrix} \begin{pmatrix} \dot{X}(t) \\ \dot{P}(t) \end{pmatrix} + \begin{bmatrix} K_s & -L \\ 0 & K_f \end{bmatrix} \begin{pmatrix} X(t) \\ P(t) \end{pmatrix} = \begin{pmatrix} R_s(t) \\ R_f(t) \end{pmatrix} \ , \tag{3.18}$$

which may be written in the frequency domain as:

$$\begin{bmatrix} -\omega^2 M_s + j\omega C_s + K_s & -L \\ -\omega^2 L^T & -\omega^2 M_f + j\omega C_f + K_f \end{bmatrix} \begin{pmatrix} \hat{X}(\omega) \\ \hat{P}(\omega) \end{pmatrix} = \begin{pmatrix} \hat{R}_s(\omega) \\ \hat{R}_f(\omega) \end{pmatrix} \ . \tag{3.19}$$

Replacing the vector $\hat{P}(\omega)$ with $\hat{\Psi}(\omega)$ as defined by the function $\hat{P}(\omega) = j\omega \cdot \hat{\Psi}(\omega)$ and dividing the second line of equation 3.19 with $-j\omega$ yields a symmetric formulation of the coupled equation of motion:

$$\begin{bmatrix} -\omega^2 M_s + j\omega C_s + K_s & -j\omega L \\ -j\omega L^T & \omega^2 M_f - j\omega C_f - K_f \end{bmatrix} \begin{pmatrix} \hat{X}(\omega) \\ \hat{\Psi}(\omega) \end{pmatrix} = \begin{pmatrix} \hat{R}_s(\omega) \\ -(j\omega)^{-1} \cdot \hat{R}_f(\omega) \end{pmatrix} \ . \tag{3.20}$$

A modal transformation is carried out analogously to equation 3.7 and 3.13 by using the uncoupled structural and acoustic modes ϕ_s and ϕ_f. The resulting coupled equation of motion in modal coordinates reads:

$$\begin{bmatrix} -\omega^2 \Phi_s^T M_s \Phi_s + j\omega \Phi_s^T C_s \Phi_s + \Phi_s^T K_s \Phi_s & -j\omega \Phi_s^T L \Phi_f \\ -j\omega \Phi_f^T L^T \Phi_s & \omega^2 \Phi_f^T M_f \Phi_f - j\omega \Phi_f^T C_f \Phi_f - \Phi_f^T K_f \Phi_f \end{bmatrix} \cdot$$

$$\cdot \begin{pmatrix} \alpha(\omega) \\ \psi(\omega) \end{pmatrix} = \begin{pmatrix} \Phi_s^T \hat{R}_s(\omega) \\ -(j\omega)^{-1} \cdot \Phi_f^T \hat{R}_f(\omega) \end{pmatrix} \ , \tag{3.21}$$

with $\psi(\omega)$ given by $\hat{\Psi}(\omega) = \Phi_f \cdot \psi(\omega)$.

In many applications such as double wall partitions an enhancement of the sound absorption capabilities is achieved by lining the fluid surface with elastic-porous absorbers as fibreglass or open-cell foam. The additional source of damping provided by those materials is included

in the fluid model by applying the Bliss boundary condition [Bliss82a] to the fluid-structure boundary:

$$\hat{P}_{sf}(\omega) + B(\omega) \cdot \nabla_{sf}^2 \, \hat{P}_{sf}(\omega) = Z(\omega) \cdot \hat{V}_n(\omega) \; . \tag{3.22}$$

$\hat{P}_{sf}(\omega)$ and $\hat{V}_n(\omega)$ are the surface sound pressure and normal particle velocity respectively. The absorber properties are defined in terms of their normal impedance $Z(\omega)$ and the bulk reacting coefficient $B(\omega)$. The normal impedance is easily determined in a Kundt's tube and a method to measure the bulk reacting coefficient has been suggested by Bliss and Burke [Bliss82b]. The operator ∇_{sf}^2 contains second derivatives in the plane of the surface and the whole term $B(\omega) \cdot \nabla_{sf}^2 \, \hat{P}_{sf}(\omega)$ takes into account the additional sound absorption on a porous surface due to velocity components in the plane of that surface.

By neglecting the bulk reacting coefficient or for normal incident sound waves, equal to $B(\omega) \cdot \nabla_{sf}^2 \, \hat{P}_{sf}(\omega) = 0$, the classical normal impedance boundary condition is obtained:

$$Z(\omega) = \frac{\hat{P}_{sf}(\omega)}{\hat{V}_n(\omega)} \; . \tag{3.23}$$

In this case, the sound absorption is governed only by the real part of the impedance and the damping matrix C_f has contributions from the real part of the impedance and the stiffness matrix K_f contains contributions from the imaginary part of Z.

3.1.2 Structural Excitation

For the primary excitation of the structure, different concepts are used. One model is thought as a very simple approximation of a buzz-saw noise type excitation: a monopole source placed at the location of the engine inlet, radiating towards the fuselage with constant power at all frequencies. This setup will allow testing the efficiency of the noise reduction system against a tonal, coherent noise source. A diffuse sound field can be modelled by using plane wave superposition and a mechanical point force excitation can be used for simple test purpose or the simulation of structure-borne sound as excited for example by engines due to rotating, unbalanced masses.

The single monopole source is located at a position r relative to the point of origin of the x,y,z-coordinate system, x and y being the axes in the panel plane and z the normal axis to the panel as depicted in Figure 3.2.

To determine the excitation sound pressure level on the panel at a position r_s the assumption is made that the structure is totally rigid. Therefore, free field propagation can be assumed and the pressure values obtained with the following equation must be multiplied with a factor of two in order to take into account the total reflection on the rigid surface. With the assumption of a small source diameter a in comparison to the acoustic wavelength, $2\pi \cdot a/\lambda \ll 1$, the complex, free field pressure radiated by a monopole source with the volume flow Q at the angular frequency ω is given by [Fahy85]:

$$p\,(r_s) = j\omega \cdot \rho_0 \cdot \frac{Q}{4\pi \cdot R} \cdot e^{-j\omega R/c_0} \; . \tag{3.24}$$

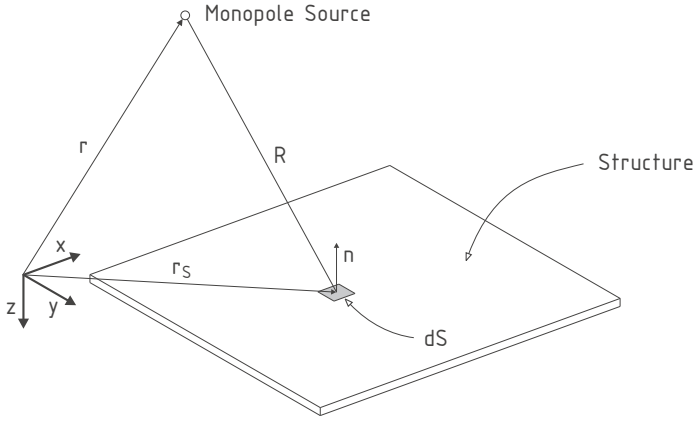

Figure 3.2: Acoustic excitation with a monopole source

The term R is the distance between the source and the observer point on the panel, $R = |r_s - r|$. The volume velocity Q is equal to $4\pi \cdot a^2 \cdot v_n$, with v_n being the normal velocity of the source. ρ_0 and c_0 are the density and the speed of sound of the fluid.

To calculate the transmission loss the acoustic power of the incident sound field on the receiving side of the panel has to be determined by integrating the sound intensity I_n perpendicular to the receiving surface S of the structure:

$$P_{Incident} = \int_S I_n(r_s) \cdot dS \ . \tag{3.25}$$

The vector quantity $I(r_s)$ denotes the sound intensity at the point r_s and describes the magnitude and direction of the net flow of acoustic energy per unit area. For harmonic time dependence the sound intensity is proportional to the real part of the product between the complex acoustic pressure and particle velocity:

$$I(r_s) = \frac{1}{2}\Re(p\,(r_s) \cdot v^*\,(r_s)) \ . \tag{3.26}$$

The superscript * designates the complex conjugate of the particle velocity v. In the far field, some wavelengths away from the original source, the sound propagation corresponds to a quasi-plane wave. The acoustic impedance, defined as the ratio between the complex acoustic pressure and complex particle velocity, is then purely real, because the periodic change of pressure and velocity occurs in phase [Heckl94]:

$$Z = \frac{p}{v} = \frac{\rho_0 \cdot c_0}{\cos\theta} \ , \tag{3.27}$$

where θ is the angle between the vector from the monopole source to the observer point and the selected velocity component at the observer point. Introducing equation 3.26 and 3.27 into relation 3.25 the incident sound power on the receiving side of the structure is obtained:

$$P_{Incident} = \frac{1}{2\rho_0 c_0} \int_S |p\,(r_s)|^2 \cdot \cos\theta \cdot dS \ . \tag{3.28}$$

Frequently, the sound power is expressed in a decibel scale in terms of sound power level. The sound power level is then defined as:

$$L_W = 10 \cdot \log \frac{P}{P_0} \quad [dB] \ , \tag{3.29}$$

where $P_0 = 10^{-12}$ Nm/s denotes the reference power.

In contrast to a single plane wave a diffuse sound field comprises an infinite number of progressive plane waves, such that all directions of propagation are equally probable and the phase relations of the waves are random at any given point in space [Witting99]. In practice a diffuse sound field is often approximated deterministically by a superposition of a finite number of plane or spherical waves. Using the basic equation 3.24 for the spherical monopole source this assumption leads to the following expression for the sound pressure:

$$p\left(r_s\right) = \sum_n j\omega \cdot \rho_0 \cdot \frac{Q_n}{4\pi \cdot R_n} \cdot e^{(-j\omega R_n/c_0 + \alpha_n/2\pi)} \ . \tag{3.30}$$

The number of monopole sources is denoted by n. The random frequency-dependant phase angles for each monopole source are given by α_n and should correspond to a stochastic uniform distribution for each angular frequency ω. To assure the required spatial uniform distribution, the single sources have to be disposed over a half sphere covering the receiving side of the structure in such a manner as to equal all directions of incidence.

3.1.3 Sound Radiation

The acoustic model to predict the sound field radiated by a vibrating structure is presented in the following section [Morse86, Skudrzyk71]. Considering the illustration in Figure 3.3 the problem of acoustic wave propagation through a homogenous, ideal fluid volume V_F can be described in the frequency domain by the Helmholtz differential equation:

$$\nabla^2 p(r) + \left(\frac{\omega}{c_0}\right)^2 \cdot p(r) = 0 \ , \tag{3.31}$$

with $p(r)$ being the complex pressure at a point r.

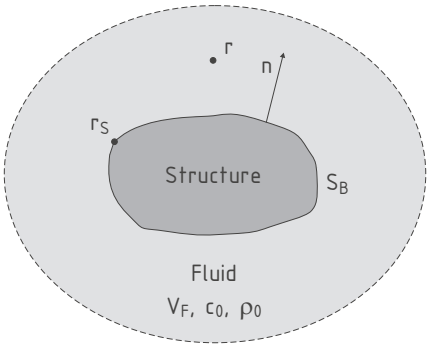

Figure 3.3: Radiation of a vibrating structure into an unbounded fluid volume

For a harmonic vibrating and closed boundary S_B radiating into an infinite, free fluid field, which satisfies the Sommerfeld infinity condition[2], equation 3.31 can be rewritten in an alternative form, known as the Kirchhoff-Helmholtz integral equation. The integral formulation relates the free field pressure to physical quantities on the boundary S_B and is in particular suited for numerical solutions with the boundary element method, where the boundary is divided into small, discrete elements:

$$p(r) = \int_{S_B} \left(p(r_s) \cdot \frac{\partial G(r, r_s)}{\partial n} - \frac{\partial p(r_s)}{\partial n} \cdot G(r, r_s) \right) dS_B \ . \tag{3.32}$$

The vector r_s denotes a point on the boundary S_B and r a field point. n is the normal vector of the boundary surface pointing into the fluid domain. The integral in equation 3.32 can be interpreted as a superposition of weighted monopole (term G) and dipole sources (term $\partial G/\partial n$) disposed on the boundary S_B. It should be noted that equation 3.32 is only valid for field points lying outside the boundary S_B. If the pressure is to be evaluated on a smooth part of the boundary S_B, the left side of equation 3.32 has to be multiplied with a factor of one half. $G(r, r_s)$ is the full space Green's function:

$$G(r, r_s) = \frac{e^{-j\omega R/c_0}}{4\pi \cdot R} \quad \text{with} \quad R = |r - r_s| \ , \tag{3.33}$$

and can be construed as the pressure at the point r caused by a monopole source with the source strength 1 at the location r_s on the boundary S_B. For the free fluid volume V_F the Green's function is a solution of the homogenous Helmholtz differential equation and fulfils the Sommerfeld infinity condition. At the point $r = r_s$ the Green's function exhibits a singularity and is the solution to the inhomogeneous Helmholtz differential equation excited by a Dirac pulse $\delta(r - r_s)$.

A fundamental simplification of equation 3.32 can be made for a vibrating, flat structure located in the x,y-plane at $z = 0$ and being surrounded by an otherwise rigid, plane and infinite boundary (baffle) as illustrated in Figure 3.4.

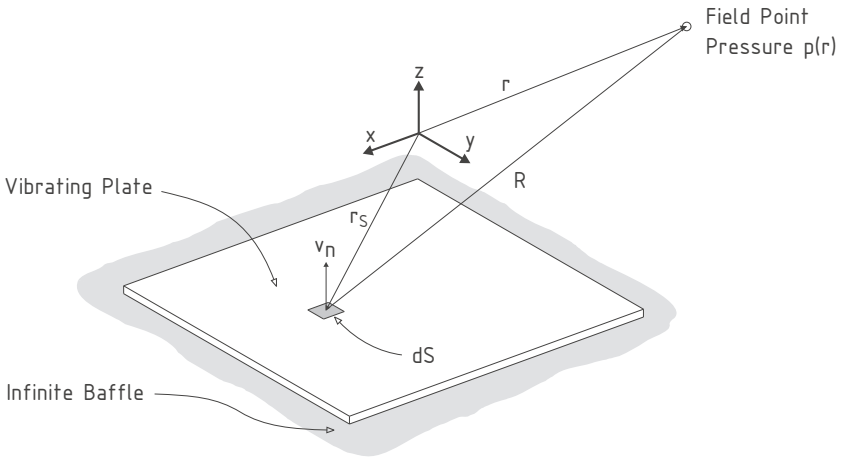

Figure 3.4: Interpretation of the Huygens-Rayleigh integral

[2]Infinite regions do not contribute to the sound radiation.

The baffle can be constructed by using the method of image sources. Thus, the half space Green's function G_h is derived by adding an image point source to the full space Green's function:

$$G_h(r, r_s, \tilde{r}_s) = \frac{e^{-j\omega R/c_0}}{4\pi \cdot R} + \frac{e^{-j\omega \tilde{R}/c_0}}{4\pi \cdot \tilde{R}} \ . \tag{3.34}$$

The vector $\tilde{r}_s$ denotes the position of the image source at $z_{\tilde{r}_s} = -z_{r_s}$ and $\tilde{R}$ the distance from the image source to the field point. If the vibrating surface lies directly on the baffle, the half space Green's function is reduced to:

$$G_h(r, r_s, \tilde{r}_s) = 2 \cdot G(r, r_s) \ , \tag{3.35}$$

and due to the symmetry of the sound field with respect to the baffle the partial derivative of G_h with respect to the normal direction vanishes:

$$\partial G_h(r, r_s, \tilde{r}_s)/\partial n = 0 \ . \tag{3.36}$$

Consequently, the Helmholtz differential equation can be expressed as:

$$p(r) = -2 \cdot \int_{S_B} \frac{\partial p(r_s)}{\partial n} \cdot G(r, r_s) \cdot dS_B \ , \tag{3.37}$$

when equation 3.35 and 3.36 are inserted into equation 3.32.

For a simple harmonic vibration of the structure the boundary condition for the plate is that the normal gradient of the pressure $\partial p(r_s)/\partial n$ is equal to $-j\omega \cdot \rho_0 \cdot v_n(r_s)$, with v_n being the normal velocity of the vibrating plate. Hence, relation 3.37 results into the Huygens-Rayleigh integral:

$$p(r) = \frac{j\omega \cdot \rho_0}{2\pi} \cdot \int_S \frac{v_n\,(r_s) \cdot e^{-j\omega R/c_0}}{R} \cdot dS \ . \tag{3.38}$$

R, S, v_n and ρ_0 are the distance between the radiating element dS and the observer point, the surface area of the vibrating structure, the normal component of the velocity on the vibrating surface and the density of the acoustic propagation medium, respectively. The Huygens-Rayleigh integral can be interpreted in such a way that the pressure $p(r)$ for free field conditions at a given field point in the baffled half space is the result of a superposition of elemental monopole sources at points r_s on the radiating surface S. Since the element dS is only radiating into a half space the source strength associated with a single monopole sources is $2 \cdot v_n(r_s) \cdot dS$, which is twice as much as it would be without the baffle.

Beside the acoustic pressure $p(r_s)$ the radiated sound field is also characterized by the particle velocity $v(r_s)$. For the acoustic far field, the sound propagation is corresponding to a quasi-plane wave, with the pressure and particle velocity having the same phase (see equation 3.27). With this assumption, and similar to equations 3.25 and 3.28, the total radiated sound power $P_{Radiated}$ is derived from the pressure values obtained with the Rayleigh integral on a field mesh completely enveloping the radiating structure:

$$P_{Radiated} = \frac{1}{2\rho_0 c_0} \cdot \oint_{S_H} |p_H(r)|^2 \cdot \cos\theta \cdot dS_H \ . \tag{3.39}$$

The terms S_H and p_H are representing the surface area and the complex pressure on the field mesh, whereas θ is the angle between the normal vector of the element dS_H and the vector from the structure's centre point to the field mesh point.

The Huygens-Rayleigh integral is the simplest approach to calculate the sound field radiated by a flat, vibrating surface. From an FEM frequency-response analysis of a vibrating structure for instance, the complex velocities are available as a function of frequency for each nodal point. Considering each node on the radiating surface as an elemental acoustic source, the integration in equation 3.38 can be evaluated numerically as a sum over all source elements. Similarly, the integral in equation 3.39 is approached numerically as a sum over the elements constituting the discretised enveloping surface S_H.

A disadvantage of the Huygens-Rayleigh integral is the fact that it is limited to plane surfaces. Nevertheless, the sound radiation from a given curved or cylindrical structure can be incorporated in the simulation model by a numerical BEM evaluation of the Kirchhoff-Helmholtz integral or by using appropriate Green's functions [Graham95, Williams97].

The structure's efficiency in reducing sound transmission is traditionally estimated by the transmission loss index, which is defined as ratio of incident acoustic power on the source side to transmitted power on the radiating side, expressed in a decibel scale:

$$TL\,(\omega) = 10 \cdot \log \frac{P_{Incindent}\,(\omega)}{P_{Radiated}\,(\omega)} \ \ [dB] \ . \tag{3.40}$$

With this vibro-acoustic model the sound radiation behaviour of passive and active flat panel systems can be determined for different types of structural and acoustic excitations. The described simulation approach does not take into account effects like the additional sound absorption in an aircraft cabin but simply illustrates how efficiently the structure itself is blocking the sound transmission. The model will be used to evaluate the effectiveness of various actuator designs and control implementations in reducing the sound radiation from the structure for a given primary perturbation.

3.2 Modelling of Piezoelectric Actuators

One possibility to investigate the effect of active elements on a global structural behaviour would be to use appropriate finite elements, which respect the coupling of mechanical and electrical degrees of freedom according to the constitutive equation of piezoelectricity 2.68 [Preumont97, Janocha92]. Such elements are available in some commercial finite element codes (e.g. *Ansys*). However, piezoelectric finite elements increase the complexity in the model preparation, especially when different actuator concepts, designs and positions have to be analyzed.

For many relevant static and dynamic problems, where only the structural response due to the piezoelectric effect of the actuators has to be investigated analytically or numerically, the mechanical coupling to the electric field may be neglected. This assumption leads to two

relative simple models, where the additional strain induced by the actuators is replaced with an equivalent thermal load or a set of external, static forces applied along the edges of the piezo-element.

To derive a suitable actuator concept for the control of sound transmission through an aircraft sidewall section, both models will be used in the simulations presented in Chapter 4. The mechanical principles and assumptions underlying those models are shortly summarized in the following sections.

Thermal-Elastic Analogy

The thermal-elastic analogy is based on the mathematical similarity between free piezoelectric and thermal strain to model the piezoelectric effect. If the governing equation 2.66 for a piezoceramic material polarized in 3-direction is expanded to include thermal strain effects, the following system of equations describing the in-plane behaviour of the material is obtained:

$$\begin{pmatrix} \sigma_1 \\ \sigma_2 \\ \tau_{12} \end{pmatrix} = \begin{bmatrix} Q_{11} & Q_{12} & 0 \\ Q_{12} & Q_{22} & 0 \\ 0 & 0 & Q_{66} \end{bmatrix} \cdot$$
$$\cdot \left(\begin{pmatrix} \epsilon_1 \\ \epsilon_2 \\ \gamma_{12} \end{pmatrix} - \begin{bmatrix} 0 & 0 & d_{31} \\ 0 & 0 & d_{31} \\ 0 & d_{15} & 0 \end{bmatrix} \cdot \begin{pmatrix} U_1/t_1 \\ U_2/t_2 \\ U_3/t_3 \end{pmatrix} - \begin{pmatrix} \alpha \\ \alpha \\ 0 \end{pmatrix} \cdot \Delta T \right) \ , \tag{3.41}$$

which can be expressed in matrix notation as:

$$\Leftrightarrow \ (\sigma) = [Q] \cdot \left(\epsilon - \Lambda - \alpha \cdot \Delta T\right) \ . \tag{3.42}$$

The term Q denotes the stiffness matrix relating the strain to the stress state of the material. As can be seen from equation 3.41, the in-plane response due to an electric field in 3-direction is similar to the thermal strain induced by the temperature load ΔT. Consequently the actuator excitation $d_{31} \cdot U_3/t_3$ can be modelled by replacing the free piezoelectric strain Λ with an equivalent thermal strain $\alpha \cdot \Delta T$ applied to the piezoelectric material [Rapp96]. The rest of the structure is assumed to have a thermal expansion coefficient equal to zero. This method is easy to use because most FEM-programs can take into account thermal strain effects and gives acceptable results when the influence of active elements on global structural displacements is examined.

To numerically validate the FEM-model of Thunder elements, a set of actuators (model TH-10R, shown on the left side of Figure 2.13) was purchased for testing. The basic properties of this actuator type, provided by the manufacturer, are listed in Table 3.1.

A simplified structural model of this actuator element was built up in Nastran using CQUAD4 elements for the substrate steel layer and CHEXA volume elements for the ceramic layer. The curvature of the element is not considered in the model, as it is very small in comparison to the length and width of the element. The adhesive layers and the mounting slots on the free tabs are neglected as well within the FEM-model. The piezoelectric effect is modelled with the thermal-elastic analogy. The material properties and various parameters used in the

Table 3.1: Thunder specifications for model TH-10R

Thunder Specifications	
Overall dimensions:	25,4 x 13,8 x 0,64 mm
PZT-dimensions:	12,7 x 12,7 mm
Composite thickness:	0,43 mm
Substrate layer thickness:	0,20 mm
PZT layer thickness:	0,20 mm
Weight:	0,8 g
Capacity:	9 nF
Max. voltage (V_{pp}):	480 V
Typical displacement*:	0,3 mm
Blocked force**:	36 N

* clamped support on one side, maximum input voltage, quasi-static deflection peak to peak of the free tip at 1 Hz

** simply supported

FEM-model are summarized in Table 3.2. When the element is clamped in a cantilevered beam configuration a sinusoidal voltage, or a temperature load respectively, applied to the ceramic layer, induces a bending moment in the element and the free tip will make an up- and downward deflection as shown in Figure 3.5 for a harmonic excitation with 450 Hz.

Table 3.2: Thunder FEM-properties

	Substrate Layer	**Ceramic Layer**
Material:	steel	PZT-5A
Y.-modulus:	210.000 N/mm^2	60.600 N/mm^2
Poisson-constant:	0,3	0,3
Density:	7,85 g/cm^3	7,80 g/cm^3
Dimensions:	0,2 mm thickness	0,2 mm thickness
	25,4 x 13,8 mm	12,7 x 12,7 mm
Mesh:	CQUAD4 elements	CHEXA elements
Boundary condition:	cantilevered mount	nil
Thermal exp. coefficient:	0 K^{-1}	$6,3 \cdot 10^{-5}$ K^{-1}
Damping:	modal damping of 1%	modal damping of 1%

On the real Thunder element this deflection of the free tip was measured with a laser vibrometer. The curves in Figure 3.6 show four frequency-response functions in terms of normal velocity per applied voltage obtained with frequency sweeps from 0 to 1 kHz. The experimental results differ in magnitude and frequency because the cantilever mounting of the elements was repeatedly dis- and reassembled for the measurements. The velocity magnitude reaches its maximum between 400 and 500 Hz when the first bending eigenmode of the element is fully excited.

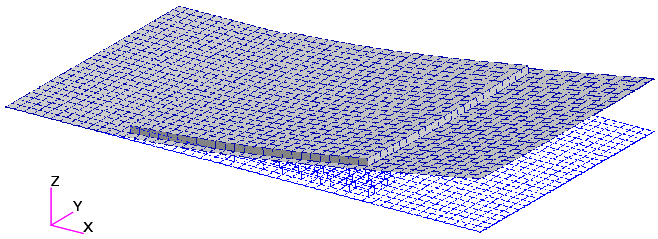

Figure 3.5: FEM-model: structural deflection, driving frequency 450 Hz

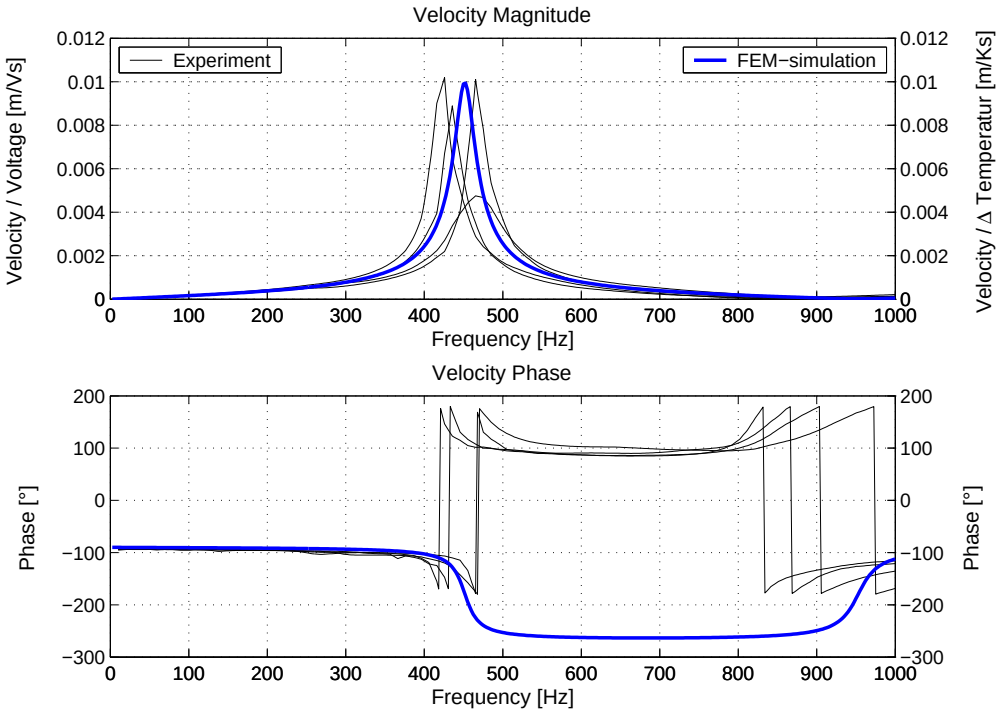

Figure 3.6: Measured and calculated actuator frequency-response

Based on the experimental data, the thermal expansion coefficient of the ceramic layer in the FEM-model was then calibrated in such a way that the velocity response of the numerical model per one degree Kelvin matches the experimental velocity response per one Volt, using the same geometrical and boundary conditions as in the experiment. The simulation results in Figure 3.6 show that a good agreement in magnitude and phase for both numerical and measured data is reached. The thermal expansion coefficient utilised in the thermal-elastic model is equal to $6,3 \cdot 10^{-5}$ K^{-1}.

Equivalent Force Model

Another method is provided by the equivalent force model in which the actuator stiffness and actuation forces are replaced by a set of equivalent line forces and moments applied to the respective FEM-nodes of the host structure along the edges of the particular piezo patch. The equivalent forces and moments correspond to the stress resultants, which are obtained from the

equilibrium of forces for a small structural element as illustrated in Figure 3.7 for a structure with a surface bonded piezo patch.

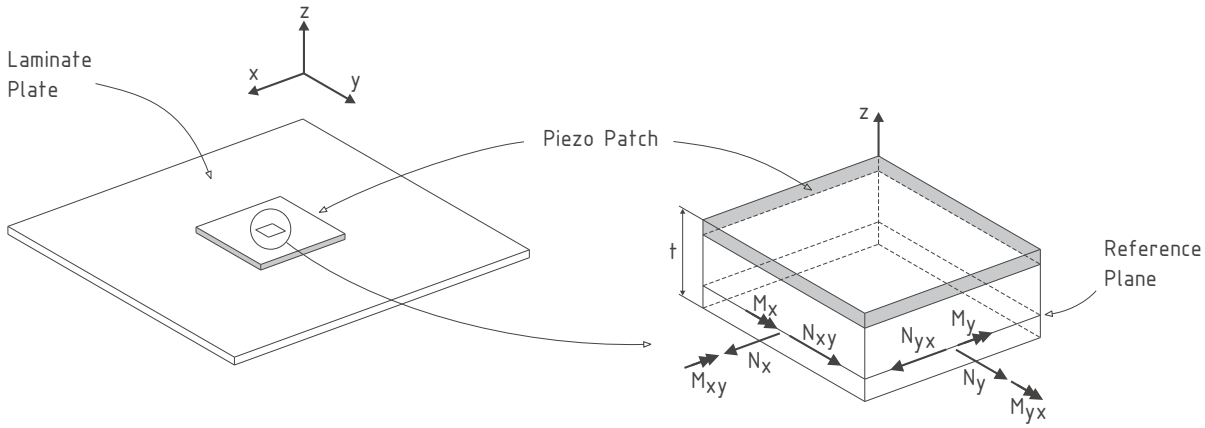

Figure 3.7: Laminate plate with a surface bonded piezo patch

For plates made of orthotropic laminate layers the equivalent force model can be derived with the classical laminate theory [Locatelli01]. The resulting equivalent in-plane forces are given by the following equation in matrix form:

$$\begin{pmatrix} N \\ M \end{pmatrix}_{eq} = \begin{bmatrix} A & B \\ B & D \end{bmatrix}_{hs} \cdot \begin{bmatrix} A & B \\ B & D \end{bmatrix}_{tot}^{-1} \cdot \begin{bmatrix} A \\ B \end{bmatrix}_{act} \cdot \Lambda \ , \tag{3.43}$$

where $N = \{N_x, N_y, N_{xy}\}^T$ and $M = \{M_x, M_y, M_{xy}\}^T$. A, B and D are the usual stiffness matrices as used in the classical laminate theory [Rohwer96, Tsai80]. Its ij-th elements are defined as:

$$\begin{aligned} \text{Matrix of in-plane stiffness:} \quad A_{ij} &= \sum_{k=1}^{N} \overline{Q}_{ij,k} \cdot (z_k - z_{k-1}) \ , \\ \text{Matrix of coupling stiffness:} \quad B_{ij} &= \frac{1}{2} \cdot \sum_{k=1}^{N} \overline{Q}_{ij,k} \cdot \left(z_k^2 - z_{k-1}^2\right) \ , \\ \text{Matrix of rotational stiffness:} \quad D_{ij} &= \frac{1}{3} \cdot \sum_{k=1}^{N} \overline{Q}_{ij,k} \cdot \left(z_k^3 - z_{k-1}^3\right) \ , \end{aligned} \tag{3.44}$$

with $\overline{Q}_{ij,k}$ being the ij-th element of the reduced stiffness matrix Q in the k-th laminate layer and z_k the coordinate through the laminate thickness t. The subscripts *hs*, *tot* and *act* refer to the summation over the host structure only, the whole structure including the actuators and the actuators only, respectively. Although equation 3.43 is only valid for static applications, it has been shown that with the equivalent force model proper results are also obtained for dynamic problems [Bebesel99, Lammering98, Locatelli01, Nijhuis03]. However, as in contrast to the thermal-elastic model the influence of actuator mass and stiffness are neglected in dynamic analysis, the dynamic application is limited to piezo patches with small dimensions in

comparison to the host structure. Furthermore, for a given material combination of structure and piezoceramic, relation 3.43 can be used to optimise the actuator thickness with respect to the actuation forces. A more detailed description and derivation of the equivalent force model is covered in the Annex A.

3.3 Control Loop Simulation

For the simulation of the control loop, the structural behaviour is described by the following set of second order differential equations:

$$M_s \cdot \ddot{X}(t) + C_s \cdot \dot{X}(t) + K_s \cdot X(t) = R_s(t) = R_p(t) + R_a(t) \ , \tag{3.45}$$

$$R_a(t) = -P_a \cdot U_a(t) = -P_a \cdot H \cdot Y_s(t) \ . \tag{3.46}$$

The vector R_s is the load vector and is composed of a primary perturbation R_p and a secondary controller generated part R_a defined in equation 3.46. The matrix P_a relates the structural load to the actuator input signal U_a, which in turn might be expressed as product of a general controller matrix H and an output signal Y_s used as error quantity. Depending on the control algorithm and sensor types either appropriate structural velocities:

$$Y_s(t) = C_1 \cdot \dot{X}(t) \ , \tag{3.47}$$

or accelerations output signals:

$$Y_s(t) = C_1 \cdot \ddot{X}(t) \ , \tag{3.48}$$

are available. The influence matrix C_1 relates the sensor distribution to the velocity or acceleration vector.

A second output Y_r is required to monitor the velocities on the radiating surfaces, which are then post-processed to calculate the radiated sound power as described in Chapter 3.1.3. They are related to the velocity vector $\dot{X}$ by a second influence matrix C_2:

$$Y_r(t) = C_2 \cdot \dot{X}(t) \ . \tag{3.49}$$

Many controller design methods are based on the state space description of the system to be controlled. With this model any linear, time-invariant, dynamical system as given by the equations 3.45 to 3.49 can be described with a set of first order differential equations [Preumont97]:

$$\dot{X}(t) = A \cdot X(t) + B \cdot U(t) \ , \tag{3.50}$$

$$Y(t) = C \cdot X(t) + D \cdot U(t) \ . \tag{3.51}$$

The first equation describes the internal dynamics of the system, represented by the state vector X, when driven by the input vector U. The matrix A is the system matrix and B the

input matrix. The system output is given by equation 3.51 and relates the output vector Y to the state and input vector by the output matrix C and the feedthrough matrix D, respectively[3]. To simplify the simulation model only the steady state response to a tonal primary perturbation is considered. With this presumption, the calculation of the structural dynamics without control and the closed-loop behaviour can both be performed in the frequency domain and a more complex description in the time domain is not necessary. The frequency domain form of the state space model is obtained by a Laplace transformation of equations 3.50 and 3.51. Thus, the state equation becomes (assuming zero initial conditions):

$$X(s) = (sI - A)^{-1} \cdot B \cdot U(s) \ , \tag{3.52}$$

and from the output equation 3.51 the relation:

$$Y(s) = \left[C \cdot (sI - A)^{-1} \cdot B + D\right] \cdot U(s) = G(s) \cdot U(s) \ , \tag{3.53}$$

is obtained. For a MIMO system $G(s)$ is the transfer matrix consisting of $N \times M$ linear, time-invariant transfer elements $G(s) = [y_i(s)/u_j(s)]$ $(i = 1, 2, \ldots, N; \mathrm{j} = 1,2,\ldots,\mathrm{M})$, with M being the number of input signals and N the number of output signals.

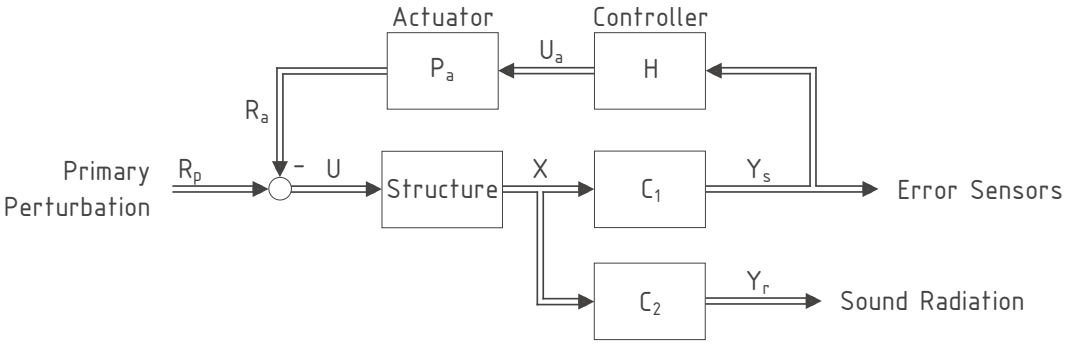

Figure 3.8: Control Loop

The block diagram of a typical control loop, representing the simulation model described by equations 3.45 to 3.49, is illustrated in Figure 3.8. It is assumed that the structure, possessing M independent degrees of freedom, is fitted with N_s sensors and N_a actuators. Additionally the sound radiation is monitored at N_r local points. According to equation 3.53 the input vector U and output vector Y_s, which is used as error signal for the control, are related by a transfer matrix $G_1 \in \mathbb{C}^{N_s \times M}$. In an analogous manner a transfer matrix $G_2 \in \mathbb{C}^{N_r \times M}$ connects the input to the second output signal Y_r. A generic control law is represented by the block containing the transfer matrix $H \in \mathbb{C}^{N_a \times N_s}$. It generates the actuator driving signal U_a, which is linked to the actuator load R_a and the input vector U by the influence matrix $P_a \in \mathbb{C}^{M \times N_a}$. If an appropriate control law is used, the effect of the primary perturbation R_p on the output signal Y_s can be compensated to a great extent. For the present application, two control algorithms, namely *local velocity feedback* and *LMS* control, are implemented in the simulation model.

[3]Note that the state vector X should not be confounded with the displacement vector X.

However, as the error signal Y_s and output signal Y_r, from which the radiated sound field is derived, do normally not correspond and given that the purpose of control is to reduce the structural sound radiation, error sensors having a good as possible correlation to the radiated sound are required. Since the square velocity of a radiating element is proportional to the radiated sound power (see equation 3.39), suitable error signals are for instance local structural velocities or accelerations as given by equations 3.47 or 3.48.

Local Velocity Feedback

Local velocity feedback control is often mentioned in literature about active structural control [Hansen97, Locatelli01, Nijhuis03] and is based on the negative feedback of a velocity sensor signal to a given actuator through a proportional gain. Because the control forces appear as viscous damping terms in the equations of motion and increase the dissipation of power, the control law is often referred to as active damping. Using collocated actuators and sensors ensures the stability of the system for a given gain range and provides a certain robustness to uncertainties in the structural model [Preumont97]. The complexity of a hardware system using velocity feedback control is rather low because only analogue elements would be required for its implementation.

The control law can be derived from the scheme in Figure 3.8. The error signal consists of the perturbation signal and the secondary signal:

$$Y_s(s) = G_1 \cdot U(s) = G_1 \cdot (R_p(s) - P_a \cdot U_a(s)) \ . \tag{3.54}$$

Replacing $Y_s(s)$ by the following relation:

$$U_a(s) = H \cdot Y_s(s) \ , \tag{3.55}$$

the driving signal $U_a(s)$ is obtained as function of the primary perturbation signal:

$$U_a(s) = (I + HG_1P_a)^{-1} \cdot H \cdot G_1 \cdot R_p(s) \ . \tag{3.56}$$

Each collocated actuator and sensor pair represents a single-input single-output system. Hence, the gain matrix H is reduced to a diagonal matrix of the form $H = diag(h_i)$ with $i = 1, 2, \ldots, N_s$ and $N_s = N_a$.

Least-mean-square control

Another control law, which might be used for the control of tonal or stochastic perturbations as in the present application, is the LMS algorithm [Hansen97, Maier00, Maier02, Nijhuis03]. The hardware implementation is more complex than for the velocity feedback algorithm and requires digital signal processing with adaptive filters [Elliott01a, Widrow85]. More details about the experimental implementation are given in Chapter 5. The objective of the control algorithm is the minimization of a cost function J. As physical quantity a mean, quadratic vibration level being proportional to the transmitted sound power is often used:

$$J(s) = Y_s^H(s) \cdot Y_s(s) \rightarrow Min \ . \tag{3.57}$$

In this case Y_s is the acceleration output signal as defined by equation 3.48. Taking into account equation 3.54, the cost function J is a quadratic function with respect to the actuator signal U_a and thus has distinct minima, which can be determined by setting the derivative of J by U_a to zero. The derivative of J with respect to U_a is expressed as:

$$\frac{\partial J}{\partial U_a} = -2 \cdot (G_1 P_a)^H \cdot G_1 \cdot (R_p(s) - P_a \cdot U_a(s)) = -2 \cdot (G_1 P_a)^H \cdot Y_s(s) = 0 \ . \tag{3.58}$$

Solving for the actuator command $U_a(s)$ results in:

$$U_a(s) = \left((G_1 P_a)^H \cdot G_1 P_a\right)^{-1} \cdot (G_1 P_a)^H \cdot G_1 \cdot R_p(s) \ . \tag{3.59}$$

The superscript ^{H} denotes the Hermitian matrix. In terms of error signal reduction, the actuator input signal $U_a(s)$ defined by equation 3.59 represents the optimal solution. Therefore, the simulated system with LMS control corresponds to an optimal adaptive feed-forward control concept without causality constraints.

Sound Radiation

As the error signals and the database needed to calculate the radiated sound field do normally not coincide, the controlled structural response has to be calculated in an analogous manner as described above using the superposition principle. With a known actuator command $U_a(s)$ the output signal $Y_r(s)$ on the vibrating surface becomes:

$$Y_r(s) = G_2 \cdot U(s) = G_2 \cdot (R_p(s) - P_a \cdot U_a(s)) \ . \tag{3.60}$$

The term $G_2 \cdot R_p(s)$ contains the velocities on the radiating structural parts due to the primary perturbation and the expression $G_2 \cdot P_a \cdot U_a(s)$ describes the velocities due to the actuator excitation. With Y_r as input, the sound radiation is evaluated by the Huygens-Rayleigh integral for the open and closed-loop system.

The computation of the actuator transfer matrices $G_i \cdot P_a$ and the primary perturbation vector $G_i \cdot R_p$, with $i = 1, 2$, is done in Nastran, whereas Matlab is used to calculate the actuator input signal U_a, the resulting output Y_r and the radiated sound power.

For broadband primary noise it is much more difficult to obtain a realistic performance prediction of the closed-loop behaviour. Nevertheless, in this case the frequency domain approach may be used as a simple performance estimate of ANVC systems if causality constraints are neglected [Elliott01a].

3.4 Validation of the Simulation Procedure

An experimental validation of the numerical transmission loss prediction tool is presented in this chapter. The test setup is consisting of a single aluminium panel, a double wall configuration consisting of two identical aluminium panels and a double wall configuration, where the absorption in the cavity is enhanced with a thin layer of porous absorption material. The model

is validated by comparing the predicted and measured relative sound power levels radiated by the structure for various excitations.

The measurements are carried out with aluminium panels having in-plane dimensions of 1 by 1 m and a thickness of 1 mm. A separation distance of 90 mm between the single panels is chosen for the double wall configuration. To determine the sound transmission behaviour the panels are clamped with a set of frames in a transmission loss test window situated between a reverberation and anechoic chamber. The reverberation room is used for the excitation on the incident side of the panel, which is either done with a diffuse sound field through a pair of loudspeakers or a point force driving directly the panel. Both excitation sources are driven by a white noise source. In the anechoic chamber the transmitted sound power is measured by scanning the sound intensity over the surface of the radiating structure with an appropriate microphone system. The incident sound power is obtained from the diffuse sound pressure level in the reverberation chamber [Heckl94]. According to equation 3.40 and the European Standard Norm EN ISO 15186-1[4], the transmission loss is derived as ratio of incident to transmitted sound power. For the point force excitation the transmitted sound power is related to the excitation force. The measurement setup and method are described in detail in Chapter 5.2.

In Nastran each panel is modelled by 1224 uniform CQUAD4 shell elements and is clamped on its edges in an infinite, rigid baffle preventing both rotational and translatory displacements. For the double wall configurations the cavity fluid is modelled with 3756 CHEXA solid elements matching the structural mesh of the aluminium panel. On the wetted surface of the structure the dynamical behaviour of the structural and fluid domain is coupled through the normal components of velocity, whereas on all surfaces of the fluid not in contact with the structure, a boundary condition of $v_n = 0$ is enforced. The dynamic response of the radiating panel is determined by a modal frequency-response analysis. As the acoustical behaviour of the setup is determined in a frequency range up to 500 Hz, eigenmodes up to 1 kHz are retained in the summation of the modal responses [Blakely93]. Thus, the solution space is based on 298 eigenmodes for a single aluminium panel and 32 eigenmodes for the cavity fluid. A step size of 2,5 Hz is selected for the frequency resolution. Material and FEM-parameters for this basic configuration, denoted as configuration one in the following, are summarised in Table 3.3.

The main parameters controlling the sound radiation in the simulation model are the structural energy dissipation governed by the modal damping parameters, the type of boundary condition applied to the structure and the energy dissipation in the cavity fluid. To demonstrate the influence of those variables two further configurations in addition to the one resumed in the table above are analysed numerically. In a second configuration the modal damping applied to the structure is increased to 3%, whereas for the third configuration the clamped panel support is replaced with a simply supported boundary condition. The influence of cavity absorption is considered with a further FEM-model, where the cavity fluid is partly covered by acoustic absorber elements.

Three different types of excitation are used in the numerical simulation. The first model consists of a single monopole source located at $x = -5$ m, $y = -1,5$ m and $z = 5$ m relative to the panel's centre point, x and y being the axes in the panel plane and z the normal axis to the panel. For a typical single aisle aircraft this source position relative to the structure corresponds to the position of the engine inlet relative to the forward fuselage and thus can be regarded as

[4]Measurement of sound insulation in buildings and of building elements using sound intensity

Table 3.3: Basic experimental and simulation configuration

Aluminium Panel	
Y.-modulus:	74.000 N/mm^2
Poisson-constant:	0,3
Density:	2,70 g/cm^3
Dimensions:	1,0 mm thickness
	1000 x 1000 mm
	90 mm double wall distance
Mesh:	36 x 36 CQUAD4 elements
Boundary condition:	clamped in infinite, rigid baffle
Damping:	modal damping of 1%

Fluid	
Density:	1,225 kg/m^3
Speed of sound:	340 m/s
Spatial decay rate:	0,0001 m^{-1}
	(equals a loss factor η of $5,5 \cdot 10^{-5}$)
Mesh:	2 x 34 x 34 CHEXA elements
	1 x 38 x 38 CHEXA elements
Boundary condition:	structural velocity or $v_n = 0$

a simple approximation for a buzz-saw noise excitation. The resulting incidence angle on the panel is about 46°, which for a typical buzz-saw noise directivity pattern corresponds to the direction with maximal intensity [Léwy00].

A diffuse excitation is modelled by plane wave superposition. According to the field incidence mass law an approximated diffuse sound field is constructed from 250 independent monopole sources with incidence angles ranging from 0° to 78° to equal all relevant directions of incidence. Their position is distributed randomly over a half sphere of radius $r = 100$ m, covering the structure's incident side. Each monopole is given a constant source strength and a random frequency-dependant phase α_n. The point force excitation is modelled with a normal unity load of 1 N placed at the same relative position as in the experiments ($x = 222$ mm and $y = 280$ mm relative to the panel's centre point).

To derive the structurally radiated sound power in the numerical model, the Rayleigh integral is evaluated on a half cube of 100 m length, which totally covers the radiating structure. The cube is discretised into a relatively coarse field point mesh consisting of 108 uniform, rectangular elements where the resulting sound pressure is analysed. The accuracy of the Rayleigh approach was checked by calculating the sound radiation from a 2 mm steel panel excited by a point force and comparing the results with those obtained from a direct BEM-analysis in *LMS/Sysnoise*. The sound power predicted by both methods was in good agreement. The mean error averaged from 0 to 500 Hz amounted 1,4% or 0,06 dB, whereas the maximum error was 6,2%, corresponding to a difference of 0,3 dB in radiated sound power level. However, the main benefit from using the Rayleigh integral in combination with the far field assumption is the fact that the computation time needed to process the sound power from the structural

vibration data is at least reduced by 95% in comparison to the BEM-method.

It should be mentioned that an absolute comparison of measured and predicted sound transmission behaviour is only possible to some extent, as due to the respective measurement setup (geometry of the test window, mounting condition of the test structure, acoustic characteristics of test chambers) measured transmission loss values may vary up to 5 dB in the considered frequency range. Detailed analysis of those effects can be found in numerous publications [Guy84, Halliwell85, Jones79, Kihlman72, Kim04, Warnock82].

Aluminium Single Wall Partition

The predicted and measured transmission loss curves for the single panel with monopole and diffuse excitation are illustrated in Figure 3.9 and 3.10. In both cases there is a reasonable agreement between the predicted and measured sound transmission behaviour. In Figure 3.9 the dashed curve represents the mass law for 45° incidence, whereas in Figure 3.10 the dashed curve is calculated from the field incidence mass law. The results obtained with the point force excitation are represented in Figure 3.11 by means of radiated sound power relative to the square excitation force.

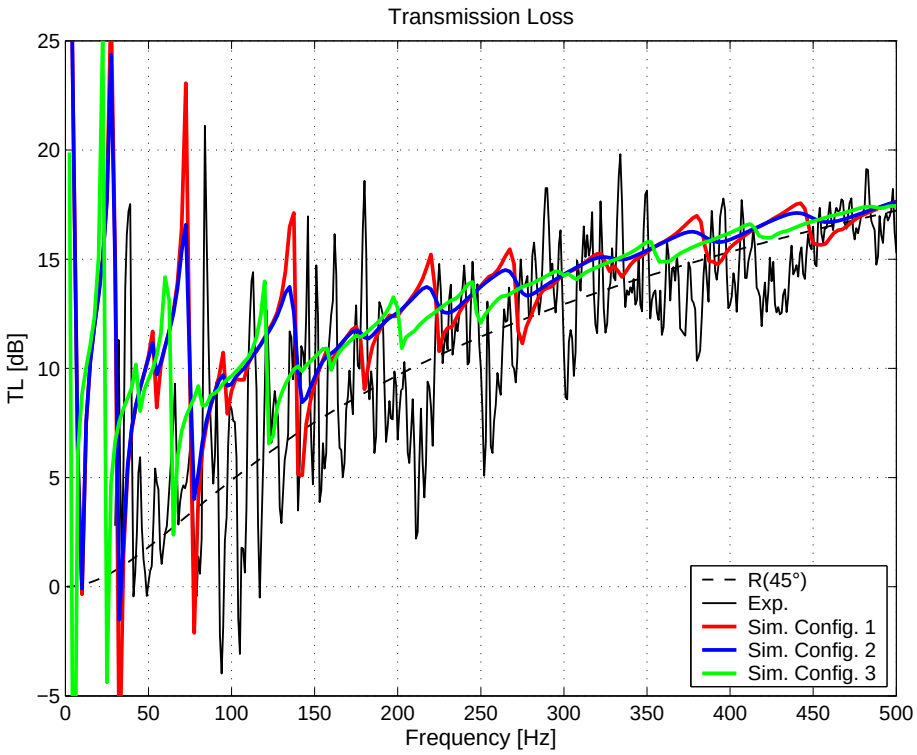

Figure 3.9: Transmission loss with monopole excitation

In the low-frequency range single eigenmodes with high radiation efficiency are excited on the real structure and in the simulation models, resulting in transmission loss values well below the one given by the analytical models. In-between those modes other eigenmodes with low sound radiation efficiency and a high transmission loss can be found. For higher frequencies the modal density is increased and the calculated and measured transmission loss curves are

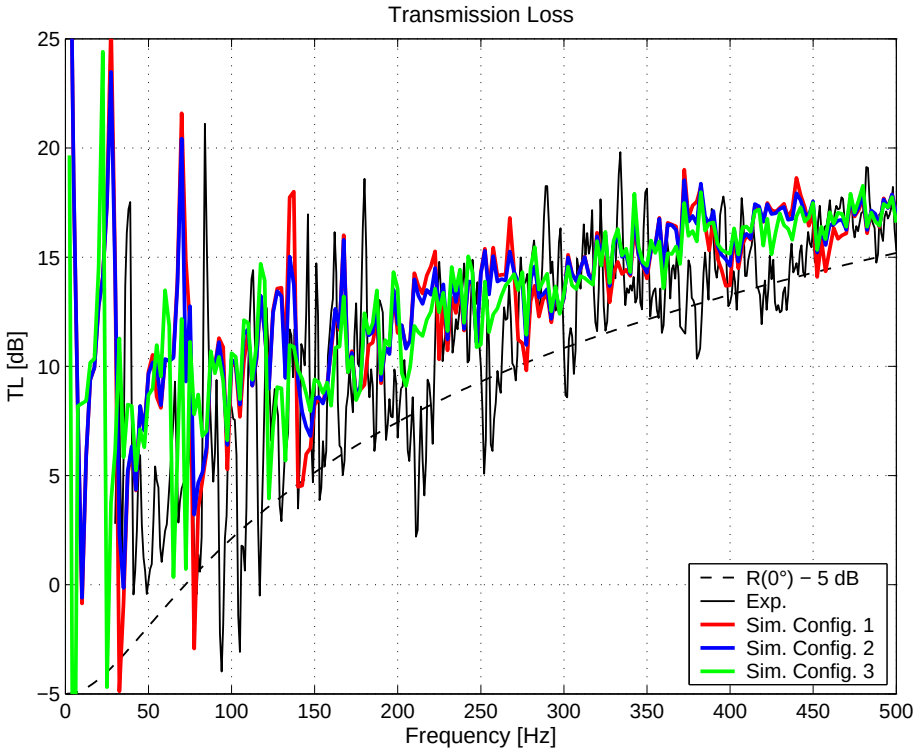

Figure 3.10: Transmission loss with diffuse excitation

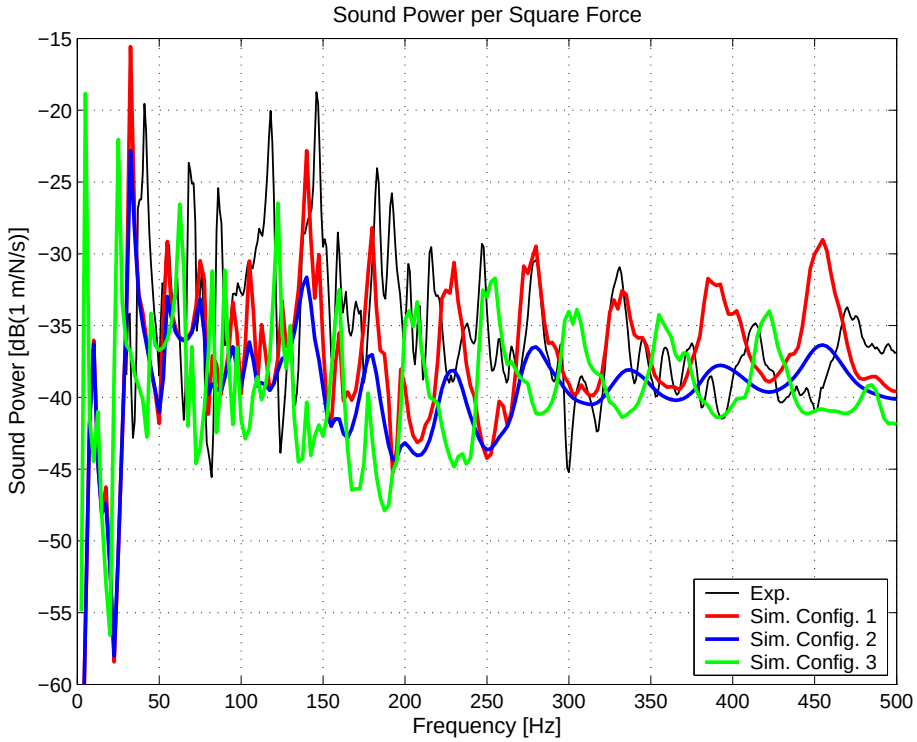

Figure 3.11: Sound power per square excitation force

smoothed and converge towards the theoretical mass laws showing the well-known behaviour of 6 dB increase per doubling of frequency.

The effect of mass control on the sound transmission, also connected with an increase of 6 dB per doubling of mass, is reproduced as well with the simulation approach, but not further shown here. In comparison to the monopole excitation the diffuse sound field results in a transmission loss behaviour exhibiting statistical fluctuations from the mean transmission loss. This is due to the random character of the incident sound field and is also observed in the measurement data.

The influence of the structural energy dissipation on the sound radiation is obvious from comparing the respective simulation results of configuration 1 to configuration 2. By increasing the modal damping up to 3% the resonant components in the sound transmission are reduced. Therefore, the distinct minima in transmission loss are increased and maxima decreased. The mean transmission loss, governed by the non-resonant mass law, is not affected.

The impact of the structural boundary condition is reflected by the curves representing configuration 3. As consequence of replacing the clamped support with a simply supported one, the shape of eigenmodes forming the solution space is changed and eigenfrequencies are shifted towards lower frequencies. Hence, the minima and maxima in transmission loss behaviour are also altered towards lower frequencies. However, as at higher frequencies the influence of the resonant transmission path is reduced, the sound transmission is mainly controlled by the mass law resulting in a similar mean transmission loss as achieved with the clamped support.

Aluminium Double Wall Partition

The results for the double wall configuration are shown in Figure 3.12 for the acoustic excitation and in Figure 3.13 for the point force excitation. The 45° incidence mass law for double wall partitions (see equation 2.47), predicting a local minimum in transmission loss at 246 Hz due to the mass-air-mass resonance[5], is illustrated by the dashed curve.

Compared to the analytical model the measured and calculated sound transmission behaviour is far more complex, but as before, especially in consideration of the complexity of the coupled system, a good agreement between measured and calculated trends can be observed. The predicted sound transmission shows the same characteristics as the measured transmission loss. A number of resonance frequencies, where the behaviour of both panels is coupled very strongly through the fluid domain, can be found in the whole frequency range. At those points the transmission loss value is well below the value of a single wall partition based upon the same total mass as used for the double wall system. Between the minima values, frequencies corresponding to acoustic anti-resonances of the cavity can be found and the motion of both plates is decoupled resulting in high transmission loss values. It should be noted that the accordance of the predicted peak at 167 and 242 Hz with the analytical mass-air-mass resonance is incidental. In contrast to the mass law, which is only valid for infinite panels, the complex coupling between structural and fluid eigenmodes in the numerical model is strongly dependant on additional parameters like the absolute dimensions of the structure and the fluid cavity and its boundary conditions.

[5]The fundamental mass-air-mass resonance occurs at 172 HZ for normal incidence.

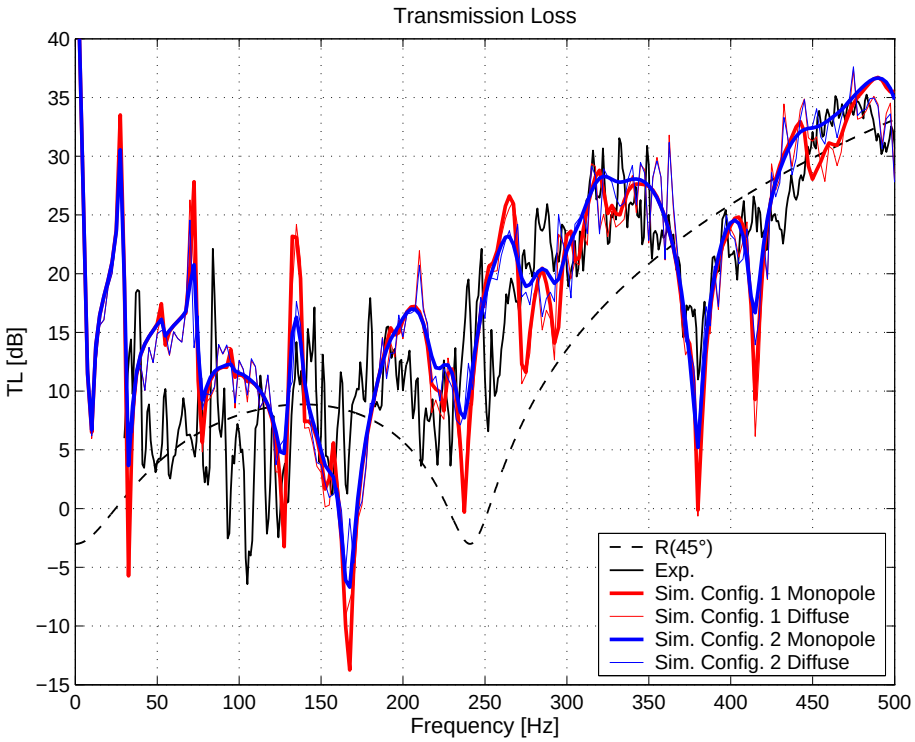

Figure 3.12: Transmission loss with acoustic excitation

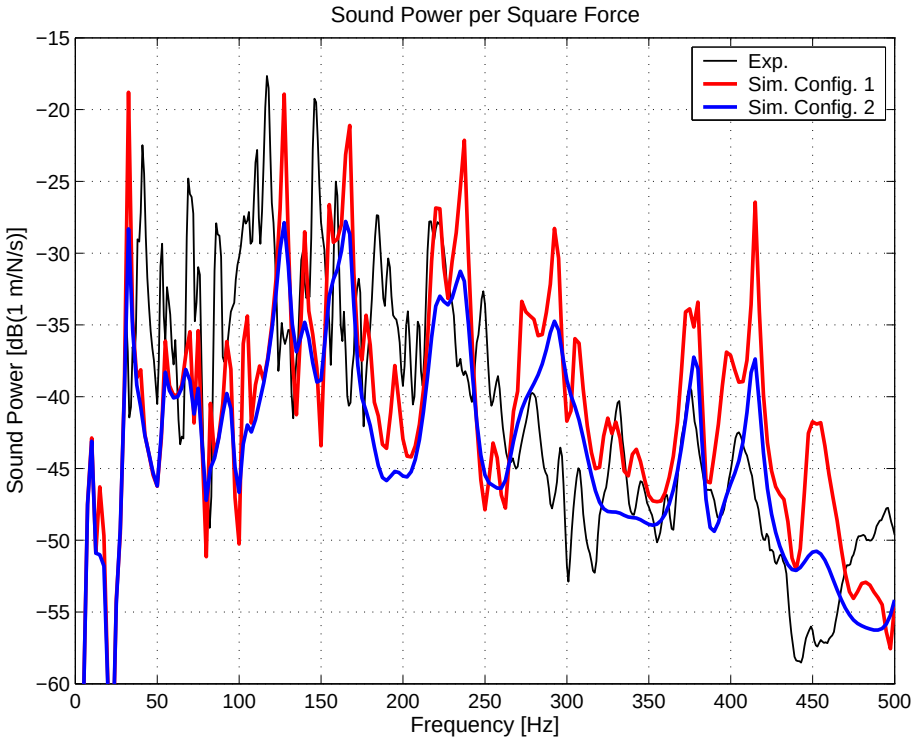

Figure 3.13: Sound power per square excitation force

At resonant peaks the sound transmission behaviour (for instance at 167, 246, 380 or 415 Hz) is overestimated by the simulation model in comparison to the experimental data. This suggests the presumption that the energy dissipation in the acoustic medium, governed by the fluid damping parameter and additional frictional losses on the fluid-structure interface, which can be taken into account by specified acoustic impedances, is not modelled correctly. Indeed the value of $\eta = 5,5 \cdot 10^{-5}$ represents probably a rather conservative estimate of the fluid damping for the considered frequency range [Schmidt96]. However, further simulations carried out with a fluid damping rate increased to $\eta = 1,1 \cdot 10^{-3}$ showed nearly no effect on the sound transmission behaviour presented in Figure 3.12 and 3.13. The effect of an increased cavity absorption achieved with an additional layer of porous material is addressed in the next section.

The influence of system parameters like damping and boundary condition applied to the structural parts is essentially the same as for the single wall partition.

Aluminium Double Wall Partition with Cavity Absorption

To examine the impact of an enhanced acoustic absorption within the experiments, the cavity on the incident panel was fitted with a layer of 10 mm thick, porous acoustic absorber foam on melamine resin basis. In the FEM-model the additional absorption is taken into account with the Bliss boundary condition by acoustic absorber elements (CAABF-elements in Nastran) covering the cavity surface on the incident side. The absorber elements are given the normal impedance properties of the foam, which were measured on a small sample in a Kundt's Tube. The bulk reacting coefficient is neglected. Table 3.4 shows the measured complex impedance values as used in the FEM-model. Interim values are interpolated linearly.

Table 3.4: Normal impedance of absorption material

Frequency	**Resistance**	**Reactance**
100 Hz	550 kg/s/m^2	-17500 kg/s/m^2
150 Hz	-	-12200 kg/s/m^2
200 Hz	-	-9350 kg/s/m^2
250 Hz	500 kg/s/m^2	-7350 kg/s/m^2
300 Hz	-	-6130 kg/s/m^2
350 Hz	-	-5300 kg/s/m^2
400 Hz	475 kg/s/m^2	-4632 kg/s/m^2
450 Hz	-	-4150 kg/s/m^2
500 Hz	340 kg/s/m^2	-3747 kg/s/m^2

The resulting sound transmission behaviours for acoustic and point force excitations are shown in Figure 3.14 and 3.15. As before, the dashed curve represents the mass law for 45° incidence (the additional cavity absorption is not considered in the analytical model).

Below a frequency of 350 Hz, the cavity absorption has barely no impact on the measured sound transmission in comparison to the results achieved without absorption layer. From 350 to 450 Hz a broadband improvement in transmission loss of up to 6 dB is realized through the additional energy dissipation on the fluid-foam interface.

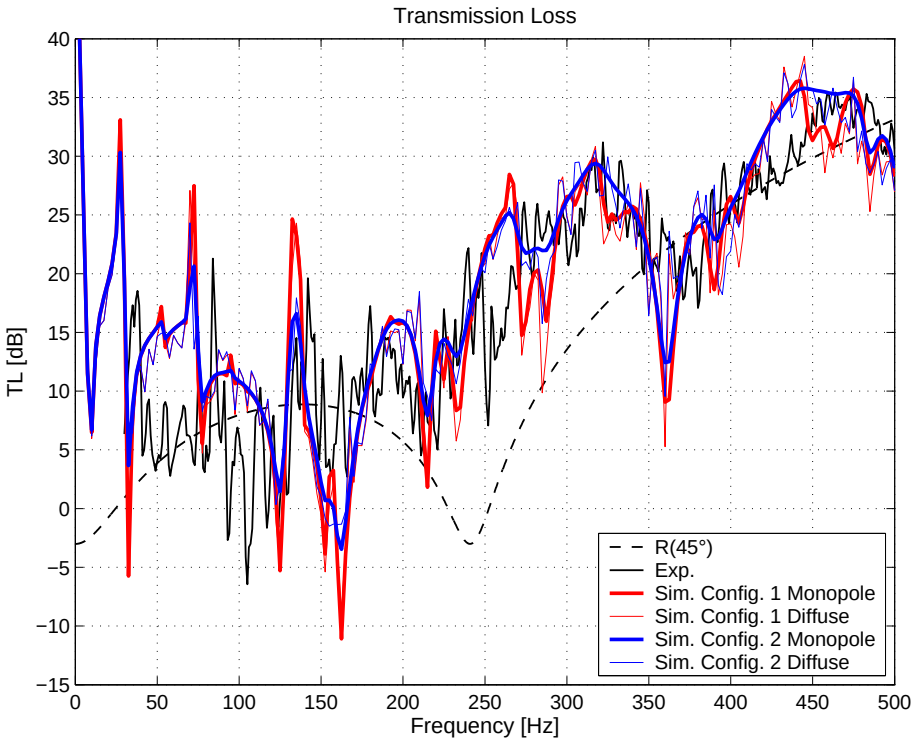

Figure 3.14: Transmission loss with acoustic excitation

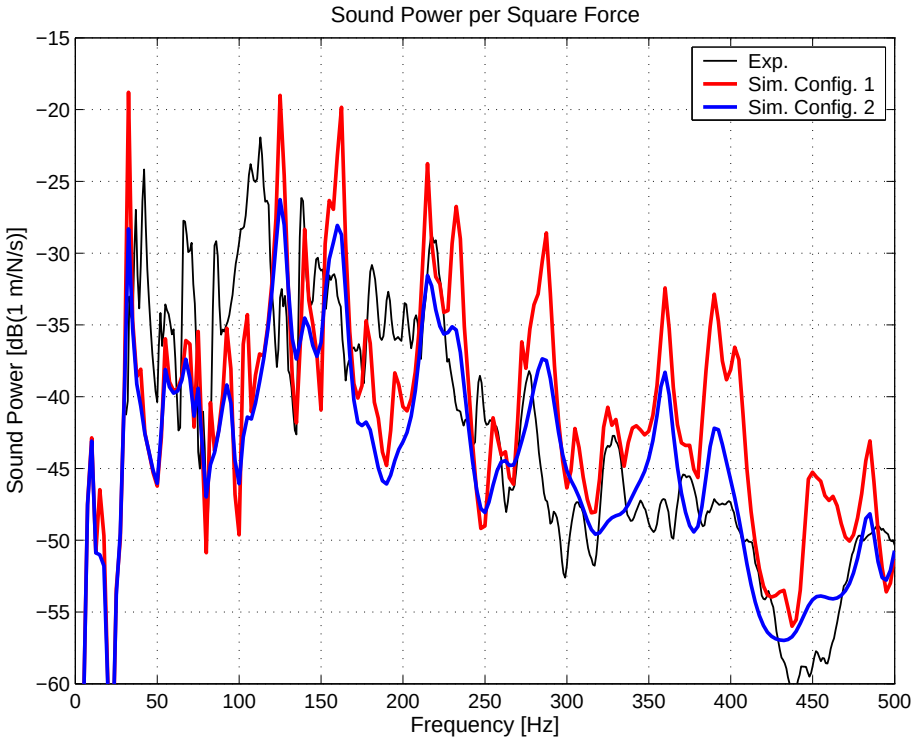

Figure 3.15: Sound power per square excitation force

This behaviour is also reflected in the numerical results. Especially in the frequency range from around 330 to 450 Hz the transmission loss is increased with maximum improvements reaching around 9 dB on the local minima at 380 and 415 Hz. This increase is mainly governed by the resistance, whereas due to the reactance the frequencies of coupled fluid-structure modes are shifted towards lower values.

Comparing the measured and predicted sound transmission trends, an acceptable correspondence is obtained, even if generally on resonance peaks the sound reduction is still overestimated by the simulation model.

3.5 Conclusions

A hybrid FEM/Huygens-Rayleigh methodology was presented to predict the sound transmission of plane single and double wall partitions in the low-frequency range. Compared to commercially available BEM-tools, the method has the advantage of being extremely fast and can also be used for relatively complex structures [Peiffer05]. Furthermore, based on the superposition principle, the influence of a control loop with active elements can be integrated in the simulation model.

The prediction tool was validated against experimental results obtained from measurements with various single and double wall configurations. It emerged from the comparison of numerical and measured results that an accurate, numerical reproduction of the measured sound transmission behaviour would be very difficult to realize. This discrepancy is mainly due to uncertainties inherent to the model, but also to the experimental results:

- A high complexity is involved with the numerical model, as for instance the solution for the double wall is based on a total of 628 eigenmodes.
- Some parameters like the structural damping and boundary conditions as well as the fluid damping and frictional losses on the fluid-structure interface are difficult to model in the considered frequency range, but have a huge impact on the sound transmission behaviour.
- It has been shown in literature that a sound transmission loss determined in experiments depends very much on the actual measurement configuration and can vary within certain limits.

However, it should be emphasized that the general sound transmission behaviour is well predicted with the simulation model and in good agreement with measured trends. In the following chapter the transmission loss prediction tool will be used in the design process of active structural acoustic control systems, intended to increase the transmission loss of aircraft sidewall structures. For this application the simulation procedure can be considered to be sufficiently accurate as the active systems will be only evaluated by their relative performances (sound transmission behaviour achieved with active control versus open-loop behaviour).

Chapter 4

Numerical Study of Active Double Wall Structures

By means of a simplified, generic double wall structure different actuator and sensor concepts are evaluated numerically based on the methodology presented in the previous chapter. The actuation is either done via a number of d_{31}-piezo patches bonded to the fuselage skin or the trim panel, or with a set of active attachment elements replacing the conventional trim panel attachments. Several sensor concepts can be combined with the actuators in the simulation model. With the piezo patches bonded to the fuselage and the trim panel, a local velocity feedback control law with collocated velocity sensors is used. The intention of such a system is to increase the power dissipation in the structure and to obtain simultaneously a reduction in radiated sound power. In combination with the active attachment elements (hereinafter also abbreviated by the term AAE) an LMS control loop with unidirectional acceleration sensors placed on the trim panel and the attachment elements is analysed. Furthermore, it is also possible to use sound pressure sensors, either located in the fluid cavity or on the radiating side of the trim panel, as an error signal in combination with the three actuator concepts.

The control concepts are evaluated by their respective performance to increase the transmission loss of the whole fuselage section, the change of mean acceleration level on the trim panel and the actuation effort measured by the required actuator voltage. Based on the simulation results, the most appropriate concept will be realized in a proof-of-concept study and tested experimentally.

4.1 Structural Model

The FEM-model of the generic, plane fuselage section (the trim panel is shown only to the half) and the enclosed cavity is illustrated in Figure 4.1. The fuselage has in-plane dimensions of 1 by 1 m and consists of a 1,6 mm thick aluminium skin stiffened by six simplified L-shaped stringers and two C-shaped frames. Both stringers and frames are also made of aluminium and 1,6 mm thick. The height of the frames is 115 mm, whereas the stringers are 29 mm high. The spacing between frames and stringers is 500 and 167 mm respectively. On the skin the stiffening effect of stringer and frame feet is taken into account by strengthening the skin thickness up to 3,2 mm as illustrated by the colored elements in Figure 4.1.

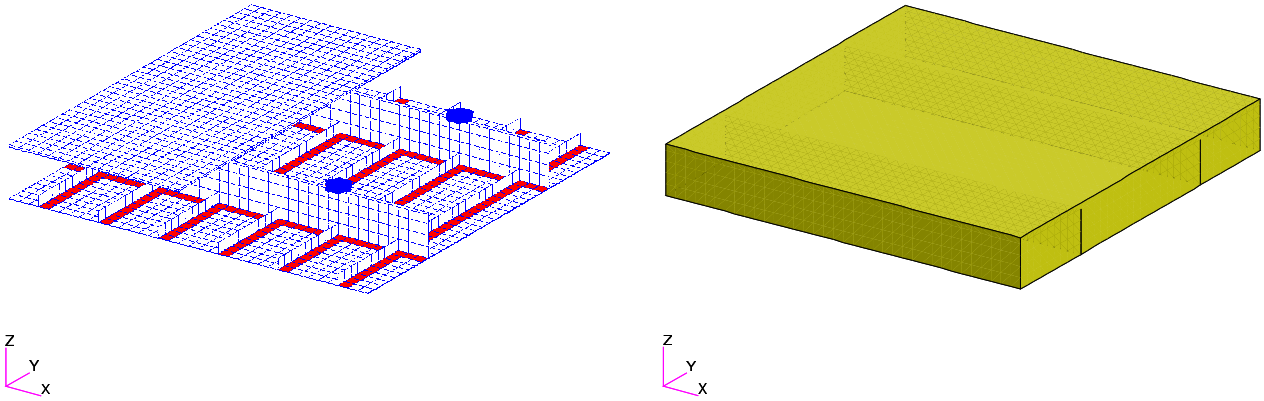

Figure 4.1: Structural and fluid FEM-model

The trim panel has the same in-plane dimensions as the fuselage skin and is located 15 mm above the frames. In the basic configuration it is attached to the fuselage by four rigid bar elements[1]. The structural connections provide a path for structure-borne sound beside the airborne path taken into account by the fluid-structure coupling. The trim panel is modelled as realistic sandwich structure (ECA-honeycomb core reinforced with phenolic fibreglass prepreg skin sheets), representative for typical aircraft interiors.

Both the trim panel and the fuselage skin are clamped on their edges into infinite, rigid baffles. Material and modelling parameters for the fuselage section, the honeycomb core and the skin sheets of the trim panel are specified in Table 4.1.

The fluid between the fuselage and the trim panel is modelled with volume elements matching the mesh size of the fuselage and trim panel. Boundary conditions of $v_n = 0$ are enforced on all surfaces of the fluid not in contact with the structure, with v_n being the normal velocity on the fluid surface. To provide an acoustic absorption in the cavity the remaining fluid surface, coupled to the structure, is covered with absorber elements, which are given the same acoustic properties as already used in the previous chapter (see Table 3.4). The FEM-model also takes into account the fluid interaction with the frames, whereas the interaction with the stringers is neglected. The properties of the fluid model are listed in Table 4.2.

The system response with and without control is simulated in the frequency range from 2,5 to 500 Hz. A step size of 2,5 Hz is selected for the frequency resolution. The whole model has 37100 degrees of freedom and 208 structural and 37 fluid eigenmodes, forming the modal space up to 1 kHz, are considered in the frequency response. As primary excitation a coherent monopole source radiating with an incidence angle of 45° towards the trim panel is used. In free field conditions the monopole source strength would be equal to a mean sound pressure level of 80 dB on the fuselage skin. To analyse the effects of further excitation mechanism a normal unity force acting on the fuselage skin[2] and a diffuse sound field similar to the one used in Chapter 3.4 are considered as well as primary excitation.

[1] Attachment points: ($x = 250$ mm; $y = 250$ mm), ($x = 250$ mm; $y = 750$ mm), ($x = 750$ mm; $y = 250$ mm) and ($x = 750$ mm; $y = 750$ mm), x and y being the in-plane coordinates as shown in Figure 4.1.

[2] Position: $x = 222$ mm and $y = 280$ mm.

Table 4.1: Parameter sidewall structure

Fuselage	
Material	Aluminium
Y.-modulus:	70.000 N/mm^2
Poisson-constant:	0,3
Density:	2,70 g/cm^3
Size:	1,6 mm thickness
	reinforced to 3,2 mm on frames & stringers
	1000 x 1000 x 115 mm
Mesh:	Skin 36 x 36 CQUAD4 elements
	Stringers 6 x 1 x 36 CQUAD4 elements
	Frames 2 x 4 x 36 CQUAD4 elements

Trim Panel, ECA-Honeycomb Core	
Material:	anisotropic
Shear-modulus:	27 N/mm^2 (L-direction)
	16 N/mm^2 (W-direction)
Poisson-constant:	0,3
Density:	29,0 kg/m^3
Size:	5,0 mm thickness
	1000 x 1000 mm
Mesh:	36 x 36 CHEXA elements

Trim Panel, Skin Sheets	
Material	phenolic E-glass prepreg
Y.-modulus:	29.000 N/mm^2 (lower skin)
	22.000 N/mm^2 (upper skin)
Poisson-constant:	0,3
Density:	2,00 g/cm^3 (lower skin)
	1,82 g/cm^3 (upper skin)
Size:	0,20 mm thickness (lower skin)
	0,28 mm thickness (upper skin)
	1000 x 1000 mm
Mesh:	36 x 36 CQUAD4 elements

General Structural Parameter	
Boundary condition:	clamped into infinite, rigid baffle
Damping:	modal damping of 1%

Table 4.2: Parameter cavity fluid

Fluid	
Density:	1,225 kg/m^3
Speed of sound:	340 m/s
Spatial decay rate:	0,0001 m^{-1} (equals a loss factor of $5,5 \cdot 10^{-5}$)
Mesh:	5 x 36 x 36 CHEXA elements
Boundary condition:	$v_n = 0$ on free fluid surfaces
	coupled surfaces covered with absorption foam

4.2 Actuator and Sensor Concepts

The efficiency of an active control system is closely linked to the efficiency of the control law, actuators and sensors. To determine the best solution for a double wall fuselage section, three different actuator and sensor concepts in combination with two control laws are numerically evaluated. From the numerous methods presented in literature (see Chapter 2.4), d_{31}-piezo patches bonded either to the fuselage or the trim panel represent a common, almost classical control strategy and are selected as two possible alternatives. Using collocated actuators and sensors with a local velocity feedback control loop ensures the stability of such a system and an experimental implementation would require relatively low hardware complexity.

A novel actuator concept is the active attachment element, which dynamically isolates the trim panel from the fuselage and is able to introduce secondary control signals into the trim panel. The system requires a different sensor layout and is evaluated with a more complex LMS control loop.

4.2.1 Active Fuselage Skin Damping

The scheme on the left side of Figure 4.2 shows the layout of the d_{31}-piezo patches and sensors on the fuselage structure and their respective denotations. From a practical point of view the actuators can only be placed inside of the fuselage leaving just the bays formed by adjacent stringer and frame pairs as a realistic position. However, a practical implementation of this control strategy may be difficult to realise as the actuators would be bonded directly to the fuselage skin, which is stressed with every flight cycle due to the cabin pressurisation. Also a large operational temperature range, roughly from -50 to 110°C considering all possible flight conditions, must be taken into account.

The main idea behind this layout is that by controlling the structural vibrations on the incident panel the perturbation source strength transmitted across the cavity to the radiating panel is reduced [Carneal93]. In literature this effect is often referred to as active damping because the control reduces the amplitude of the vibrating modes.

In this study each bay of the generic fuselage model is fitted with a 55 by 55 mm d_{31}-piezo patch resulting in a rather complex system with a total of 15 actuators. Therefore, the results achieved with this active system will present an upper bound in terms of performance and complexity. In the FEM-model the actuators are taken into account by the equivalent force

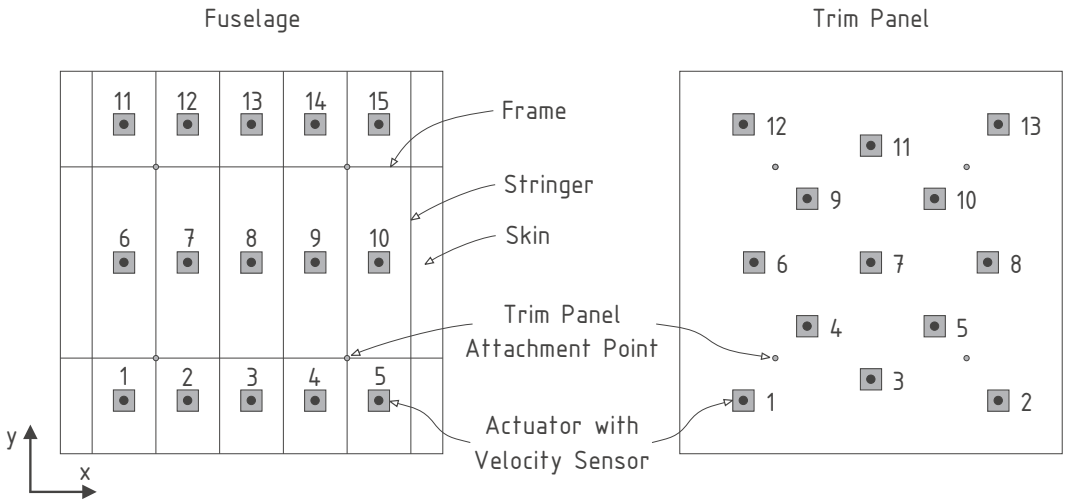

Figure 4.2: Denotation and layout of actuators and sensors used for active fuselage skin damping and active trim panel damping

approach presented in Chapter 3.2. The thickness of the piezoelectric d_{31}-actuators is optimised with respect to the actuation moments using equation 3.43. Based on the material parameters mentioned in Table 4.1 for the fuselage and in Table 4.3 for the piezoceramic patches, the optimisation results in a thickness of 0,86 mm. The corresponding in-plane actuation line forces and bending line moments to be used with the equivalent force model are 5769,3 N/m and 6,3 Nm/m respectively, for a supposed excitation with an electric field of 1000 V/mm.

Table 4.3: Material properties of d_{31}-piezo patches

Piezoceramic Properties	
Y.-modulus:	60.600 N/mm^2
Poisson-constant:	0,3
Size:	55 x 55 mm in plane dimensions
	0,86 mm thickness
d_{31}:	$-340 \cdot 10^{-12}$ m/V
d_{33}:	$585 \cdot 10^{-12}$ m/V

The collocated velocity sensors needed for the local velocity feedback control are supposed to be placed in the middle of each actuator. Based on the control law for local velocity feedback, given in equation 3.56, the system response is computed and analysed at each frequency step with the relation 3.60. Furthermore, it is assumed that a constant feedback gain h_i is used on every local control loop. As the behaviour of the controlled system with respect to the frequency depends mainly on the gain utilised in the feedback loop, the impact of different feedback gains is investigated. The effect of a frequency constant gain is demonstrated with values of 20 and 50 Vs/mm^2.

To optimise the control loop with respect to the sound transmission behaviour a further simulation is carried out, where the gain is used as a parameter and varied between values of 0 and

300 Vs/mm^2. For each frequency step the values yielding the best transmission loss behaviour are selected. If the resulting transmission loss value obtained with active control should drop below the one achieved with open control loop, the control system is consequently turned off for the respective frequency step. These results will thus present an optimum, which can be attained with a relatively simple local velocity feedback control law.

4.2.2 Active Trim Panel Damping

Another possibility to control the structural response and sound radiation of the trim panel is to use d_{31}-piezo patch actuators, which are placed or directly embedded onto the trim panel. In contrast to the first solution, this configuration allows a direct control of the radiating surface. Due to a better coherence between the controlled quantities and the sound radiation, the active trim panel is expected to give better results than the active fuselage skin damping.

The employed actuator layout is shown on the right side of Figure 4.2. Altogether 13 actuators are distributed over the trim panel surface. It is assumed that the actuators are placed on the upper skin sheet and as before each active element is fitted with a collocated velocity sensor, which is used for local velocity feedback control.

The thickness optimisation with the equivalent force model results in an optimal actuator thickness of 0,96 mm and the line force and moments to be used in the FEM-model are 2243,6 N/m and 1,3 Nm/m. Regarding the sensitivity of the results with respect to the feedback gain, a similar variation as for the active fuselage skin damping is performed.

4.2.3 Active Attachment Elements

For the evaluation of the concept with active attachment elements the four rigid trim panel attachments are replaced with a set of particular actuators. The sound radiation of the trim panel is mainly controlled by bending waves [Fahy85, Heckl94] that are excited either by the fluid path through the cavity or by normal translatory and rotational displacement components in the plane of the panel and transmitted from the fuselage frames into the trim panel at each attachment point. Therefore, to control the dynamic behaviour of the trim panel and achieve a substantial reduction in sound transmission, it is essential that with each active attachment element three degrees of freedom can be controlled independently. To assure the best possible integration into the fuselage section, the elements should also have small overall dimensions and a low weight.

The actuator layout and denotation as well as a prototype CAD-model of an attachment element meeting the requirements mentioned above, are illustrated in Figure 4.3. The design is based on Thunder d_{31}-actuators mounted in a clamshell configuration as presented in Chapter 2.3.1. In comparison to the Thunder model TH-10R the size of the metal substrate layer is increased to 32 by 19 mm and the PZT layer to 22 by 19 mm. Otherwise the actuator properties as listed in Table 3.1 and 3.2 are retained. The increase of the actuator dimensions is necessary because a mounting hole with a diameter of about 4 mm would be required on a real Thunder element for the force transmission and the attachment of the clamshell units (see also Figure 2.15). By using an axis-symmetric layout of three independent clamshell elements arranged between two mounting plates around the attachment points to the trim panel or the fuselage frames respectively, it is possible to excite normal displacements in the z-direction as well as

x- and y-rotations between the trim panel and the fuselage. A more detailed illustration of a clamshell actuator unit and an active attachment element is given in Annex B.

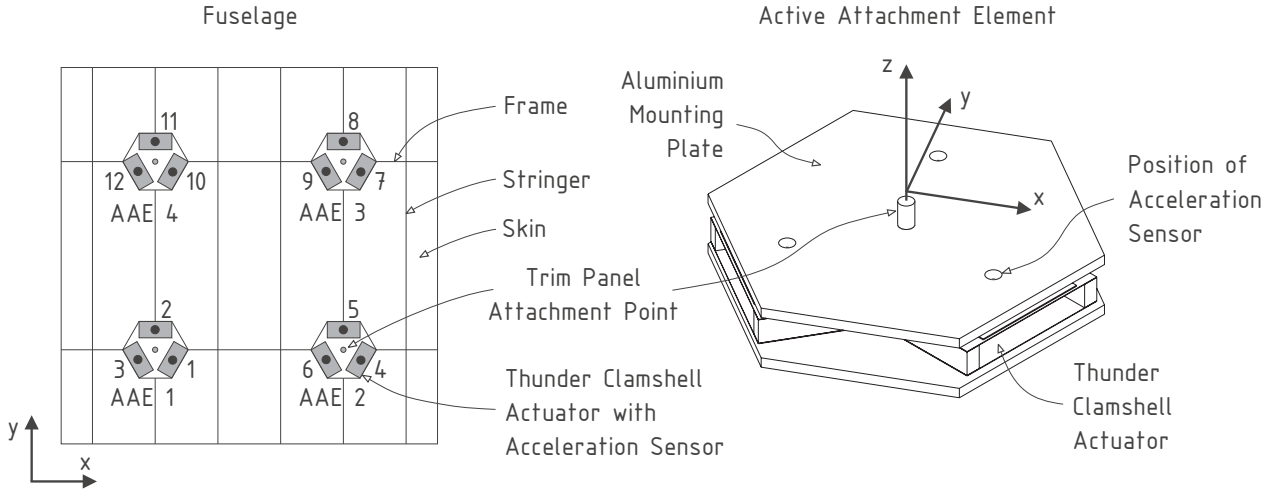

Figure 4.3: Denotation and layout of active attachment elements and sensors, CAD-model of an active attachment element

The hexagonal mounting plates should have a high stiffness to assure the best possible transmission of control forces. In the FEM-model they are supposed to be made from aluminium (thickness 3 mm) and their width across the flat side is around 60 mm, whereas the spacing between the plates is 10 mm. The radius from the trim panel and fuselage attachment points to the attachment of a clamshell unit is 20 mm.

The piezoelectric behaviour of the Thunder elements is modelled by the thermal elastic analogy and a similar structural FEM-model as the one presented in Chapter 2.3.1 is used. The other structural parts of the attachment elements are conventionally modelled with shell (mounting plates), solid (clamshell clamping for the Thunder elements) and bar elements (structural connections to the mounting plates). By incorporating the active trim panel attachments in the FEM-model the total number of degrees of freedom is increased to around 130000. The modal structural base contains a total of 236 modes up to 1 kHz. Fluid interaction with the attachment elements is neglected because for the considered frequency range up to 500 Hz the maximum dimension of the element is much smaller than the minimum fluid wave length. Otherwise the same simulation parameters as with the other control concepts are used.

Control is performed by the LMS-algorithm with a sensor array of up to 19 unidirectional accelerometers. Preliminary investigations with various sensor layouts indicated that for an efficient control of sound radiation different sensor layouts may be required. This is mainly due to the frequency-dependant dynamic trim panel behaviour and the fact that a single sensor layout does not give optimal results in terms of sound reduction for the whole frequency range. For this reason the simulation procedure is done for six different sets of sensors containing the information of up to 19 unidirectional acceleration sensors placed on the actuators and the trim panel. By comparing the resulting transmission loss values for every single frequency step the best suited sensor concept out of the six is identified.

The six sensor concepts are summarized in Table 4.4. For the first three setups each active attachment element is fitted with three acceleration sensors placed on the respective upper

mounting plate at the connection points to the clamshell actuators (see Figure 4.3). Taking into consideration the trim panel response shape at frequencies having a high sound transmission, additional sensors are positioned on the trim panel at points where a local acceleration maximum occurs. At higher frequencies the trim panel response is usually dominated by higher modes and results in a more complex deformation shape, thus requiring an increased number of sensors. Sensor concepts 3 to 6 require only information available directly from the trim panel. Four sensors are placed on the trim panel attachment points, whereas the remaining sensors are distributed over the whole trim panel surface.

Table 4.4: Sensor positions for concepts 1 to 6, x- and y-position [mm]

Sensor	**Concept 1**	**Concept 2**	**Concept 3**	**Concept 4**	**Concept 5**	**Concept 6**
1:	AAE 1	AAE 1	250, 250*	250, 250*	250, 250*	250, 250*
2:	AAE 1	AAE 1	750, 250*	750, 250*	750, 250*	750, 250*
3:	AAE 1	AAE 1	250, 750*	250, 750*	250, 750*	250, 750*
4:	AAE 2	AAE 2	750, 750*	750, 750*	750, 750*	750, 750*
5:	AAE 2	AAE 2	500, 500	750, 639	889, 333	694, 861
6:	AAE 2	AAE 2	833, 833	750, 333	500, 361	306, 861
7:	AAE 3	AAE 3	833, 194	611, 500	500, 639	194, 500
8:	AAE 3	AAE 3	167, 194	472, 500	861, 639	833, 528
9:	AAE 3	AAE 3	167, 805	833, 861	361, 250	861, 806
10:	AAE 4	AAE 4	500, 861	306, 861	111, 500	667, 444
11:	AAE 4	AAE 4	500, 167	250, 472	111, 222	333, 417
12:	AAE 4	AAE 4	361, 694	806, 167	639, 278	694, 139
13:	500, 500	500, 500	667, 667	278, 694	278, 111	139, 250
14:	778, 500	806, 833	694, 333	111, 639	278, 889	861, 250
15:	222, 500	806, 167	333, 333	306, 139	389, 500	306, 139
16:	500, 778	194, 167	167, 527	111, 361	639, 889	917, 417
17:	500, 222	194, 833	-	500, 833	250, 389	111, 389
18:	-	750, 500	-	472, 250	-	694, 639
19:	-	250, 500	-	-	-	306, 639

* trim panel attachment point

The motive behind this layout is that sensors placed directly on the actuator elements or at the trim panel attachment points will reduce the structure-borne perturbation components introduced from the fuselage structure into the trim panel. Furthermore, they will also have a limiting effect on the magnitude of the control input and minimize causality problems for broadband control. The remaining sensors on the trim panel are used to reduce the amplitudes of the vibrating modes and damp the radiation behaviour of the trim panel.

In addition to the LMS control law with the sensors mentioned above, the system response is also determined for a hypothetical control system, where the entire trim panel feedback (information of 1225 nodal points) is used as system transfer matrix G_1 in the LMS control loop. This type of control leads to an optimal trim panel response in terms of kinetic energy and is used to analyse the efficiency of the active trim panel attachments.

4.3 Simulation Results

The simulation results are presented by means of general sound transmission loss behaviour, mean trim panel acceleration and actuator voltage for the frequency range up to 500 Hz. Only the results that are achieved with the acoustical monopole primary excitation are retained in this chapter as, in principle, similar results are obtained for the point force as well as diffuse field primary excitation. The same excitation source strength is used for all three actuator configurations, thus allowing a direct comparison of absolute results. The mean trim panel acceleration is defined as the sum of the squared trim panel accelerations, computed on each discrete node of the trim panel FEM-mesh.

4.3.1 Preliminary Investigation

The fundamental sound transmission behaviour of the passive fuselage section is shown in Figure 4.4 for various configurations with and without taking into consideration the fluid-structure coupling between the trim panel and the fuselage as well as rigid, active and no trim panel attachment elements.

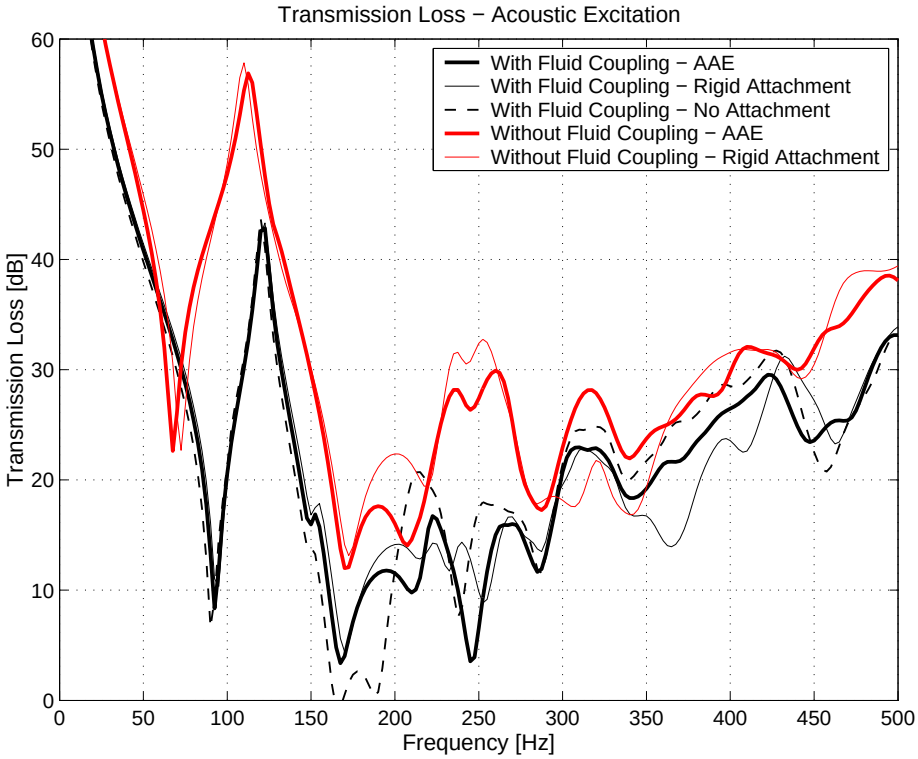

Figure 4.4: Fundamental transmission loss behaviour for various sidewall configurations

By comparing the results, it is obvious that for most of the considered frequency range the overall sound transmission is dominated by the fluid path. Only from about 300 to 430 Hz the difference in transmission loss is about 3 dB, indicating that roughly the same amount of energy is transmitted by the airborne and structure-borne sound path. Due to the additional

stiffness of the fluid, natural eigenfrequencies of coupled models are shifted towards higher values.

With fluid-structure coupling, the sound transmission behaviour in the low-frequency range up to 150 Hz is characterized by a global 1,1-eigenmode of the fuselage. Local skin modes in the bays formed by adjacent stringer and frame pairs are only excited to a small extent. Due to the boundary conditions applied to the model, an effective excitation of the fuselage skin at frequencies considerably lower than the first resonance is not possible, thus resulting in high transmission loss values. At around 92 Hz a first strong coupling between the structure and the enclosed fluid occurs. In this frequency range the trim panel radiates in a very efficient 1,1-mode resulting in a local TL minima at 92,5 Hz. Above 100 Hz the dynamic behaviour of the fuselage and the trim panel is virtually completely decoupled by the fluid behaviour. The trim panel radiates in a 3,1-mode having a low radiation efficiency and a local TL maxima is reached at 122,5 Hz.

With increasing frequencies the transmission loss decreases again and sound transmission through the airborne sound path augments. Above 165 Hz the fuselage response is mainly dominated by local skin modes and adjoining bays on the fuselage skin start to vibrate in counter phase. The modal density is also increasing on the trim panel, resulting in a more smooth transmission loss behaviour, where obvious resonant effects, as observed for the low-frequency range, are less distinct.

In contrast to the simulation without trim panel attachments, the rigid and active attachment elements slightly increase the transmission loss on the first and second minima, because the trim panel displacement is partly retained in its free movement by the attachment elements. At higher frequencies the different mechanical attachment properties cause two distinct sound transmission behaviours.

The requirement to control both translatory and rotational vibrations with the active attachment elements is explained by means of the following example. Considering as example the simulation model of the fuselage section without taking into account the airborne sound transmission through the fluid cavity, control is performed with the active attachment elements, which are either driven in their normal mode so that both translatory and rotational displacements are excited at the trim panel attachment points, or in a mode where each element is restrained to produce a pure translatory displacement. This is achieved by an in-phase excitation of each active attachment element. As the fluid-structure coupling is neglected, only the acceleration error sensors placed directly on the attachment elements are required in the control loop. The resulting transmission loss behaviour is given in Figure 4.5.

The results, obtained from this rather simple case of pure structure-borne sound transmission, reveal the potential of the active attachment elements. By controlling twelve degrees of freedom, a transmission loss, which is around 20 dB higher for the whole frequency range than the one achieved with control of only four degrees of freedom, is achieved. The sound radiation, being proportional to the squared normal velocity of the trim panel, is governed by both rotational displacements in the plane of the panel and its normal translatory component. Controlling only the normal translation at the attachment points generates a translatory node on each attachment point. But residual moments are still introduced from the frames into the panel, causing an out-of-plane movement and sound radiation from the panel.

With the active attachment element driven independently for rotational and translatory perturbations, these residual moments are also controlled and a far better mechanical isolation and

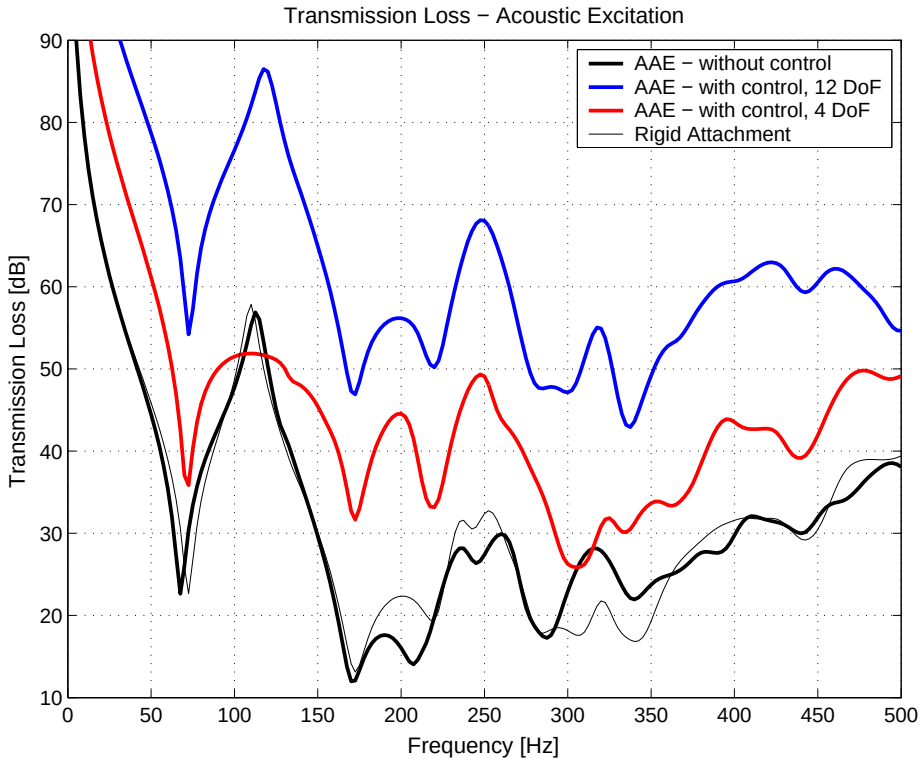

Figure 4.5: Active attachment elements: control with 12 DoF versus 4 DoF, no fluid-structure coupling, error sensors on attachment elements only

reduction in sound radiation is obtained. Theoretically, with adequate sensors for the three perturbation components placed directly in the loading path at the trim panel attachment points, the sound radiation could be even completely suppressed with such a control concept. However, as moments or rotational displacements are difficult to measure in reality, such a configuration is not used in the simulation model. Instead, the more realistic sensor setup described in Chapter 4.2.3 is chosen. Unidirectional acceleration error sensors are located on the mounting plate and connected to the attachment points via a certain mechanical stiffness, which is determined by the plate properties and the attachment element to the panel. A high stiffness is therefore required for these structural elements to guarantee the best possible correlation of error signals to the actual perturbations and allow for the best possible control.

4.3.2 Active Fuselage Skin Damping

Figure 4.6 and 4.7 show the transmission loss and mean trim panel acceleration for active damping of the fuselage skin. Two configurations are calculated with a constant feedback gain of 20 and 50 Vs/mm^2, whereas in a third configuration the gain is optimised with regard to the transmission loss results.

The velocity error signal is reduced on each sensor for the whole frequency range. As expected from the velocity feedback control law, the local power dissipation on the sensors increases with higher gains but also requires a higher actuation voltage. However, this trend is not reproduced by the transmission loss results. To some extent this is an expected result, mainly

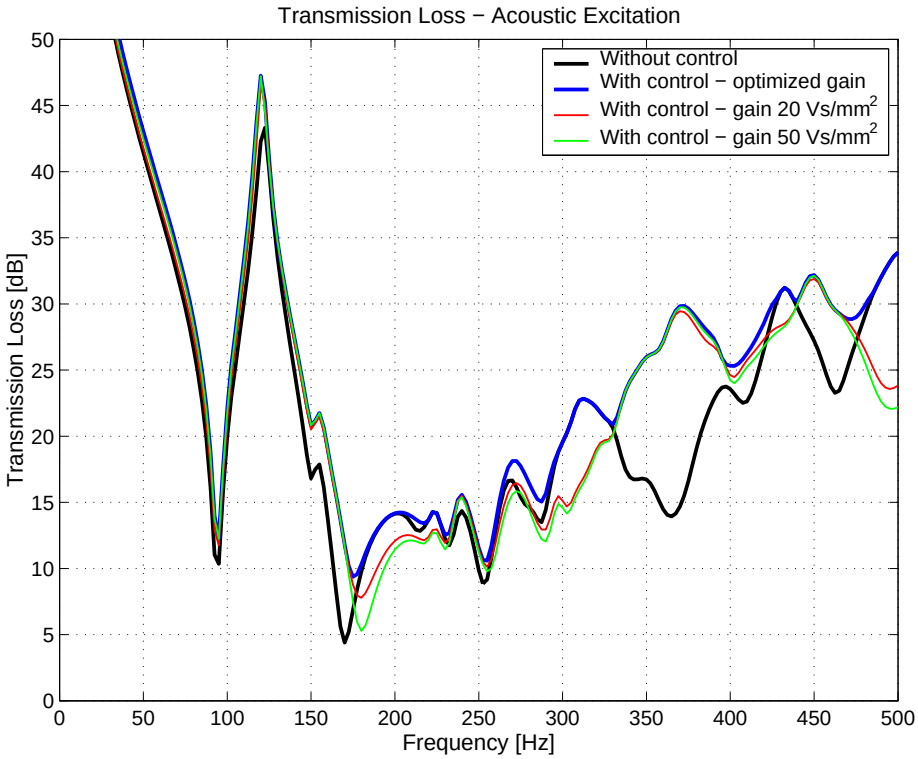

Figure 4.6: Active fuselage skin damping: transmission loss, with and without control

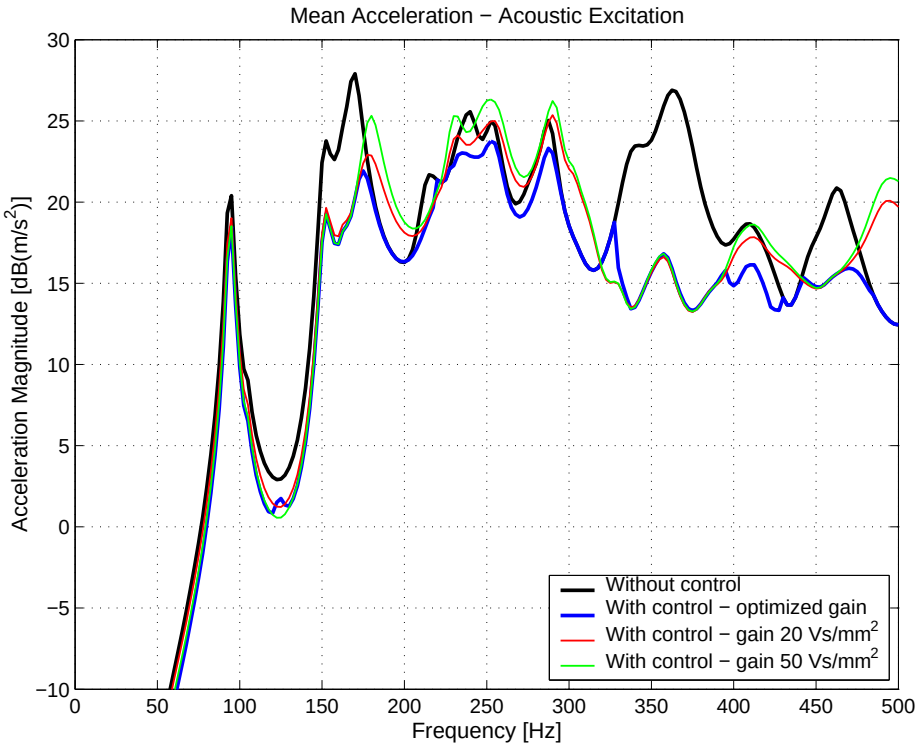

Figure 4.7: Active fuselage skin damping: mean trim panel acceleration, with and without control

because the velocity on the main structure and not the radiated sound field is controlled. On the first and second TL minima at 95 and 170 Hz a maximal increase of only 2 and 5 dB respectively, is realized with the closed control loop. The acceleration levels on the trim panel are reduced as well.

In the frequency range from 180 to 320 Hz nearly no amelioration in the transmission loss behaviour can be noted. At some frequencies the sound transmission with active control is even increased for the two configurations with constant feedback gain. This spill-over effect results from the control forces inadvertently exciting higher structural modes and leads to a better sound transmission and an increase of the mean trim panel acceleration level, while at the sensor position on the main structure a nodal point is enforced. In the optimised gain configuration spill-over is avoided by a gain reduction or even turning the control off. Spill-over effects are also observed at higher frequencies, mainly where the passive TL is already relatively high.

Only starting with around 330 Hz a broadband increase in terms of transmission loss performance is achieved by the additional damping forces applied to the fuselage skin. A maximum improvement in TL of around 15 dB is obtained at 365 Hz. The kinetic trim panel power is also reduced substantially in this frequency range.

To explain this sound transmission behaviour with active control one has to consider the fuselage response to both the primary and secondary excitations. In the low-frequency range the fuselage is excited by the primary perturbation in a global 1,1-mode including frames and stringers. Only at higher frequencies is this global behaviour changed into a more local one with the skin patches in each bay vibrating in situ between the nodal lines formed by the stiffening effect of frames and stringers. However, in the low-frequency range a piezoceramic patch can only excite a local skin mode in the bay where it is located. The adjacent stringer and frames act as nodal lines. With increasing frequencies higher local skin modes are still excited and the fuselage response is also expanded to surrounding bays, whereas stringers and frames still behave as nodal lines due to their stiffening effect. As a result of this different dynamic behaviour the sound radiation cannot be controlled efficiently in the low-frequency range because small piezo patches located on the fuselage skin do not have enough control authority over the global modes such as the 1,1-mode. Only at higher frequencies, where the fuselage response is dominated by local skin modes similar to the modes excited by the actuators, the additional damping results in an efficient reduction of sound transmission. Another explanation is the fact that at some frequency ranges, for instance at around 200 Hz, a strong local vibration of the frames is also excited. This disturbance introduces bending moments into the trim panel and cannot be effectively controlled with relatively small piezo patches bonded to the fuselage skin.

The magnitude values of the required, complex actuator excitation signals are illustrated in Figure 4.8 for the configuration with optimised feedback gain. The absolute values are to be seen in context with an excitation level corresponding to an average SPL of about 80 dB on the fuselage skin.

Below 250 Hz the largest structural deflections are measured by the sensors 6 to 10, hence the respective collocated actuators also require the highest actuation voltages. The highest voltage input, around 10 V/mm, is generated for the centre actuator patch 8 at 170 Hz, which also corresponds to the frequency with the maximum trim panel acceleration level. Due to the symmetrical fuselage design and rather homogenous primary excitation of a single monopole

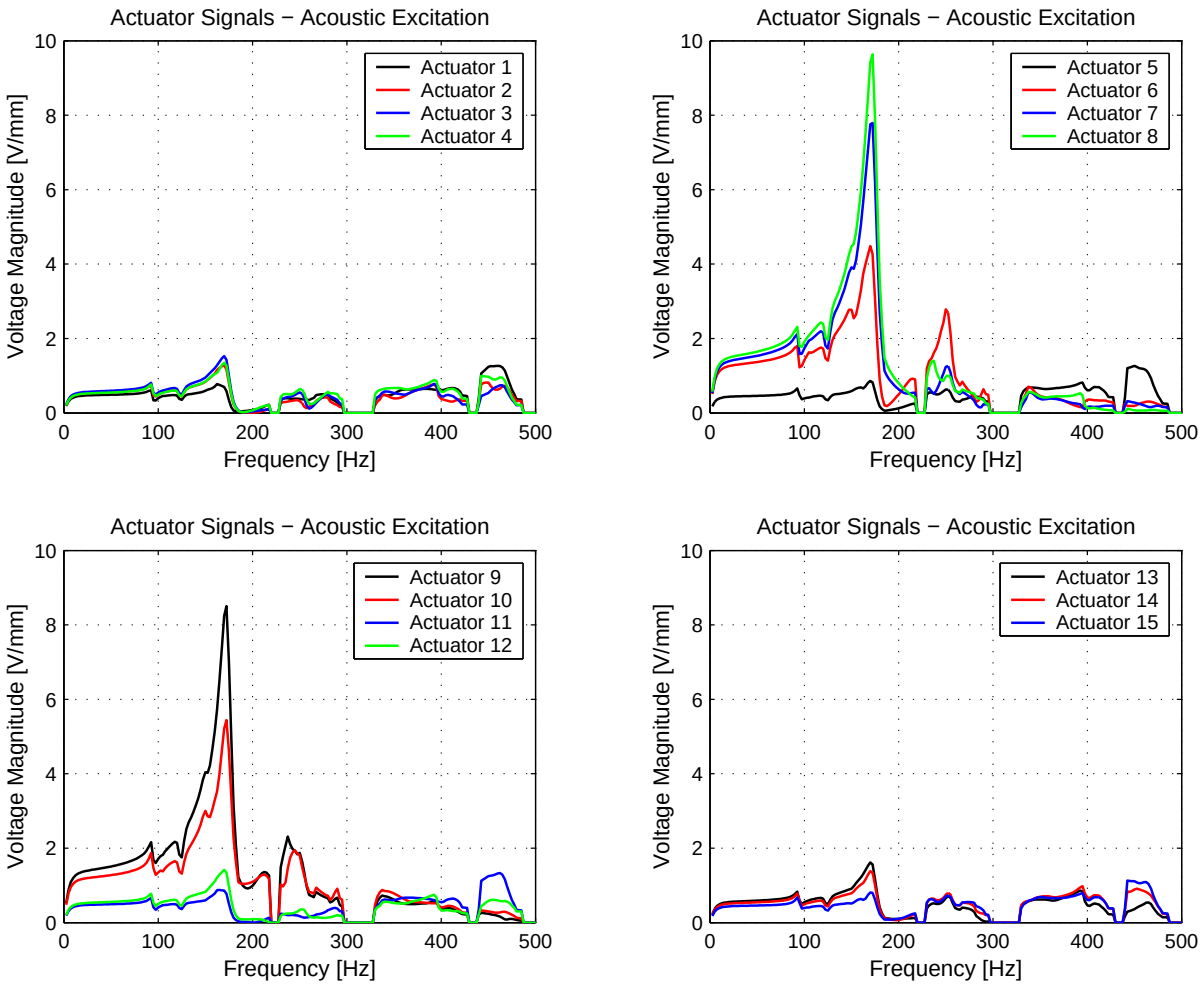

Figure 4.8: Active fuselage skin damping: actuator voltage, optimised gain setting

source, actuators 1 to 5 and 11 to 15 behave in a similar manner and are less excited at lower frequencies. At higher frequencies, the structural response is more evenly distributed over the fuselage skin and all actuators are excited to a similar amount.

4.3.3 Active Trim Panel Damping

By controlling directly the trim panel response better results in terms of sound transmission behaviour are expected. The resulting transmission loss and mean trim panel acceleration levels without and with control (gain h_i is set to 20, 50 Vs/mm^2 and optimised with respect to the TL) are presented in Figure 4.9 and 4.10. Absolute values refer to an excitation SPL of 80 dB on the fuselage skin.

As before, the velocity feedback control law is very efficient in reducing the vibration level on the collocated error sensor. A reduction, proportional to the gain in the feedback loop, is obtained on each sensor for the whole frequency range up to 500 Hz. However, the effect of active control on the sound radiation and mean acceleration level of the trim panel is variable and depending on the excitation frequencies.

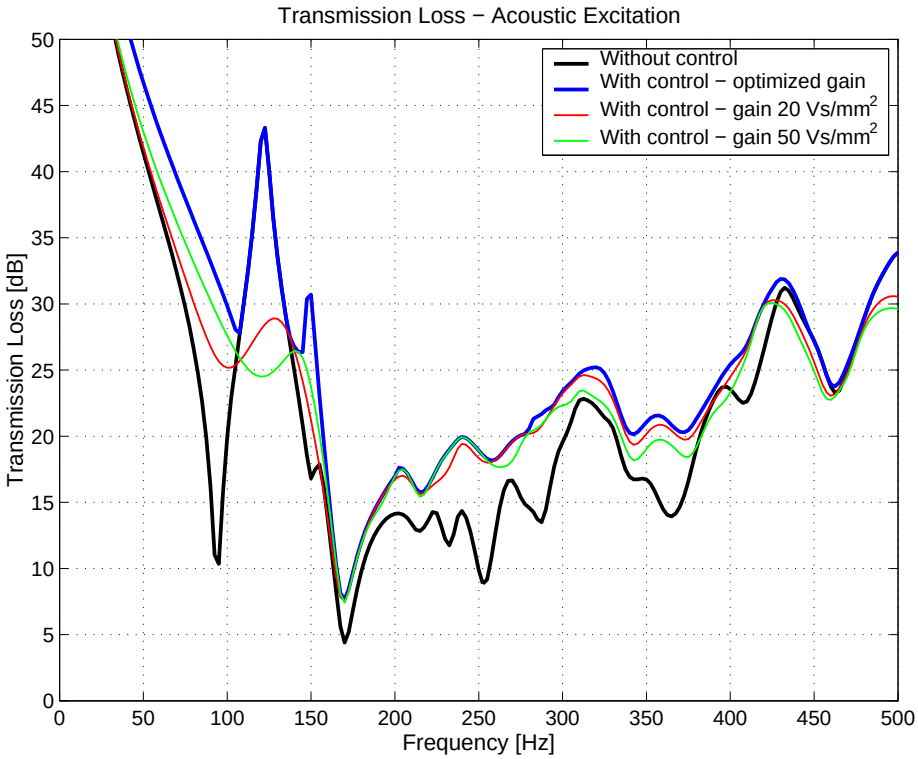

Figure 4.9: Active trim panel damping: transmission loss, with and without control

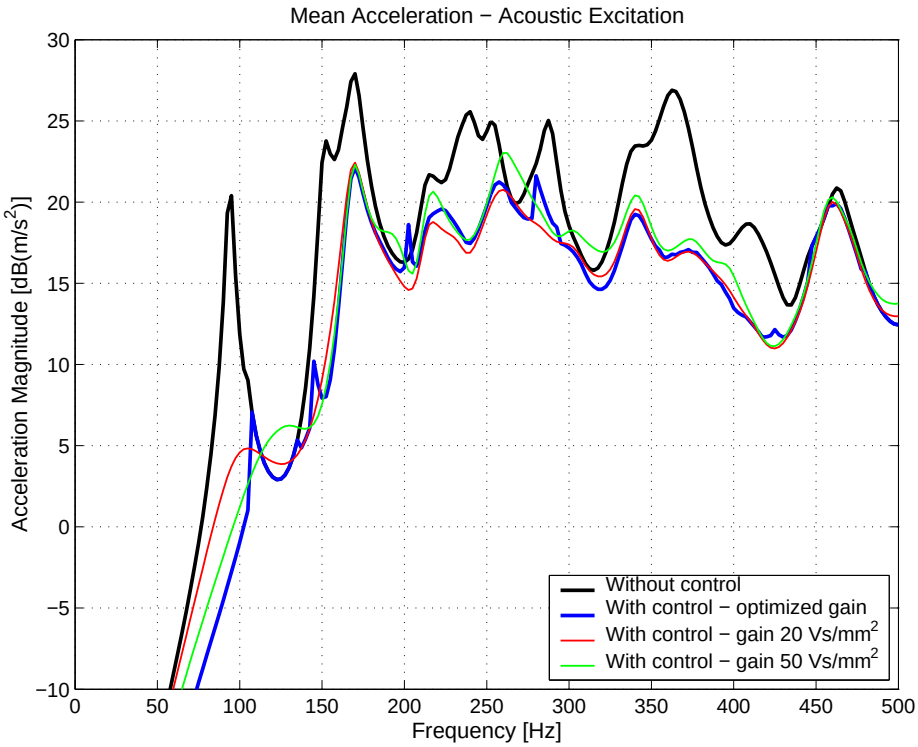

Figure 4.10: Active trim panel damping: mean trim panel acceleration, with and without control

Up to 430 Hz a broadband increase in transmission loss is achieved in the model by controlling the trim panel response. The first TL minimum at 95 Hz is increased by around 20 dB, however on the second peak only a reduction of about 3 dB is obtained. At higher frequencies gains in TL of up to 9 or 7 dB are obtained on frequencies that exhibit a relatively low transmission loss, as for instance at 250 or respectively 365 Hz. This reduction in sound radiation is mainly due to the increased damping on the trim panel and the resulting decrease in vibration energy, as shown by the overall acceleration level in Figure 4.10. Comparing the results with those obtained with the active skin damping concept, a significant better increase in TL is achieved for the frequency range below 330 Hz (except for 170 Hz).

The acoustic and structural results indicate that spill-over problems also occur with the active trim panel damping concept, mainly on frequencies having already a low radiation efficiency and high transmission loss. To avoid diminutions in transmission loss, control is therefore turned off in the frequency ranges of 120, 450 and 500 Hz.

With increasing frequencies the acoustic benefit from the active trim panel control is reduced and vanishes completely for frequencies above 450 Hz. Although a substantial control reduction is still obtained locally on the error sensors, the overall structural trim panel and sound radiation behaviour depends on too many degrees of freedom and thus becomes too complex to be controlled with the present actuator concept. The control enforces a nodal point at each sensor, but the remaining, uncontrolled areas of the panel are no longer affected by the control or even excited to a greater extent than without control. To increase the efficiency at higher frequencies a different actuator setup, compromising more and smaller piezo patches, would be required.

The magnitude of the actuator voltage, resulting from the optimised feedback gain setting, is shown in Figure 4.11. In comparison to the active skin damping concept, higher actuation voltages are required with active trim panel damping. The largest signals are generated for actuators 3 and 11 with around 16 V/mm at 170 Hz. Above 300 Hz the voltage is reduced to levels well below 2 V/mm on all actuators.

4.3.4 Active Trim Panel Attachments

The main simulation results for the active attachment elements are shown in Figure 4.12 and 4.13 in terms of sound transmission loss and mean trim panel acceleration using the acoustic monopole source as the primary perturbation source.

Each of the figures contains the resulting information from two different configurations without control (structure fitted with active and rigid attachment elements). Two different configurations are also available for the analysis of the closed-loop behaviour with LMS control. One variant represents the results from the transmission loss optimisation process (denoted with *AAE - with control*) that is obtained from the six sensor setup listed in Table 4.4. For the second controlled configuration, abbreviated with *AAE - optimal control*, the hypothetical LMS control loop containing the entire trim panel response as error signal is used.

The simulation results indicate that by controlling the trim panel response with the active attachment elements, sound transmission through the aircraft sidewall section is considerably reduced over nearly the whole frequency range (except for 120 and 460 Hz where no amelioration is obtained with the examined sensor configurations). The first minimum in transmission

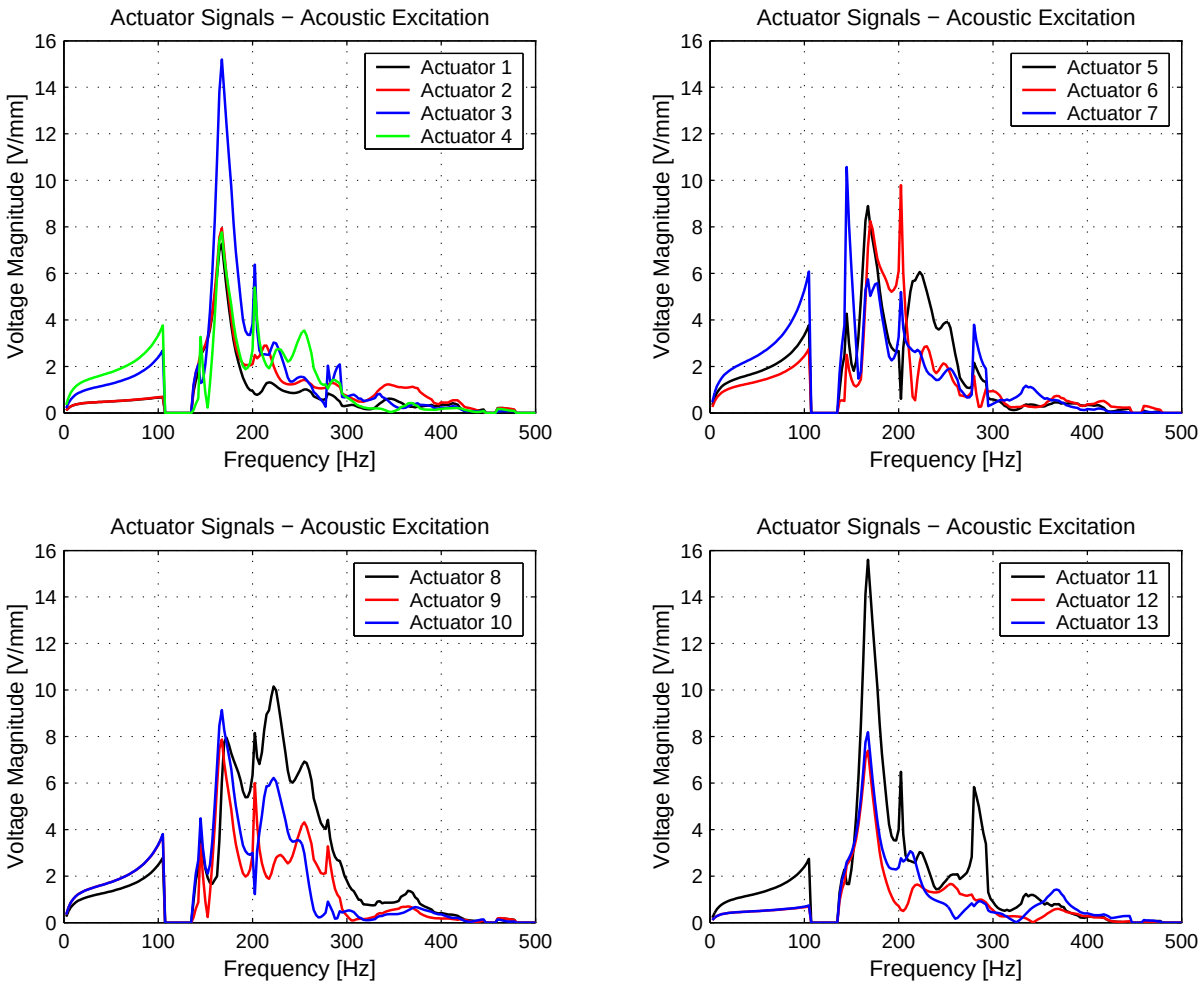

Figure 4.11: Active trim panel damping: actuator voltage, optimised gain setting

loss occurring at 92 Hz disappears totally with control. With the secondary forces and moments introduced by the actuators on each attachment point, the 1,1-mode on the trim panel can be largely suppressed and the mean trim panel acceleration and sound radiation are reduced by 30 and more than 35 dB respectively. On the second peak at 167 Hz an amelioration of 10 dB is obtained in TL, whereas at 245 Hz the transmission loss is increased from 3,5 dB up to 22 dB with control. With further increasing frequency up to 450 Hz a broadband attenuation of about 5 to 10 dB in sound transmission is achieved with the active attachment actuators.

At higher frequencies the general tendency is that the benefit from control decreases and the efficiency limit of the selected actuator concept is apparently reached. The modal density on the trim panel increases and the dynamic response becomes too complex and an efficient control with only twelve degrees of freedom for the secondary signals is not possible anymore. This can be seen by the fact that with the optimal trim panel control, having around 100 times more error information from the trim panel at its disposal than the normal LMS algorithm (and thus representing an optimal solution in terms of trim panel acceleration with the available twelve actuation degrees of freedom), no significant better results are achieved above 350 Hz. Nevertheless, the transmission loss behaviour is still improved at frequencies above 450 Hz.

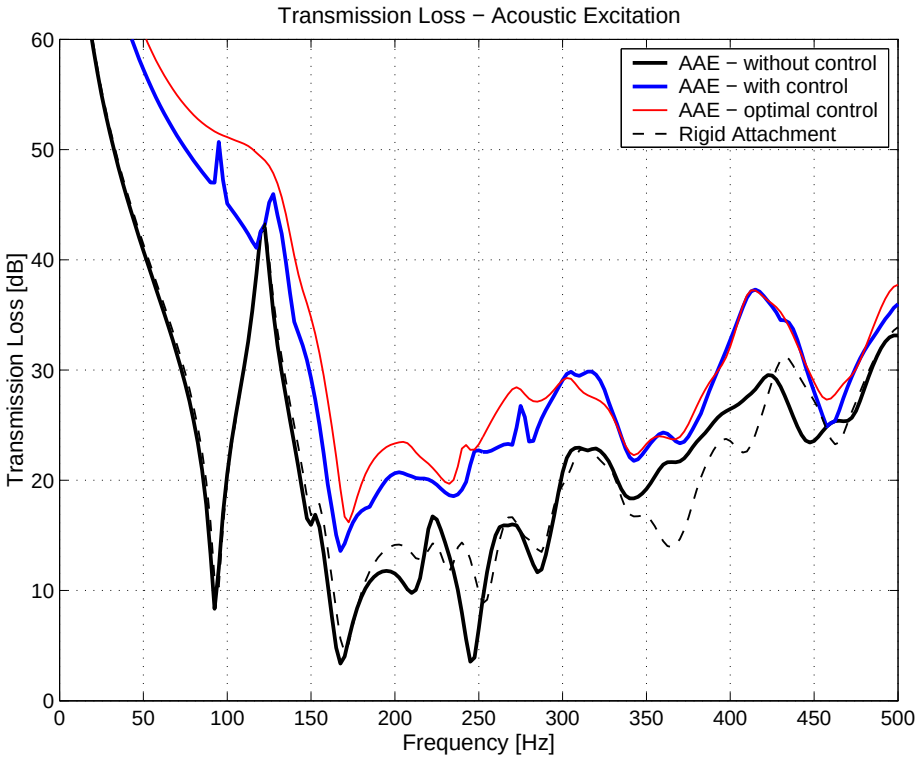

Figure 4.12: Active attachment elements: transmission loss, with and without control

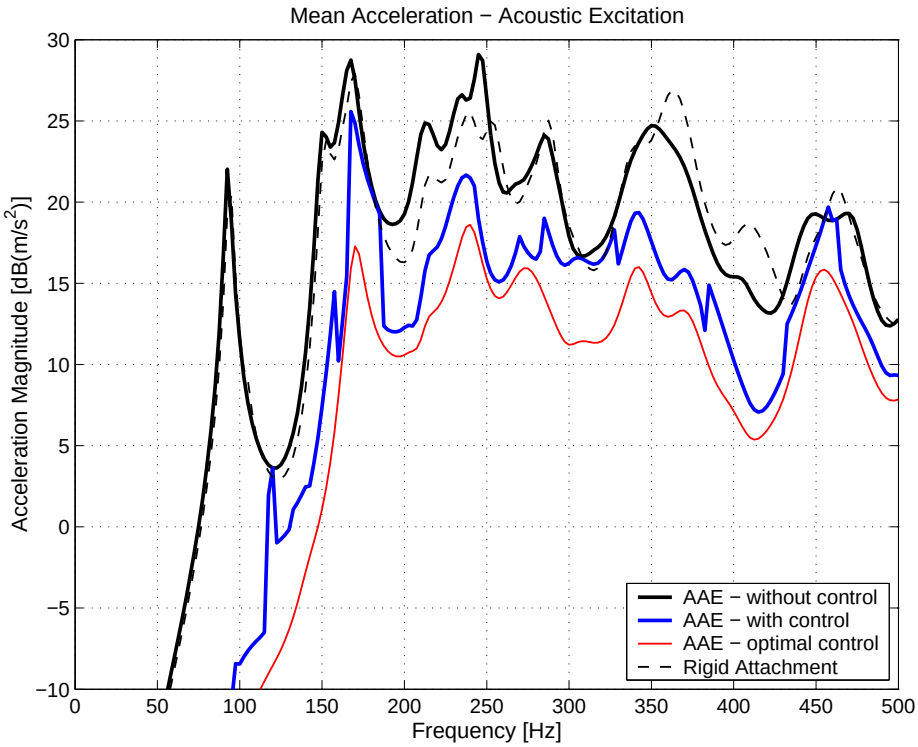

Figure 4.13: Active attachment elements: mean trim panel acceleration, with and without control

The reduction in sound radiation is mainly obtained by a large decrease of the mean trim panel acceleration as illustrated in Figure 4.13. This signifies that the active structural control works mainly in an active damping mode, reducing the overall kinetic power of the trim panel. Modal restructuring, characterised by an increase in vibration power, does not occur with the LMS control in the considered frequency range. In terms of acceleration reduction the configuration with the hypothetical, optimal trim panel control represents the best possible global solution and hence a lower bound that cannot be further decreased with the active attachment elements and available twelve degrees of freedom.

Figure 4.14 shows which out of the six sensor concepts listed in Table 4.4 is chosen in respect to the optimum sound transmission behaviour. The results depend on the excitation frequency and it can be seen that no single layout is preferred over the others. On two frequencies (120 and 460 Hz) the control is switched off to avoid spill-over. Furthermore, it should be mentioned that the sensor selection is also dependent on the structural properties and the type of primary excitation and that the presented results do not represent the absolute optimal solution that can be achieved with such a type of control.

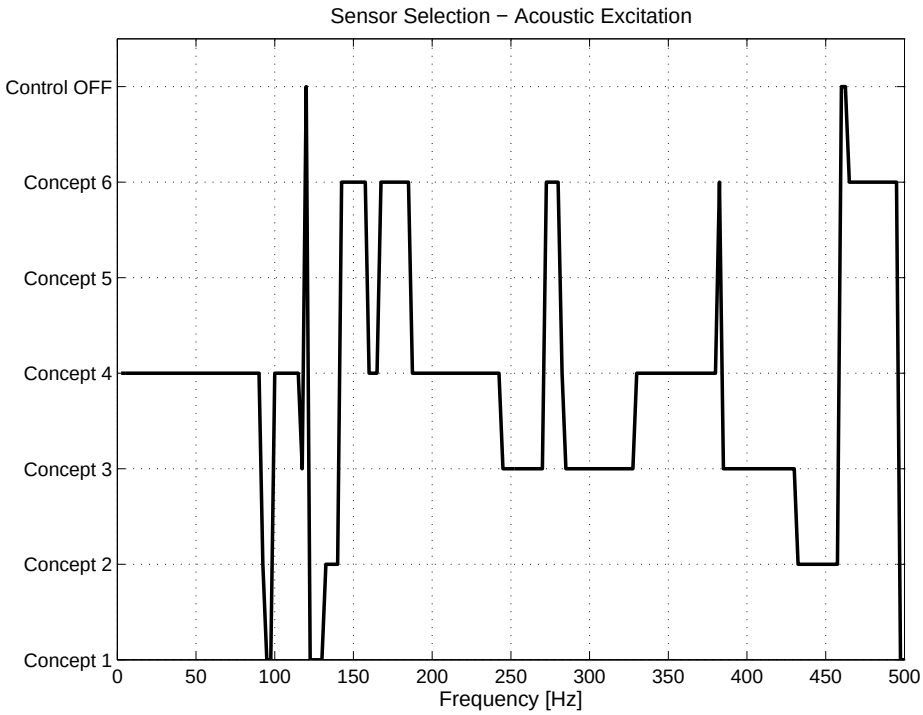

Figure 4.14: Active attachment elements: selected sensor concepts

The magnitude of the complex actuation signals derived with the LMS algorithm is shown in Figure 4.15 (configuration: *AAE - with control*). The maximum values are reached on actuators 1, 4 and 10 with around 80 V at 170 Hz. In this frequency range both the overall acceleration level on the panel and the sound transmission exhibit a global maximum. As in the previous example, the absolute values are calculated for a perturbation source strength giving a mean sound pressure level of 80 dB on the incident panel. By assuming a more realistic excitation level of 100 dB, all absolute quantities must be multiplied by a factor of ten. Thus, a maximum voltage of around 800 V would be required to control the structural system. As

the maximum voltage that can be applied to the Thunder elements is limited to 240 V, such an excitation is not possible without accepting a destruction of the actuators.

Figure 4.14 indicates that in the frequency range, where the actuator voltage limit would be exceeded, sensor concepts three to six are selected by the TL optimisation process. They have in common that only sensors placed directly on the trim panel are used in the control loop as error signal. If, instead, one of the concepts with error sensors integrated on the attachment elements would be used, a considerable reduction in the actuator voltage could be obtained and even for an excitation strength of 100 dB the voltage limit of 240 V would not be exceeded as the error signal used on the attachment elements have the effect of providing an additional control effort reduction. On the other hand, this would also reduce the control perfomance, but for instance on the three global minimum TL values at 92, 167 and 245 Hz gains of about 30, 5 and 9 dB respectively in TL could still be realized with such a type of control. In this case the actuators would be excited up to a level of about 80% of their maximum voltage.

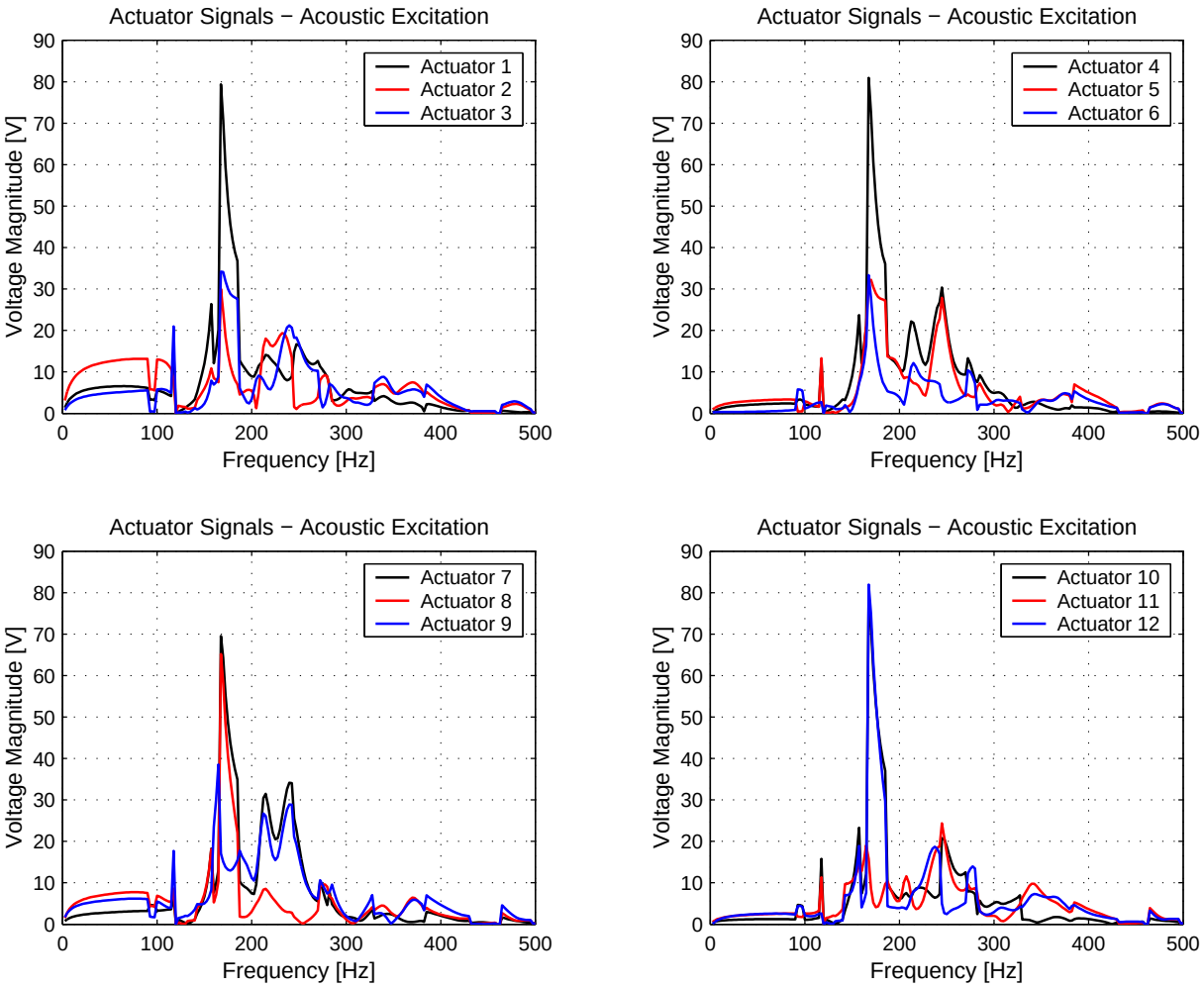

Figure 4.15: Active attachment elements: actuator voltage

In order to evaluate how the electrical actuation power is transformed into normal z-translations and x,y-rotations, the actuator command signal is transformed into an appropriate coordinate

system for each attachment element. The electrical power P is defined by the product of actuator voltage U and current I. The power magnitude is proportional to the square of the actuator voltage, because the piezoceramic behaves electrically as capacity with the actuator current being proportional to the applied voltage:

$$P_{Actuator}(s) = U(s) \cdot I(s) \sim U^2(s) \ . \tag{4.1}$$

The normal translation part of the actuator excitation can be calculated from the complex command signal parts, which are in phase:

$$U_{translation}(s) = a \cdot (U_1 + U_2 + U_3) \ . \tag{4.2}$$

The rotational parts around the orthogonal axes x and y are derived by using the geometrical setup illustrated in Figure 4.3:

$$\begin{aligned} U_{rot,x} &= -b \cdot U_1 + b \cdot \sin 30^\circ \cdot U_2 + b \cdot \sin 30^\circ \cdot U_3 \ , \\ U_{rot,y} &= -b \cdot \cos 30^\circ \cdot U_1 + b \cdot \cos 30^\circ \cdot U_3 \ . \end{aligned} \tag{4.3}$$

In matrix form equation 4.2 and 4.3 can be rewritten as:

$$\begin{aligned} \begin{pmatrix} U_{translation} \\ U_{rot,x} \\ U_{rot,y} \end{pmatrix} &= \begin{bmatrix} a & a & a \\ -b & b \cdot \sin 30^\circ & b \cdot \sin 30^\circ \\ 0 & -b \cdot \cos 30^\circ & b \cdot \cos 30^\circ \end{bmatrix} \cdot \begin{pmatrix} U_1 \\ U_2 \\ U_3 \end{pmatrix} \\ \Leftrightarrow \ U_T(s) &= M \cdot U(s) \ . \end{aligned} \tag{4.4}$$

To satisfy the principle of energy conservation, the transformation must fulfil the following condition:

$$U_T^T \cdot U_T = U^T \cdot U \ . \tag{4.5}$$

Taking into account expression 4.4 leads to:

$$U_T^T \cdot U_T = (M \cdot U)^T \cdot M \cdot U = U^T \cdot M^T \cdot M \cdot U \ . \tag{4.6}$$

Condition 4.5 is only satisfied when the term $M^T M$ equals the unity matrix. With this condition parameter a and b are derived as:

$$a = \frac{1}{\sqrt{3}} \qquad \text{and} \qquad b = \sqrt{\frac{2}{3}} \ . \tag{4.7}$$

The final power ratios for the normal translatory and rotational components in the transformed system with respect to the total power are given for each attachment element by the following relation:

$$L_{translation} = \frac{|U_{translation}|^2}{\sum_{i=1}^{12} U_i^2} , \quad L_{rot,x} = \frac{|U_{rot,x}|^2}{\sum_{i=1}^{12} U_i^2} , \quad L_{rot,y} = \frac{|U_{rot,y}|^2}{\sum_{i=1}^{12} U_i^2} . \tag{4.8}$$

The power ratios obtained with equation 4.8 are plotted in Figure 4.16 for each attachment element. Due to the non-symmetrical primary excitation on the fuselage skin and non-symmetrical layout of sensors the actuation power is not evenly distributed on each attachment element. For instance at frequencies up to 100 Hz the attachment element *AAE 1*, being the nearest to the primary excitation source, requires more than 60% of the total actuation power. Otherwise, for most of the frequency range, the actuation signal is mainly dominated by a rotation in the x-direction, which also corresponds to the direction of the frames and is perpendicular to the direction with the highest bending stiffness. Rotations y-direction are also strongly excited at some frequencies, whereas normal translations are only generated around 130 and 450 Hz. These results confirm the assumption from the preliminary investigations that both translatory and rotational perturbation components must be controlled in order to achieve a substantial reduction in sound transmission.

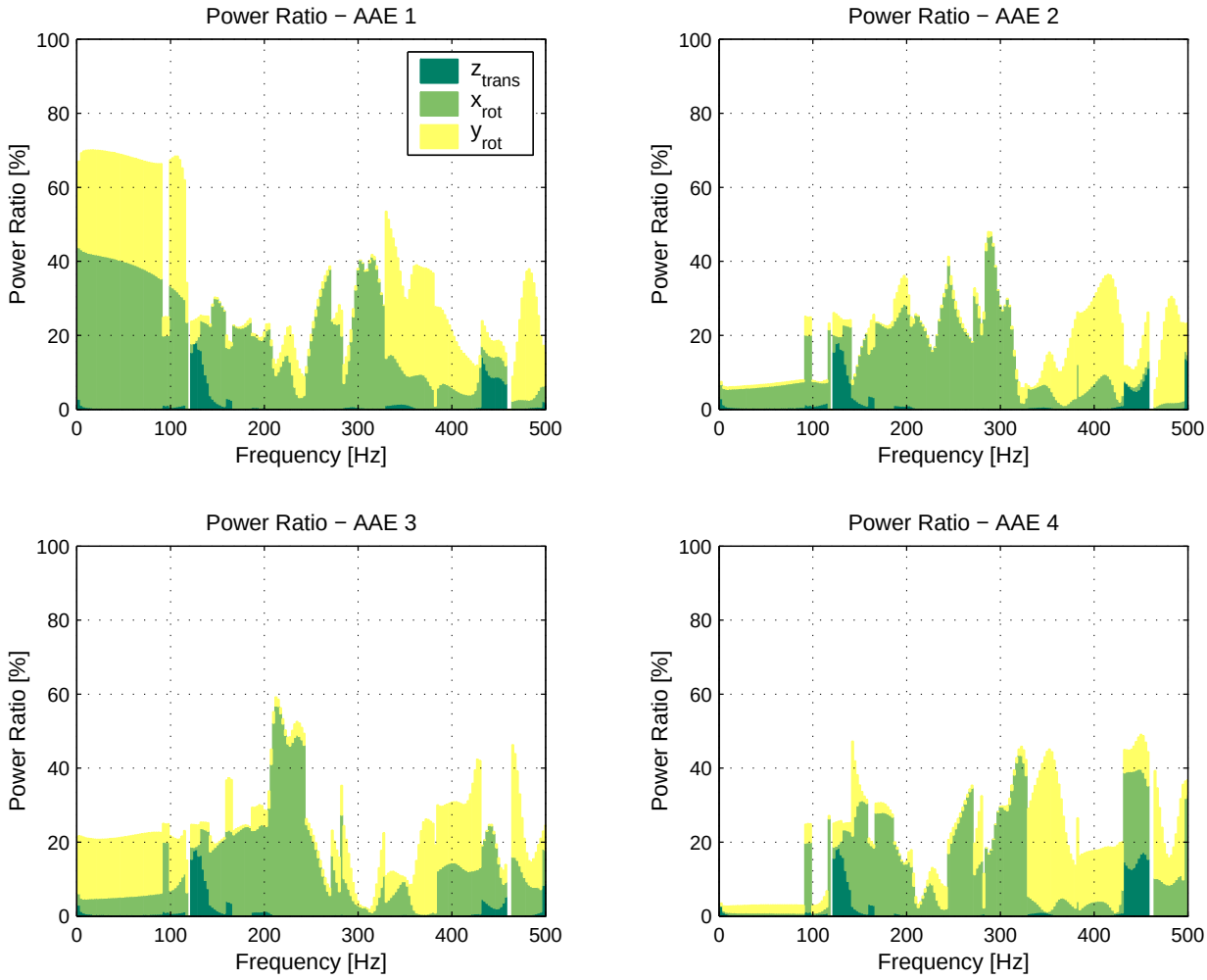

Figure 4.16: Active attachment elements: translatory and rotational actuation power components

In contrast to the simulation study presented by Gardonio and Elliott [Gardonio98], good results are obtained with the active attachment elements because translatory and rotational control forces can be excited at each trim panel attachment point and additional sensors located on the trim panel and monitoring the sound radiation are used in the control loop.

4.4 Analysis and Comparison

As the primary goal of all three active technologies is to increase the transmission loss of the fuselage section with respect to various primary perturbations in the lower frequency range (buzz-saw noise, jet noise, TBL noise and structure-borne noise), a direct comparison of the best results obtained with each control concept is made in order to determine the technology having the highest potential for an active structural control application. For this purpose simulation results obtained with three different primary excitations of the fuselage skin (acoustic monopole source, diffuse sound field and point force excitation) are analysed. The same setup as in Chapter 3.4 is used for the primary sources.

Figure 4.17 and 4.18 summarize the acoustic and structural results for the monopole excitation. The direct comparison reveals that the concept with active attachment elements is by far giving the best sound transmission behaviour for the considered frequency range. Only at two frequency ranges, 330 to 380 Hz and 440 to 470 Hz, better acoustic results are obtained with the active damping technology applied to the fuselage skin, as at those particular frequencies the sound transmission is dominated by locally vibrating skin patches. In terms of trim panel acceleration the best results are also obtained with the active attachment elements.

For the diffuse field and point force primary excitations the feedback gain optimisation output for the active damping configurations and the frequency-dependant sensor selection used with the active attachment elements are different to ones selected for the monopole excitation. However, very similar simulation results are achieved for the acoustic and structural quantities. The respective results obtained with the diffuse field primary excitation are presented in Figure 4.19 for the TL and in Figure 4.20 for the mean trim panel acceleration, whereas in Figure 4.21 and 4.22 the total sound power radiated by the trim panel and its mean acceleration level are shown for the point force perturbation. In both cases on nearly the whole frequency range the best TL results, respectively decrease in radiated sound power, are obtained with the active attachment technology.

The collocated actuators and sensor of the active damping concepts were also tested in combination with the LMS control algorithm. Typically such type of control results in higher local control reductions at the error sensors than the ones obtained with a local velocity feedback control. However, in terms of transmission loss increase, no amelioration in comparison to the ones obtained with the feedback variants was achieved. Hence, these results are not presented in this study.

In addition to the ASAC control performed with all active technologies, an evaluation of an active noise control configuration was also carried out. In this mode the acceleration error sensors are replaced with an array of microphones located either in the cavity or in the acoustic near-field radiated by the trim panel. In both cases the control loop is driven with the LMS algorithm. By controlling directly the acoustic sound field superior acoustic results in comparison to an active structural acoustic control are obtained. Yet, this control concept was not

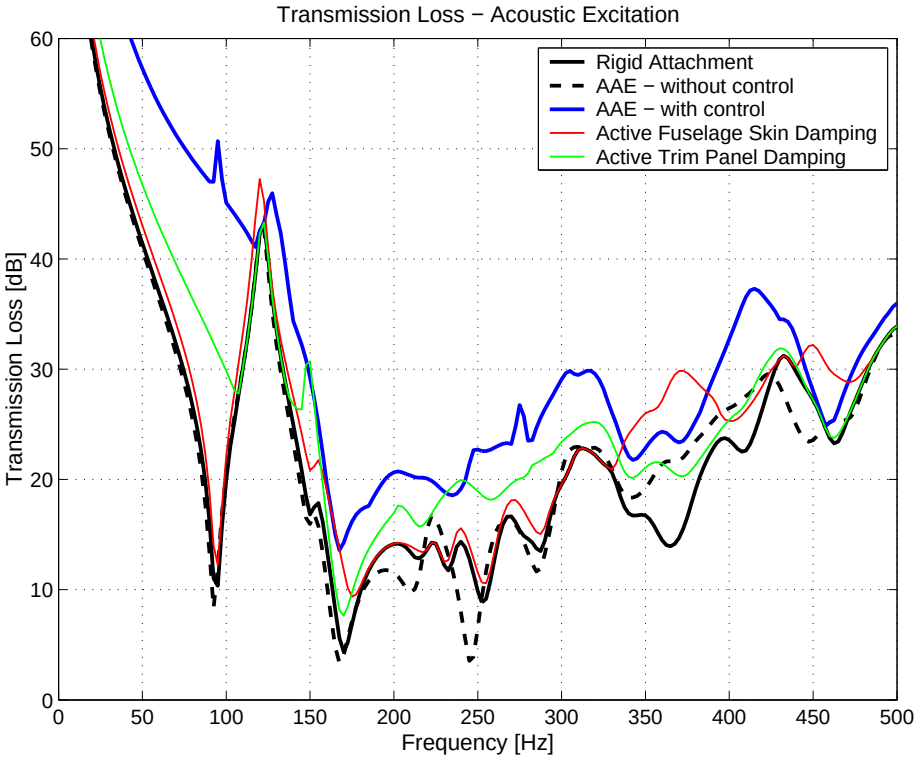

Figure 4.17: Comparison of resulting TL (active attachment elements, fuselage skin and trim panel damping), with and without control, acoustic monopole excitation

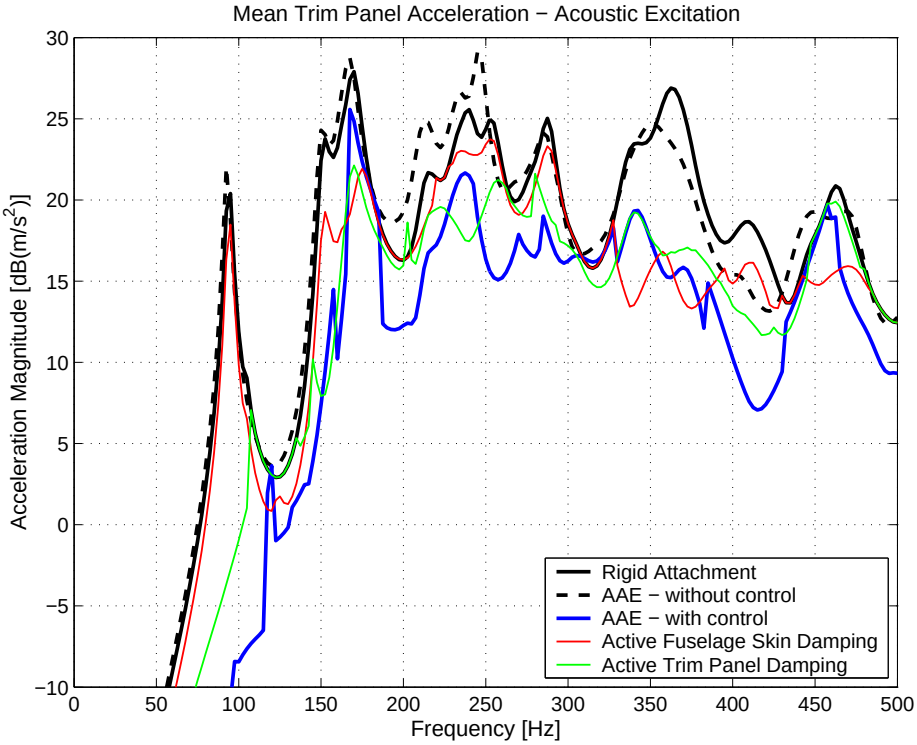

Figure 4.18: Mean trim panel acceleration level (active attachment elements, fuselage skin and trim panel damping), with and without control, acoustic monopole excitation

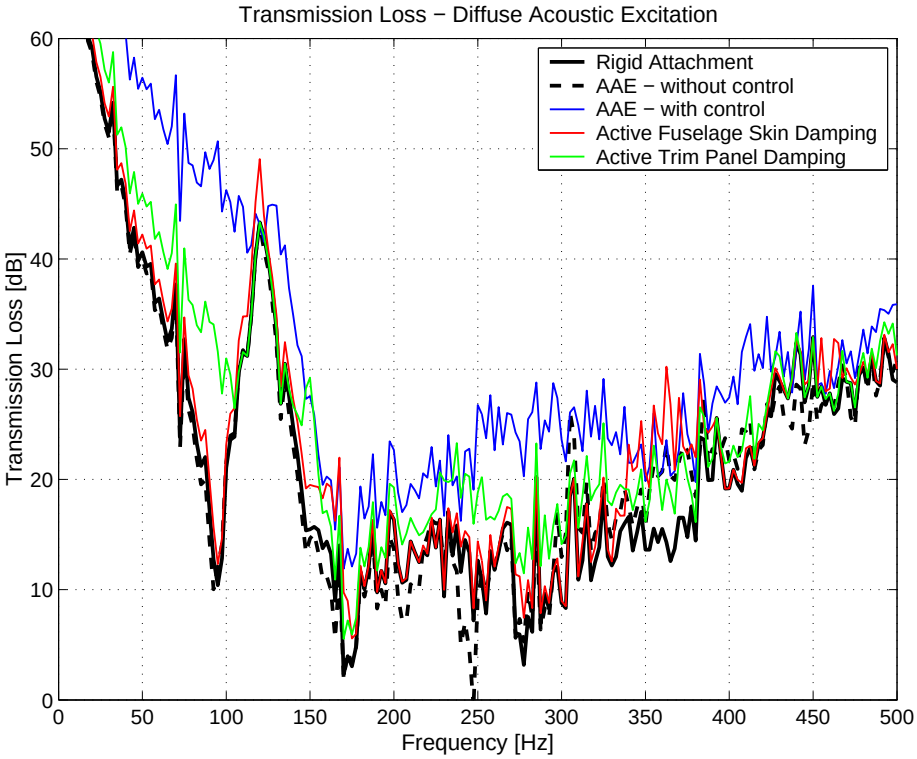

Figure 4.19: Comparison of resulting TL (active attachment elements, fuselage skin and trim panel damping), with and without control, acoustic diffuse excitation

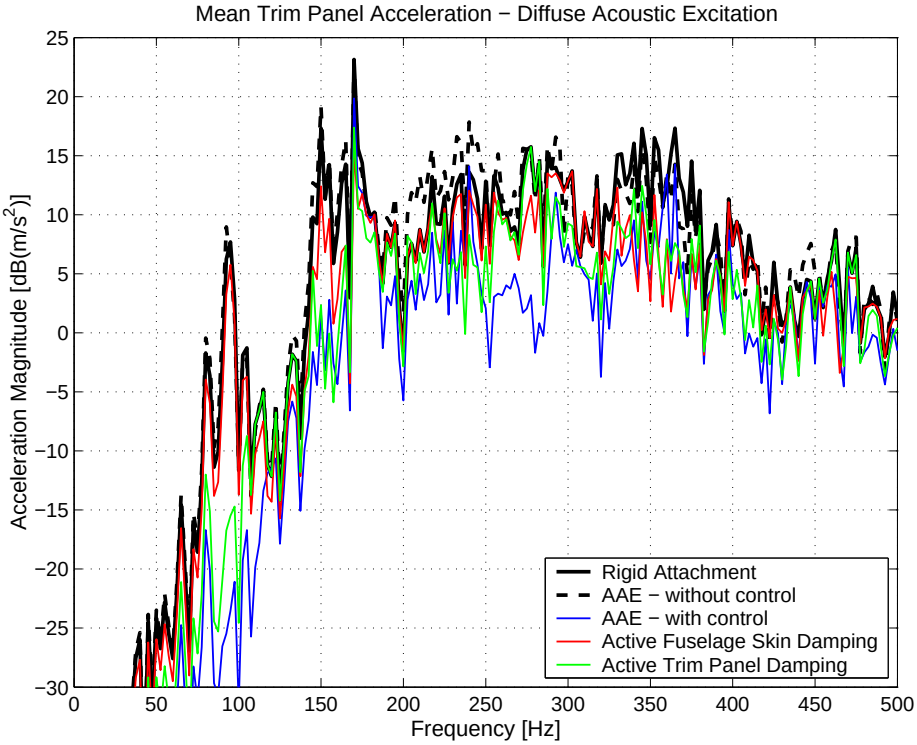

Figure 4.20: Mean trim panel acceleration level (active attachment elements, fuselage skin and trim panel damping), with and without control, acoustic diffuse excitation

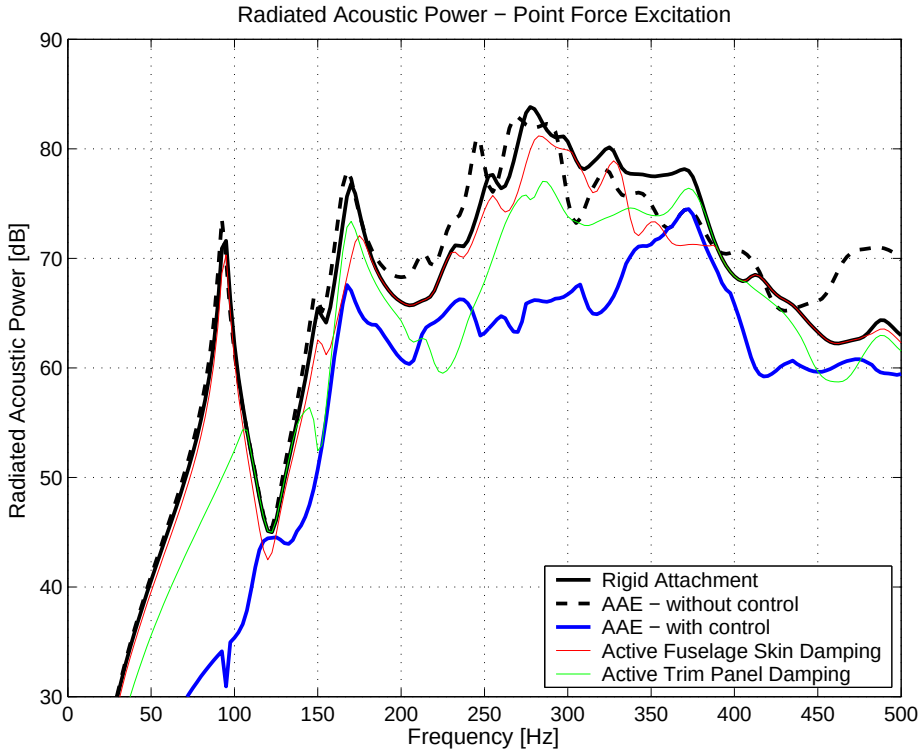

Figure 4.21: Comparison of radiated sound power (active attachment elements, fuselage skin and trim panel damping), with and without control, point force excitation

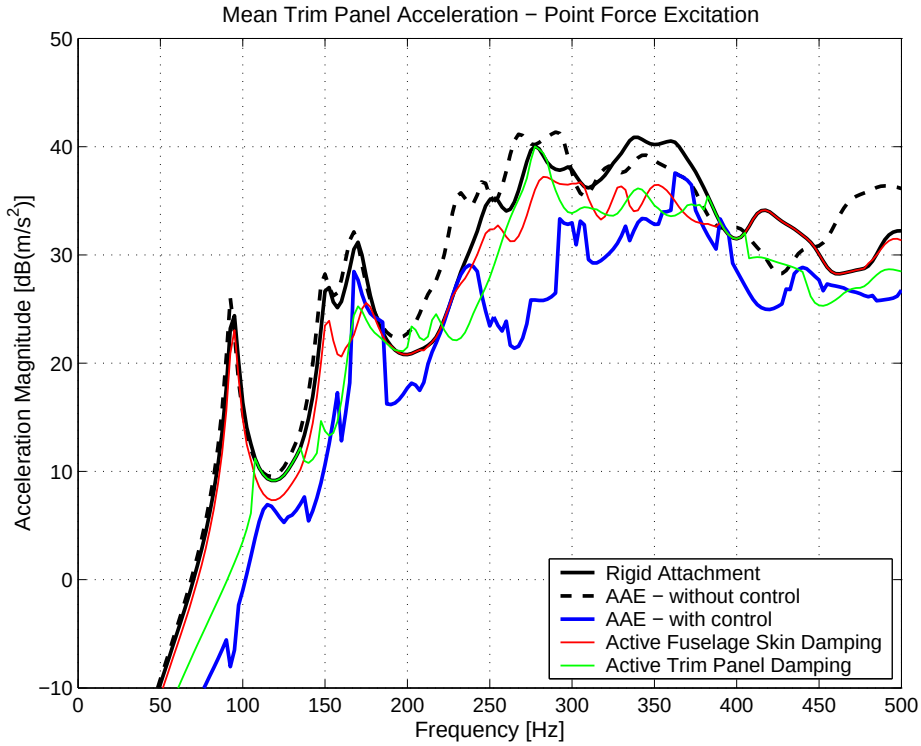

Figure 4.22: Mean trim panel acceleration level (active attachment elements, fuselage skin and trim panel damping), with and without control, point force excitation

pursued, as the trim panel is driven in an efficient radiation mode, which results in far higher trim panel acceleration levels than without control and thus could cause structural problems in the worst case. Also the actuation effort needed for this type of control is much increased in comparison to the various ASAC control configurations. Furthermore, in reality it might be problematic or even impossible to place microphones in front of the radiating structure.

The control in the cavity is aimed at reducing the cavity sound pressure and thus the loading and sound radiation of the trim panel. In combination with the d_{31}-actuators placed on the fuselage skin this sensor concept showed some promising results at frequencies below 200 Hz, but at higher frequencies sound transmission is increased due to spill-over effects and strong excitation of higher cavity modes. An increased actuation effort in contrast to the structural control approach is also required. The active attachment elements and actuators placed on the trim panel are not suited to a cavity pressure control as, besides the obtained reduction in cavity pressure, which is indirectly controlled by the trim panel behaviour in this case, an increase of the mean acceleration level and thus of the sound radiation is typically excited by the actuators as well.

4.5 Conclusions

In this chapter the performance of three different actuator and sensor concepts aimed at reducing the sound transmission through aircraft sidewall sections at low frequencies was numerically analysed for various primary excitations. The simulation model is based on a generic, plane double wall fuselage section and takes into account structure-borne as well as airborne noise propagation. An ASAC system is used to control the dynamic response of the structure to an external primary perturbation of the fuselage skin and to improve the transmission loss.

Two of the active systems are intended to increase the structural damping and make use of d_{31}-piezo patches either bonded to the fuselage skin or the trim panel. In this configuration the controller is implemented as local velocity feedback algorithm in combination with collocated actuators and unidirectional acceleration sensors. In general, it is demonstrated by the simulation results that an increase in transmission loss can be obtained with actuator sensor pairs located directly on the trim panel. The additional damping forces reduce the mean acceleration level on the trim panel, which in turn is correlated to the total radiated sound power. On some frequencies the sound transmission through the double wall is essentially determined by locally vibrating fuselage skin modes. At those frequencies better results in terms of TL increase are achieved with the actuators placed on the fuselage skin. However, this configuration is not adapted to low-frequency perturbations as the actuators do not have a sufficient control authority on global modes, which are mainly excited on the fuselage skin at low frequencies.

The third active technology is based on active trim panel attachment elements, which replace the standard shock mounts used to attach the trim panel on the main fuselage. The actuators utilize the piezoelectric d_{31}-bending effect and through a particular design of the elements both normal translatory and rotational perturbation components induced at the attachment points can be controlled. The controller is implemented as LMS algorithm and error signals from acceleration sensors integrated within the attachment elements and the trim panel are controlled. In the simulation model, out of the three proposed active technologies, the active attachment approach gives the best control performance in terms of acoustic and structural

results. Furthermore, if the sound transmission is dominated by structure-borne noise, the active attachment elements also represent the most adequate active technology.

Taking into consideration these simulation results, the active damping systems do not seem to represent suitable solutions for the improvement of the transmission loss of aircraft sidewall sections. Further experimental investigations will focus on the development and testing of prototype active attachment elements.

Chapter 5

Experimental Study

The experimental results, which were achieved with a prototype control and actuator system, are presented in this chapter. In general the basic layout resembles the simulation model described in the previous chapter. A plane section of a generic aircraft double wall structure, consisting of a main fuselage and trim panel, is installed between two acoustic chambers. The chamber facing the fuselage skin panel is used for the excitation of the structure, which is either done acoustically by loudspeakers or with a mechanical point force, whereas in the chamber facing the trim panel the global and local sound power transmitted by the structure is measured.

The trim panel is attached to the fuselage via four active attachment elements, which are used to control the dynamic response and sound radiation of the trim panel. The control algorithm is implemented on a DSP system, driving the actuators in such way that an error vibration level, measured on the structure, is minimized. The performance and efficiency of the active structural acoustic control system is evaluated against various deterministic and random disturbances. The deterministic perturbation represents a harmonic noise source similar to a buzz-saw noise excitation, whereas a random excitation like the turbulent boundary layer noise is simulated by band-filtered white noise disturbances.

5.1 Design of a Prototype Active Attachment Element

Based on the simulation results obtained with the fuselage trim-panel model presented in Chapter 4, a Thunder actuator for a prototype active attachment element has been designed and manufactured. The design is derived from the commercially available Thunder actuators TH-10R and features a similar composite lay-up and PZT properties. The dimensions of the metal substrate and PZT layer are changed to the values listed in Table 5.1. A photo of the basic element is shown on the left side of Figure 5.1. In contrast to the model TH-10R, no mounting slots are provided on the tabs, because the element will be used in a pure clamshell configuration. Furthermore, the actuator design includes a hole in the centre of the actuator. This hole accepts screws up to a size of M2.5 and is used to connect the clamshell actuator unit to the mounting plate through a spacer clamping-sleeve construction. The actuator top layer is made of copper and provides a good soldering base for the attachment of the electrodes. The maximum input voltage at which the Thunder elements may be operated is 480 V peak

to peak. This voltage is equivalent to an electric field strength of around 2360 V/mm across the thickness of the PZT layer.

Table 5.1: Specifications of the basic Thunder element

Thunder Specifications	
Overall dimensions:	32,0 x 19,0 x 1,1 mm
PZT-dimensions:	23,0 x 18,0 mm
Composite thickness:	0,43 mm
Substrate layer thickness:	0,20 mm
PZT layer thickness:	0,20 mm
ø mounting hole substrate:	2,6 mm
ø mounting hole PZT:	6,0 mm
Weight:	1,4 g
Capacity:	18 nF
Max. voltage (V_{pp}):	480 V
Typical displacement*:	approx. 1 mm
Blocked force:	not available

* clamped support on one side, maximum input voltage, quasi-static deflection peak to peak of the free tip at 1 Hz

The actuator unit used in the active attachment element consists of two Thunder actuators and two clamshell mounts. Integrated in each clamshell mount is a 0,2 mm thick and 3 mm deep slot, which is used to retain the Thunder elements on their free tabs, thus providing a clamped support that holds the actuator end at a fixed angle when the device tries to bend. However, the mounting elements are not prevented from moving relative to each other when the whole actuator unit flexes. Hence, a pure translation perpendicular to the PZT surface is generated at the centre of the actuator device. The mounting elements are manufactured in steel by an electrical discharge machining process. As adhesive the two-part epoxy resin system *Ciba Epocast 52-A* and *B* is used. The resulting spacing between the Thunder elements is 5,9 mm. An image of the finished clamshell element is reproduced on the right side of Figure 5.1 with the spacer clamping-sleeve element already in place. The overall dimensions of the clamshell element are 34 by 19 by 8,3 mm. An additional technical drawing of the basic actuator unit is presented in Annex B.

To demonstrate the design and construction of the active attachment element, a picture with the individual components prior to assembling and an exploded view of the actuator element are shown in Figure 5.2 and 5.3. The mounting plates are made from 3 mm thick aluminium and must provide a stiff support for both the actuators and the error sensors. Otherwise the piezoelectric actuator would not couple efficiently into the host structure and the error signals would not correlate with the actual disturbances. An FEM normal modes analysis of the mounting plate (free boundary conditions) showed that the first bending mode occurs only at 3,8 kHz. Therefore, the hexagonal shape already used in the simulation model is retained. The width across the flat side of the hexagon is 62 mm. Since the mounting plate is electrically connected to the actuator's substrate layer, it also serves as common electric ground for the power supply.

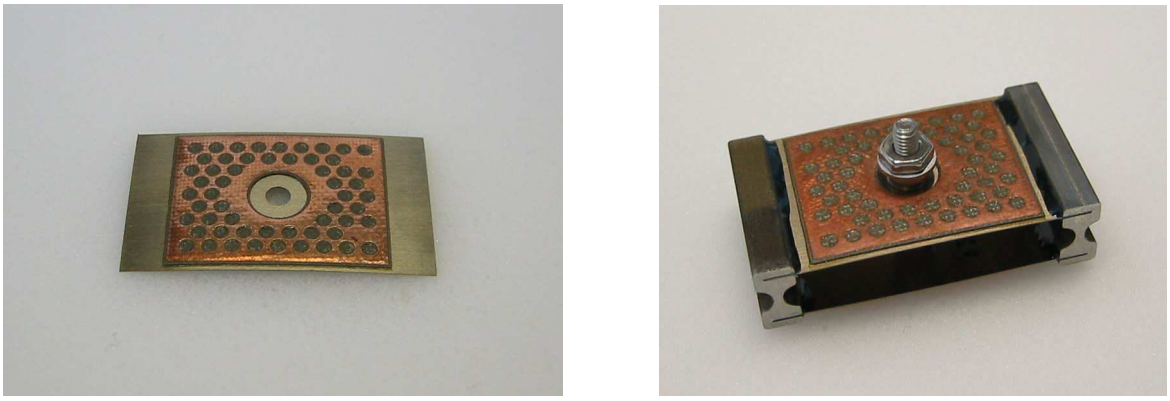

Figure 5.1: Basic Thunder element and actuator unit in clamshell configuration

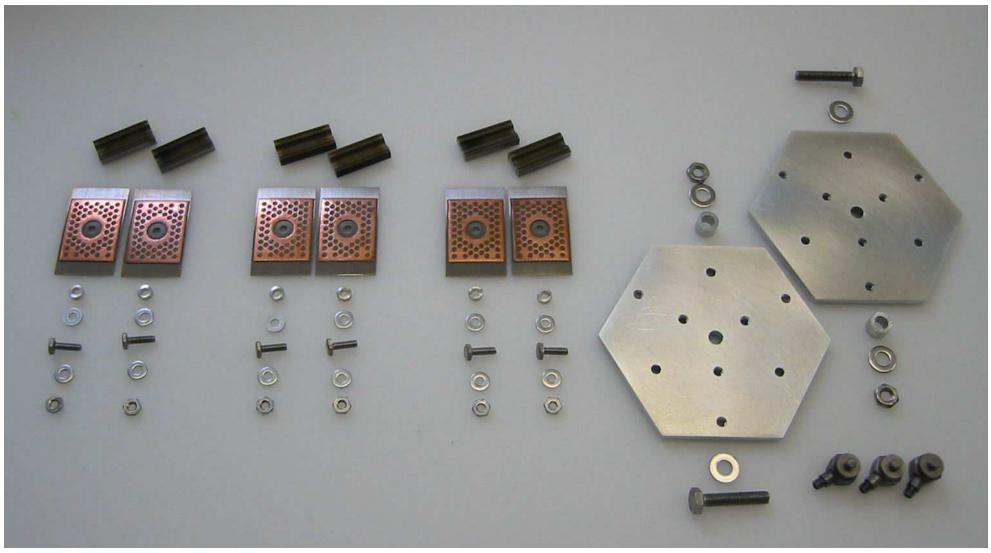

Figure 5.2: Components of an active attachment element

Three actuators as well as three error sensors are disposed axially symmetric by 120 degrees around the centre of the mounting plate. For the actuators the leverage distance to the centre point is 21,5 mm, whereas the radius for the error sensors is 26,5 mm. The unidirectional acceleration sensors of the type PCB M353B65 are directly integrated in the upper mounting plate with M3 screw threads provided in the plate. The active attachment element is clamped to the host structure with a similar spacer clamping-sleeve construction as on the clamshell elements by using M4 screws. To ensure that the elements can be mounted inside a double wall partition that may not be accessible from outside, the attachment screws are glued to the mounting plate. Figure 5.4 shows a fully assembled and functional prototype. The overall height is 22,6 mm and the total weight sums up to 98 g (without taking into account cables for power supply and acceleration sensors). A technical drawing of the prototype attachment element is also reproduced in Annex B.

Figure 5.5 shows the measured complex frequency-response function in terms of acceleration per applied unity voltage for an active attachment element. The attachment element is excited by a voltage applied to the first actuator unit and the response of the three acceleration sensors

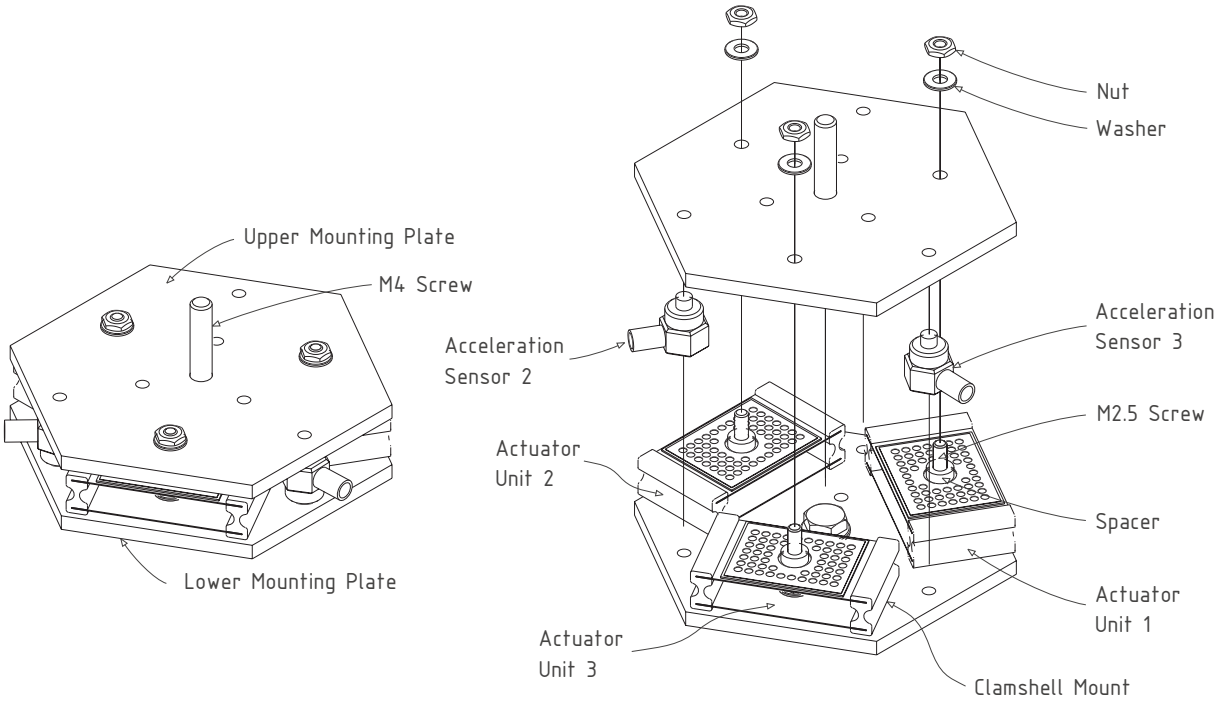

Figure 5.3: CAD-model of active attachment element

Figure 5.4: Prototype active attachment element

attached to the upper mounting plate is measured. The lower mounting plate is clamped to a fixed support, whereas the upper mounting plate is not constrained in its free displacement. The designation of actuators and sensors is made in respect to Figure 5.3.

The general dynamic behaviour of the element resembles that of a mass-spring system and is characterized by a succession of resonance and anti-resonance frequencies. Due to the symmetrical configuration the response of sensor 1 and sensor 3 are very much identical in magnitude and phase, whereas the phase of sensor 2 is shifted about 180° in comparison to those of sensors 1 and 3, thus indicating that mainly a rotation parallel to an axis pointing from sensor 1 to sensor 3 is generated. The global maxima is found at a frequency of 221 Hz with a magnitude of 0,67 g/V or 0,35 μm/V expressed as displacement. For frequencies above 800 Hz, the actuator generates a constant acceleration level of about 0,03 g/V at sensor 1 and 3 and around 0,015 g/V at sensor 2. Taking into consideration the axis-symmetric layout of the attachment element, a respective excitation of actuator unit 2 or 3 will result in a similar behaviour. With

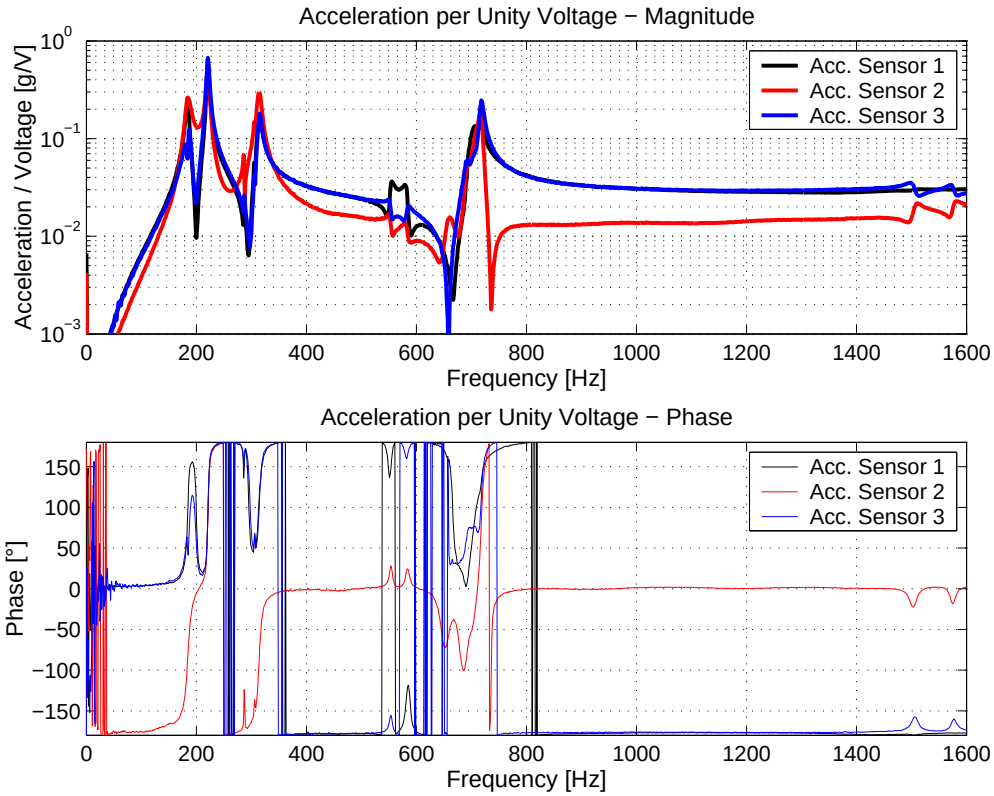

Figure 5.5: Measured actuator response per unity voltage applied to actuator unit 1

an appropriate simultaneous excitation of all three actuator units, it is possible to excite an arbitrary relative displacement between the upper and lower mounting plate, which is composed of a normal translation and two perpendicular rotations in the plate's plane.

This prototype design provides a good starting point for further developments and may be optimised in terms of size, weight, actuator performance and degree of structural integration into the fuselage and trim panel. The displacement and force generated by a single actuator unit are easily scalable for different requirements. The main design variables are the piezoceramic thickness relative to the substrate layer, the length and width of the Thunder element and the mounting condition for the clamshell configuration. Thus, with a thicker piezoceramic layer, a greater force will be generated at the expense of the displacement. The actuator width is directly proportional to the force and a less stiff mounting condition will provide a greater displacement, but also less force.

The unidirectional force and displacement components generated by a single actuator unit are converted at the trim panel attachment point into a force and two orthogonal moments, respectively a translation and two perpendicular rotations. Whether the active attachment element will be mainly a force or displacement actuator depends primarily on the leverage distance between the force transmitting point of the clamshell device to the mounting point of the attachment element. With increasing leverage distance the attachment element will generate a greater moment and less rotational displacement.

5.2 Test Setup and Experimental Methods

The effectiveness of a structural noise and vibration control system based on active trim panel attachments is demonstrated in laboratory scale on a generic aircraft fuselage section installed into a transmission loss suite between a reverberation and anechoic room. The test structure, measurement method and various types of excitation as well as the control loop implementation are presented in the following chapters. For each single test constellation an intensity measurement of the radiating trim panel surface is carried out with and without active control. Thus, the total sound power transmitted through the structure is determined, permitting a direct evaluation of the active control effectiveness.

5.2.1 Test Structure Description

For the evaluation of the active control system a double wall partition consisting of a plane generic fuselage section combined with a typical trim panel, as depicted on the left side of Figure 5.6, is used. The fuselage panel is manufactured from a CFRP skin panel reinforced by five stringers in one direction and two additional CFRP frames in perpendicular direction. The panel meets the TANGO[1] specifications for advanced composite airframe structures. The T-sectioned stringers are structurally fully integrated in the skin panel. In-plane dimensions of the skin panel are about 1 by 1 m and the nominal skin thickness is 2,5 mm. Stringer height is 37 mm and the stringer pitch amounts 175 mm. The C-sectioned carbon fibre frames, also designed to TANGO requirements, are riveted to the skin panel and additional aluminium clips are used to connect the frames to the stringers. The frame height is 90 mm while the frame pitch is 533 mm. The overall weight of the fuselage structure adds up to 8,2 kg.

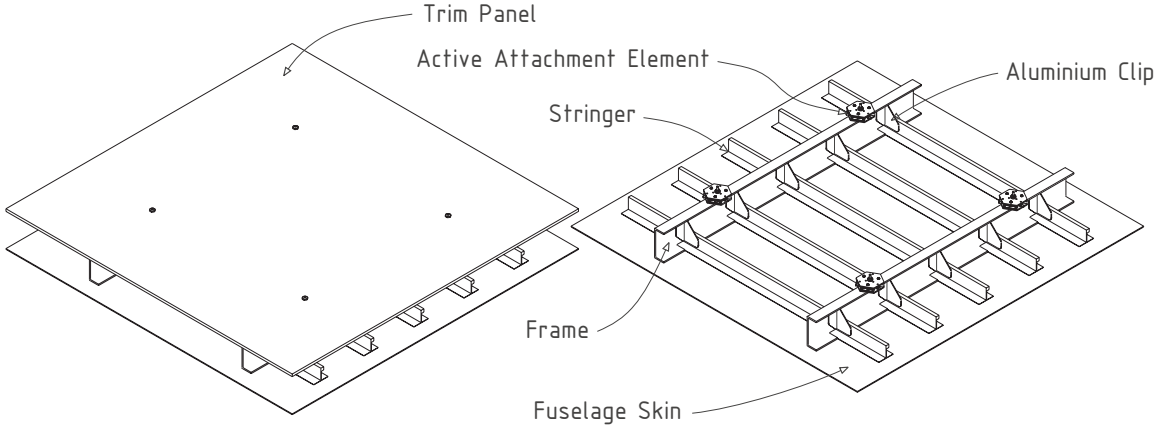

Figure 5.6: Test structure CAD-model

Two different trim panels, possessing identical in-plane dimensions as the fuselage, are available for various active structural control tests. Both panels are designed as honeycomb core sandwich construction and based on trim panel designs already used in real aircraft. The first panel is composed of a 8 mm thick Nomex honeycomb core layer and is reinforced by fabric fibreglass skin sheets on both sides, while a 4 mm thick Nomex honeycomb layer constitutes

[1]TANGO is a research project within the EU Fifth Framework Programme (FP5).

the core for the second panel, which is stiffened by fabric carbon fibre skin sheets. As matrix a phenol-resin system is used on the first panel and a cyanate-ester system on the second trim panel. The overall weight of the first trim panel is 1,7 kg, whereas the structural mass for the second panel is only 0,92 kg. Additional material parameters for the fuselage and the trim panels are listed in Annex C.1.

The resulting cavity between the fuselage and the trim panel is partly filled with fibreglass wool blankets[2] to provide an additional source of acoustic dissipation in the airborne sound transmission path.

An important point influencing the sound transmission behaviour of double wall sections, is the kind of connection used for the attachment of the individual partitions. In real aircraft, the trim panels may be attached to the main fuselage structure by various types of constructions, ranging from rails embedded in the cabin floor or ceiling to different bracket designs and soft shock mounts connecting the trim panel to the fuselage frames. As the present study examines the possibility to use active attachment elements instead of passive brackets or shock mounts, the trim panel will be attached to the fuselage frames via four attachment points as depicted in Figure 5.6. This configuration is similar to the one used in the simulation model. A representation of the actual actuator layout with respect to the fuselage geometry and the denotation used in the following is shown in Figure C.1. A detailed view of the actuator mounting between the frame and trim panel is given in Figure 5.7. It shows a cross sectional view through one attachment point parallel to the frames. The offset between the trim panel and the frames must be at least 23 mm, in order to provide enough space for the mounting of the active attachment elements. This requirement results in a separation distance of 113 mm between the fuselage skin and the trim panel. On both sides of the active suspension elements a clamping-sleeve assembly is used to fasten the active element to the frame and the trim panel respectively. To compare the sound transmission behaviour achieved with active control versus the original passive configuration, it is possible to replace the active attachment elements with passive shock mounts, which incorporate soft elastomer joints.

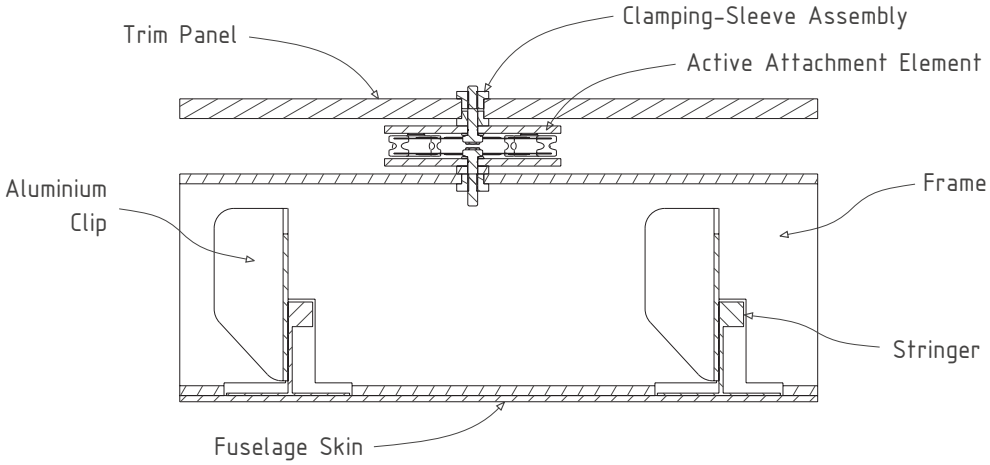

Figure 5.7: Detail of actuator mounting between fuselage frame and trim panel

Figure 5.8 shows the fuselage panel installed to the transmission loss test suite. The trim panel

[2]Microlite AA, thickness 25 mm, density 9,6 kg/m^3, used as acoustic and thermal insulation in aircraft.

is not yet installed thus making visible the active attachment elements as well as the wiring needed for the actuator power supply and the acceleration error sensors. Also visible are the glass wool absorption blankets covering the whole fuselage skin apart from the frames.

Figure 5.8: Fuselage panel installed in TL test suite, active attachment elements already installed

5.2.2 Transmission Loss Test Facility

Figure 5.9 shows a schematic view of the transmission loss test facility used for the experimental investigation of the structural acoustic control system. The test facility consists of an anechoic chamber, a reverberation room and a transmission loss test window representing the only connection between the two rooms. To avoid a flanking path transmission of energy, both rooms, the anechoic and reverberation chamber, are structurally isolated from each other and the rest of the building by an elastic suspension system.

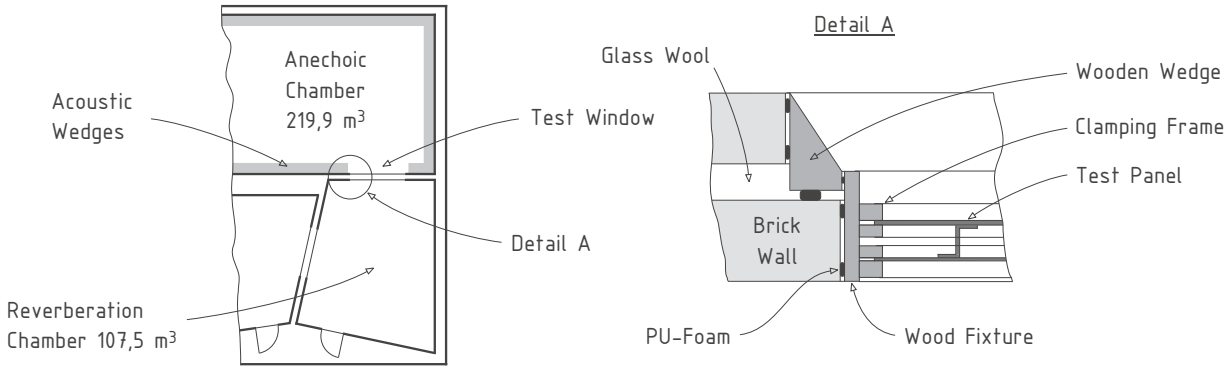

Figure 5.9: Schematic plan of the transmission loss test facility and detail of test structure installation

The anechoic chamber has inner dimensions of 12,0 m in length, 4,8 m in width and 3,8 m in height resulting in a volume of 220 m^3. The volume of the reverberation room is 108 m^3 and

its mean dimensions are approximately 6,1 m by 4,5 m by 3,9 m in length, width and height. The transmission loss test window is designed to accommodate double wall test panels with in-plane dimensions of up to 1 by 1 m. Each test panel is clamped on its edges between a set of two wooden frames. On the clamping area the frames are covered with a layer of soft rubber, providing an elastic but acoustically sealed support to the panels.

The whole frame assembly with the test structure is then installed on a 30 mm thick wooden fixture into the transmission loss test window. To prevent energy transmission of structure-borne noise from the supporting brick wall, the wood fixtures as well as the wooden wedge on the radiating side are fixed with a thin layer of polyurethane foam to the walls. Furthermore, cavities between the two chambers are filled with fibreglass wool in order to minimize a possible flanking path transmission of airborne sound.

Figure 5.10: Transmission loss test window (view from the reverberation room on the left side and view from the anechoic chamber on the right side)

In Figure 5.10 two photographs of the transmission loss test window, with the whole test structure assembly installed, are reproduced. On the left side a view from the reverberation room with the skin panel corresponding to the aircraft exterior is shown. Also visible are one of the loudspeakers and the shaker used for the primary excitation of the test structure. On the right side of Figure 5.10 a view of the test window from the anechoic chamber can be seen. The trim panel, corresponding to the aircraft interior and the intensity probe with the traverse mechanism, both located in front of the trim panel, are visible.

5.2.3 Sound Intensity Measurement

The sound power radiated from the trim panel into the anechoic chamber is determined by sound intensity measurements [Crocker98, Fahy89, Heckl94]. The sound intensity at a given point in a sound field represents a vector quantity and specifies the magnitude of sound energy flow rate passing through a unity area as well as its direction. By integrating the normal intensity distribution over a surface, which encloses an acoustical source, the overall sound power radiated by the source is determined. In comparison to measurement methods, where the sound power is derived from the sound pressure alone, the intensity method offers various advantages such as:

- Measurements can be made in almost every environment and are not restricted to special laboratory rooms as anechoic or reverberation chambers.
- A spatial localisation of noise sources is possible, because magnitude and direction of the energy flow are locally measured.
- Parasitic effects due to the presence of incoherent, static background noise sources are mostly compensated by the measurement method itself and do not contribute to the measured sound power.

A typical application for sound intensity measurement techniques is the determination of transmission loss as described in the European Standard Norm EN ISO 15186-1[3]. Compared to the standard measurement method, where the transmission loss of a partition is measured between two reverberation rooms [Heckl94], the sound intensity technique is advantageous because:

- The sound transmission behaviour of the partition is evaluated over individual sections. Regions with high intensity can thus be identified and interpreted as locations of noise sources.
- It is possible to detect and quantify possible leaks and flanking path transmission of the measurement test window.
- The receiving chamber does not need to be calibrated for its reverberation time.

The definition of sound intensity I is given by the product of the sound pressure p and particle velocity v averaged over a measurement time T:

$$I = \overline{p(t) \cdot v(t)} = \frac{1}{T} \int_0^T p(t) \cdot v(t) \cdot dt \ , \tag{5.1}$$

and indicates the sound power passing through a unity area normal to the particle velocity. Hence, the sound intensity can be integrated over a measurement surface S to yield the total sound power P passing through that surface:

$$P = \int_S I \cdot dS = \int_S \overline{p(t) \cdot v(t)} dS = \frac{1}{T} \int_S \int_0^T p(t) \cdot v(t) \cdot dt \cdot dS \ . \tag{5.2}$$

In practice the above integral is replaced by a numerical summation and the sound intensity perpendicular to the surface enclosing the radiating structure is determined at a number of discrete, fixed points with an intensity probe consisting of a microphone pair separated by a distance d. A typical arrangement for a plane sound wave incident upon an intensity probe is depicted in Figure 5.11.

Taking into consideration Euler's relationship between pressure and velocity for a given direction n in a linear sound field:

$$-\frac{\partial p(t)}{\partial n} = \rho \cdot \frac{\partial v_n(t)}{\partial t} \ , \tag{5.3}$$

[3]Measurement of sound insulation in buildings and of building elements using sound intensity

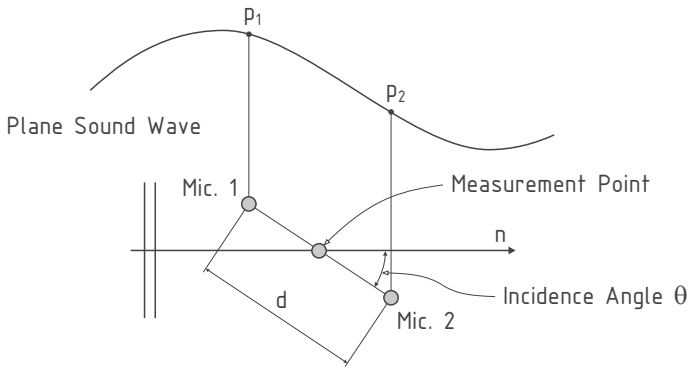

Figure 5.11: Plane wave incidence on a two point intensity probe

the velocity derivative with respect to the time at the centre measurement point can be expressed by the numerical derivative of the pressure over the distance d, resulting in the finite difference estimation $\dot{v}_n = (p_1 - p_2)/(\rho \cdot d)$. The pressure midways between the two microphones is estimated by the finite sum $p = (p_1 + p_2)/2$. Hence, the estimate of the time averaged intensity I' in direction from measurement point 1 to 2 is given by the following relationship:

$$I' = \frac{1}{2\rho d} \cdot \frac{1}{T} \int_0^T \left(p_1(t) + p_2(t)\right) \int_0^t \left(p_1(\tau) - p_2(\tau)\right) \cdot d\tau \cdot dt \ . \tag{5.4}$$

By applying a Fourier transformation, equation 5.4 is transformed into the frequency domain and I' can be represented by the imaginary part of the sound pressure cross correlation G_{12} measured between point 1 and 2:

$$I'(\omega) = -\frac{1}{\omega \cdot \rho \cdot d} \cdot \Im\left(G_{12}(\omega)\right) \ . \tag{5.5}$$

However, it should be kept in mind that this measurement method is limited to a certain frequency range [Cazzolato00, Fahy77, Jacobsen02, Parkins00]. For a plane sound wave having an incidence angle of θ with respect to the microphone direction, the intensity bias error made through the finite sum and finite difference estimations can be evaluated analytically by the next expression:

$$I_{bias} = \frac{I'}{I} = \frac{\delta_m \cdot \sin\left(\sigma \pm |\delta_p|\right)}{\sigma} \ , \tag{5.6}$$

where $\sigma = 4\pi \cdot (c/f) \cdot d \cdot \cos\theta$. I' and I are the approximated and exact intensity respectively. The term δ_p denominates the absolute phase difference between the microphones and δ_m is the relative magnitude mismatch defined as $\delta_m = |P_1| \,/\, |P_2|$.

The high-frequency limit depends mainly on the microphone distance d, because the finite difference approximation used in equation 5.4 is only valid when the acoustic wavelength is large in comparison to the microphone separation distance. Assuming perfectly matched microphones ($\delta_m = 1$ and $\delta_p = 0$) and an incidence angle θ of zero, it follows from equation 5.6 that the bias error in the approximated intensity is less than 1 dB for plane waves with normal incidence if the following condition is fulfilled:

$$f < \frac{1,14 \cdot c}{4\pi \cdot d} \ . \tag{5.7}$$

In the low-frequency range the bias error is mainly dominated by the phase mismatch δ_p of the microphone pair. In this case the acoustic wavelength is large compared to the separation distance d. Thus, the measured pressure phase angle difference between both microphones becomes small and for a frequency smaller than a certain lower limit, this difference will be of the same order than the microphone phase mismatch inherent to the measurement hardware, thus leading to a substantial false estimation of the sound intensity. For small values of σ and δ_p the bias error in equation 5.6 can be approximated by:

$$I_{bias} \approx \frac{\delta_m \cdot (\sigma - \delta_p)}{\sigma} \ = \delta_m \cdot \left(1 \pm \frac{|\delta_p| \cdot c}{4\pi \cdot f \cdot d \cdot \cos\theta}\right) \ , \tag{5.8}$$

which becomes very large when the enumerator of equation 5.8 approaches zero. With the assumptions of a phase error of 0,3°, which in practice represents a typical value, a sensitivity mismatch of 1 and normal incidence, the bias error is smaller than 1 dB if the constraint:

$$f > \frac{0,025 \cdot c}{4\pi \cdot d} \ , \tag{5.9}$$

is satisfied.

A downside of the sound intensity technique is the fact that the measurement procedure, depending on the number of discrete measurement points, is highly time consuming. However, this disadvantage can also be seen as an appropriate test for the stability of the active control system, which must thus be ensured for the whole duration of a transmission loss test.

5.2.4 Acoustic Excitation

The acoustic excitation of the fuselage is done through a pair of loudspeakers located in the reverberant chamber (see Figure 5.10). The loudspeakers are either driven by various tonal frequencies, band-filtered white noise or combinations of both. On the anechoic side of the test window an in-plane area covering the whole trim panel surface is scanned automatically by the intensity probe, which is mounted on an appropriate traverse mechanism (also depicted in Figure 5.10).

The sound power $P_{Radiated}$ radiated by the trim panel is found by integrating the measured spatial intensity I over the area S of the measurement grid:

$$P_{Radiated} = \int_S I \cdot dS \ . \tag{5.10}$$

For a regular measurement grid as illustrated in Figure 5.12 with a length l_x and a number of n_x discrete measurement points in the x-direction and a length l_y and n_y measurement points in the y-direction, equation 5.10 can be expressed as:

$$P_{Radiated} = \sum_{j=1}^{n_x \cdot n_y} I_j \cdot \frac{l_x}{n_x - 1} \cdot \frac{l_y}{n_y - 1} \ , \tag{5.11}$$

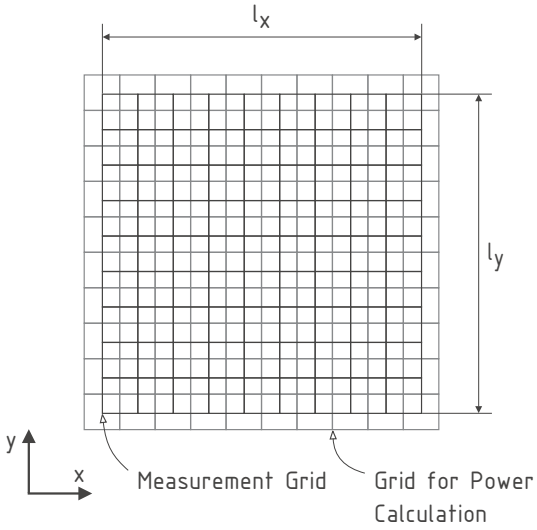

Figure 5.12: Definition of the intensity measurement grid

where I_j is the intensity of the j-th measurement point.

With the assumption of a diffuse acoustic sound field, the excitation sound power $P_{Excitation}$ in the source room is given by the relation [Heckl94]:

$$P_{Excitation} = \frac{S_{Rev} \cdot p_s^2}{4 \cdot \rho c} \ , \tag{5.12}$$

where p_s is the spatial averaged sound pressure in the source room and S_{Rev} is the area of the test panel on the excitation side. ρ and c are the density and the speed of sound of the fluid in the reverberant room. According to the Norm EN ISO 15186-1 the excitation power is averaged as in the following expression over the number of discrete measurement points:

$$P_{Excitation} = \frac{1}{n_x \cdot n_y} \sum_{j=1}^{n_x \cdot n_y} \frac{S_{Rev} \cdot p_j^2}{4 \cdot \rho c} = \frac{S_{Rev} \cdot p_M^2}{4 \cdot \rho c} \ . \tag{5.13}$$

In the above expression p_j is the spatial averaged sound pressure in the source room temporally corresponding to the j-th measurement point of the intensity probe. p_M designates the resulting mean sound pressure level of all measurements.

The sound transmission loss TL expressed in a decibel scale is computed from the ratio of excitation sound power to radiated sound power:

$$TL(\omega) = 10 \cdot \log \frac{P_{Excitation}(\omega)}{P_{Radiated}(\omega)} \ \ [dB] \ . \tag{5.14}$$

5.2.5 Point Force Excitation

To investigate the effects of a second type of primary perturbation source on the behaviour of the active control system the test structure is subjected to a forced vibration using an electrodynamical vibration exciter mounted directly on the skin panel in the reverberation

room as illustrated in Figure 5.10. The x- and y-positions of the shaker mounting point are 233 mm and 320 mm, with x and y being the horizontal and vertical axes in the plane of the skin panel relative to its lower left corner. This point corresponds to an intersection of a stringer-frame pair located on the other side of the skin panel. To monitor the excitation input levels the shaker attachment point is equipped with an additional acceleration sensor and force transducer.

With the transfer function $g(\omega)$ computed from the normal velocity signal $\dot{x}(\omega)$ and point force $F(\omega)$, both measured at the shaker mounting point:

$$g(\omega) = \frac{\dot{x}(\omega)}{F(\omega)} = \frac{\ddot{x}(\omega)}{j \cdot \omega \cdot F(\omega)} \ , \tag{5.15}$$

the structural excitation power can be determined as the real part of the product between force and velocity:

$$P_{Shaker}(\omega) = \Re\left(\dot{x}(\omega) \cdot F(\omega)\right) = \Re\left(g(\omega) \cdot F^2(\omega)\right) \ . \tag{5.16}$$

In accordance to the acoustic excitation and the norm for intensity measurement of sound TL the mean average excitation power for n_x by n_y discrete measurement points is established by:

$$P_{Shaker}(\omega) = \frac{1}{n_x \cdot n_y} \cdot \sum_{j=1}^{n_x \cdot n_y} \Re\left(g_j(\omega) \cdot F_j^2(\omega)\right) \ , \tag{5.17}$$

where g_j and F_j are the transfer function and force temporally corresponding to the j-th measurement point of the intensity probe. The sound power radiated by the trim panel into the anechoic chamber due to the forced vibration of the fuselage is determined by equation 5.11 in the same way as for the acoustic excitation. Analogical to the transmission loss for the acoustic excitation a power ratio PR expressed in decibel can be defined for the point force excitation from the ratio of excitation power to radiated sound power:

$$PR(\omega) = 10 \cdot \log \frac{P_{Shaker}(\omega)}{P_{Radiated}(\omega)} \ \ [dB] \ . \tag{5.18}$$

5.2.6 Measurement Implementation

The following sensor types and settings are used for the intensity and transmission loss measurements:

- *Intensity probe:* The experiments are carried out using a TFS SIP 101/SBS3i intensity probe, which is fitted with three Sennheiser back electret condenser KE4-211-2 1/8 inch microphones in a side-by-side configuration. The separation distance of two microphones is adjustable with respect to the reference microphone, thereby combining two different measurement ranges into a single probe. For frequencies below 1250 Hz the microphone distance is adjusted to 50 mm, whereas for frequencies above 1250 Hz a separation distance of 8 mm is used. According to equations 5.7 and 5.9 as well as to information of the manufacture, the lower and upper frequency limits when allowing maximal intensity bias errors of up to 1 dB are 175 and 7800 Hz for the small microphone distance and 30 and 1250 Hz for the microphone pair separated by a distance of 50 mm.

- *Microphone for acoustic excitation:* A half-inch pre-polarized random incidence microphone from G.R.A.S. Type 40 AQ mounted on a rotating transverse is used in the reverberation chamber for the determination of the excitation power.

- *Point force excitation:* The shaker excitation is realized with an electrodynamical vibration exciter from Brüel & Kjaer Type 4809. The excitation force level is measured with a Kistler force transducer Type 9301B, whereas the structural response at the mounting point normal to the skin panel is monitored with a unidirectional acceleration sensor of the type PCB M353B65.

The output signals of the sensors are processed on an eight-channel Dolch FlexPAC system using the signal analyser software Ceasar μ-Remus. The analyser software also drives the intensity probe traverse mechanism so that the measurement grid is scanned automatically by the intensity probe. A frequency range from 0 to 1,6 kHz with a resolution bandwidth of 1 Hz is used. For both the acoustic and point force excitation the measurement data and calculated results are available as narrowband data as well as in 1/24, 1/12, third octave and octave bands. Further post-processing of the measurement data for the calculation of sound power, transmission loss and intensity maps is carried out in Matlab. For the representation of intensity maps the measured data is interpolated linearly up to 400 points in the x- and y-directions and drawn on the measurement grid represented in Figure 5.12.

The excitation area S_{Rev} of the fuselage skin panel is 932 by 901 mm, which corresponds to the inner dimensions of the clamping frame. As measurement grid, a 1 by 1 m area covering the trim panel with ten measurement points in the x- and y-directions is chosen. The distance of the measurement plane to the trim panel is 300 mm. For a single point 20 individual measurements are averaged, requiring a time of about 20 seconds. This time is equal to the duration for a traverse period of the rotating microphone in the excitation room. The whole measurement procedure requires about 50 minutes.

The calibration of the intensity probe is done in two steps. First the absolute sensitivity of the reference microphone is determined with an acoustic calibrator giving a sound pressure level of 94 dB at 1 kHz. To minimize errors in the intensity measurement, the intensity probe is calibrated with a special piston-phone, which allows the measurement of phase and magnitude mismatches of the microphones relative to the reference microphone. These transfer functions are then used as a correction factor when the sound intensity is calculated from the measured cross spectral densities.

5.2.7 Measurement Repeatability

The acoustic performance evaluation of the ASAC system requires the variation in measured transmission loss and power ratio to be considerably smaller than the change caused by the active system itself.

In general the following procedure is applied for the intensity measurements. The absolute sensitivity of the intensity probe is calibrated directly before each measurement. As the intensity analysis is very sensitive to small changes in the relative magnitude and phase mismatch of the microphones, the use of dissimilar calibration functions for the intensity probe, differing only within the limits of measurement accuracy, could cause relatively large variations in the

calculated intensity level for one and the same measurement. Hence, to exclude such effects, a single calibration function is used when several measurements have to be compared with each other.

To ensure the quality of the measurements with the active system the back-to-back variation of the results was investigated by repeating an intensity measurement within a period of 24 hours. Figure 5.13 and 5.14 show the resulting transmission loss and power ratio curves for these back-to-back measurements using acoustic and point force broadband excitations in the frequency range from 0 to 1,6 kHz. The results are plotted as narrowband data using a frequency resolution of 1 Hz. As test structure, the double wall configuration with the fuselage and the first trim panel was used. The trim panel was attached to the fuselage frames via four passive shock mounts.

For the acoustic excitation the variations in the measurement results are considerably higher than for the forced vibration excitation. This can be explained by the fact that for the latter case the actual perturbation on the skin panel has a good coherence to the measured excitation power at the shaker mounting point as no spatial averaging is required to determine the excitation power. In contrast to that, the acoustic excitation power is obtained from a temporally and spatial averaged signal using the rotating microphone system in the reverberant chamber. Due to the spatial averaging the coherence between the measured sound power and the actual perturbation on the structure is not as good, resulting in a greater variation from one measurement to another. The frequency averaged difference between the two measurements is found to be 0,8 dB in the frequency range from 50 to 1600 Hz for the acoustic excitation, whereas the mean deviation in the same frequency range for the point force excitation is only 0,2 dB. Both deviations are acceptable for the evaluation of active control treatments. Nevertheless, to minimize possible errors and to guarantee the comparability of the results, the corresponding measurements with and without control for a specific test configuration will be carried out directly in succession.

As a dis- and reassembling of the test structure is not required, when carrying out the measurements for the different test configurations, variations due to possible changes in the installation of the test structure and the transmission loss window were not assessed.

5.3 Control Loop Implementation

A general block diagram of the control system is illustrated in Figure 5.15. The control algorithm is implemented in the programming language C on a laboratory *dSpace DS1005* controller board and represents an adaptive feedforward controller. The adaptive control system is realized with digital filters, which are driving the secondary system paths. The filters are adjusted by an adaptive algorithm according to given reference and error signals. To ensure a good controller performance, a narrowband control mode optimised for tonal primary perturbations and a broadband mode for random primary perturbations are available. The control mode and various parameters are selected by the user via a real-time monitoring software installed on a separate PC. This software is also used to monitor the DSP output and input signals as well as the control performance and stability.

In addition to the DSP hardware, the control loop incorporates digital low-pass filters to avoid aliasing effects and high-frequency excitation of the actuators (denoted by the blocks

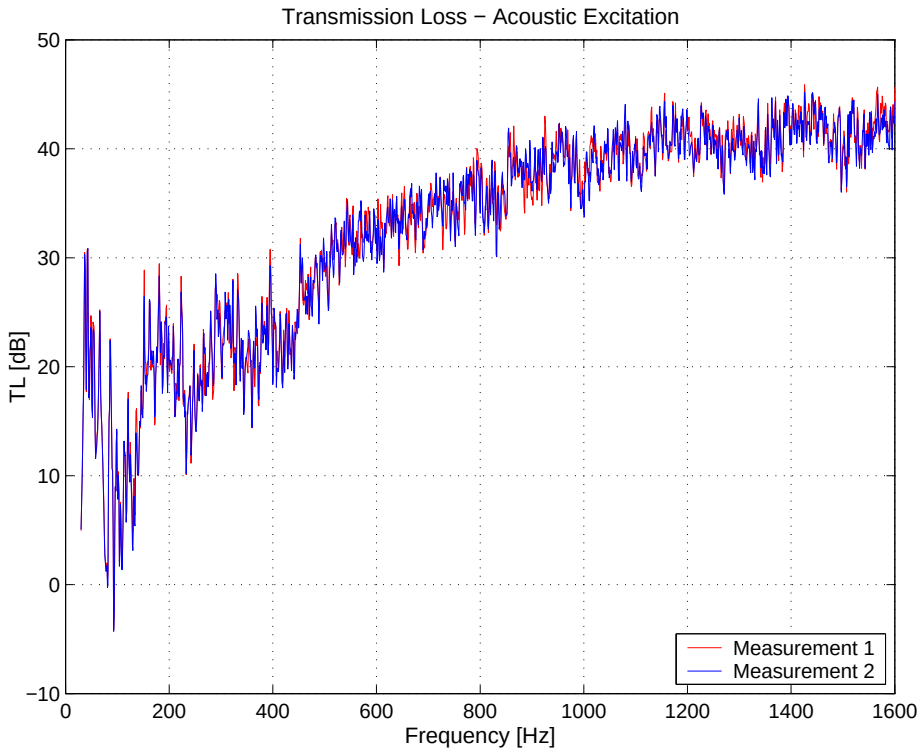

Figure 5.13: Transmission loss for back-to-back measurements

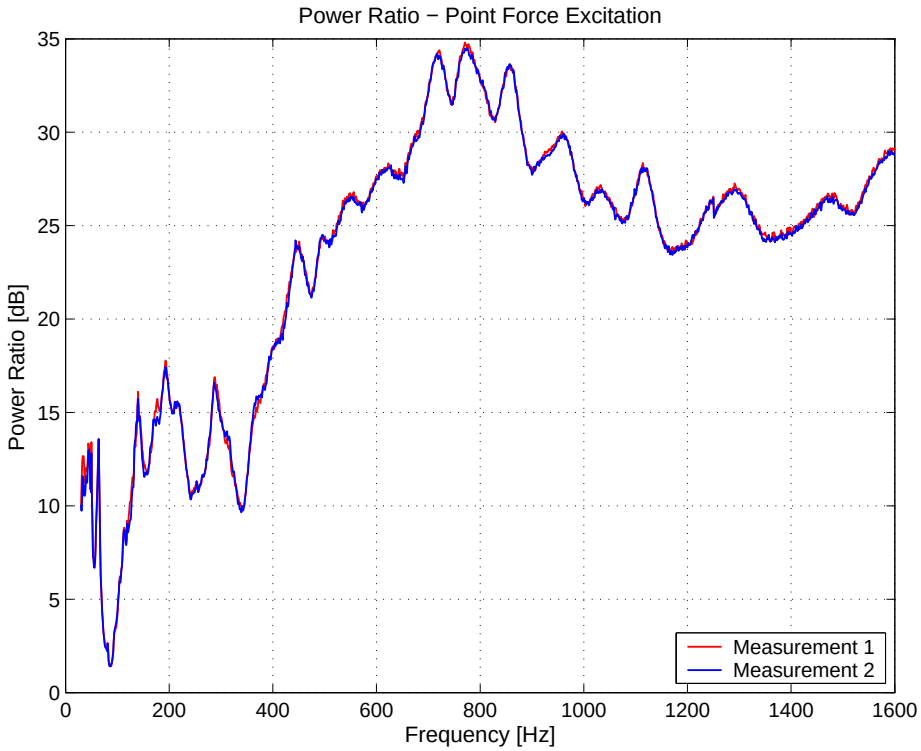

Figure 5.14: Power ratio for back-to-back measurements

termed AF and RF in Figure 5.15), power amplifiers for driving the actuators and a signal conditioning of the error signals. The matrix of transfer functions C' describes the complete dynamical behaviour of the actuators and sensors installed on the fuselage and the trim panel.

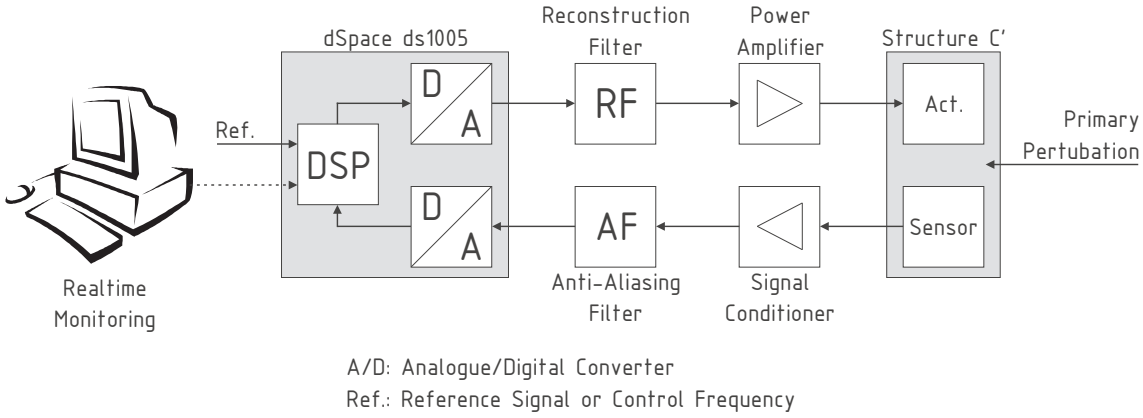

Figure 5.15: Block diagram of the control system

The control system is consisting of four active attachment elements resulting in a system with twelve independent actuators. Each attachment element is fitted with three acceleration sensors to provide an adequate error signal of the structure-borne noise transmitted at the trim-panel mounting points. Furthermore, to obtain some information correlated to the actual sound radiation, up to 13 additional acceleration sensors, attached directly to the internal face of the trim panel, are used in the control loop. The sensors are either of the type PCB M353B65 or M353B66. Their position is chosen on an ad-hoc basis without having knowledge of the acoustically significant structural modes of the trim panel. The relative x- and y-positions of these sensors are listed in Table 5.2, x and y denoting the horizontal and vertical axis in the plane of the trim panel. This configuration results in a fully coupled control system with twelve actuators and up to 25 error sensors. In contrast to the numerical simulations, the sensor arrangement on the trim panel has to be restricted to a single layout, as a more comprehensive study including different sensor layouts would be too time consuming to be carried out within the experimental investigation.

For the present application the adaptive feedforward control system is realized with a narrow-band filtered-X LMS algorithm for tonal excitations. Broadband control relies on a filtered-X LMS algorithm, where the filtering and adaptation algorithm is implemented in the frequency domain. The control algorithms are shortly recapitulated in the following four sections. A more comprehensive insight into adaptive signal processing and control of active systems is covered in the references [Elliott01a, Fuller96, Hansen97, Kuo96, Nelson92, Widrow85].

5.3.1 Adaptive Digital Filters

The time-continuous physical structure, abbreviated by the matrix of transfer functions C' in Figure 5.15, is controlled by using sampled and quantised system data. The sampling time is assumed to be T, resulting in a sampling frequency $1/T$. A continuous time signal $x(t)$ is thus sampled at discrete time steps $t = n \cdot T$ with n being an integer value. The discretized signal sampled at the time step n is denoted with $x(n)$.

Table 5.2: Position of error sensors on the trim panel, x- and y-position [mm]

Sensor	**Trim Panel 1**	**Trim Panel 2**
13	497, 790	840, 147
14	346, 645	804, 480
15	220, 535	854, 835
16	322, 330	672, 322
17	463, 185	691, 640
18	625, 329	490, 212
19	789, 481	500, 500
20	655, 620	531, 793
21	470, 487	350, 345
22	816, 286	377, 655
23	145, 810	150, 157
24	125, 294	220, 520
25	n/a	137, 834
Ref.*	500, 500	500, 500

* reference signal on fuselage skin for broadband control

The manipulation of such signals is done with digital filters. In causal, linear systems the filter's output signal $y(n)$ is affected by the current and all previous samples of the input signal $x(n)$. Hence, the output $y(n)$ may be written as:

$$y(n) = \sum_{i=0}^{\infty} h_i \cdot x(n-i) \ , \tag{5.19}$$

with h_i being the samples of the filter impulse response. The impulse response corresponds to the filter output when the input is equal to the Kronecker delta function[4].

A possibility to implement a digital filter in reality is to truncate the infinite summation after I samples, thus resulting in a finite calculation time for each output sample:

$$y(n) = \sum_{i=0}^{I-1} w_i \cdot x(n-i) \ . \tag{5.20}$$

These filters are known as finite impulse response (FIR) filters, because the impulse response will be zero after I samples. By making the coefficients w_i adaptive through a method that minimises a mean square error criterion, a given input signal $x(n)$ can be transformed into an output $y(n)$, representing a negative estimation of the external signal $d(n)$. The general structure of such an adaptive filter element is shown on the left side of Figure 5.16.

The measured error signal $e(n)$ can be expressed by the sum of the desired signal $d(n)$ and the reference signal $x(n)$ filtered by the adaptive FIR element:

$$e(n) = d(n) + y(n) = d(n) + \sum_{i=0}^{I-1} w_i(n) \cdot x(n-i) \ . \tag{5.21}$$

[4] $x(n) = \delta(n)$, which is equal to one if $n = 0$ and otherwise zero.

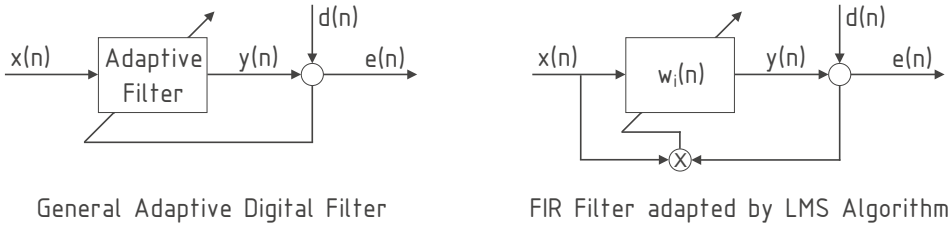

Figure 5.16: Adaptive digital filter and LMS adaptation

The objective of the adaptation algorithm is to determine the coefficients w_i in such a way to minimise a quadratic cost function J depending on the error signal $e(n)$:

$$J = E[e^2(n)] \rightarrow \ Min \ . \tag{5.22}$$

E is an abbreviation for the expectation operator, which, for stationary signals and by assuming that w_i, $i \in \{0, \ldots, I-1\}$ is time-invariant[5], is equal to the average mean square value of the error signal. The cost function represents a quadratic shaped surface possessing a global minimum. The exact solution of this minimisation problem, known as the Wiener solution, is found by differentiating J with respect to each filter coefficient and setting the derivatives to zero, $\partial J/\partial w_i = 0$.

In practice, the optimisation problem 5.22 is solved by adjusting the filter coefficients in an opposite direction proportional to the local gradient of the cost function J, thus moving the remaining error nearer towards the global minimum. The update rule for the new coefficients may be written as:

$$w_i(n+1) = w_i(n) - \mu \cdot \frac{\partial J(n)}{\partial w_i} \ , \tag{5.23}$$

with $i \in \{0, \ldots, I-1\}$ and $\partial J/\partial w_i = 2 \cdot E[x(n-i) \cdot e(n)]$. The term μ is a convergence factor. Instead of using this true gradient, the filter coefficients are updated every sample by an estimation of the gradient, which is equal to the derivative of the current error with respect to the filter coefficients:

$$\frac{\partial e^2(n)}{\partial w_i} = 2 \cdot e(n) \cdot \frac{\partial e(n)}{\partial w_i} = 2 \cdot x(n-i) \cdot e(n) \ . \tag{5.24}$$

Thus, the adaptation rule for the filter coefficients of the next data sample becomes:

$$w_i(n+1) = w_i(n) - \alpha \cdot x(n-i) \cdot e(n) \ . \tag{5.25}$$

This algorithm is known as the *least-mean-square* (LMS) algorithm (depicted on the right side of Figure 5.16) and converges for $0 < \alpha < 2/(I \cdot \overline{x^2})$, where $\overline{x^2}$ is the mean square value of $x(n)$ and $\alpha = 2 \cdot \mu$. For stationary signals the adaptation will automatically converge towards the optimal Wiener filter. Advantages of the LMS algorithm are that it is simple to implement, numerical robust and represents a fast approximation to the Wiener filter problem. Besides the LMS algorithm other adaptation rules like the Newton method or the recursive least-square algorithm are also used for adaptive filtering operations.

[5]The adaptive filter varies slowly in comparison to the dynamic response of the forward path.

5.3.2 Filtered-X LMS Algorithm

Figure 5.17 shows the block diagram of an active control application where the adaptive FIR filter is used to control the dynamic behaviour of the plant C. In this case, the filter output can be seen as a secondary signal (anti-noise) used to suppress a primary perturbation $d(n)$. Since there is the dynamic system C between the filter output and the estimation of the desired signal, the reference signal $x(n)$ used for the filter adaptation has to be modified by an additional filter in order to ensure the stability of the controller. This particularity also explains the name *filtered-X LMS algorithm*.

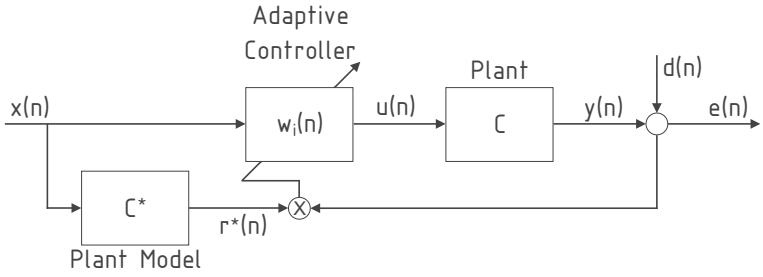

Figure 5.17: Block diagram of the filtered-X LMS algorithm

With the assumption that the plant C may be described by an FIR filter of the order M, the error signal is expressed as:

$$e(n) = d(n) + y(n) = d(n) + \sum_{j=0}^{M-1} c_j \sum_{i=0}^{I-1} w_i(n-j) \cdot x(n-j-i) \ . \tag{5.26}$$

The filter is adapted in the opposite direction to the gradient of the current square error signal with respect to the filter coefficients, which are assumed to be nearly time-invariant:

$$\frac{\partial e^2(n)}{\partial w_i} = 2 \cdot e(n) \cdot \frac{\partial e(n)}{\partial w_i} = 2 \cdot e(n) \cdot \sum_{j=0}^{M-1} c_j \cdot x(n-j-i) \ , \tag{5.27}$$

where $i \in \{0, \ldots, I-1\}$. From equation 5.27 it can be seen that, in comparison to the unmodified LMS-algorithm presented in the previous chapter, the reference signal $x(n)$ is filtered by the system behaviour C. Therefore, the adaptation rule for the filtered-X LMS algorithm reads as follows:

$$w_i(n+1) = w_i(n) - \alpha \cdot r^*(n-i) \cdot e(n) \ , \tag{5.28}$$

with $r^*(n-i) = \sum_{j=0}^{M-1} c_j^* \cdot x(n-j-i)$ being the filtered-reference signal $x(n)$ used for the filter update. In practice, an estimate C^* of the plant impulse response is used as an internal model for the filter operation. This plant model must include the entire dynamical behaviour between the output of the controller and the input, where the residual error signal is measured. Adaptive filter methods can be used to represent the real plant response. Basically, differences between the estimation and the true plant response will negatively affect the stability and convergence rate of the controller, but it has been shown in literature that the algorithm is quite robust to errors in the plant model.

Since the filtered-X LMS algorithm necessitates two filter operations, the computational complexity is increased in comparison to the unfiltered algorithm. For this reason an efficient implementation of the control law is required and, depending on the type of application, the algorithm is optimised either for tonal or stochastic perturbations.

5.3.3 Multichannel Narrowband Filtered-X LMS Algorithm

It is assumed that the primary perturbation is tonal and of angular frequency ω. Control is achieved by driving the secondary control signals with the same frequency and an amplitude and phase adjusted to minimise the perturbation. The block diagram in Figure 5.18 shows an interpretation of the adaptive feedforward system in terms of an equivalent feedback controller.

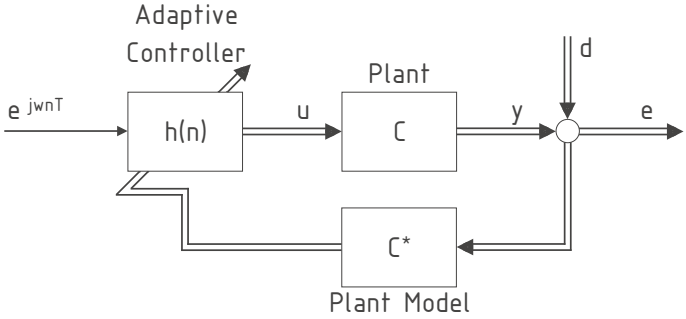

Figure 5.18: Block diagram of the multiple error LMS algorithm operated at the frequency ω

In the frequency domain L individual disturbance signals and M secondary control signals are described by the complex vectors $d(j\omega)$ and $u(j\omega)$. The $L \times M$, time-invariant plant responses are grouped together in a complex matrix $C(j\omega)$. The vector $e(j\omega)$ containing the L residual error signals can thus be written as:

$$e(j\omega) = d(j\omega) + C \cdot u(j\omega) \ . \tag{5.29}$$

For the prevention of large control efforts, a simple modification is made to the cost function J by including a component of the mean squared control signal u proportional to the positive weighting parameter β. Hence, the cost function becomes:

$$J = e^H(j\omega) \cdot e(j\omega) + \beta \cdot u^H(j\omega) \cdot u(j\omega) \rightarrow \ Min \ , \tag{5.30}$$

where e^H and u^H denote the Hermitian transpose of e and u. J is a quadratic function with respect to the control signal u and thus has a minimum, which can be determined by setting the derivative of J with respect to u to zero:

$$\frac{\partial J}{\partial u} = 2 \cdot C^H \cdot e(j\omega) + 2 \cdot \beta \cdot u(j\omega) = 0 \ . \tag{5.31}$$

The optimal control signal u_{opt} for the steady state response is obtained as:

$$u_{opt}(j\omega) = -(\beta + C^H \cdot C)^{-1} \cdot C^H \cdot d(j\omega) \ . \tag{5.32}$$

This optimal solution can be approximated with the filtered-X LMS algorithm. Instead of using the frequency transformation, the complex signals are modulated by the adaptive filter with the term $e^{j\omega nT}$. This modulation factor replaces the external reference signal $x(n)$ shown in Figure 5.17 and is generated by the controller itself or synthesised from an adequate reference signal. Hence, the resulting control signal and the adaptation rule for the update of the filter coefficient vector h can be expressed by following two expressions:

$$u(n) = \Re\left(h(n) \cdot e^{j\omega nT}\right) \ , \tag{5.33}$$

$$h(n+1) = (1 - \alpha \cdot \beta) \cdot h(n) - \alpha \cdot C^{*H} \cdot e(n) \cdot e^{j\omega nT} \ , \tag{5.34}$$

where the matrix C^* represents an estimation of the plant impulse responses. As the controller is reducing the primary disturbance in a narrow band around the control frequency, the algorithm is also known as adaptive notch filter. The bandwidth and convergence rate of control depend directly on the parameter α. An augmentation of α will increase the bandwidth and reduce the iteration time needed to determine the optimal filter coefficients. The effort weighting parameter β governs the control reduction. With smaller values of β a greater reduction of the error signal will be achieved at the expense of a larger control effort [Maier00]. Thus, β always represents a compromise between optimal control performance and minimal control effort.

Multiple tonal disturbances can be controlled by several controllers working in parallel. If a sufficient distance between the disturbance frequencies in comparison to the bandwidth of control is ensured, the single algorithms do barely interfere with one another.

For the current ASAC application it can be assumed that the plant response is nearly time-invariant. Therefore, prior to closing the control loop, the plant identification is made without external perturbations for every system path. This off-line system identification is realized with an FIR filter model, which is adapted by a filtered-X LMS algorithm using the real plant response as desired signal $d(n)$.

5.3.4 Multichannel Broadband Filtered-X LMS Algorithm

The multiple error filtered-X LMS algorithm for control of broadband noise requires reference signals having a good correlation with the original disturbance. It is assumed that a number of K reference signals, described by the vector $x(n)$, are available in the forward path. For the adaptation algorithm each reference signal is filtered by the $L \times M$ paths of the plant response resulting in a set of LMK filtered-reference signals for the controller update (M and L being the number of actuators and error sensors). Each FIR filter of the adaptive controller is supposed to have I coefficients. A block diagram of the control system is shown in Figure 5.19.

The output from the L error sensors is expressed in the error signal vector $e(n)$ as superposition from the primary and secondary path:

$$e(n) = d(n) + R(n) \cdot w(n) \ , \tag{5.35}$$

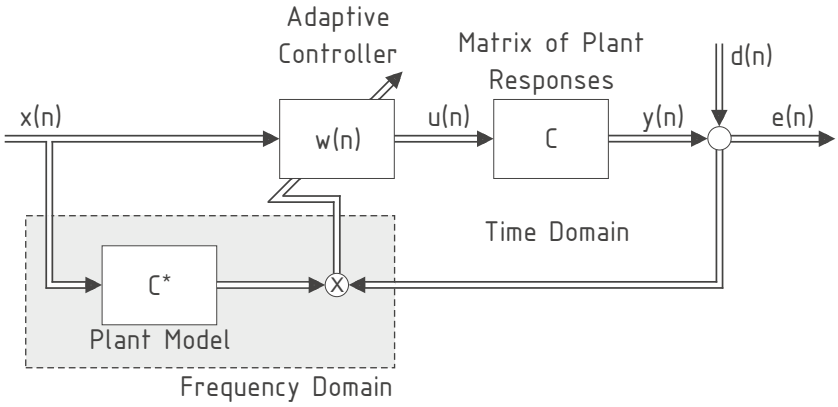

Figure 5.19: Block diagram of the multichannel filtered-X LMS algorithm used for broadband applications

where $w(n)$ is a vector containing the coefficients from MKI FIR filters, $R(n)$ a $L \times MKI$ matrix containing the filtered-reference signal and $d(n)$ a vector of L primary perturbations [Elliott01a].

The LMS algorithm will minimise a cost function J given by the sum of squared error signals and a term proportional to the sum of squared controller coefficients. The controller coefficients are included in the cost function to improve the controller stability with respect to inaccuracies in the plant model C^*:

$$J(n) = e(n)^T \cdot e(n) + \beta \cdot w^T(n) \cdot w(n) \ . \tag{5.36}$$

β is a positive weighting parameter of the controller coefficients. The gradient vector of the cost function with respect to the filter coefficients becomes:

$$\frac{\partial J}{\partial w(n)} = 2 \cdot \left(R^T(n) \cdot e(n) + \beta \cdot w(n) \right) \ , \tag{5.37}$$

and is used in the adaptation algorithm of the control filters, which can be expressed as:

$$w(n+1) = \gamma \cdot w(n) - \alpha \cdot R^{*T}(n) \cdot e(n) \ , \tag{5.38}$$

with α being the convergence rate of the filter adaptation and a leakage factor γ defined as $\gamma = 1 - \alpha \cdot \beta$. The matrix R^* contains the reference signals filtered by an estimation C^* of the true plant response C.

For the present ASAC application the filtering operation of the reference signal and the filter update as defined in equation 5.38 are realized in the frequency domain. The adaptation algorithm for the filter coefficients at the κ-th discrete frequency and for the m-th iteration can be written as:

$$w_{m+1}(\kappa) = \gamma \cdot w_m(\kappa) - \alpha \cdot \left\{ C^{*H}(\kappa) \cdot e_m(\kappa) \cdot x_m^H(\kappa) \right\}_+ \ , \tag{5.39}$$

where the notation $\{\ \}_+$ indicates that for the frequency transformation of the quantities inside the brackets only causal parts are taken into account. The FIR control filters are still implemented in the time domain.

The motivation to transfer the reference filtering and adaptation into the frequency domain is due to the fact that the computational effort is reduced in comparison to a time domain based solution. The computational benefit can either be used to increase the number of degrees of freedom in the ASAC system or the sampling rate might be increased to control primary perturbations at higher frequencies. Furthermore, the reaction time of the controller is reduced and it is possible to restrict control to a certain frequency range.

In the current application a single reference signal, obtained with an acceleration sensor placed at the centre of the fuselage skin, is used (referred as *Ref.* in Table 5.2). As both the reference and error signals are accelerations and the radiated sound power of a vibrating structure is proportional to its squared mean velocity, both the reference and error signal are integrated with respect to time. Thus, the weighting of the control effort at different frequencies is more adapted to the human hearing perception and not distorted by the factor $\omega = 2\pi f$ with regard to the velocity.

5.4 Experimental Results

The ASAC technique with active attachment elements was tested against several acoustic and structural perturbations. For both types of excitation various tonal and band-filtered random signals were used. The tonal excitation represents a temporally and spatially coherent noise source and is similar to the buzz-saw noise excitation in real aircraft, whereas the characteristic of a random noise source, exhibiting no temporal coherence (and also no spatial coherence when using the acoustic excitation), resembles more to a jet noise or turbulent boundary layer noise excitation.

As a real excitation spectrum was not available for the experimental study, the choice of perturbation frequencies is based upon the general transmission loss and power ratio performance measured with built-in active attachment elements, but with no control applied to the ASAC system. By selecting perturbation frequencies or frequency ranges corresponding to local minima in transmission loss and power ratio, the worst case for sound transmission and thereby for the acoustic passenger comfort is assumed.

Figures 5.20 and 5.21 show the resulting narrowband transmission loss and power ratio behaviour for the acoustic and point force excitation, which were determined in preliminary tests by using a white noise excitation in the frequency band ranging from 0 to 1,6 kHz. These results apply for the double wall partition in combination with the first trim panel configuration. In both diagrams, the black and grey curves correspond to the respective configurations with passive shock mounts and active attachments used as connection elements between the fuselage and the trim panel.

For both types of perturbation, the different dynamic properties of the active attachment elements and the shock mounts lead to a dissimilar sound transmission behaviour. In the frequency ranges from 300 to 400 Hz and above 1 kHz a substantial reduction in sound transmission is already achieved with the active attachment elements employed in a purely passive manner. Only around 200 Hz the performance of the system with active attachment elements is worse than the configuration with shock mounts. At around 80 Hz the first strong coupling between the cavity fluid and the structure occurs and a 1,1-mode with a high radiation efficiency is excited on the trim panel, resulting in the global minima for transmission loss and

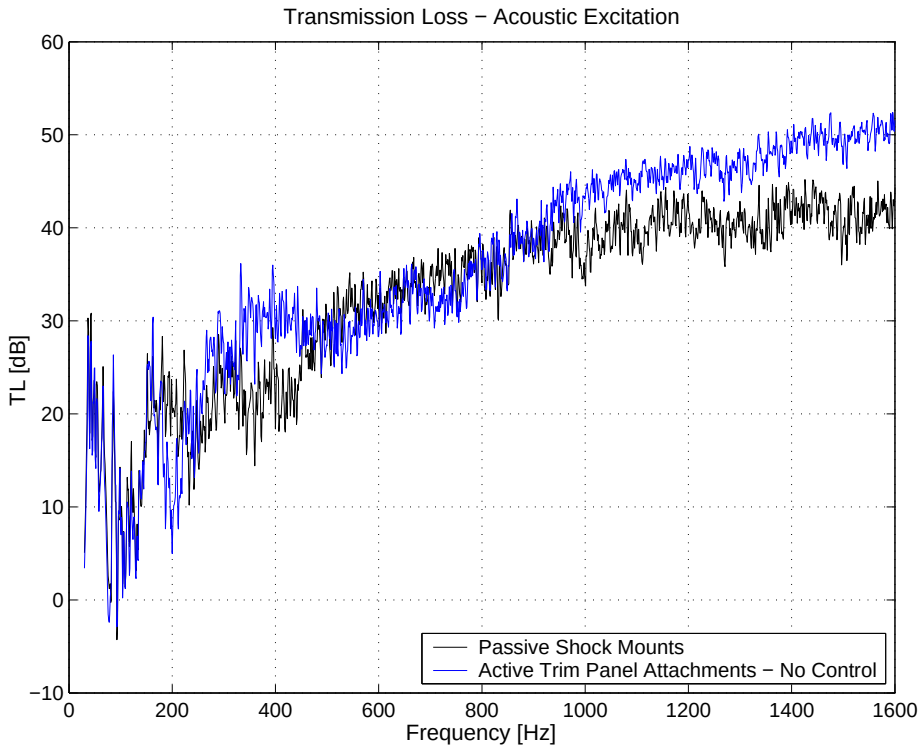

Figure 5.20: Transmission loss of the passive system

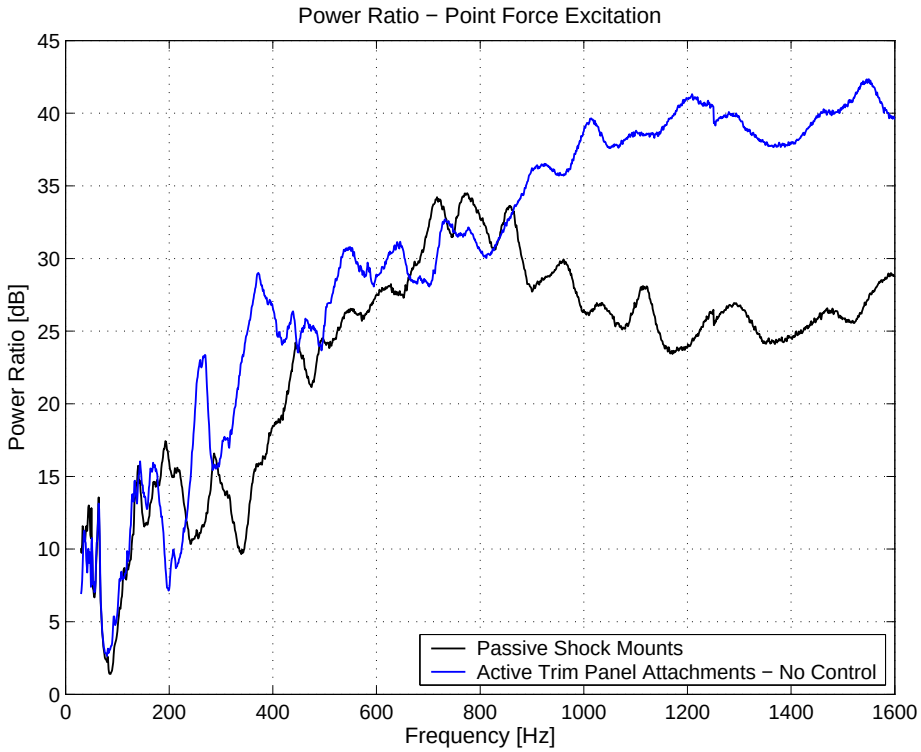

Figure 5.21: Power ratio of the passive system

power ratio, respectively. In this range of frequency the transmission loss values are partially negative, because the acoustic excitation power is underestimated by applying the diffuse field assumption (equations 5.12 and 5.13), which is not fulfilled at low frequencies. In the high-frequency range above 800 Hz, the passive sound reduction is higher than 30 dB and the sharp dips in the transmission loss or power ratio curves, due to a resonant sound transmission, are far less pronounced than at lower frequencies.

5.4.1 Test Configuration

As the active technology is mainly aimed at enhancing the sound reduction in the frequency range up to 500 Hz, the frequencies selected for a control of tonal acoustic perturbations are 78, 200, 326 and 530 Hz. Each frequency is corresponding to a local TL minima and is selected upon the passive transmission loss behaviour in Figure 5.20. For broadband excitation with random noise a frequency band corresponding to the 80 Hz third octave band (ranging from 71 to 90 Hz) is chosen for a first test of the broadband LMS algorithm. In a second test a simultaneous random excitation in the 80 and 200 Hz third octave band (ranging from 71 to 90 Hz and 178 to 225 Hz, respectively) will be used.

The tonal perturbation frequencies for the point force excitation are 80, 199, 284 and 702 Hz, each one corresponding to a frequency with high sound transmission according to Figure 5.21. A random broadband excitation is also tested for the 80 Hz third octave band. In addition to those tests, the double wall configuration in combination with the second trim panel (see Chapter 5.2.1) is tested against an artificially generated, acoustic buzz-saw noise excitation. The fundamental frequency of this signal is 80 Hz and includes harmonics up to 3,2 kHz. The first twelve frequencies will be controlled with the narrowband filtered-X LMS algorithm. The resulting test matrix for the active structural acoustic control system is summarized in Table 5.3.

Table 5.3: ASAC test matrix

Excitation	**Frequency**	**Structure**
Tonal acoustic:	78, 200, 326, 530 Hz	Trim panel 1
Random acoustic:	80 Hz, 80 & 200 Hz third oct. band	Trim panel 1
Tonal point force:	80, 199, 284, 702 Hz	Trim panel 1
Random point force:	80 Hz third octave band	Trim panel 1
Art. buzz-saw noise:	80 Hz and harmonics	Trim panel 2

5.4.2 Results with Acoustic Excitation

The main results obtained with the ASAC control system for tonal acoustic excitations are summarized in Table 5.4 and are given in terms of total sound power radiated by the trim panel and mean sound pressure level in the excitation chamber for the tests with and without control respectively. The spectral data is expressed in magnitude values using a 1 Hz frequency resolution and the actuator voltage is defined as the ratio between the actual maximum peak

actuator voltage measured during control and the absolute maximum voltage, which can be applied to the Thunder elements (240 V_{Peak}). Further details in terms of spectra for the radiated sound power, excitation sound pressure level and corresponding intensity plots are listed in Annex C.

Table 5.4: Measurement results for tonal acoustic excitation

	Radiated Sound Power [dB]		**Excitation SPL [dB]**		**Voltage**
Freq.	control off	control on	control off	control on	[%]
78 Hz	91,7	69,4	97,5	97,4	48,8
200 Hz	87,1	73,1	97,4	99,5	n/a
326 Hz	73,5	62,4	99,6	99,7	5,3
530 Hz	77,8	65,8	109,4	109,3	18,8

From analyzing the values given in Table 5.4, it can be seen that by controlling the dynamic behaviour of the trim panel with the active attachment elements a substantial reduction in the total radiated sound power can be achieved over a large band of frequencies. For example at 78 Hz the measured reduction in radiated sound power is 22,3 dB. At 200 Hz the sound power attenuation is equal to 16,1 dB, whereas for 326 and 530 Hz the decrease in radiated sound power amounts to around 11 dB. Stability problems with the control system were not encountered during the measurements and spill-over effects (unintentional excitation of higher harmonic frequencies [Fuller96, Hansen97]) did not appear with tonal primary excitations (see respective spectra given in Annex C). The sound pressure level in the excitation room is ranging from around 97 dB for the 78 Hz excitation to about 109 dB at 530 Hz. The maximum actuator workload occurs at the first eigenfrequency of the system at 78 Hz. This eigenfrequency is characterized by a strong coupling between the structure and the enclosed fluid domain. At this frequency the tonal sound pressure level in the excitation room of around 97 dB corresponds to an actuator workload of around 50%. At higher frequencies the actuator workload is reduced to a great extent, for instance to less than 20% at 530 Hz.

To explain the general operating mode of the ASAC control system, the results achieved with the 78 Hz tonal excitation are analyzed in more detail within the following section. The sound pressure level in the excitation room is illustrated in Figure 5.22. Rather than using a simple sinusoidal primary perturbation signal, a triangle pulse having a fundamental frequency of 78 Hz is superimposed with a band-filtered white noise signal. For both measurements with and without active control a nearly identical excitation spectrum is used. The excitation sound pressure level at 78 Hz is 97 dB, whereas for the harmonics at 156, 234, 312 and 390 Hz the sound pressure levels are 105, 94, 92 and 90 dB respectively.

The ASAC narrowband control tests are carried out with a system sampling rate of 5 kHz. The structural response of the trim panel is controlled on the first five harmonic frequencies of the triangle pulse with the multichannel narrowband filtered-X LMS algorithm. After identification of the plant model C^*, various control parameter such as the convergence factor α and the effort weighting parameter β are adjusted to obtain a good control performance in combination with a reasonable control effort while maintaining the system's stability. The input signal from the error sensors as well as the actuator commands are filtered by an adjustable low-pass

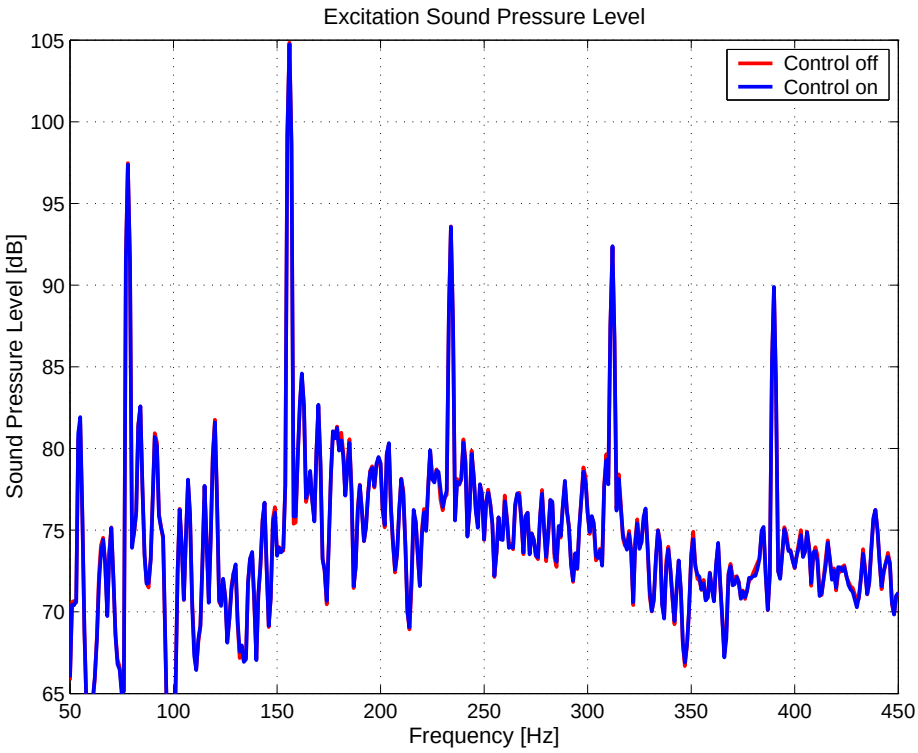

Figure 5.22: Excitation sound pressure level

filter having a cut-off frequency of 900 Hz in this case. As the filtered error signal is further modulated with the term $e^{j\omega nT}$ for each frequency that is controlled, a harmonic actuator command is derived by the LMS algorithm. A tenth second sample of the actuator voltage is shown in Figure 5.23. The signal is dominated by the fundamental frequency of 78 Hz and the maximum voltage with a magnitude of around 117 V_{Peak} is applied to the third and ninth actuator unit. On each attachment element the respective actuator units are not excited completely in phase, indicating that combinations of both translatory and rotational displacements are induced in the trim panel. This behaviour is similar to the one predicted with the simulation model in Chapter 4.

The secondary signals induced by the actuators into the trim panel lead to a reduction of the vibration levels, which are measured by the respective error sensors. This relationship is illustrated in Figure 5.24, showing the time dependency of the sensor signals 6 and 21 for a period of five seconds and one tenth of a second with and without control respectively. Sensor 6 is mounted on the second attachment element, whereas sensor 21 is located at the centre of the trim panel. On both sensor positions the vibration level is reduced with active control. On sensor 21 the magnitude is decreased by more than 50%, whereas on sensor 6 mounted at one of the trim panel attachment elements, only a small reduction is achieved.

Using all available error sensor data, the obtained overall control reduction is represented by the two spectra plotted in Figure 5.25. The figure on the left side represents the squared sum of the twelve error signals located directly on the trim panel, whereas on the right-hand side the equivalent quantity for the twelve error sensors mounted on the attachment elements is reproduced. On the first four harmonics, reductions ranging between 6 and 17 dB are obtained

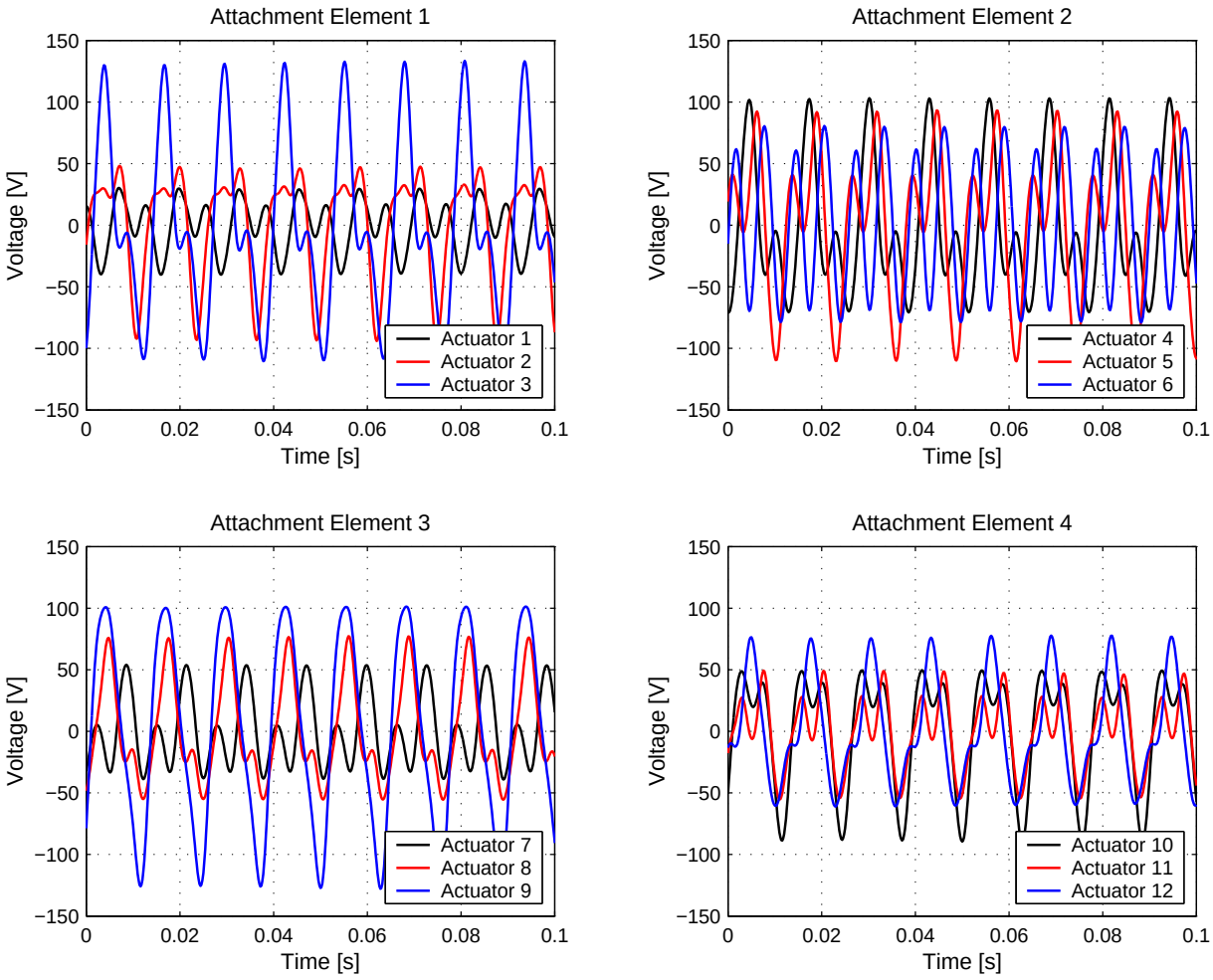

Figure 5.23: Actuator voltage

on the trim panel sensors. At 390 Hz the error signal is only slightly decreased by 2 dB. In the frequency range of 220 Hz, which is not controlled, an increase of around 7 dB is noticed. This is probably due to nonlinearities in the actuator response. The general behaviour of the overall control reduction measured on the attachment elements is similar to the one detected on the trim panel. However, at the fundamental frequency of 78 Hz, the error level obtained without control is approximately 8 dB smaller than the one on the trim panel, which is due to the global 1,1-mode excited on the trim panel. On the remaining harmonics both vibration levels on the panel and on the attachment elements are of the same order of magnitude, yet the achieved control reduction on the AAE is smaller in comparison to the one on the trim panel and is ranging from 3 to around 7 dB. In the 220 Hz band the error signal is also increased.

These results demonstrate the effectiveness of the active attachment elements as structural actuators in combination with an LMS control loop and the available sensor array. The local vibration levels measured at the sensor positions are attenuated over a large range of frequencies. However, the acoustic success of the control system depends furthermore on the correlation of the acceleration signals measured on the trim panel with the actual, radiated sound power.

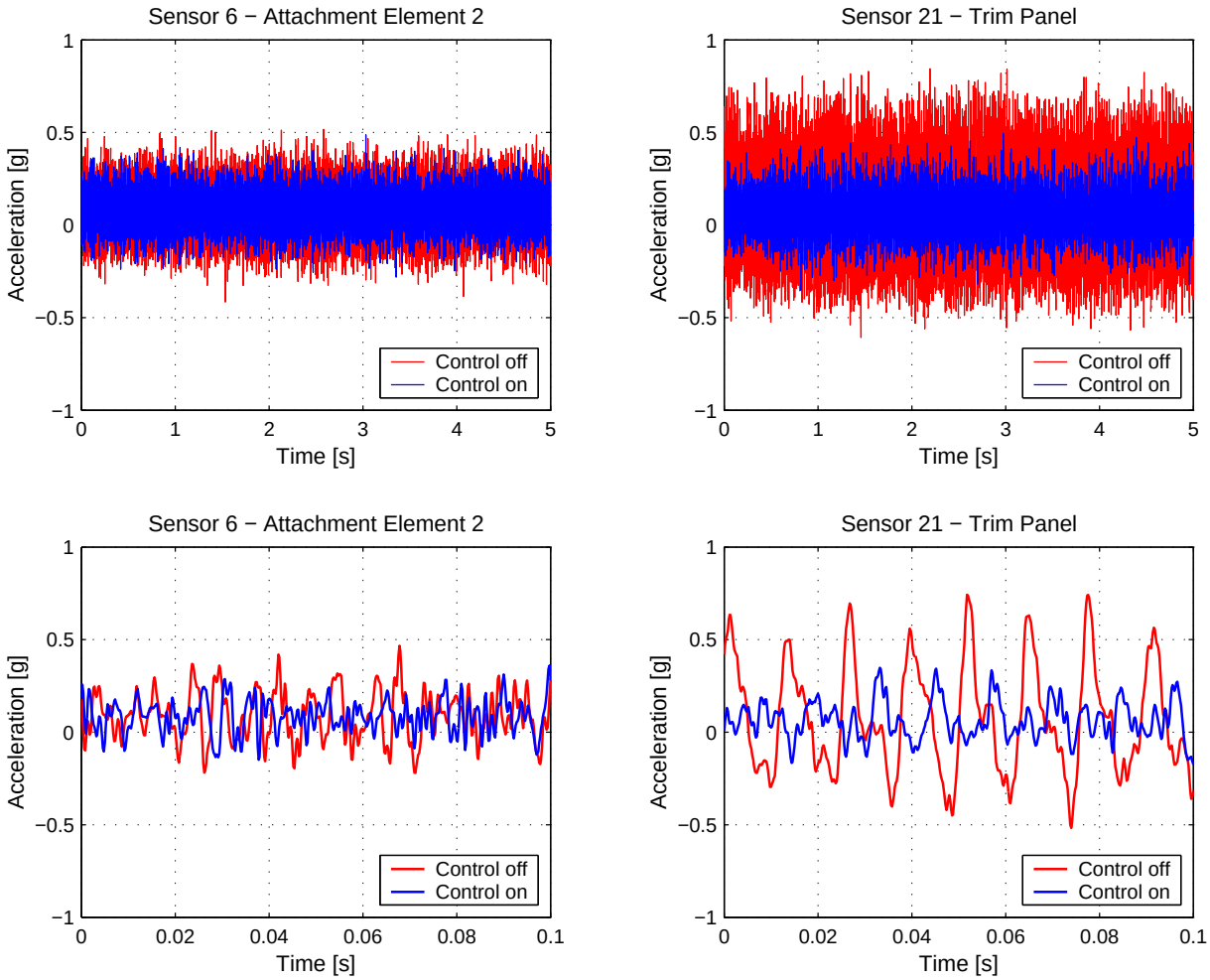

Figure 5.24: Acceleration measured by error sensors 6 and 21, with and without control

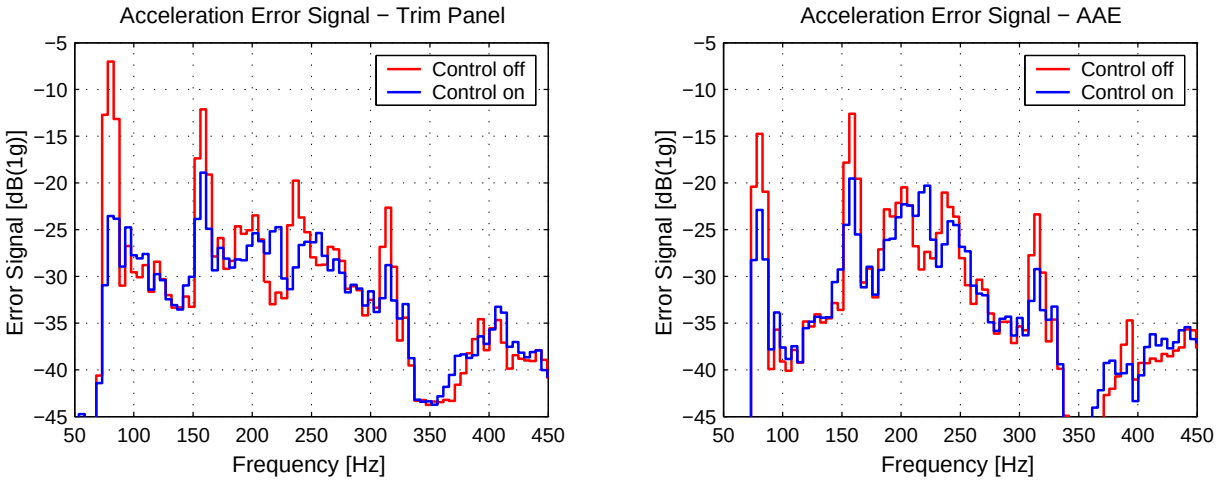

Figure 5.25: Squared sum of error signals on trim panel and attachment elements

The global sound power radiated from the trim panel into the anechoic chamber, resulting from the different structural behaviour with and without control as described above, is represented in Figure 5.26.

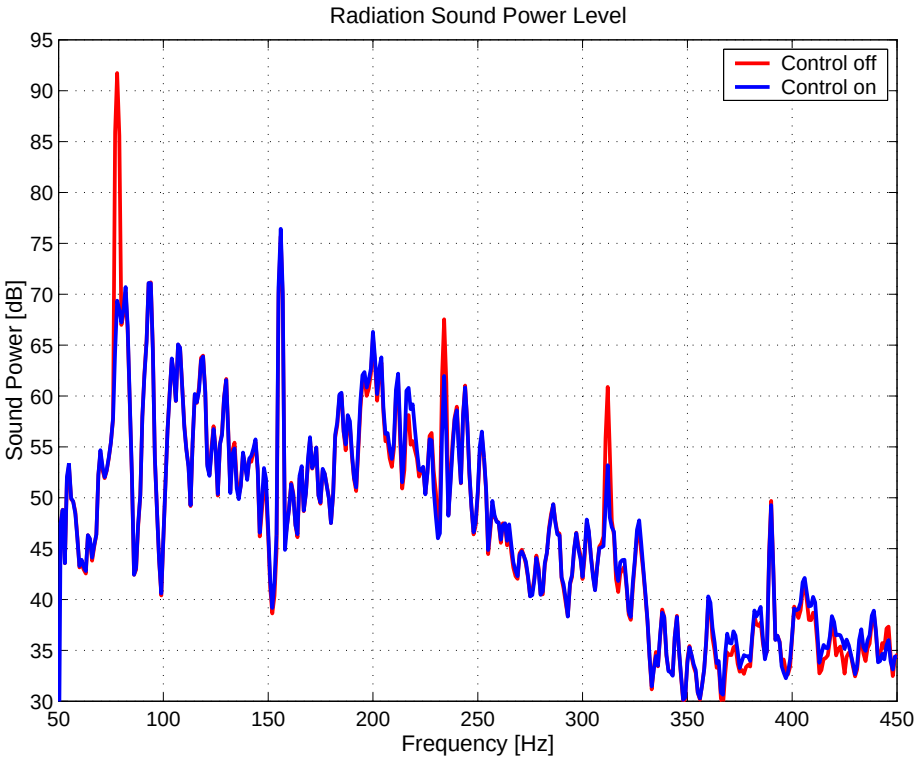

Figure 5.26: Radiation sound power level

On the fundamental frequency of 78 Hz the radiated sound power is well correlated with the error signal and is thus attenuated by the active control from 91,7 to 69,4 dB corresponding to a reduction of around 22 dB or 99,4% expressed on a linear scale. On the third and fourth harmonic a reduction of about 5,6 and 7,7 dB is achieved, whereas on the harmonics at 156 and 390 Hz no attenuation of radiated sound power is attained. The sound power remains at a constant level despite the obtained control reduction on the attachment elements and the trim panel. Probably the sensor arrangement on the trim panel is not sufficiently correlated to the sound radiation for those particular perturbation frequencies. It is difficult to explain this lack of performance in more detail as the global structural behaviour of the trim panel is not available from the experimental database. A possible explanation might be given by one of the following two suppositions:

- Although the vibration level at the sensors is reduced locally, the global vibration level of the panel is increased. Usually this goes along with an increase in sound radition.

- The global vibration energy on the trim panel is reduced by the active control. Yet, additional modes with higher radiation efficiencies than without control are excited by the controller, resulting in a similar or even greater sound radiation than without control. This is, for example, the case when it is attempted to control perturbations at frequencies

well below the critical frequency, which already exhibit a high passive transmission loss, as for instance at 156 Hz (TL 25,2 dB, compare with Figure 5.20) or 390 Hz (TL 31,6 dB).

Nevertheless, judging from the structural results on the sensors and the actuator effectiveness at those perturbation frequencies, it is expected that the radiation behaviour could certainly be ameliorated by using a more appropriate sensor layout having a better correlation to the sound power radiated by the trim panel.

The sound radiation on the remaining, uncontrolled frequency bands is not affected by the active control system, except for an increase of around 2 dB in the frequency range of 220 Hz, which was also noticed for the error signal.

The local sound intensity map for the fundamental perturbation frequency of 78 Hz is shown in Figure 5.27 for the 80 Hz third octave band with and without control. Without control a global 1,1-mode with a corresponding sound intensity pattern is excited on the trim panel. The maximum intensity is reached in the middle of the measurement grid with around 92 dB. With active control the radiation mode is still dominated by the 1,1-mode on the panel, but the influence of higher modes in the response is increased. While controlling the structural vibrations, the intensity is attenuated on every measurement point and the local intensity maximum is consequently reduced to 76 dB. The mechanism associated with this type of control is active damping as the modal participation of the 1,1-mode in the structural response to the primary perturbation is reduced for the most part.

For higher frequencies the sound radiation behaviour is more complex as, in general, besides the global attenuation in sound intensity, the radiation pattern is also changed due to the control as can be seen for instance from further intensity plots listed in Annex C. This indicates that with the closed control loop additional modes are excited on the trim panel and the control mechanism is also governed by a modal restructuring occurring alongside the modal damping mechanism.

The results obtained with the control of acoustic broadband perturbations are listed in Table 5.5. Numerical values are specified in the respective third octave bands. The DSP sampling rate is reduced to 1,4 kHz to take into account the increased computational costs of the broadband filtered-X LMS algorithm. An additional acceleration sensor, denoted as *Ref.* in Table 5.2, is placed on the fuselage skin and used as a reference signal for the filter adaptation. The controlled frequency domain ranges from 65 to 100 Hz for the excitation in the 80 Hz third octave band and from 65 to 400 Hz for the combined primary perturbations in the 80 and 200 Hz band.

Table 5.5: Measurement results for random acoustic excitation

	Radiated Sound Power [dB]		**Excitation SPL [dB]**		**Voltage**
Freq.	control off	control on	control off	control on	[%]
80 Hz band	86,5	76,1	100,5	100,5	55,8
80 & 200 Hz band*	86,1	81,1	100,0	100,1	57,4
80 & 200 Hz band**	85,0	78,0	105,2	105,3	57,4

* 80 Hz band results; ** 200 Hz band results

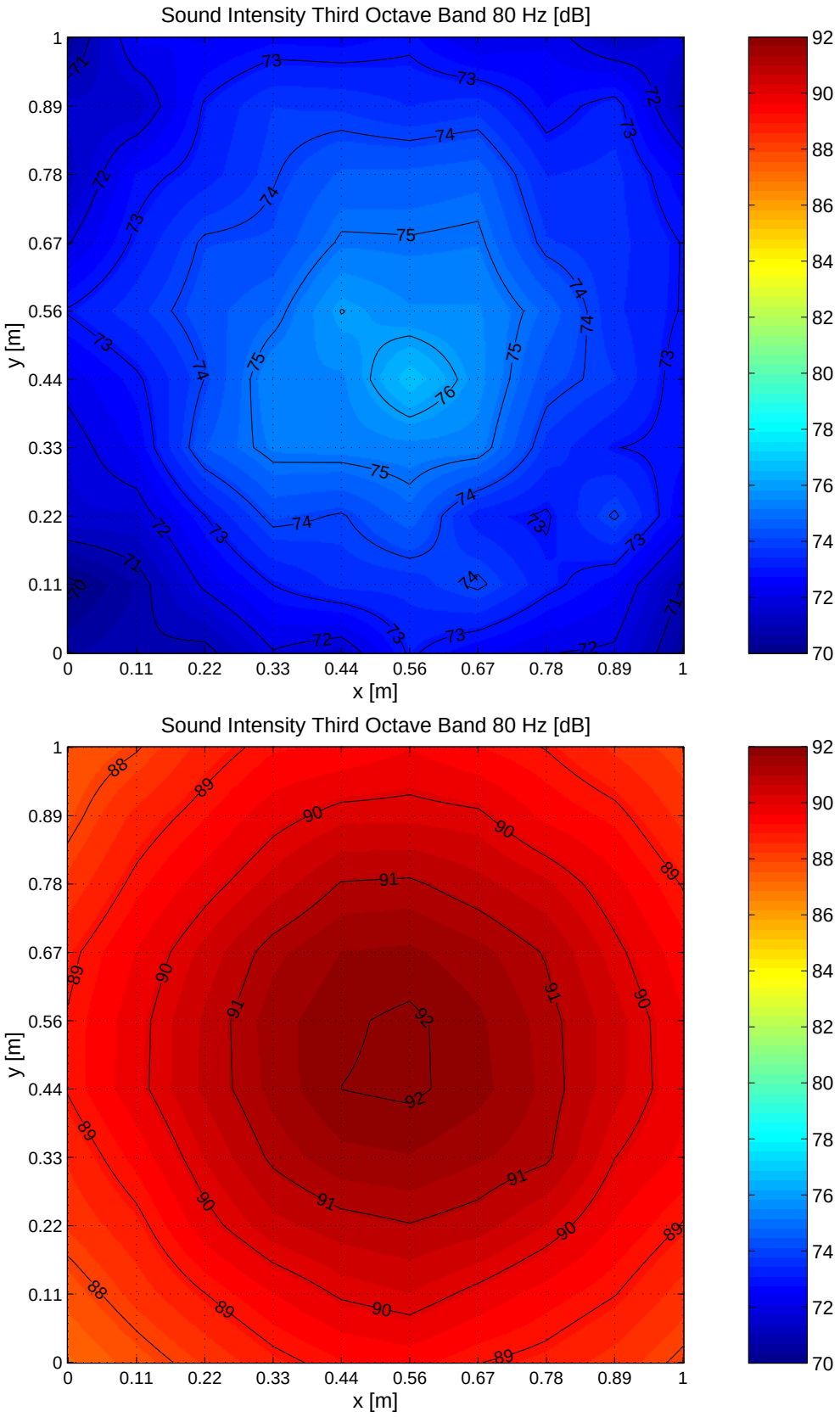

Figure 5.27: Sound intensity level with (above) and without (below) ASAC control

In contrast to the results achieved with tonal control, minor attenuations in radiated sound power are obtained. This is mainly due to the stochastic character of the primary signal, which makes the active control more difficult. Nevertheless, for the excitation in the 80 Hz third octave band a reduction of 10,4 dB in radiated sound power is still achieved, whereas for the simultaneous random excitation in the 80 Hz and 200 Hz third octave band a decrease of 5,1 and 7,0 dB respectively is attained. The corresponding sound pressure levels measured in the excitation room are about 100 dB for the 80 Hz third octave band, whereas in the 200 Hz band the SPL is around 105 dB. Detailed narrowband results are also listed in Annex C.

In principle the broadband filtered-X LMS algorithm works in a similar manner as already explained for the tonal control loop. The velocity error signals are reduced in the controlled frequency range as shown in Figure C.18 and C.19 for the combined 80 and 200 Hz band excitation. As the error signals have a good correlation to the radiated sound power for the controlled frequency range, the sound intensity in front of the trim panel is as well globally attenuated, as indicated by the local intensity distributions shown in Figure C.16 and C.17.

Similar to the tonal excitations, the actuator voltage is dominated by the system response in the 80 Hz third octave band. In this case a relative actuator workload of 56% (80 Hz third octave band excitation) and 58% (simultaneous 80 and 200 Hz third octave band excitation) is resulting. An exemplary sample of the actuator excitation is given in Figure C.20 for the simultaneous excitation in both frequency bands. The actuators of each attachment element are driven mainly in phase, which is also noticed for the 80 Hz third octave band excitation. At those specific frequencies and probably without an important loss in performance, the control system could also be operated with simplified attachment elements, generating only pure translatory displacements. However, this would also limit the control performance at higher perturbation frequencies.

Typical for broadband control is the fact that energy is shifted to frequency bands having a lower energy content within the controlled frequency range. In particular this so-called waterbed effect is observed for the random excitation in the 80 and 200 Hz third octave band (see Figure C.14), where the sound radiation is increased in the 315 Hz third octave band and a reduction is achieved in the 400 Hz band. In both test cases increased sound radiation is also noticed in uncontrolled frequency bands. For instance, while controlling the excitation in the 80 Hz third octave band, sound power is amplified in the 200 Hz third octave band from 29 to 38 dB and in the 250 Hz band from 24 to 47 dB (Figure C.11). This effect has not been investigated in detail but may be explained by nonlinearities of the actuators. Anyway, the levels are still well below the mean sound power level of 76,1 dB measured in the controlled 80 Hz band. For the configuration with a combined 80 and 200 Hz third octave band excitation this effect is less distinctive, but still present. An increase in sound radiation from 22 to 32 dB can be observed with the closed control loop in the 500 Hz band, compared to levels in the controlled 80 and 200 Hz third octave bands of 81,1 dB and 78,0 dB respectively.

5.4.3 Results with Point Force Excitation

The general results obtained with the ASAC control of point force perturbations are listed in Table 5.6 and 5.7. The values are given in terms of total radiated sound power and excitation force for the tests with and without control. For the tonal excitations the results are given

in magnitude values with a 1 Hz frequency resolution, whereas for the random broadband excitation the results are integrated into the corresponding third octave bands.

Unlike for the acoustic excitation the structural response for the tonal excitations at 80 and 199 Hz was controlled at the same time. The radiated sound power is decreased by 23,9 dB and 10,0 dB respectively. However a strong excitation of harmonic frequencies appeared with the closed control loop behaviour, indicating that the control coefficient setup might have been too aggressive for this particular configuration. For instance the sound radiation at the harmonic frequencies of 240 and 320 Hz is increased from 29 to 55 dB and from 40 to 49 dB, respectively (see Figure C.21), compared to sound power levels of 73,5 and 82,4 dB at the controlled frequencies of 80 and 199 Hz. With the 284 Hz primary excitation the measured sound power reduction is 8,1 dB. A single harmonic frequency at 856 Hz is increased from 31 to 40 dB. At 702 Hz the radiated sound power is attenuated by 7,0 dB. Spill-over effects are not observed with this excitation. The shaker excitation force varies from around 4,5 N for the 199 Hz excitation to 5,4 N for the 284 Hz test case. As before the actuator workload is dominated by the system response in the 80 Hz range. At this frequency the excitation level of about 5 N equals an actuator workload of around 60%.

Table 5.6: Measurement results for tonal point force excitation

	Radiated Sound Power [dB]		**Excitation Force [N]**		**Voltage**
Freq.	control off	control on	control off	control on	[%]
80 Hz*	97,4	73,5	4,8	5,0	58,9
199 Hz*	92,5	82,4	4,5	4,5	58,9
284 Hz	84,8	76,7	5,4	5,4	15,3
702 Hz	72,7	66,0	4,7	4,7	n/a

* measured and controlled simultaneously

A random excitation was applied in the 80 Hz third octave band and a reduction of 8,6 dB in radiated sound power is achieved by controlling the trim panel response. The shaker excitation force is 1,7 N. The actuator workload is not available because the voltage was not measured. Analogous to the acoustic excitation, the sound radiation in the third octave bands of 200, 250 and 400 Hz was amplified from 27 to 37 dB, from 25 to 43 dB and from 20 to 25 dB (see Figure C.31). Yet, these levels are still relatively low in comparison to the sound power level of 75,9 dB in the controlled 80 Hz band.

Table 5.7: Measurement results for random point force excitation

	Radiated Sound Power [dB]		**Excitation Force [N]**		**Voltage**
Freq.	control off	control on	control off	control on	[%]
80 Hz band	84,5	75,9	1,7	1,7	n/a

Similar to the various acoustic excitations, stability problems with the control loop were not

observed. Further details in terms of spectra for the radiated sound power, excitation sound pressure level and corresponding intensity plots are listed in Annex C.

5.4.4 Results with Artificial Buzz-Saw Noise Excitation

The experimental results presented in the previous chapters were achieved with a relatively complex control system based on a fully coupled interaction between 12 actuators and 24 or 25 acceleration error sensors respectively. A possible application and integration into a real aircraft cabin would certainly be easier for a less complex system. This could either be achieved by reducing the number of actuators or error sensors involved in the control loop. However, the results achieved so far also revealed that, mainly for excitation frequencies higher than 200 Hz, the actuators of an attachment element are always driven to some extent out of phase, implying that a combination of both translatory and rotational displacements is induced by the DSP system at the trim panel attachment points and thus required for a good control performance. Reducing the number of degrees of freedom by driving the respective three actuators of each attachment element in phase (hence simulating a system with four degrees of freedom instead of twelve) would thus limit the control authority to excitation frequencies under 200 Hz. For this reason and as a typical buzz-saw noise excitation also involves higher perturbation frequencies, it was decided to test the ASAC control system with a reduced number of error sensors in order to assess the potentials of a system with decreased control complexity.

As a test case for this experimental investigation an artificial buzz-saw noise excitation is used. According to the buzz-saw noise data given in Chapter 2 the fundamental frequency is chosen to equal 80 Hz. The excitation signal contains 40 harmonics up to 3,2 kHz and is shaped to give a similar radiation spectrum as the one presented in Figure 2.6. In contrast to the other tests a second trim panel had to be used, denoted as *Trim Panel 2* in Table 5.3. The reduction in the number of error sensors is achieved by using only sensors placed directly on the trim panel. The remaining sensors on the attachment elements are not used in the control loop, but are still available to measure the respective acceleration levels with and without control. In total 13 sensors are used. Their respective position on the trim panel is listed in Table 5.3.

The first twelve perturbation frequencies up to 960 Hz are controlled with the narrowband filtered-X LMS algorithm, using the same controller parameters as for the previous tonal tests (sample rate 5 kHz, low-pass filter with cut-off frequency set to 1,1 kHz). The main results are summarized in Annex C, Figure C.34 and C.35 for the global radiated sound power and excitation sound pressure level. The following reductions on the controlled harmonic frequencies, starting with 80 Hz, are obtained in radiated sound power by controlling the local dynamic trim panel response at the sensor positions: 5, 12, 6, 2, 0, 4, 2, 5, 9, 1, 0 and 2 dB. The overall reduction, integrated from 0 to 1,6 kHz, is dominated by the peak at 240 Hz and equals 6,2 dB or about 76% on a linear scale. It should be noted that for instance the excitations at 400 and 560 Hz coincide with local high transmission loss values, which makes the active control more difficult. Presumably, the global attenuations could be further improved by using different sensor arrangements, optimised in regard to their correlation to the radiated sound power.

Samples of the acceleration signals measured with sensor 6 (on the second attachment element 2 and not controlled) and sensor 21 (trim panel) are presented in Figure C.36. On the trim panel a substantial reduction is achieved, whereas on the attachment element only a slight

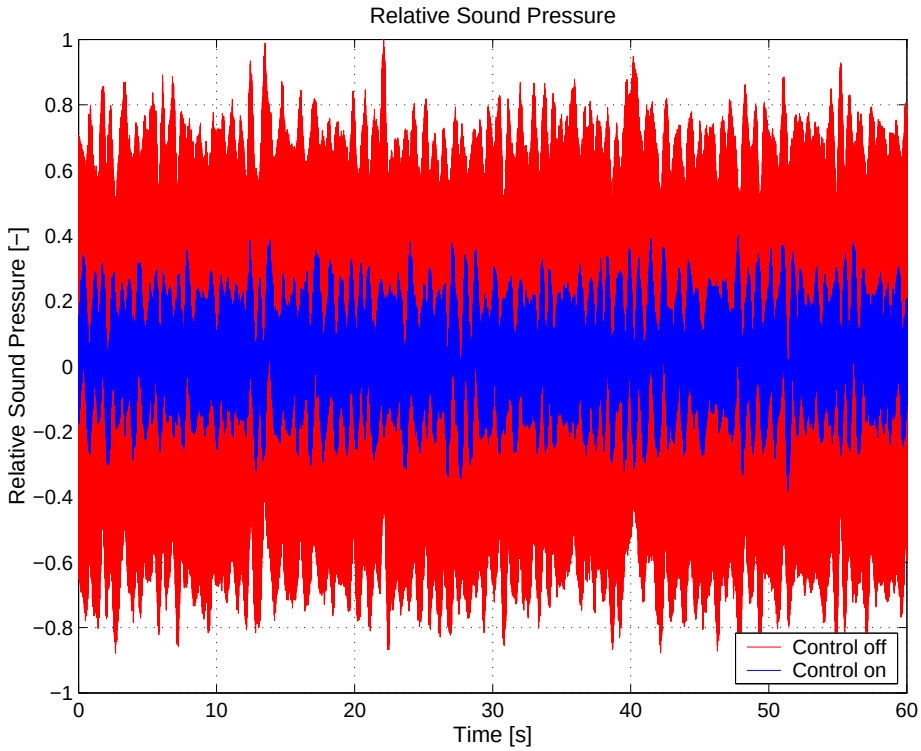

Figure 5.28: Relative sound pressure response to the artificial buzz-saw noise excitation, with and without control

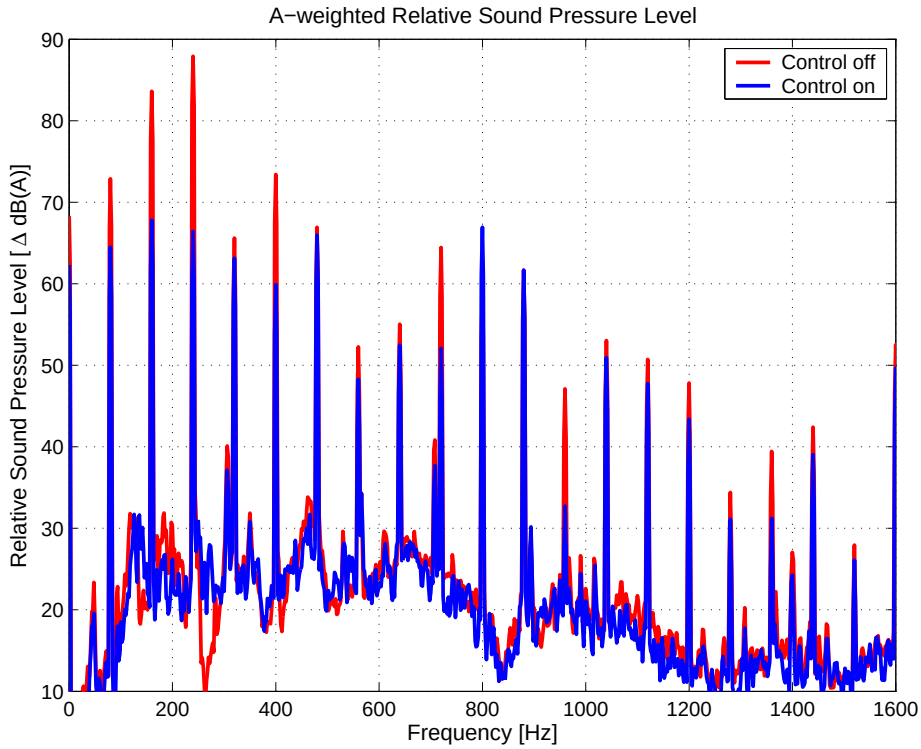

Figure 5.29: A-weighted frequency spectrum of measured sound pressure response, with and without control

improvement is gained with control. The frequency domain response of the summed error signal is illustrated in Figure C.37. It can be seen that the acceleration level on the panel is reduced at each of the twelve excitation frequencies. Furthermore, it is interesting to note that, apart from the perturbation at the second, fourth and fifth harmonics, the acceleration levels are also attenuated on the attachment elements, although the respective sensors are not included in the control loop.

The measured actuator voltage is shown in Figure C.38 for a 50 ms sample. The actuator workload is dominated by the excitation at the 240 Hz harmonic (SPL in the excitation room: 110 dB) and a maximum voltage of 104 V_{Peak} is applied to actuator 9.

To demonstrate the effect of the active control system on the subjective human hearing perception, the relative sound pressure at one point in front of the trim panel was also recorded. For this purpose a microphone was placed at a distance of 1,5 m relative to the middle of the trim panel. The time dependency of the pressure signals and the corresponding frequency spectra with and without control are shown in Figure 5.28 and 5.29. To take into account the frequency dependence of the human hearing perception, an A-weighted frequency filter is applied to the spectral data.

After the filter adaptation of the controller has converged to an optimal solution, here requiring a time of about 15 seconds for a filter setup, which has not previously been pre-conditioned by the actual error signal, the microphone pressure signal is approximately reduced by 60% with the activated control system. In the frequency domain an overall attenuation of 9,5 dB(A), integrated from 0 to 1,6 kHz, is achieved with the ASAC control system.

To judge the system's performance and potentials the following relationship between the perceived sound pressure level and human perception has to be considered. A 3 dB increase in SPL is the threshold of perceptibility and corresponds to a doubling of acoustic energy. Without having the possibility of direct comparisons a change smaller than 3 dB will not be distinguished by the average person. A 10 dB increase in SPL is typically perceived as a doubling in loudness to the average person and represents a tenfold change in acoustic energy. Therefore, the average person will judge the overall reduction of 9,5 dB(A) approximately half as loud as without control.

5.5 Comparison with Numerical Results

Figure 5.30 shows a comparison between the measured and predicted passive transmission loss behaviour for the acoustic diffuse field excitation obtained either with built-in active attachment elements or passive shock mounts, respectively rigid connections as used in the simulations. It is obvious that a direct comparison of absolute simulation and experimental results is not possible as, in addition to the points already mentioned in Chapters 3.4 and 3.5, the particular structural systems used in the numerical model and in the experiment differ too much in their respective geometries, mechanical properties and boundary conditions.

The measured and predicted relative power attenuations in sound transmission due to the ASAC control are illustrated in Figure 5.31. Here, in contrast to absolute results, a good agreement between the relative measured and simulation results is obtained and the experimental decrease in sound transmission obtained with activated control system is well predicted with the numerical model and follows the general trends from the simulations given in the

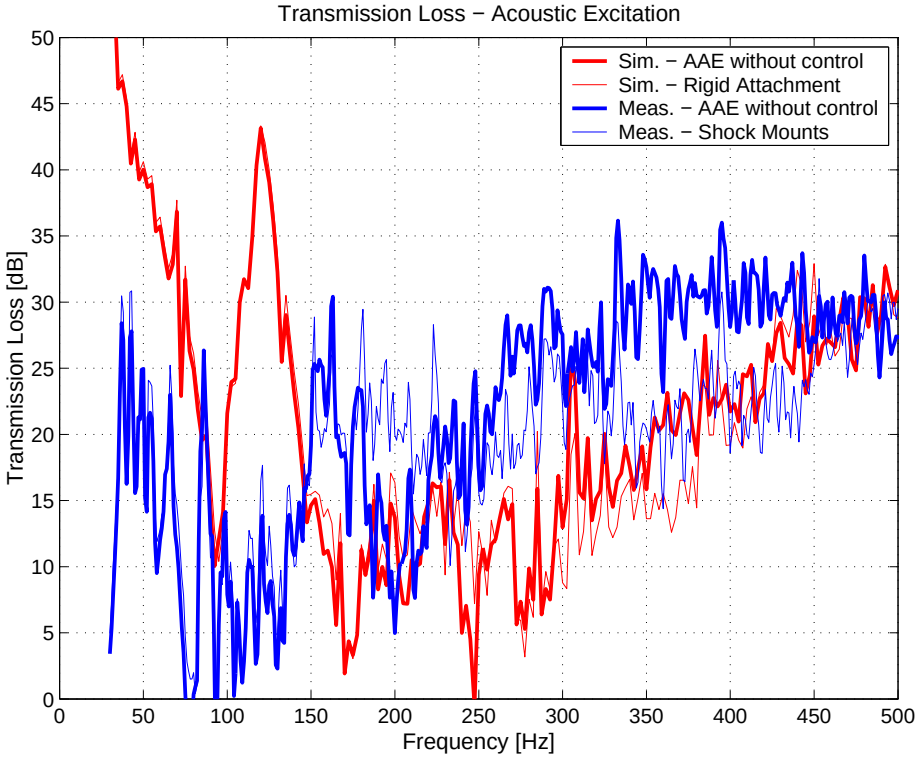

Figure 5.30: Measured and predicted passive transmission loss behaviour

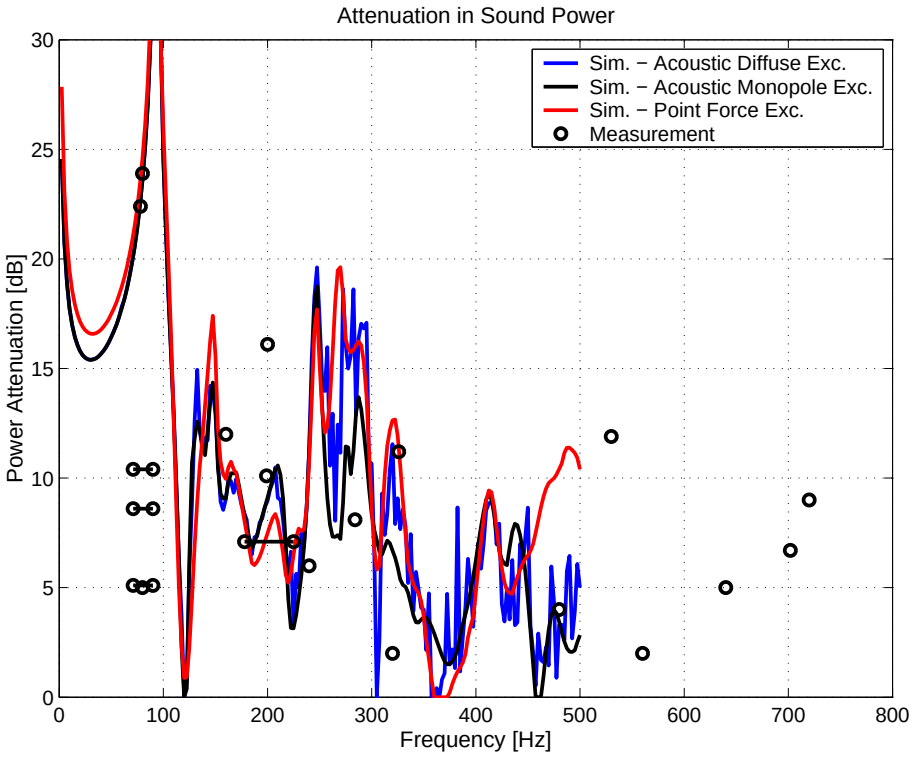

Figure 5.31: Measured and predicted relative attenuation in sound power obtained with the active structural acoustic control concept

previous chapter. Furthermore, the results confirm that with the active attachment elements a sufficient control authority is guaranteed for a large band of frequencies and even at relatively high frequencies, as for instance at 720 Hz, a good performance can be attained, despite using a single, non-optimised sensor configuration on the trim panel. Also, the measured actuator voltage lies within the limits given by the simulation model. This proves that reliable simulation results can be obtained for relatively complex systems such as the considered double wall structure, which allows the transmission of sound by airborne and structure-borne paths and has an incorporated active control system. Thus, the use of adequate numerical models enables and facilitates the development and design process of ASAC systems.

5.6 Conclusions

A prototype of an active system to reduce the low-frequency sound transmission through aircraft sidewall structures was developed and tested on a representative generic aircraft structure installed in an acoustic test facility between a reverberant sending room and anechoic receiving room.

The control system consists of active trim panel attachment elements replacing the existing passive shock mounts. The actuator design is based on commercially available piezoelectric bending elements and the unique design of the elements enables the excitation of both translatory and rotational perturbations on each attachment point, thus permitting an efficient structural acoustic control of the trim panel. The controller is either implemented in a multichannel narrowband or broadband filtered-X LMS configuration on a laboratory DSP system and uses structural accelerations as an error signal. The functionality and performance of the whole system was successfully demonstrated with various tonal and broadband disturbances at different frequencies. Either loudspeaker or shaker point force excitations of realistic levels were used as primary perturbation source.

The experimental results prove that the sound radiation from lightweight structures such as trim panels can be substantially reduced by means of a structural acoustic control concept based on active trim panel attachment elements. The best experimental results were achieved in the low-frequency range where typical aircraft sidewalls are less efficient in reducing the sound transmission into the cabin. Reductions in radiated sound power in the order of 20 dB and more were obtained with active control in contrast to the uncontrolled configuration. With increasing frequencies the dynamic behaviour of the trim panel is more and more dominated by higher modes and therefore more difficult to control with a limited number of actuators and sensors. Nevertheless, even at tonal perturbations of 530 and 702 Hz, reductions of 11 and 7 dB in sound power were obtained with the prototype control system. The sound intensity measurements show that the sound field radiated by the trim panel is spatially evenly reduced in magnitude with active control, indicating that a reduction of structural vibration energy is the main mechanism underlying the active control concept.

Mechanical problems with the actuators as well as stability problems within the control loop were not encountered during the experiments. As expected, the critical case for the actuator design turns out to be the first eigenfrequency of the system, where a strong coupling between the structure and the enclosed cavity occurs, resulting in the maximum structural displacements and thus requiring the most important actuation effort. Considerably lower actuator

voltages are needed for controlling higher frequency disturbances.

In contrast to the simulations, only a single sensor configuration was tested in the main investigations. However, further testing with a second available trim panel was possible and an active control system with a reduced number of error sensors also improved the sound transmission behaviour by a considerable amount for a hypothetical buzz-saw noise excitation. Based on the two items, experimental and simulation results, it is therefore presumed that the active system could be further optimised in terms of acoustic gains and system complexity by using error signals having a better correlation to the actual excitation and sound radiation behaviour.

A direct comparison of absolute simulation and experimental results is not possible, as the respective structural systems differ too much in geometry and mechanical properties. However, the relative experimental results obtained with and without control match the general trends from the simulation predictions given in the previous chapter. The increase in TL is well predicted with the numerical model and also the measured actuator voltage lies within the limits given by the simulation model. This proves that, even for a relative complex system as the considered double wall structure with fluid-structure coupling and incorporated active control loop, reliable results can be obtained with an adequate numerical model.

Chapter 6

Summary and Recommendations

Current commercial aircraft have the least capacity in reducing structural sound transmission at low frequencies and it is expected that, with the development and introduction of composite fuselage structures in future aircraft, the low-frequency transmission loss behaviour will become even worse. Hence, for the preservation and further improvement of acoustical passenger comfort at low audible frequencies, appropriate noise control methods are required. Yet, due to mass and volume requirements in aircraft design, the successful use of conventional noise control technologies (acoustic insulation, constrained layer damping, etc.) is limited in the lower frequency range. An alternative noise control solution, requiring less additional weight and volume, is provided with the concept of active structural acoustic control. ASAC systems are based on the principle that by controlling the vibration response of a structure with appropriate actuators and sensors, its structural sound radiation can be reduced. Subsequently, the development and testing of a prototype ASAC system, intended to increase the low-frequency transmission loss of aircraft sidewalls by controlling its structural response, has been addressed in this thesis.

In a first step the conception and basic design of such a control concept has been investigated with a numerical, modular simulation model. The simulation methodology is based on an FEM-description of the structure since with this approach relatively complex structures can be taken into account (for instance, double wall partitions with fluid-structure coupling, sound transmission by airborne and structure-borne paths, stiffened structures and complex materials). Assuming a weak coupling to the surrounding fluid, the resulting sound radiation is modelled with the Huygens-Rayleigh integral by post-processing the vibration results obtained for a given excitation on the radiating surface. The vibro-acoustic simulation model was validated with a series of transmission loss experiments carried out on a single and double wall aluminium partition. A good agreement between the predicted and measured sound transmission behaviour has been found and the simulation method has been proved to be an efficient tool for TL calculations.

Active elements, such as piezoelectric patches bonded to the structure, are described within the FEM-model by simplified actuation laws such as the thermal-elastic analogy or the equivalent force model. These actuation models provide a linear relationship between the applied voltage and the actuation forces introduced into the substrate structure and are considered to be sufficiently accurate since only the general impact of the control input on the global structural response has to be determined. A simplified control loop is incorporated in the computation

model by applying the superposition principle. By minimising an error signal, the required actuation signal is derived and, based on the assumption of a linear structural behaviour, the controlled structural response can be computed as a linear combination of the structural response due to the primary perturbation and the secondary, controller-generated responses. Thus, the system response represents an estimate of the best possible controller performance for a given system configuration and can be compared to the uncontrolled response or alternative control systems in terms of structural and sound radiation behaviour.

The numerical model has been used to determine an appropriate active control system intended to reduce the low-frequency sound transmission through typical aircraft sidewalls. The basic structural model consists of a simplified, flat aluminium fuselage structure stiffened by perpendicular stringers and frames in conjunction with a generic honeycomb core trim panel. Sound transmission is dominated by the cavity fluid path but also possible through the trim panel attachments that mechanically couple the fuselage behaviour to the trim panel. Three different ASAC systems have been evaluated against several primary excitations applied to the fuselage skin (acoustic monopole field, diffuse field and point force excitation). Two of the active systems are based on piezoceramic patches either bonded directly to the fuselage skin or the trim panel. As control law, a local velocity feedback control loop in conjunction with collocated sensors was used in both cases, thus increasing the structural damping and energy dissipation in the sound transmission path. A new ASAC concept was devised with the third concept. The system consists of active attachment elements that are mounted between the fuselage and the trim panel and replace the conventional trim panel mounts. The active attachment element is designed to provide three independent degrees of freedom, allowing the control of both normal translatory and rotational perturbation components induced on the trim panel at the attachment points. Actuation is done by piezoceramic elements. The controller was implemented in an LMS-configuration and combined with acceleration sensors located on the trim panel and the attachment elements.

Out of the three investigated systems, the best low-frequency control performance in terms of radiated sound power and structural vibration reduction was obtained with the active attachment elements. An added advantage of such a system in comparison to the other control technologies is that for a sidewall system, where sound transmission is dominated by structure-borne components, the active attachments elements also represent the most adequate control solution.

To demonstrate the efficiency of such a system, further work was directed on the development and experimental testing of a prototype control system based on active attachment elements. For the actuation, commercially available piezo actuators have been used. The prototype active attachment element has a weight of just 100 g and dimensions of 23 mm in height and of 62 mm in diameter. A plane aircraft sidewall section (dimensions 1 by 1 m), consisting of a generic CFRP fuselage and a honeycomb core trim panel, was fitted with four prototype attachment elements and subsequently installed in a transmission loss test suite between a reverberation and an anechoic chamber. The LMS controller was implemented on a laboratory DSP system and consisted of 12 control channels combined with a total of up to 26 acceleration error signals. Excitation was carried out in the reverberation chamber on the fuselage skin, either acoustically by loudspeakers or mechanically by a point force excitation. In the anechoic chamber, facing the trim panel, the transmitted sound power was determined by intensity measurements. The performance and efficiency of the active system was evaluated against several deterministic and

random disturbances, representing noise sources similar to buzz-saw noise, jet noise and TBL noise excitations. The disturbance frequencies were chosen according to the sound transmission behaviour measured without control and correspond to local frequencies where the sidewall structure has the least efficiency in reducing the sound transmission. Realistic excitation levels have been used.

From the experimental results one can conclude that the active attachment elements represent an efficient technology for the active control of sound transmission through aircraft sidewall structures and thus provide new possibilities to attenuate low-frequency disturbances in the cabin and improve passenger comfort. The effect of control has been clearly audible and substantial decreases in sound transmission have been obtained for a large band of frequencies. Best results were achieved at low frequencies, as for instance on the mass-air-mass resonance, where tonal reductions in radiated sound power in the order of 20 dB or even more were obtained. Control authority is reduced with increasing frequency but even at relatively high frequencies good attenuations in radiated sound power can be attained. For non-deterministic perturbations third octave band reductions of up to 10 dB have been measured with the prototype system. The main mechanism of control is a reduction of the overall kinetic trim panel energy, which is linked to a spatial evenly attenuation in the magnitude of the sound intensity radiated by the trim panel.

Problems with the control system and the actuators were not encountered throughout the different test configurations. In all cases the control loop remained stable during the duration of each individual intensity measurement, which typically required a time of around 50 minutes. In terms of actuator performance, the critical frequency was the mass-air-mass resonance of the system, requiring the highest actuation efforts due to the large displacements excited on the trim panel. At higher frequencies the actuators were driven well below their maximum operating voltage. Furthermore, the control concept with active attachment elements provides some advantages compared to other technologies like active noise control with loudspeakers, active damping of the main structure or active panels with structurally integrated actuators. Active attachment elements allow an easy retrofitting and maintenance, they are fail-safe, the acoustic performance is easily scalable according to the primary excitation and the elements can be designed to improve the transmission loss by means of passive and active vibration isolation.

Yet, further work is needed to optimise the presented ASAC concept with respect to a successful commercial application. The most important point concerns the array of error sensors used on the trim panel. In the experimental investigations only one particular sensor layout, chosen on an ad-hoc basis without having knowledge of the exact radiation modes of the trim panel, was used. The particular sensor array was probably sub-optimally placed, an effect having a greater influence at higher perturbation frequencies. Therefore, no reduction in sound power was obtained with control on some frequencies, even though the vibration levels on the error sensors in the feedback loop were reduced. This indicates that in these configurations acoustically non-relevant vibrations were controlled. It is believed that better results in terms of sound power reduction can be obtained if suitable error sensors correlated to the actual sound radiation are used. Furthermore, some experimental results confirmed that the active control system is also able to work with a reduced number of error sensors. In addition to that, a reduction in the number of control channels could be possible for the lowest perturbation frequency such as the mass-air-mass resonance. This would reduce the complexity of the control system, but is also

dependant on the actual structural boundary conditions.

Another point concerns directly the design of the active attachment elements. For future applications the performance, weight and volume of the actuators can be further optimised. In the current application, for instance, it would be possible to integrate the aluminium mounting plates directly into the trim panel and the frames respectively. Consequently, with a structurally integrated design the required installation height could be reduced from around 23 to 11 mm. Furthermore, the basic clamshell units also have a potential for further miniaturising and, by redesigning the structural attachment to the individual Thunder elements, actuator performance could be improved as well.

Finally, the electronic hardware components used in the laboratory test have a high weight and require a large volume. With respect to one of the main objectives typically claimed for active control systems, which is the reduction of weight and volume in comparison to conventional passive noise control methods, this may be seen as problematic by potential customers. For a successful demonstration of an integral ASAC system in aircraft and for a possible commercial application, it is therefore strongly recommended to miniaturise the electronic hardware components such as the DSP system, power amplifiers, filters and signal conditioners.

Bibliography

Achkire, Y. (1997). *Active Tendon Control of Cable-Stayed Bridges.* Active Structures Laboratory, Université Libre de Bruxelles, Belgium.

Bao, C. and J. Pan (1997). *Experimental study of different approaches for active control of sound transmission through double walls.* Journal of Acoustical Society of America, 102(3), pp. 1664-1670.

Barisciano, L.P. (1999). *Broadband Transmission Loss Due to Reverberant Excitation.* NASA/CR-1999-209687, Langley Research Center.

Bathe, K.-J. (1982). *Finite Element Procedures in Engineering Analysis.* Prentice-Hall, Inc., Englewood Cliffs, New Jersey.

Baumann, W.T., F.-S. Ho, and H.H. Robertshaw (1992). *Active structural acoustic control of broadband disturbances.* Journal of Acoustical Society of America, 92(4), pp. 1998-2005.

Bebesel, M. (1999). *Aktive Schwingungsdämpfung zur Lärmminderung in Fahrzeugkabinen.* Physik-Departement Institut E15, Technische Universität München.

Beranek, L.L. and G.A. Work (1949). *Sound Transmission through Multiple Structures Containing Flexible Blankets.* Journal of Acoustical Society of America, 21(4), pp. 419-428.

Berry, A., J.L. Guyader, and J. Nicolas (1990). *A general formulation for the sound radiation from rectangular, baffled plates with arbitrary boundary conditions.* Journal of Acoustical Society of America, 88(6), pp. 2792-2802.

Bianchi, E., P. Gardonio, and S.J. Elliott (2004). *Smart panel with multiple decentralized units for the control of sound transmission. Part III: control system implementation.* Journal of Sound and Vibration, 274, pp. 215-232.

Blakely, K. (1993). *MSC/Nastran - Basic Dynamic Analysis, Version 68.* MacNeal-Schwendler Corporation.

Bliss, D.B. (1982). *Study of bulk reacting porous sound absorbers and a new boundary condition for thin porous layers.* Journal of Acoustical Society of America, 71(3), pp. 533-545.

Bliss, D.B. and S.E. Burke (1982). *Experimental investigation of the bulk reaction boundary condition.* Journal of Acoustical Society of America, 71(3), pp. 546-551.

Bossens, F. (2001). *Amortissement actif des structures câblées: de la théorie à l'implémentation.* Active Structures Laboratory, Université Libre de Bruxelles, Belgium.

Bräunling, W. (2004). *Flugzeugtriebwerke - Grundlagen, Aero-Thermodynamik, Kreisprozesse, Thermische Turbomaschinen, Komponenten und Emissionen.* Springer-Verlag, Berlin, Heidelberg, New York.

Burdisso, R.A., J.S. Vippermann, and C.R. Fuller (1993). *Causality analysis of feedforward-controlled systems with broadband inputs.* Journal of Acoustical Society of America, 94(1), pp. 234-242.

Bushnell, G.S., T.M. Anderson, M.D. Becraft, and A. Dean Jacot (1997). *Active rack isolation system development for the international space station.* AIAA-97-1203, 38th AIAA/ASME/AHS/ASC Structures, Structural Dynamics and Material Conference, Kissimmee, USA.

Cabos, C. and F. Ihlenburg (2003). *Vibrational Analysis of Ships with Coupled Finite and Boundary Elements.* Journal of Computational Acoustics, Vol. 11, No. 1, pp. 91-114.

Cady, W.G. (1964). *Piezoelectricity 2: An introduction to the theory and applications of electromechanical phenomena in crystals.* Dover Publications, New York.

Carneal, P.J. and C.R. Fuller (1993). *Active Structural Acoustic Control of Noise Transmission through Double Panel Systems.* AIAA-93-4421, 15th Aeroacoustics Conference, Long Beach.

Carneal, P.J. and C.R. Fuller (2003). *An analytical and experimental investigation of active structural acoustic control of noise transmission through double panel systems.* Journal of Sound and Vibration, 272, pp. 749-771.

Carneal, J.P., F. Charette, and C.R. Fuller (2004). *Minimization of sound radiation from plates using adaptive tuned vibration absorbers.* Journal of Sound and Vibration, 270, pp. 781-792.

Cazzolato, B.S. and C.H. Hansen (2000). *Errors in the measurement of acoustic energy density in one-dimensional sound fields.* Journal of Sound and vibration, 256(5), pp. 801-831.

Charette, F., C.R. Fuller, and J.P. Carneal (1997). *Adaptive vibration absorbers for control of sound radiation from panels.* AIAA-97-1619, 3rd AIAA/CEAS Aeroacoustics Conference 1997, Atlanta, USA.

Charette, F., A. Berry, and C. Guigou (1997). *Radiation modes and the active control of sound power.* Journal of Acoustical Society of America, 103(3), pp. 1493-1503.

Chen, Y., X.G. Wang, C. Sun, F. Devine, and C.W. de Silva (2003). *Active Vibration Control with State Feedback in Woodcutting.* Journal of Vibration and Control, 9, pp. 645-664.

Clark, R.L. and C.R. Fuller (1992). *Experiments on active control of structurally radiated sound using multiple piezoceramic actuators.* Journal of Acoustical Society of America, 91(6), pp. 3313-3320.

Clark, R.L. and C.R. Fuller (1992). *Modal sensing of efficient acoustic radiators with polyvinylidene fluoride distributed sensors in active structural acoustic control.* Journal of Acoustical Society of America, 91(6), pp. 3321-3329.

Clark, R.L. and C.R. Fuller (1992). *Optimal placement of piezoelectric actuators and polivinylidene fluoride error sensors in active structural control approaches.* Journal of Acoustical Society of America, 92(3), pp. 1521-1533.

Coanda, H. (1930). *Procédé de protection contre les bruits.* French Patent FR 722.274. Filed: Oct. 21, 1930. Patented: Dec. 29, 1931.

Coanda, H. (1932). *Procédé et dispositif de protection contre les bruits.* French Patent FR 762.121. Filed: Dec. 31, 1932. Patented: Jan. 18, 1934.

Collins, S.G. and A.H. von Flotow (1991). *Active vibration for spacecraft.* IAF-91-289, 42nd Congress of the International Astronautical Federation, Montreal, Canada.

Cook, R.D., D.S. Malkus, and M.E. Plesha (1989). *Concepts and Applications of Finite Element Analysis.* Springer-Verlag, Berlin, Heidelberg.

Conover, W.B. and W.F.M. Gray (1955). *Noise Reducing System for Transformers.* U.S. Patent US 2,776,020. Filed: Feb. 9, 1955. Patented: Jan. 1, 1957.

Corcos, G.M. (1963). *Resolution of Pressure in Turbulence.* Journal of Acoustical Society of America, 35(2), pp. 192-199.

Cremer, L. and M. Heckl (1996). *Körperschall - Physikalische Grundlagen und technische Anwendung.* Springer-Verlag, Berlin, Heidelberg.

Crighton, D.G., A.P Dowling, J.E. Ffowcs Williams, M. Heckl, and F.G. Leppington (1992). *Modern methods in analytical acoustics: lecture notes.* Springer-Verlag, Berlin Heidelberg New York.

Crocker, M.J. (1998). *Measurement of Sound Intensity.* In Harris, C.M.: *Handbook of Acoustical Measurements and Noise Control*, Acoustical Society of America.

De Fonseca, P., P. Sas, and H. Van Brussel (1998). *Active control of sound transmission through an aircraft fuselage test section.* AIAA-98-2233, Proceedings of the Fourth AIAA/CEAS Aeroacoustics Conference 1998, Toulouse, pp. 184-194.

De Fonseca, P., P. Sas, and H. Van Brussel (1999). *Experimental Study of the Active Sound Transmission Reduction Through a Double Panel Test Section.* Acustica & Acta Acustica, Vol. 85, pp. 538-546.

De Man, P., A. Francois, and A. Preumont (2003). *Active control of noise transmission through double wall structures. An overview of possible approaches.* NCTAM-2003-099, 6th National Congress on Theoretical and Applied Mechanics, Ghent, Belgium.

Denkena, B., A. Harms, and P. Hesse (2004). *Adaptronischer Werkzeugadapter zur aktiven Schwingungsdämpfung in CNC-Drehmaschinen.* Adaptronic Congress 2004.

Elliott, S.J. and M.E. Johnson (1993). *Radiation modes and the active control of sound power.* Journal of Acoustical Society of America, 94(4), pp. 2194-2204.

Elliott, S. (2001). *Signal Processing for Active Control.* Academic Press Limited, London.

Elliott, S.J. and P. Gardonio (2001). *Active Control of Sound Transmission.* Internoise 2001, The Hague, Netherlands.

Estorff, O. von (2000). *Boundary elements in acoustics: advances & applications.* WIT Press, Southampton, UK.

Fahy, F.J. (1977). *Measurement of acoustic intensity using cross-spectral density of two microphone signals.* Journal of Acoustical Society of America, 62(4), pp. 1057-1059.

Fahy, F.J. (1985). *Sound and Structural Vibration: Radiation, Transmission and Response.* Academic Press Limited, London.

Fahy, F.J. (1989). *Sound Intensity.* Elsevier Applied Sciences, New York.

Franchek, M.A., R.J. Bernhard, and M. Ryan (1993). *Adaptive/passive noise and vibration control.* AIAA-93-1147, AIAA/AHS/ASEE Aerospace Design Conference 1993, Irvine, USA.

Fuller, C.R. and R.J. Silcox (1992). *Active structural acoustic control.* Journal of Acoustical Society of America, 91(1), pp. 519.

Fuller, C.R., S.J. Elliot, and P.A. Nelson (1996). *Active Control of Vibration.* Academic Press Limited, London.

Gardonio, P. and S.J. Elliott (1998). *Active control of structure-borne and airborne sound transmission through a double panel.* AIAA-98-2353, Proceedings of the Fourth AIAA/CEAS Aeroacoustics Conference 1998, Toulouse, pp. 864-879.

Gardonio, P., Y.-S. Lee, S.J. Elliott, and S. Debost (2001). *Analysis and measurement of a matched volume velocity sensor and uniform force actuator for active structural acoustic control.* Journal of Acoustical Society of America, 110(6), pp. 3025-3031.

Gardonio, P. and S.J. Elliott (2004). *Smart panel for active structural acoustic control.* Journal of Smart Materials and Structures, 13, pp. 1314-1336.

Gardonio, P., E. Bianchi, and S.J. Elliott (2004). *Smart panel with multiple decentralized units for the control of sound transmission. Part I: theoretical predictions.* Journal of Sound and Vibration, 274, pp. 163-192.

Gardonio, P., E. Bianchi, and S.J. Elliott (2004). *Smart panel with multiple decentralized units for the control of sound transmission. Part II: design of the decentralized control units.* Journal of Sound and Vibration, 274, pp. 193-213.

Graham, W.R. (1995). *The influence of curvature on the sound radiated by vibrating panels.* Journal of Acoustical Society of America, 71(3), pp. 533-545.

Groeneweg, J.F., G. Sofrin, E.J. Rice, and P.R. Gliebe (1995). *Turbomachinery Noise.* In Hubbard, H.: *Aeroacoustics of Flight Vehicles: Theory and Practice - Volume 1: Noise Sources*, pp. 151-209, Acoustical Society of America, Woodbury.

Grosveld, F.W. (1996). *Numerical Comparison of Active Acoustic and Structural Noise Control in Stiffened Double Wall Cylinder.* American Institute of Aeronautics and Astronautics.

Guicking, D. (2003). *From a Laboratory Curiosity to Commercial Products.* Drittes Physikalisches Institut, University of Göttingen.

Guy, R.W. and P. Sauer (1984). *The influence of sills and reveals on sound transmission loss.* Journal of Applied Acoustics, 17, pp. 453-476.

Halliwell, R.E. and A.C. Warnock (1985). *Sound transmission loss: Comparison of conventional techniques with sound intensity techniques.* Journal of Acoustical Society of America, 77, pp. 2094-2103.

Hansen, C.H. and S.D. Snyder (1997). *Active Control of Noise and Vibration* . E. & F.N. Spon, London.

Heckl, M. and H.A. Müller (1994). *Taschenbuch der technischen Akustik.* Springer-Verlag, Berlin, Heidelberg.

Henderson, T.C. (1996). *Design and testing of a broadband active vibration isolation system using stiff actuators.* Proceedings of the Annual AAS Rocky Mountain Guidance and Control Conference 1999, Breckenridge, USA.

Henrioulle, K. and P. Sas (2001). *A PVDF sensor/actuator pair for active control of sound transmission.* Internoise 2001, The Hague, Netherlands.

Henrioulle, K. and P. Sas (2003). *Experimental validation of a collocated PVDF volume velocity sensor/actuator pair.* Journal of Sound and vibration, 265(3), pp. 489-506.

Hyde, T.T. (1997). *An experimental study of active vibration isolation.* AIAA-97-1354, 38th AIAA/ASME/AHS/ASC Structures, Structural Dynamics and Material Conference, Kissimmee, USA.

Ingard, K.U. (1994). *Notes on Sound Absorption Technology.* Noise Control Foundation, Arlington Branch, Poughkeepsie.

Jacobsen, F. (2002). *A note on finite difference estimation of acoustic particle velocity.* Journal of Sound and Vibration, 256(5), pp. 849-859.

Jakob, A. (1999). *Aktive Minderung der Schallabstrahlung schwingender Platten.* Fortschritt-Berichte VDI, Reihe 11, Nr. 280, Düsseldorf.

Janocha, H. (1992). *Aktoren - Grundlagen und Anwendung.* Springer-Verlag, Berlin, Heidelberg.

Johnson, M.E. and S.J. Elliott (1995). *Active control of sound radiation using volume velocity cancellation.* Journal of Acoustical Society of America, 98(4), pp. 2174-2186.

Jones, R.E. (1979). *Intercomparison of laboratory determinations of airborne sound transmission loss.* Journal of Acoustical Society of America, 66(1), pp. 148-164.

Kihlman, T. and A.C. Nilsson (1972). *The effects of some laboratory designs and mounting condition on reduction index measurements.* Journal of Sound and Vibration, 24, pp. 349-364.

Kim, B.-K., H.-J. Kang, J.-S. Kim, H.-S. Kim, and S.-R. Kim (2004). *Tunnelling effect in sound transmission loss determination: Theoretical approach.* Journal of Acoustical Society of America, 115(5), pp. 2100-2109.

Kropp, A. and D. Heiserer (2003). *Efficient Broadband Vibro-Acoustic Analysis of Passenger Car Bodies using an FE-based Component Mode Synthesis Approach.* Journal of Computational Acoustics, Vol. 11, No. 2, pp. 139-157.

Kubo, Y. (2004). *Prospects for the Suppression of Aerodynamic Vibrations of a Long-Span Bridge Using Boundary-Layer Control.* Journal of Vibration and Control, 10, pp. 1359-1373.

Kuo, S.M. and D.R. Morgan (1996). *Active Noise Control Systems - Algorithms and DSP Implementations.* John Wiley & Sons, Inc., New York.

Lagö, T.L. (2002). *Industry Overview of Active Control Methods and Applications.* Adaptronic Congress 2002.

Lammering, R. and S. Wiesemann (1998). *Numerical and Experimental Investigations on Smart Structures with Piezoelectric Devices.* In Gabbert, U.: *Modelling and Control of Adaptive Mechanical Structures*, Fortschritt-Berichte VDI, Reihe 11, Nr. 268, Düsseldorf.

Lee, C.K. (1990). *Theory of laminated piezoelectric plates for the design of distributed sensors/actuators. Part I: Governing equations and reciprocal relationships.* Journal of Acoustical Society of America, 87(3), pp. 1144-1158.

Lee, C.K., W.W. Chiang, and T.C. O'Sullivan (1991). *Piezoelectric modal sensor/actuator pairs for critical active damping vibration control.* Journal of Acoustical Society of America, 90(1), pp. 374-384.

Lee, Y.-S., P. Gardonio, and S.J. Elliott (2002). *Volume velocity vibration control of a smart panel using a uniform force actuator and an accelerometer array.* Journal of Smart Materials and Structures, 11, pp. 863-873.

Léwy, S. (2000). *Experimental study of fan broadband noise on a turbofan model.* 7th International Congress on Sound and Vibration, Garmisch-Partenkirchen.

Li, Q.S., D.K. Liu, J. Tang, N. Zhang, and C.M. Tam (2004). *Combinatorial optimal design of number and positions of actuator in actively controlled structures using genetic algorithms.* Journal of Sound and Vibration, 270, pp. 611-624.

Lilley, G.M. (1995). *Jet Noise - Classical Theory and Experiments.* In Hubbard, H.: *Aeroacoustics of Flight Vehicles: Theory and Practice - Volume 1: Noise Sources*, pp. 211-289, Acoustical Society of America, Woodbury.

Locatelli, G. (2001). *Piezo-actuated adaptive structures for vibration damping and shape control - modelling and testing.* Fortschritt-Berichte VDI, Reihe 11, Nr. 303, Düsseldorf.

Lorkowski, T. (2001). *Piezoelektrische Hybridaktuatoren für eine dynamische Profilvariation als Hochauftriebshilfe an Helikopterrotoren.* Fortschritt-Berichte VDI, Reihe 12, Nr. 451, Düsseldorf.

Lueg, P. (1933). *Verfahren zur Dämpfung von Schallschwingungen.* Austrian Patent No. 141998. Filed: Feb. 2, 1933. Patented: Jan. 15, 1935.

Maier, R. (2000). *Innenlärmminderung bei Helikoptern durch aktive Körperschallisolation.* In *Automatisierungstechnik 48*, Oldenbourg Verlag, pp. 191-198.

Maier, R., F. Hoffmann, S. Tewes, and M. Bebesel (2002). *Active Vibration Isolation System for Helicopter Interior Noise Reduction.* AIAA 2002-2495, 8th AIAA/CEAS Aeroacoustic Conference, Breckenridge.

Maillard, J.P. and C.R. Fuller (1994). *Advanced time domain wave-number sensing for structural acoustic systems. I. Theory and design.* Journal of Acoustical Society of America, 95(6), pp. 3252-3261.

Maillard, J.P. and C.R. Fuller (1994). *Advanced time domain wave-number sensing for structural acoustic systems. I. Active radiation control of a simply supported beam.* Journal of Acoustical Society of America, 95(6), pp. 3262-3272.

Maillard, J.P. and C.R. Fuller (1995). *Advanced time domain wave-number sensing for structural acoustic systems. I. Experiments on active broadband radiation control of a simply supported plate.* Journal of Acoustical Society of America, 98(5), pp. 2613-2621.

Maillard, J.P. and C.R. Fuller (1997). *Comparison of two structural sensing approaches for active structural acoustic control.* Journal of Acoustical Society of America, 103(1), pp. 396-400.

Mangiante, G.A. (1977). *Active sound absorption.* Journal of Acoustical Society of America, 61(6), pp. 1516-1523.

Marburg, S. and H.-J. Hardtke (2003). *Investigation and Optimization of a Spare Wheel Well to Reduce Vehicle Interior Noise.* Journal of Computational Acoustics, Vol. 11, No. 3, pp. 425-449.

Masson, P., A. Berry, and J. Nicolas (1997). *Active structural acoustic control using strain sensing.* Journal of Acoustical Society of America, 102(3), pp. 1588-1599.

Maury, C., P. Gardonio, and S.J. Elliott (2001). *Model for Active Control of Flow-Induced Noise Transmitted through Double Partitions.* AIAA-2001-2111, AIAA/CEAS 7th Aeroacoustics Conference, Maastricht, Netherlands.

May, D.N., K.J. Plotkin, R.G. Selden, and B.H. Sharp (1985). *Lightweight Sidewalls for Aircraft Interior Noise Control.* NASA/CR-172490, McDonnell Douglas Corporation, Douglas Aircraft Company, Long Beach.

McAlpine, A. and M.J. Fisher (2001). *On the prediction of buzz-saw noise in aero-engines inlet ducts.* Journal of Sound and Vibration, 248, pp. 123-149.

McKenna, J.T. (1993). *Airline Outlook: Silencing Saab 340s.* Aviation Week & Space Technology, February 1, pp. 17.

Mechel, F.P. (2002). *Formulas of Acoustics.* Springer-Verlag, Berlin, Heidelberg, New York.

Mixson, J.S. and J.F. Wilby (1995). *Interior Noise.* In Hubbard, H.: *Aeroacoustics of Flight Vehicles: Theory and Practice - Volume 2: Noise Control*, pp. 271-355, Acoustical Society of America, Woodbury.

Moosrainer, M. (2000). *Fluid-Struktur-Kopplung. Vibroakustische Lösungsmethoden und Anwendungen.* Fortschritt-Berichte VDI, Reihe 11, Nr. 289, Düsseldorf.

Morse, P.M. and K. Uno Ingard (1986). *Theoretical Acoustics.* Princeton University Press, Princeton, USA.

Nelson, P.A. and S.J. Elliott (1992). *Active Control of Sound.* Academic Press Limited, London.

Nijhuis, M.O. (2003). *Analysis Tools for the Design of Active Structural Acoustic Control Systems.* Ponsen & Looijen bv., Wageningen, Netherlands.

Olson, H.F. and E.G. May (1953). *Electronic Sound Absorber.* Journal of Acoustical Society of America, 25(6), pp. 1130-1137.

Olson, H.F. (1953). *Electronic Sound Absorber.* U.S. Patent US 2,983,790. Filed: April 30, 1953. Patented: May 9, 1961.

Olson, H.F. (1956). *Electronic Control of Noise, Vibration, and Reverberation.* Journal of Acoustical Society of America, 28(5), pp. 966-972.

Padula, S.L. and R.K. Kincaid (1999). *Optimization Strategies for Sensor and Actuator Placement.* NASA/TM-1999-209126.

Palumbo, D.L., R. Cabell, J. Cline, and B. Sullivan (1999). *Flight Test of ASAC Aircraft Interior Noise Control System.* AIAA-99-1933.

Palumbo, D., R. Cabell, J. Cline, and B. Sullivan (2000). *Active Structural Acoustic Control of Interior Noise on a Raytheon 1900D.* NASA/TM-2000-209846.

Pan, J. and C.H. Hansen (1990). *Active control of noise transmission through a panel into a cavity. I: Analytical study.* Journal of Acoustical Society of America, 87(5), pp. 2098-2108.

Pan, J. and C.H. Hansen (1991). *Active control of noise transmission through a panel into a cavity. II: Experimental study.* Journal of Acoustical Society of America, 90(3), pp. 1488-1492.

Pan, J. and C.H. Hansen (1991). *Active control of noise transmission through a panel into a cavity. III: Effect of the actuator location.* Journal of Acoustical Society of America, 90(3), pp. 1493-1501.

Pan, J. and C. Bao (1998). *Analytical study of different approaches for active control of sound transmission through double walls.* Journal of Acoustical Society of America, 103(4), pp. 1916-1922.

Pan, X., J. Sutton, and S.J. Elliott (1998). *Active control of sound transmission through a double-leaf partition by volume velocity cancellation.* Journal of Acoustical Society of America, 104(5), pp. 2828-2835.

Papadopoulos, C.I. (2003). *Development of an optimised, standard procedure to calculate sound transmission loss: numerical results.* Journal of Applied Acoustics, 64 (2003), pp. 1069-1085.

Parkins, J.W., S.D. Sommerfeldt, and J. Tichy (2000). *Error analysis of a practical energy density sensor.* Journal of Acoustical Society of America, 108(1), pp. 211-222.

Peiffer, A., S. Brühl, C. Moeser, and S. Tewes (2005). *Zeitoptimierte Berechnung des Schalldurchgangs durch Wandstrukturen mittels FEM.* DAGA 2005, München.

Preumont, A. (1997). *Vibration Control of Active Structures.* Kluwer Academic Publishers, Dordrecht.

Rafaely, B., S.J. Elliott, and J. Garcia-Bonito (1999). *Broadband performance of an active headrest.* Journal of Acoustical Society of America, 106(2), pp. 787-793.

Rapp, H. (1996). *Faserverbundwerkstoffe und Piezokeramiken - eine Materialkombination mit Zukunft.* In *Faserverbundstrukturen und -bauweisen in der Luft- und Raumfahrt*, DGLR-Tagung, Ottobrunn.

Rohwer, K. (1996). *Modelle und Methoden zur Berechnung von Laminaten aus unidirektionalen Faserverbunden.* Fortschritt-Berichte VDI, Reihe 01, Nr. 264, Düsseldorf.

Rosen, C.Z. and B.V. Hiremath (1992). *Piezoelectricity.* AIP American Institute of Physics, New York.

Schmidt, H. (1996). *Schalltechnisches Taschenbuch: Schwingungskompendium.* VDI-Verlag, Düsseldorf.

Sessler, G.M. (1981). *Piezoelectricity in polyvinylidenefluoride.* Journal of Acoustical Society of America, 70(6), pp. 1596-1608.

Skudrzyk, E. (1971). *The Foundations of Acoustics.* Springer-Verlag, Wien.

Sollo, A., L. Lecce, V. Quaranta, and N. Doelman (1998). *Active noise control on ATR fuselage mock-up by piezoceramic actuators.* AIAA-98-2230, Proceedings of the Fourth AIAA/CEAS Aeroacoustics Conference 1998, Toulouse, pp. 174-183.

Swanson, D.A. and L.R. Miller (1993). *Design and Effectiveness Evaluation of an Active Vibration Isolation System for a Commercial Jet Aircraft.* AIAA-93-1145, AIAA/AHS/ASEE Aerospace Design Conference, Irvine, CA, USA.

Thayer, D., M. Campbell, and J. Vagners (1999). *Six axis vibration isolation using modern control techniques.* Proceedings of the Annual AAS Rocky Mountain Guidance and Control Conference 1999, Breckenridge, USA.

Thomas, D.R. and P.A. Nelson (1995). *Feedback control of sound radiation from a plate excited by a turbulent boundary layer.* Journal of Acoustical Society of America, 98(5), pp. 2651-2662.

Thomas, R., M. Choudhari, and R. Joslin (2002). *Flow and Noise Control: Review and Assessment of Future Directions.* NASA/TM-2002-211631, Langley Research Center.

Tran, B.N., G.P. Mathur, and P.G. Bremner (1995). *Modal energy analysis of aircraft sidewall response to acoustic fields.* Internoise 95, Newport Beach, CA, USA.

Tsai, S.W. and H. Hahn (1980). *Introduction to Composite Materials.* Technomic Publ. Co., Westport, USA.

Ungar, E.E., J.F. Wilby, D.B. Bliss, B. Pinkel, and A. Galaitsis (1977). *A Guide for Estimation of Aeroacoustic Loads on Flight Vehicle Surfaces - Volume 1.* AFFDL-TR-76-91-Vol.1, U.S. Air Force.

Wallace, C.E. (1972). *Radiation Resistance of a Rectangular Panel.* Journal of Acoustical Society of America, 51(3), pp. 946-952.

Wang, B.T., C.R. Fuller, and E.K. Dimitriadis (1991). *Active control of noise transmission through rectangular plates using multiple piezoelectric or point force actuators.* Journal of Acoustical Society of America, 90(5), pp. 2820-2830.

Warnock, A.C. (1982). *The influence of specimen frame on sound transmission loss measurements.* Journal of Applied Acoustics, 15, pp. 307-314.

Widrow, B. and S.D. Stearns (1985). *Adaptive Signal Processing.* Prentice-Hall, Inc., Englewood Cliffs, New Jersey.

Wilby, J.F. and T.D. Scharton (1973). *Acoustic transmission through a fuselage sidewall.* NASA/CR-132602, Bolt Beranek and Newman Inc., Cambridge, MA, USA.

Williams, E.G. (1997). *On Green's function for a cylindrical cavity.* Journal of Acoustical Society of America, 102(6), pp. 3300-3307.

Witting, M. (1999). *Modelling of Diffuse Sound Field Excitations and Dynamic Response Analysis of Lightweight Structures.* Herbert Utz Verlag, München.

Wright, R.I. and M.R.F. Kidner (2004). *Vibration Absorbers: A Review of Applications in Interior Noise Control of Propeller Aircraft.* Journal of Vibration and Control, 10, pp. 1221-1237.

Appendix A

Modelling of Piezoelectric Actuators

A.1 Mechanical Behaviour of Laminate Plates with Active Elements

Considering a small element of a multi-layer laminate plate with integrated piezoceramic patches as illustrated in Figure 3.7, the force induced by the actuators into the substrate layers can be calculated by using the classical laminate theory [Locatelli01, Rohwer96, Tsai80]. This approach expands the following analysis to plates made of orthotropic laminate layers. For a single orthotropic laminate layer the constitutive material equations for plane stress and linear elasticity are described by:

$$\begin{pmatrix} \sigma_1 \\ \sigma_2 \\ \tau_{12} \end{pmatrix} = \begin{bmatrix} Q_{11} & Q_{12} & 0 \\ Q_{12} & Q_{22} & 0 \\ 0 & 0 & Q_{66} \end{bmatrix} \cdot \left(\begin{pmatrix} \epsilon_1 \\ \epsilon_2 \\ \gamma_{12} \end{pmatrix} - \begin{bmatrix} 0 & 0 & d_{31} \\ 0 & 0 & d_{31} \\ 0 & d_{15} & 0 \end{bmatrix} \cdot \begin{pmatrix} U_1/t_1 \\ U_2/t_2 \\ U_3/t_3 \end{pmatrix} \right)$$

$$\Leftrightarrow \ (\sigma) = [Q] \cdot \big(\epsilon - \Lambda\big) \ . \tag{A.1}$$

The subscript 1 denotes the local principal material direction (for instance the fibre orientation) and 2 its transversal direction. The vector Λ contains the free piezoelectric strain that is induced in the actuator layers with the assumption of a uniform electric field U_i/t_i. The piezoelectric characteristics in 1- and 2-direction are similar, $d_{32} = d_{31}$. For a passive laminate layer Λ has to be set to zero. Q is the reduced stiffness matrix of the orthotropic layer and its elements Q_{ij} are given by[1]:

$$Q_{11} = \frac{E_1}{1 - \nu_{12}\nu_{21}} \ , \qquad Q_{12} = \frac{\nu_{12} \cdot E_2}{1 - \nu_{12}\nu_{21}} \ ,$$

$$Q_{22} = \frac{E_2}{1 - \nu_{12}\nu_{21}} \ , \qquad Q_{66} = G_{12} \ . \tag{A.2}$$

[1] For a unidirectional composite layer the material parameters in the local principle directions can be calculated from the fibre and matrix properties [Rohwer96, Tsai80].

With the known principal orientation φ_k of each layer k defined relative to the x-axis of the global x,y,z-coordinate system, the reduced stiffness matrix Q is transformed into the global coordinate system.

$$\bar{Q_k} = T_\sigma^{-1} \cdot Q_k \cdot \left(T_\sigma^{-1}\right)^T \ , \tag{A.3}$$

where T_σ is the stiffness transformation matrix as defined by the following expression:

$$T_\sigma = \begin{bmatrix} \cos^2\varphi_k & \sin^2\varphi_k & 2\cdot\sin\varphi_k\cdot\cos\varphi_k \\ \sin^2\varphi_k & \cos^2\varphi_k & -2\cdot\sin\varphi_k\cdot\cos\varphi_k \\ -\sin\varphi_k\cdot\cos\varphi_k & \sin\varphi_k\cdot\cos\varphi_k & \cos^2\varphi_k - \sin^2\varphi_k \end{bmatrix} \ . \tag{A.4}$$

It follows from the assumption of the Kirchhoff hypothesis[2] that the strain field is linear through the thickness direction of the plate. This also implies a perfect bonding for each layer. The strain in the plate can then be written as:

$$\begin{pmatrix} \epsilon_x \\ \epsilon_y \\ \gamma_{xy} \end{pmatrix} = \begin{pmatrix} \epsilon_x^0 \\ \epsilon_y^0 \\ \gamma_{xy}^0 \end{pmatrix} + z \cdot \begin{pmatrix} \kappa_x \\ \kappa_y \\ \kappa_{xy} \end{pmatrix} \ . \tag{A.5}$$

The vector ϵ^0 is denoting the deformation of the reference plane and κ its curvature. They are defined as:

$$\begin{aligned} \begin{pmatrix} \epsilon_x^0 \\ \epsilon_y^0 \\ \gamma_{xy}^0 \end{pmatrix} &= \begin{pmatrix} \partial u_0/\partial x \\ \partial v_0/\partial y \\ \partial u_0/\partial y + \partial v_0/\partial x \end{pmatrix} \ , \\ \begin{pmatrix} \kappa_x \\ \kappa_y \\ \kappa_{xy} \end{pmatrix} &= -\begin{pmatrix} \partial^2 w_0/\partial x^2 \\ \partial^2 w_0/\partial y^2 \\ 2\cdot\partial^2 w_0/\partial x\partial y \end{pmatrix} \ , \end{aligned} \tag{A.6}$$

where u_0, v_0 and w_0 are the displacements of the structure in x-, y- and z-direction respectively. Introducing expressions A.3 and A.5 into equation A.1 leads to the stress-strain equation for a single layer expressed in the global coordinate system.

$$\begin{aligned} \begin{pmatrix} \sigma_x \\ \sigma_y \\ \tau_{xy} \end{pmatrix} &= \begin{bmatrix} \overline{Q}_{11} & \overline{Q}_{12} & \overline{Q}_{12} \\ \overline{Q}_{12} & \overline{Q}_{22} & \overline{Q}_{26} \\ \overline{Q}_{16} & \overline{Q}_{26} & \overline{Q}_{66} \end{bmatrix} \cdot \left(\begin{pmatrix} \epsilon_x \\ \epsilon_y \\ \gamma_{xy} \end{pmatrix} - \begin{bmatrix} 0 & 0 & d_{31} \\ 0 & 0 & d_{31} \\ 0 & d_{15} & 0 \end{bmatrix} \cdot \begin{pmatrix} U_1/t_1 \\ U_2/t_2 \\ U_3/t_3 \end{pmatrix} \right) \\ &\Leftrightarrow \ (\sigma) = \left[\bar{Q}\right] \cdot \left(\left(\epsilon^0 + z\cdot\kappa\right) - \Lambda \right) \ . \end{aligned} \tag{A.7}$$

By integrating the stresses in expression A.7 over the thickness t of the laminate the external forces are obtained:

[2] A section perpendicular to the undeformed mid-plane remains straight and perpendicular to the deformed mid-plane.

$$\begin{pmatrix} N_x \\ N_y \\ N_{xy} \end{pmatrix} = \int_t \begin{pmatrix} \sigma_x \\ \sigma_y \\ \tau_{xy} \end{pmatrix} \cdot dz = \sum_{k=1}^{N} \int_{z_{k-1}}^{z_k} \begin{pmatrix} \sigma_x \\ \sigma_y \\ \tau_{xy} \end{pmatrix}_k \cdot dz =$$
$$= \int_{tot} \left[\bar{Q}\right] \cdot \left(\epsilon^0 + z \cdot \kappa\right) \cdot dz - \int_{act} \left[\bar{Q}\right] \cdot \Lambda \cdot dz \ ,$$

$$\begin{pmatrix} M_x \\ M_y \\ M_{xy} \end{pmatrix} = \int_t \begin{pmatrix} \sigma_x \\ \sigma_y \\ \tau_{xy} \end{pmatrix} \cdot z \cdot dz = \sum_{k=1}^{N} \int_{z_{k-1}}^{z_k} \begin{pmatrix} \sigma_x \\ \sigma_y \\ \tau_{xy} \end{pmatrix}_k \cdot z \cdot dz =$$
$$= \int_{tot} \left[\bar{Q}\right] \cdot \left(\epsilon^0 + z \cdot \kappa\right) \cdot z \cdot dz - \int_{act} \left[\bar{Q}\right] \cdot \Lambda \cdot z \cdot dz \ , \tag{A.8}$$

where z_k is the z-coordinate of the surface between the layers k and $k+1$ with respect to the reference plane. The subscripts *tot* and *act* refer, respectively, to an integration over the whole structure incorporating the passive laminate layers as well as the actuator layer, and over the actuator layer only. In matrix form equation A.8 can be rewritten as:

$$\begin{pmatrix} N \\ M \end{pmatrix} = \begin{bmatrix} A & B \\ B & D \end{bmatrix}_{tot} \cdot \begin{pmatrix} \epsilon^0 \\ \kappa \end{pmatrix} - \begin{bmatrix} A \\ B \end{bmatrix}_{act} \cdot \Lambda \ . \tag{A.9}$$

The abbreviations A, B and D denote the usual stiffness matrices used in the classical laminate theory. Its elements ij are given by:

$$\text{Matrix of in-plane stiffness:} \quad A_{ij} = \sum_{k=1}^{N} \overline{Q}_{ij,k} \cdot (z_k - z_{k-1}) \ ,$$
$$\text{Matrix of coupling stiffness:} \quad B_{ij} = \frac{1}{2} \cdot \sum_{k=1}^{N} \overline{Q}_{ij,k} \cdot \left(z_k^2 - z_{k-1}^2\right) \ ,$$
$$\text{Matrix of rotational stiffness:} \quad D_{ij} = \frac{1}{3} \cdot \sum_{k=1}^{N} \overline{Q}_{ij,k} \cdot \left(z_k^3 - z_{k-1}^3\right) \ . \tag{A.10}$$

The in-plane stiffness matrix A connects the in-plane deformation ϵ^0 to the in-plane forces, the matrix D of rotational stiffness relates the curvature κ with the moments, whereas the coupling stiffness matrix B associates in-plane deformations with moments and curvature with in-plane forces. For a symmetrical laminate lay-up the coupling matrix B is zero.

A.2 Actuator Force Models

In order to determine the forces induced by the actuator patches into the structure, the external forces in equation A.9 are set to zero and the equivalent deformations ϵ^0 and κ, induced into the structure when applying an electric field Λ to the actuators, are obtained:

$$\begin{pmatrix} \epsilon^0 \\ \kappa \end{pmatrix}_{eq} = \begin{bmatrix} A & B \\ B & D \end{bmatrix}^{-1}_{tot} \cdot \begin{bmatrix} A \\ B \end{bmatrix}_{act} \cdot \Lambda \ . \tag{A.11}$$

Replacing the deformations in equation A.9 (without taking into account the free piezoelectric strain Λ) with those obtained from equation A.11 results in the equivalent external forces that have to be applied along the edges of the piezo patch in the selected reference plane to give the same strain distribution as by excitation of the actuators:

$$\begin{pmatrix} N \\ M \end{pmatrix}_{eq} = \begin{bmatrix} A & B \\ B & D \end{bmatrix}_{tot} \cdot \begin{pmatrix} \epsilon^0 \\ \kappa \end{pmatrix}_{eq} = \begin{bmatrix} A \\ B \end{bmatrix}_{act} \cdot \Lambda \ . \tag{A.12}$$

If the reference plane is chosen to be located in the mid-plane of the actuator, the coupling matrix B_{act} is zero due to the symmetry. Applying an electric field in 3-direction will result in a force of $N = A_{act} \cdot \Lambda$. The amount of this force is equal to the blocked force of the actuator, hence this model is also referred to as *blocked force model*.

If the mass and stiffness added by an active element is small in comparison to the substrate layers, the global behaviour of the laminate plate may be analysed without considering the piezoelectric material. In this case the integration in equation A.12 has to be made over the thickness of the laminate plate only and the equivalent forces are defined by:

$$\begin{pmatrix} N \\ M \end{pmatrix}_{eq} = \begin{bmatrix} A & B \\ B & D \end{bmatrix}_{hs} \cdot \begin{pmatrix} \epsilon^0 \\ \kappa \end{pmatrix}_{eq} = \begin{bmatrix} A & B \\ B & D \end{bmatrix}_{hs} \begin{bmatrix} A & B \\ B & D \end{bmatrix}^{-1}_{tot} \cdot \begin{bmatrix} A \\ B \end{bmatrix}_{act} \cdot \Lambda \ . \tag{A.13}$$

The subscript *hs* refers to an integration over the host structure. For a static analysis this model will give the same results in terms of global structural deformation as the blocked force model represented by equation A.12. However, in a dynamic analysis, the influence of the added actuator mass and stiffness on the eigenfrequencies and mode shapes of the plate is not taken into account. Nevertheless, it has been shown that this method provides a good approximation to analyse the transversal dynamic behaviour of plates fitted with small piezoceramic d_{31}-patches [Bebesel99, Lammering98, Locatelli01, Nijhuis03].

In addition expression A.13 can be used to optimise the actuator thickness with respect to a given laminate lay-up and material parameters. A common application is the bimorph arrangement with surface-bonded piezo patches located on one side of the laminate plate. With increasing actuator thickness the in-plane forces will augment, whereas the bending moments, introduced into the structure by an excitation of the actuators, will exhibit a maximum for a certain piezoceramic thickness.

This relation is illustrated in the following figure where the equivalent forces are plotted as functions of the actuator thickness for a 2 mm steel and aluminium plate used as substrate layer (material properties are listed in Table A.1). It is assumed that a constant electric field of -1000 V/mm, regardless of the actuator thickness, is applied in 3-direction. As reference plane, the symmetry plane of the substrate layer is chosen. Due to the isotropic material behaviour the in-plane forces in x- and y-direction are of the same magnitude.

For an optimal coupling of the bending moments into the structure the actuator thickness would have to be 1,7 mm for the steel plate and 1,1 mm for the less stiff aluminium plate.

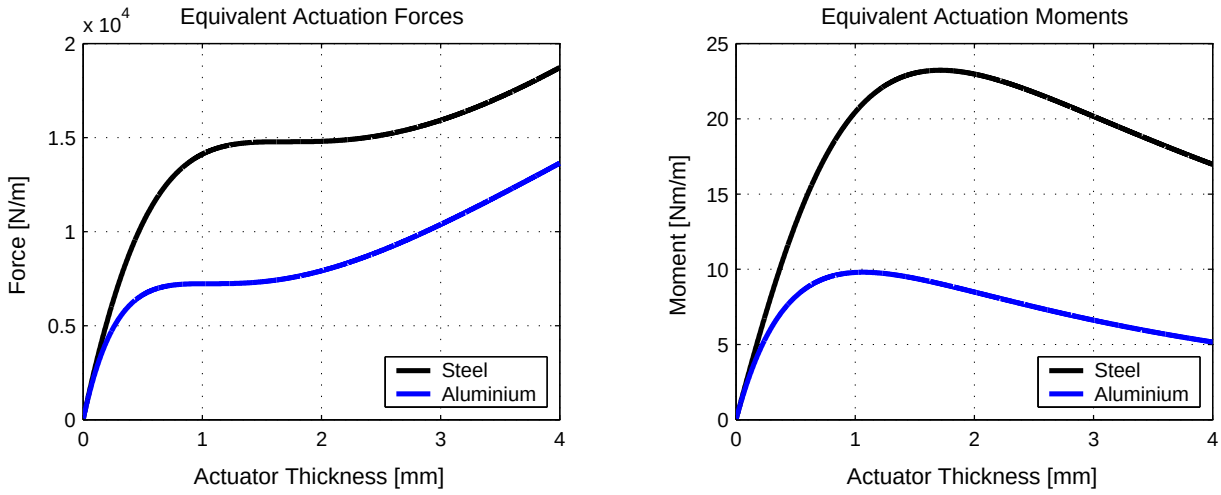

Figure A.1: Equivalent forces as functions of the actuator thickness

Table A.1: Material parameters

	Steel	**Aluminium**	**PZT-Ceramic**
Thickness [mm]:	2	2	var.
Y.-modulus [N/mm^2]:	$2,1 \cdot 10^5$	$0,7 \cdot 10^5$	$0,606 \cdot 10^5$
Poisson constant [-]:	0,3	0,3	0,3
d_{31}-constant [m/V]:	nil	nil	$-340 \cdot 10^{-12}$
Electric field [V/mm]:	nil	nil	-1000

Hence, for a good coupling of the active elements to the transversal vibration of the plate, the product of in-plane actuator force and its leverage distance to the neutral line (defined by $\epsilon = 0$ for pure bending) is the decisive factor. For a small actuator thickness compared to the plate thickness the in-plane force is approaching zero, whereas for very thick actuators the leverage distance of the in-plane forces to the neutral line of the plate is practically zero.

Appendix B

Technical Drawings

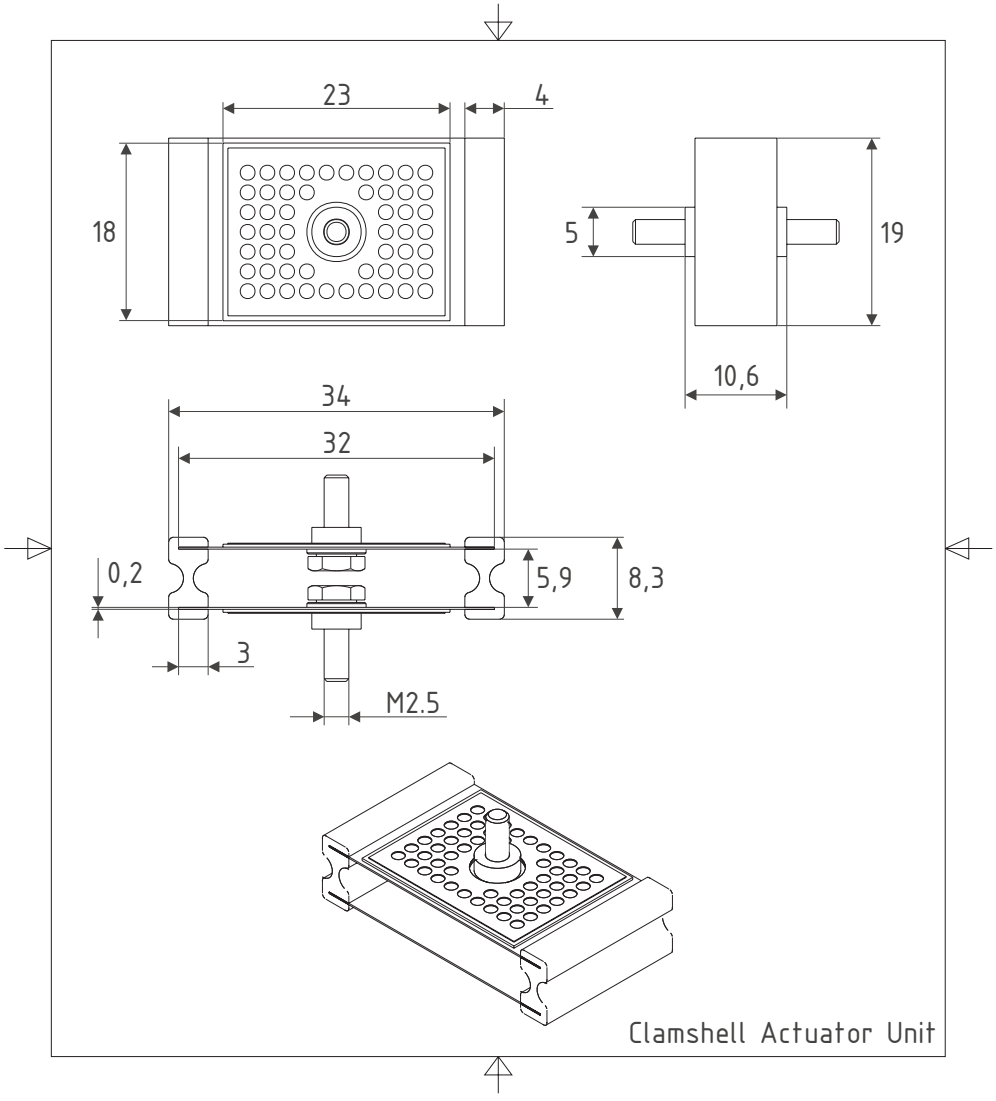

Figure B.1: Clamshell actuator unit

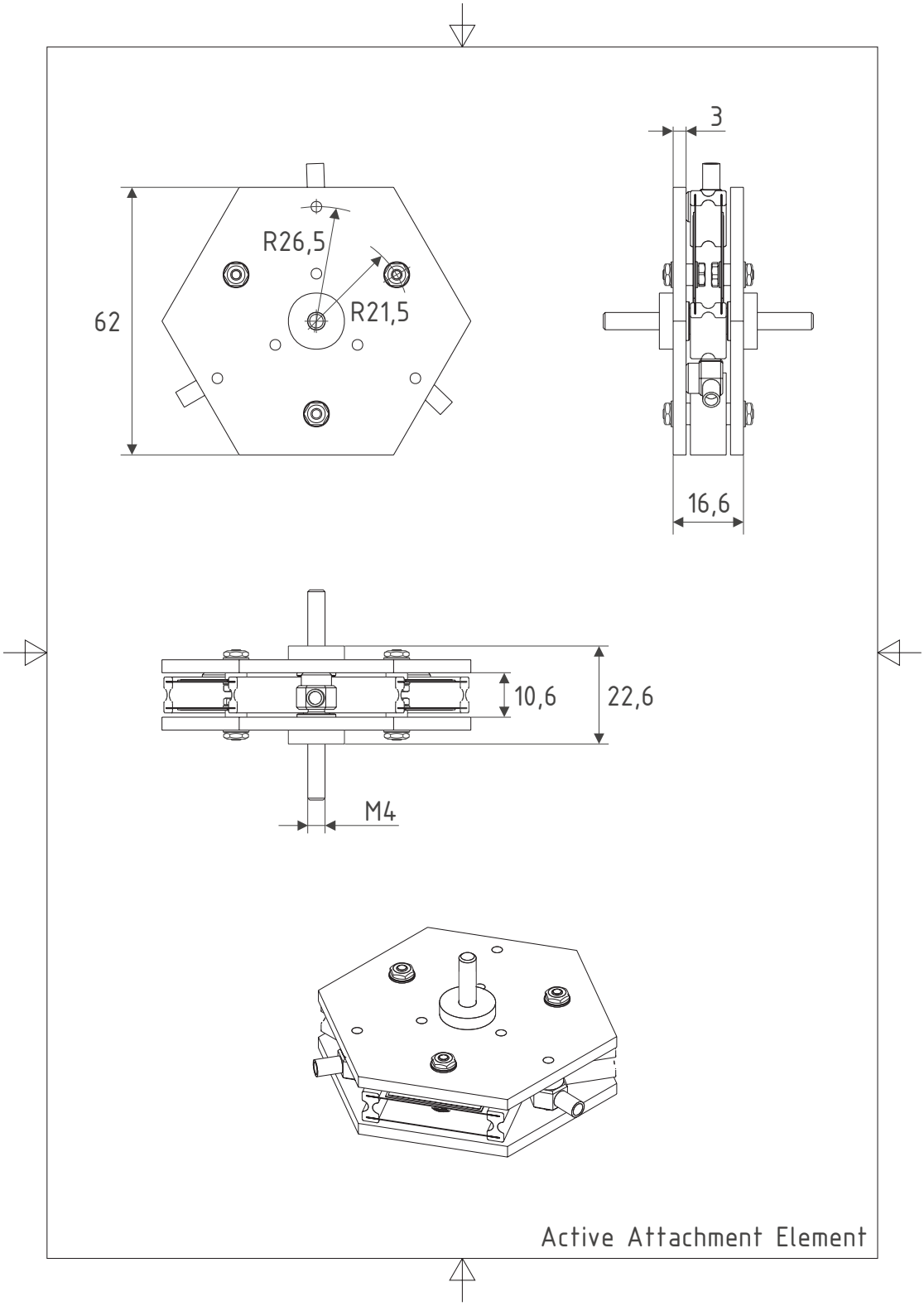

Figure B.2: Active attachment element

Appendix C

Experimental Investigation

C.1 Test Structure

C.1.1 Material Parameters Fuselage Panel

The CFRP skin panel is stiffened by five CFRP-stringers (structurally integrated into the skin, spacing 175 mm) and two perpendicular CFRP-frames (riveted to the skin and stringers respectively, spacing 533 mm). Materials and stacking sequence for the skin panel are listed in Table C.1.

Table C.1: Material parameters fuselage skin

Layer	**Material* and Orientation****
1	Cytec Adhesive Film BMS5-154 TY2CL1GR5 Melt Bond 1515
2	Expanded foil
3	Fiberite Dry fabric 3k70-T400H-PW, 0°, 90°
4	Saertex Multiaxial fabric IM7-12K, 0°, +45°, -45°
5	Saertex Multiaxial fabric IM7-12K, -45°, +45°, 0°
6	Saertex Multiaxial fabric IM7-12K, 0°, +45°, -45°
7	Saertex Multiaxial fabric IM7-12K, +45°, -45°, 0°
8	Fiberite Dry fabric 3k70-T400H-PW, 0°, 90°
9	Saertex Multiaxial fabric IM7-12K, 0°, +45°, 0°, -45°
10	Saertex Multiaxial fabric IM7-12K, 0°, 90°, 0°

* manufactured in resin infusion technique, epoxy resin type 977-2-1000gsm (Cytec); ** 0° direction is defined along the stringer direction

The stringers are made from a braided tube reinforced with a prepreg bulb:

- Foot and web: braided triaxial sleeving in carbon fibre HTA-6K ID 58 mm - FAW 917 gmq, Wth 0,86 mm, 167 g/m - 58% 0°, 42% ±57°
- Bulb: carbon fibre prepreg Tape HYE 977-2/ HTA-12K / 35 268/ 300, TH. 0.25, DAN 432 REV. 2, (Cytec/Fiberite)

The frames are built in a C-sectioned design and have a total thickness of 3,75 mm. The frame height is 90 mm, while the length of the flange is 35 mm:

- Material: carbon fibre HTS/977-2, thickness 0,25 mm for one single ply
- Stacking sequence: -45°, 0°, 0°, 90°, 0°, 0°, 45°, 0°, 45°, 0°, 0°, 90°, 0°, 0°, -45° (60% 0°, 27% ±45°, 13% 90°)

C.1.2 Material Parameters Trim Panel

Table C.2: Material parameters trim panel 1

Layer	**Material***
1	Hexcel V260/38/7781 fibreglass fabric
2	Nomex HRH 10 3/16.2, thickness 8 mm
3	Hexcel V260/38/7781 fibreglass fabric
4	Hexcel V260/60/1080 fibreglass fabric
5	PVF film (cabin side)

* honeycomb core trim panel, phenolique resin system

Table C.3: Material parameters trim panel 2

Layer	**Material***
1	PN 900-C08-45 carbon fibre fabric, thickness 0,18 mm
2	LN 29964-A2 Nomex honeycomb core, thickness 4 mm
3	PN 900-C08-45 carbon fibre fabric, thickness 0,18 mm
4	PN 900-44-43 fibreglass fabric, thickness 0,09 mm

* honeycomb core trim panel, cyanate-ester resin system

C.2 Additional Results

The actuator and sensor denotation and their layout with respect to the fuselage structure is given in Figure C.1. The relative positions of the attachment points with respect to the lower, left corner of the main structure are: ($x = 250$ mm; $y = 233,5$ mm), ($x = 750$ mm; $y = 233,5$ mm), ($x = 250$ mm; $y = 766,5$ mm) and ($x = 750$ mm; $y = 766,5$ mm). The ASAC test matrix is summarized in Table C.4:

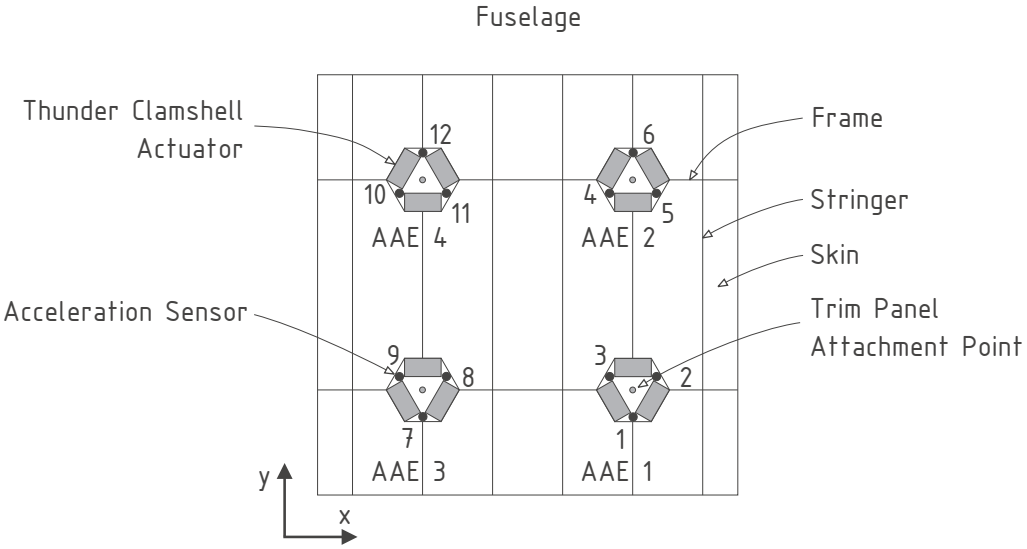

Figure C.1: Denotation and layout of active attachment elements and sensors

Table C.4: ASAC test matrix

Excitation	**Frequency**	**Structure**
Tonal acoustic:	78, 200, 326, 530 Hz	Trim panel 1
Random acoustic:	80 Hz, 80 & 200 Hz third oct. band	Trim panel 1
Tonal point force:	80, 199, 284, 702 Hz	Trim panel 1
Random point force:	80 Hz third octave band	Trim panel 1
Art. buzz-saw noise:	80 Hz and harmonics	Trim panel 2

Results are presented in terms of radiated sound power level, excitation sound pressure level or force and intensity plots with and without control respectively. For some selected configurations the control error signal and actuation voltage are also shown.

Acoustic Excitation - 200 Hz

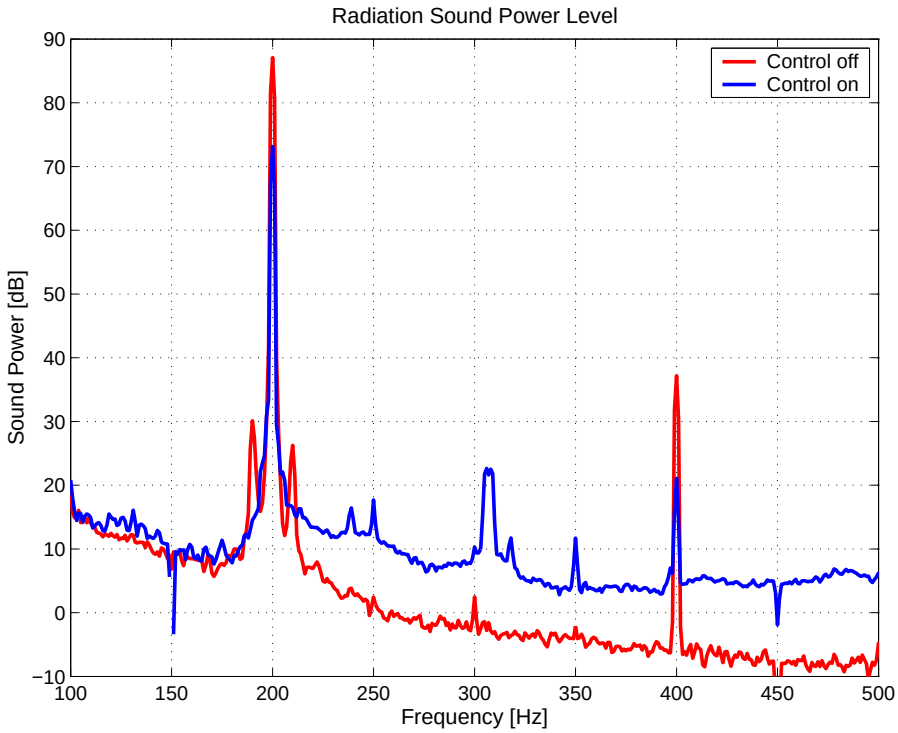

Figure C.2: Radiation sound power level

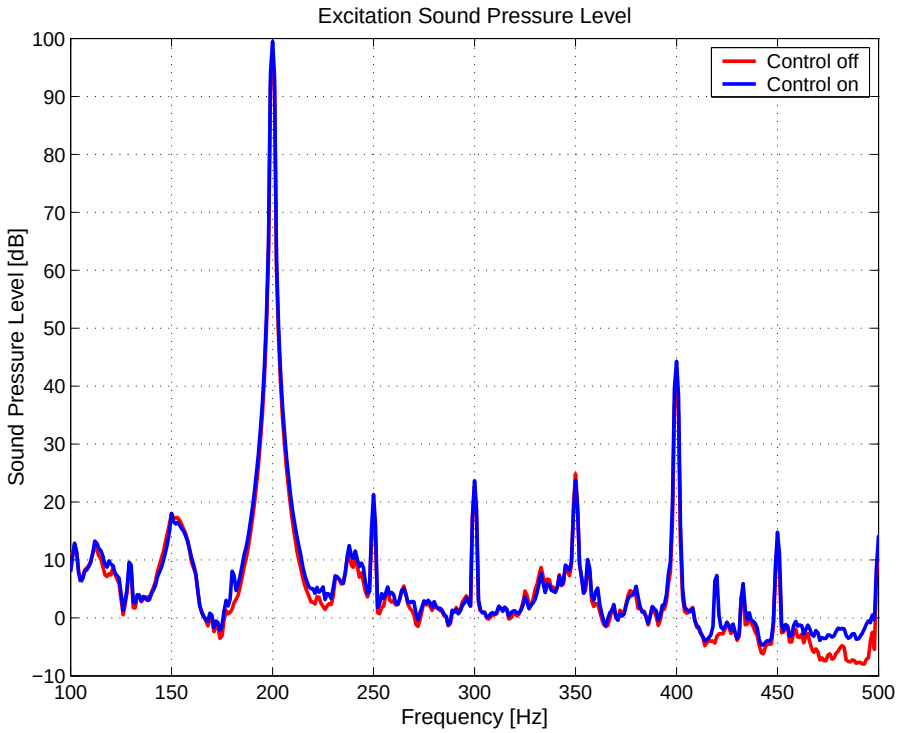

Figure C.3: Excitation sound pressure level

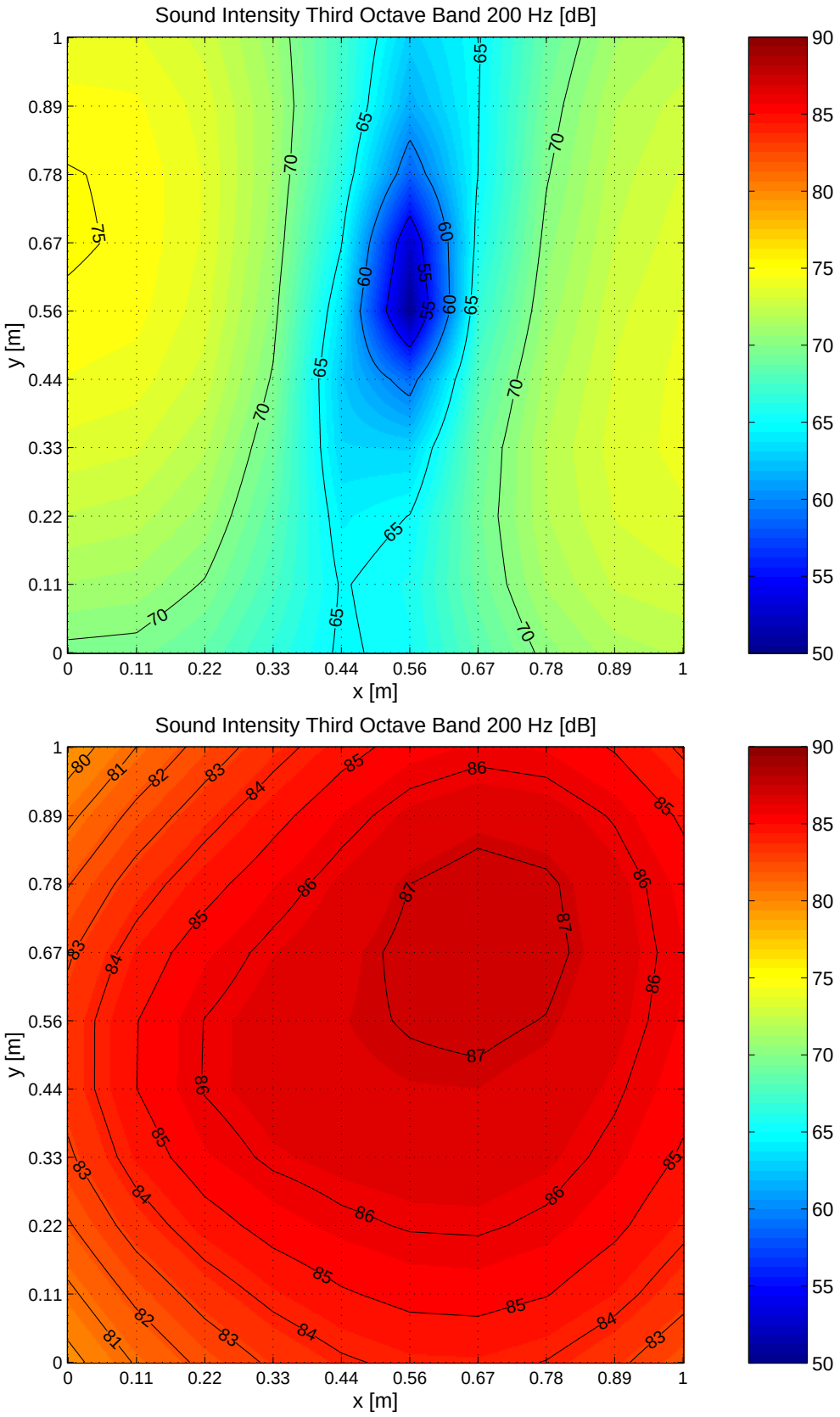

Figure C.4: Sound intensity level with (above) and without (below) ASAC control

Acoustic Excitation - 326 Hz

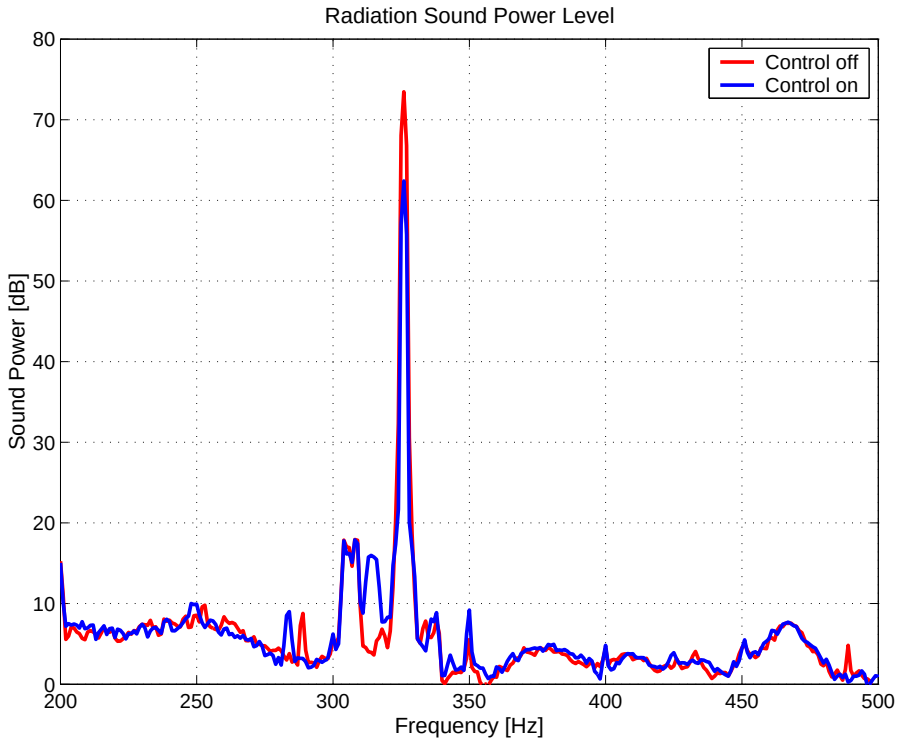

Figure C.5: Radiation sound power level

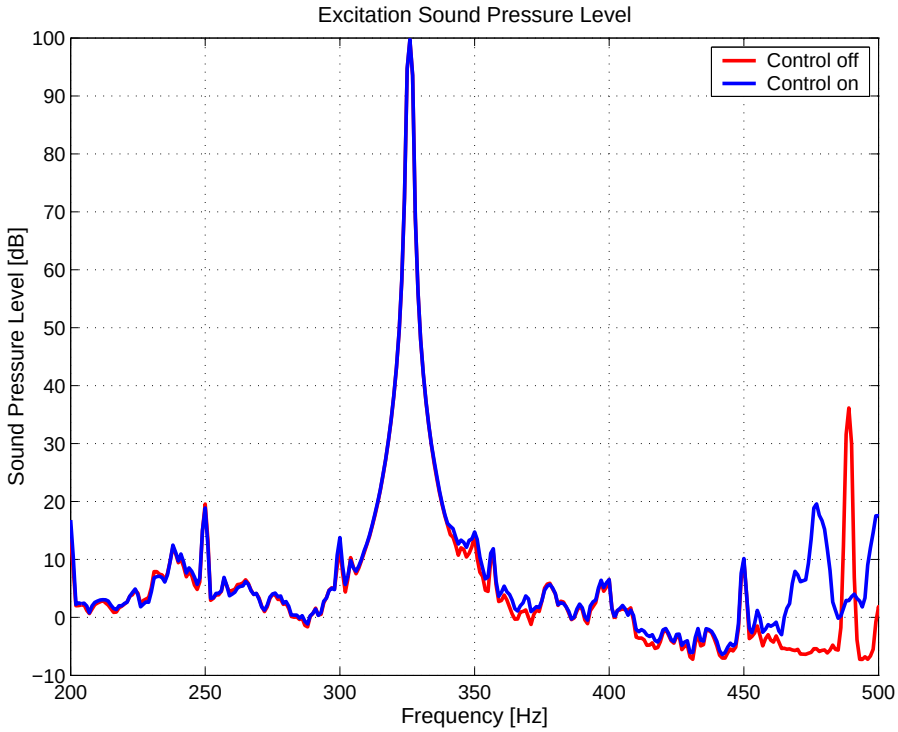

Figure C.6: Excitation sound pressure level

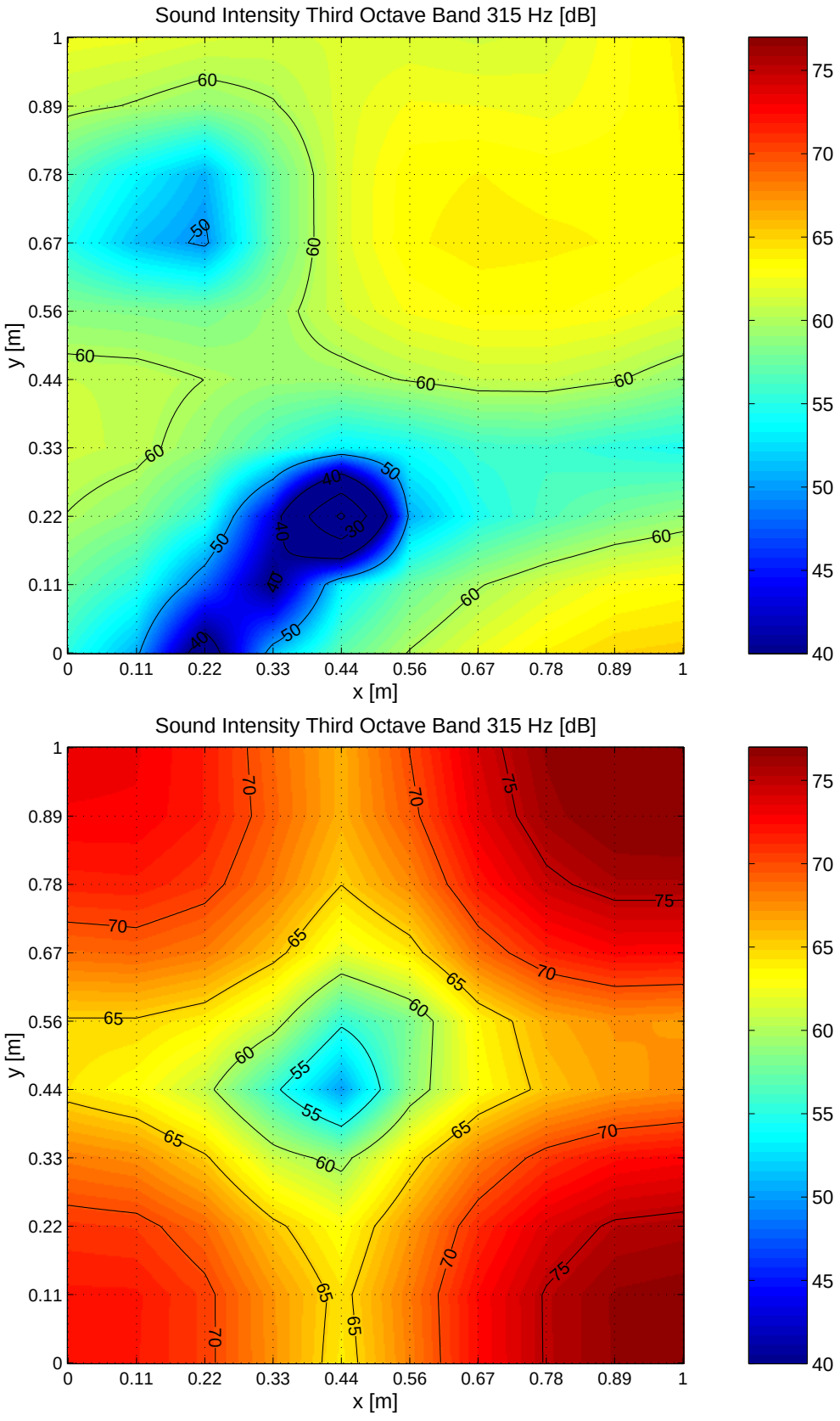

Figure C.7: Sound intensity level with (above) and without (below) ASAC control

Acoustic Excitation - 530 Hz

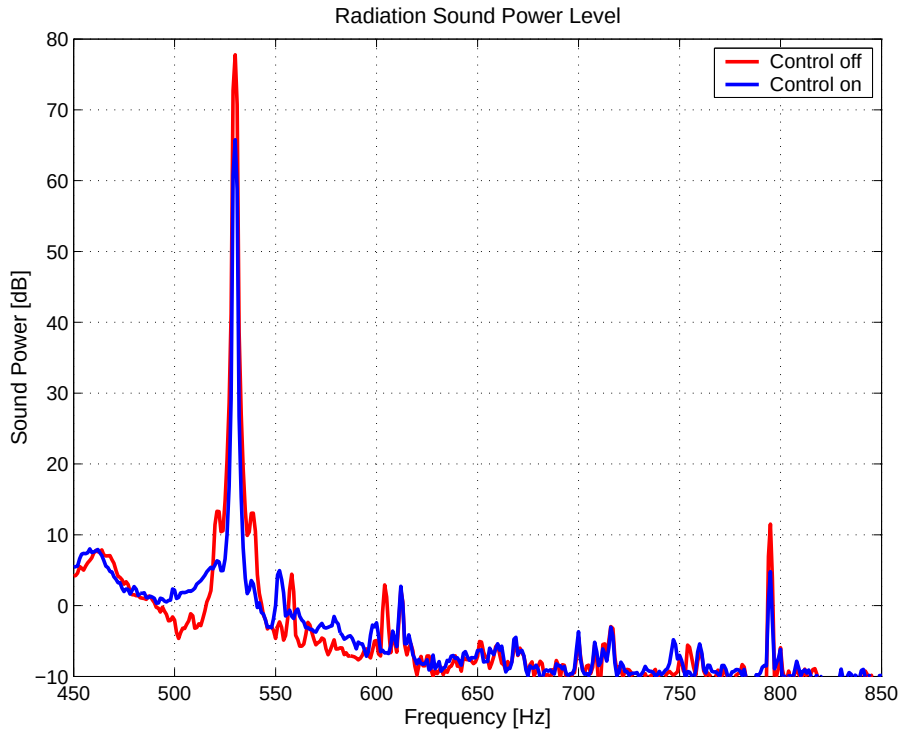

Figure C.8: Radiation sound power level

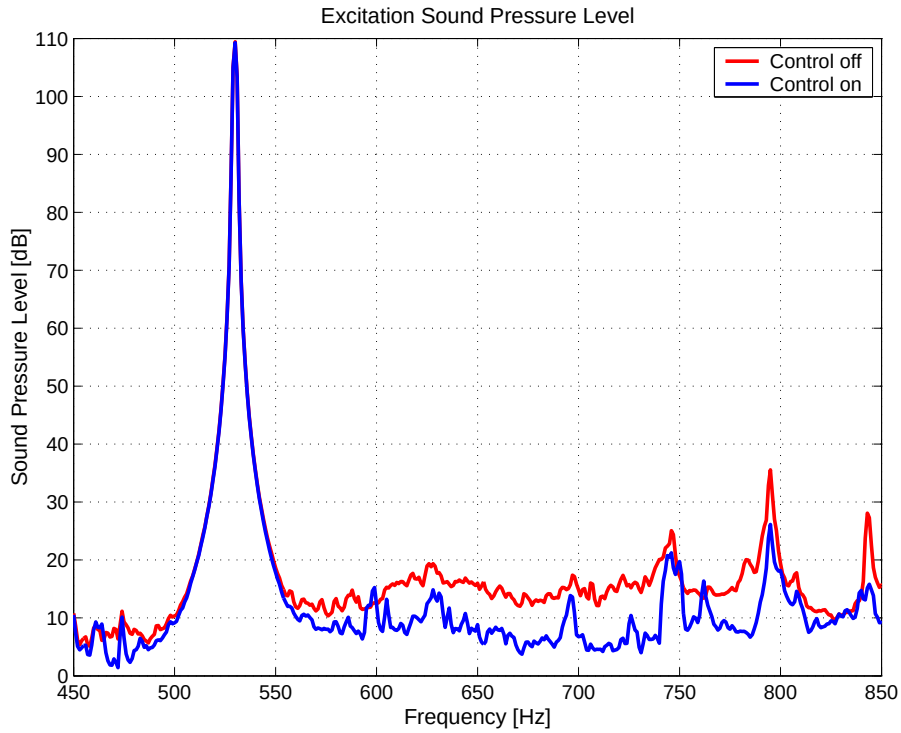

Figure C.9: Excitation sound pressure level

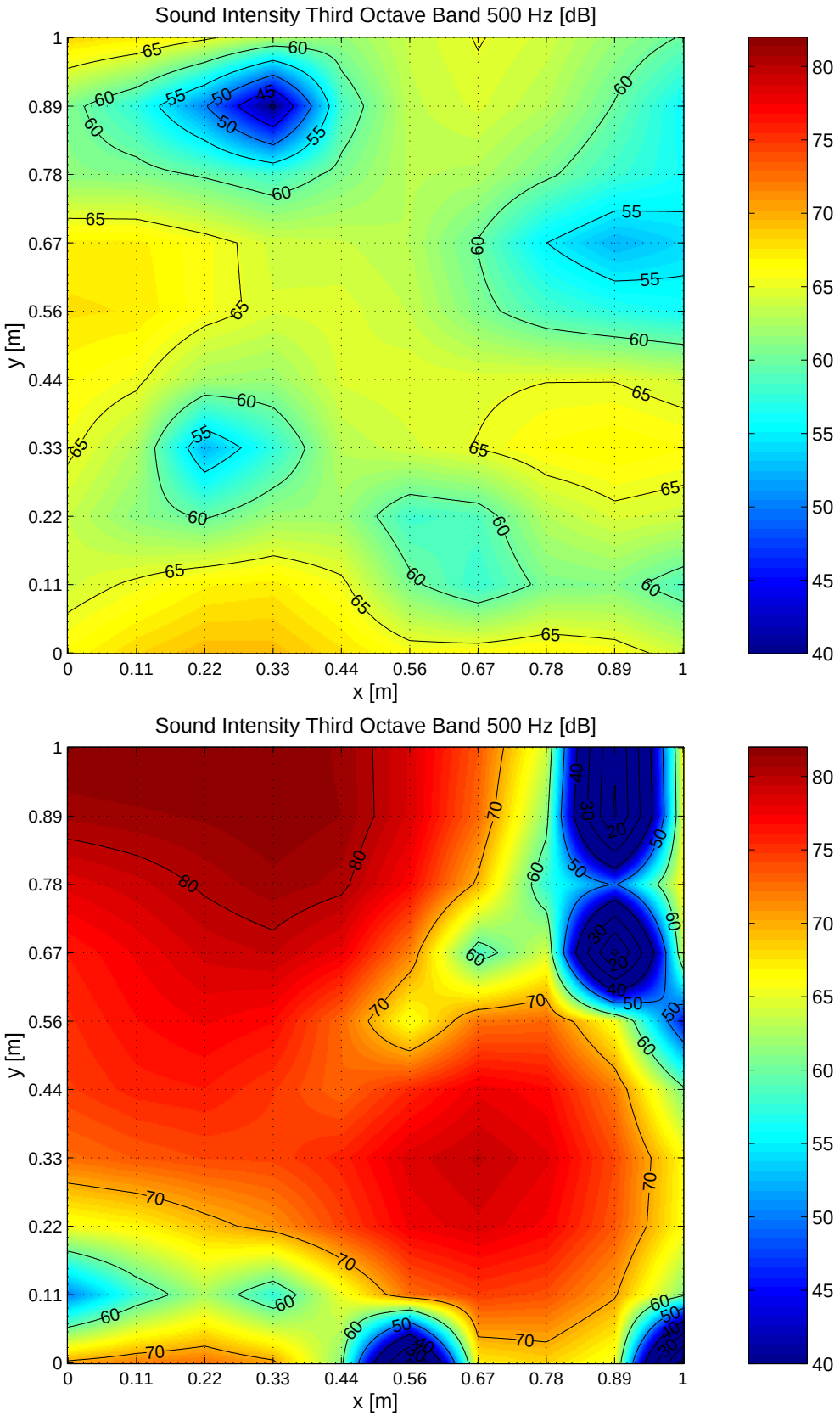

Figure C.10: Sound intensity level with (above) and without (below) ASAC control

Acoustic Excitation - Broadband Excitation 80 Hz Third Octave Band

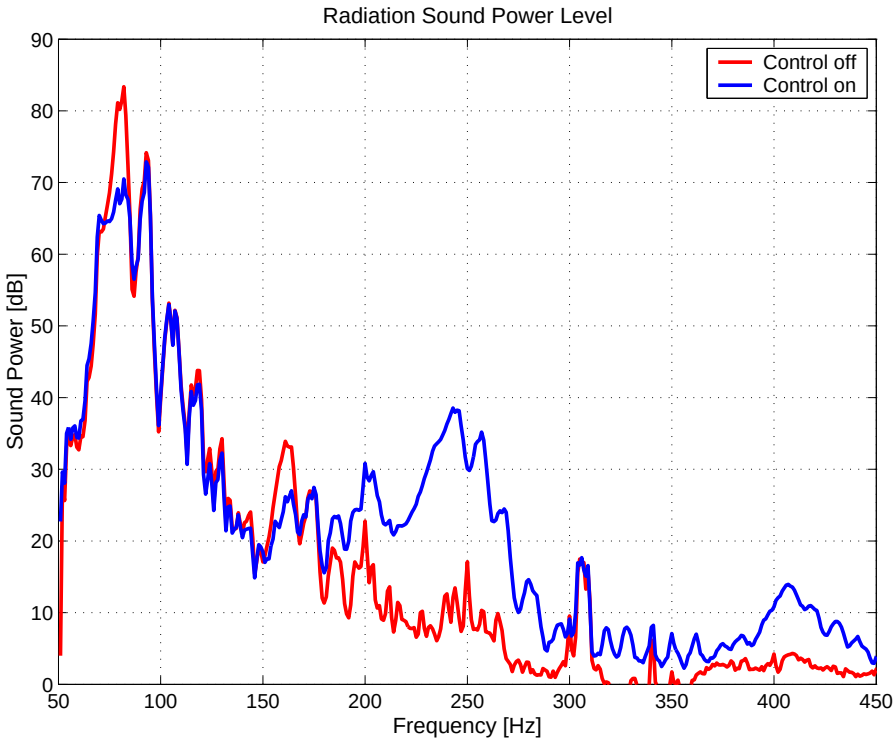

Figure C.11: Radiation sound power level

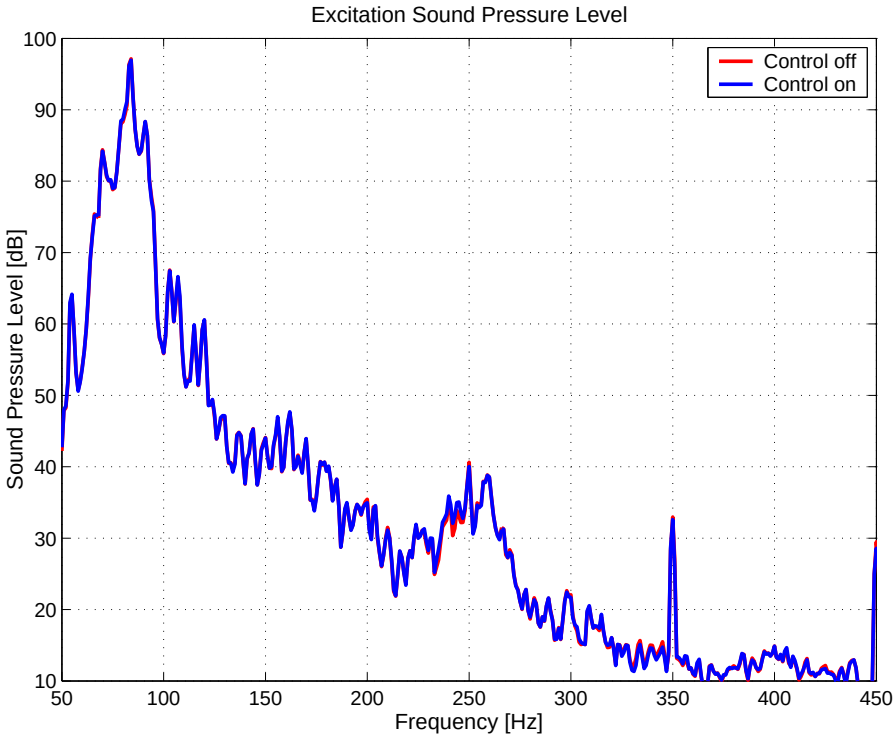

Figure C.12: Excitation sound pressure level

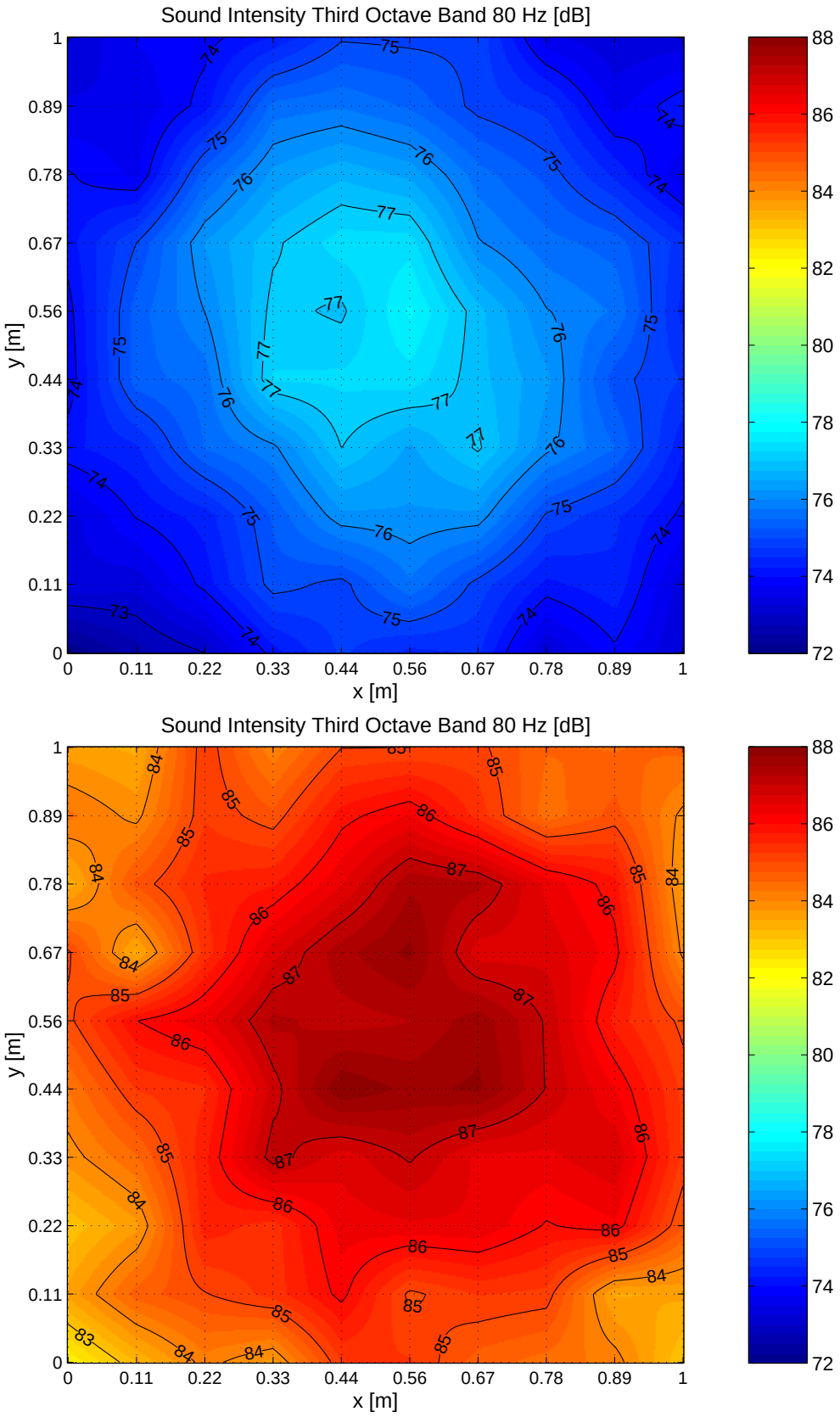

Figure C.13: Sound intensity level with (above) and without (below) ASAC control

Acoustic Excitation - Broadband Excitation 80 and 200 Hz Third Octave Band

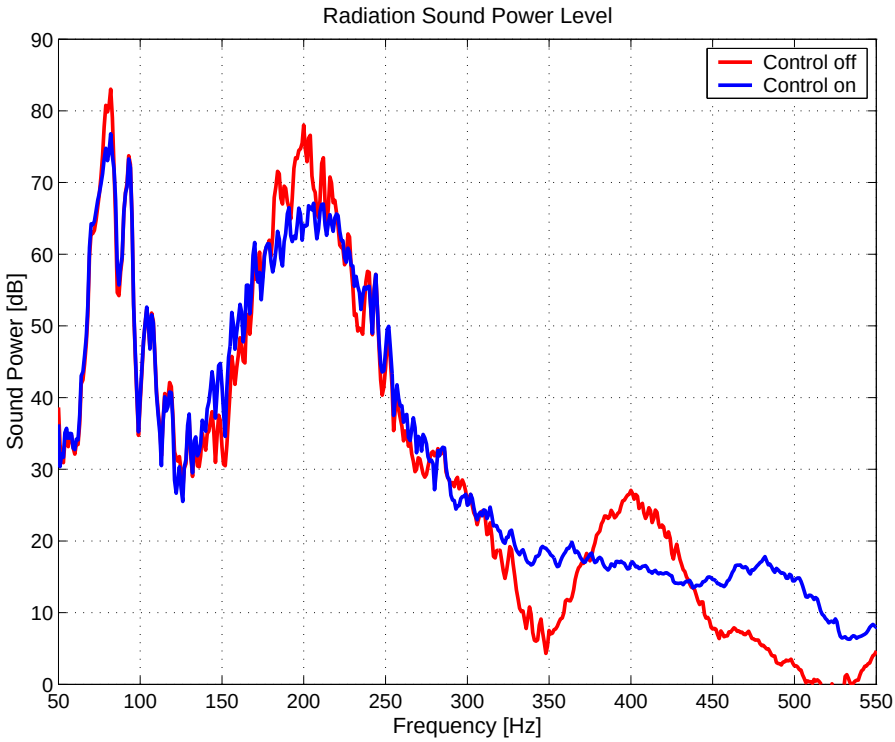

Figure C.14: Radiation sound power level

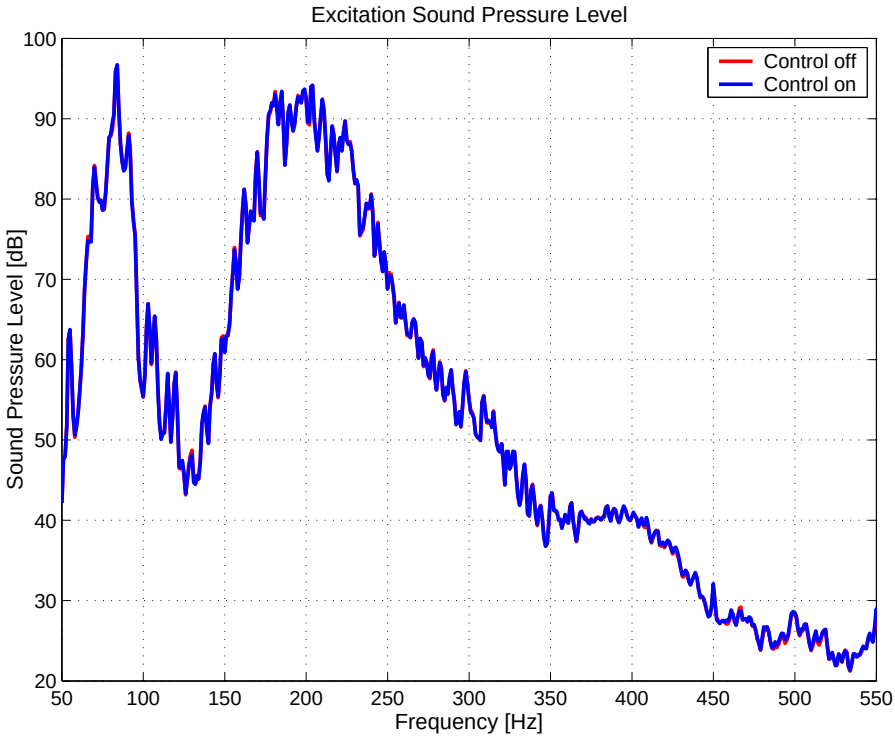

Figure C.15: Excitation sound pressure level

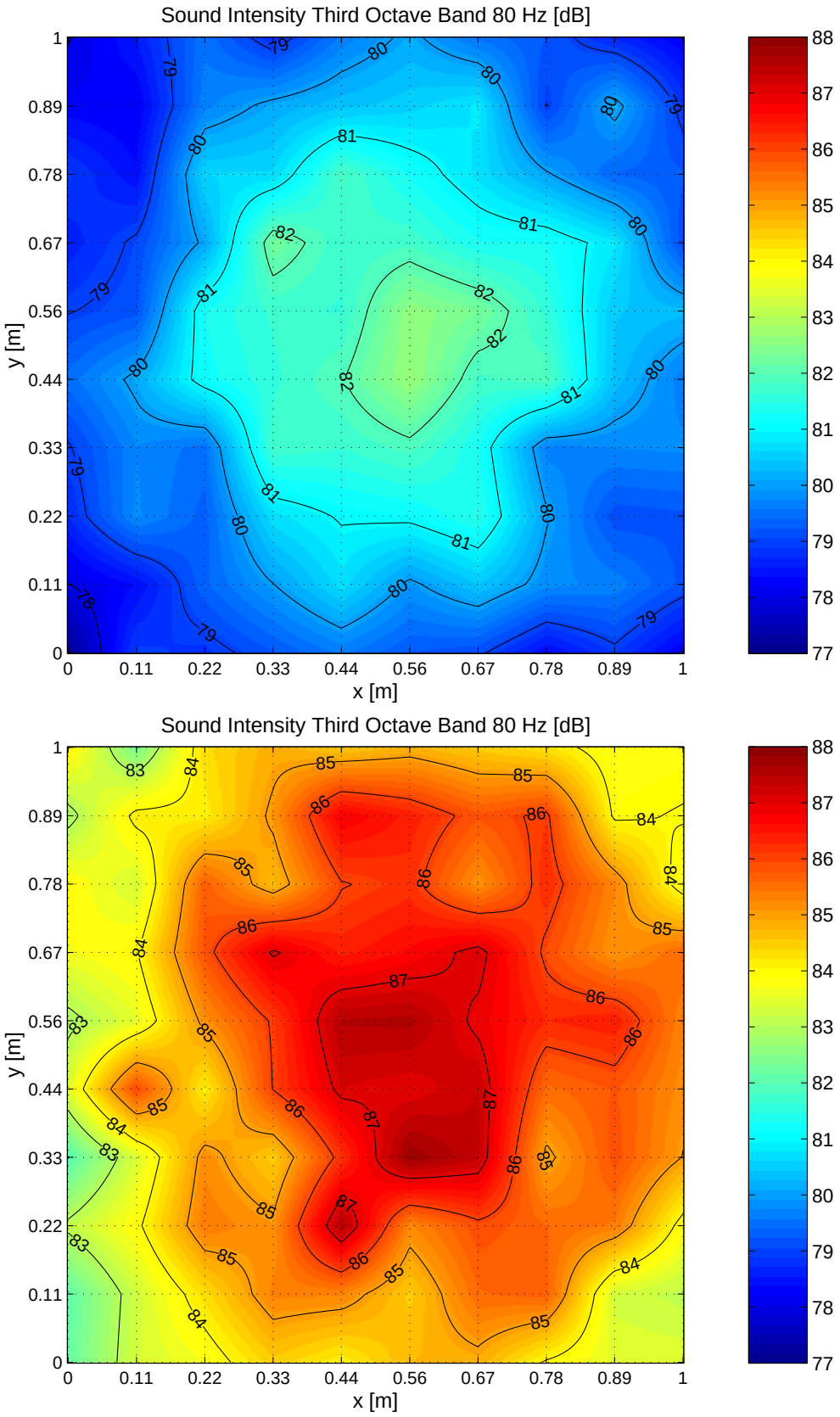

Figure C.16: Sound intensity level with (above) and without (below) ASAC control

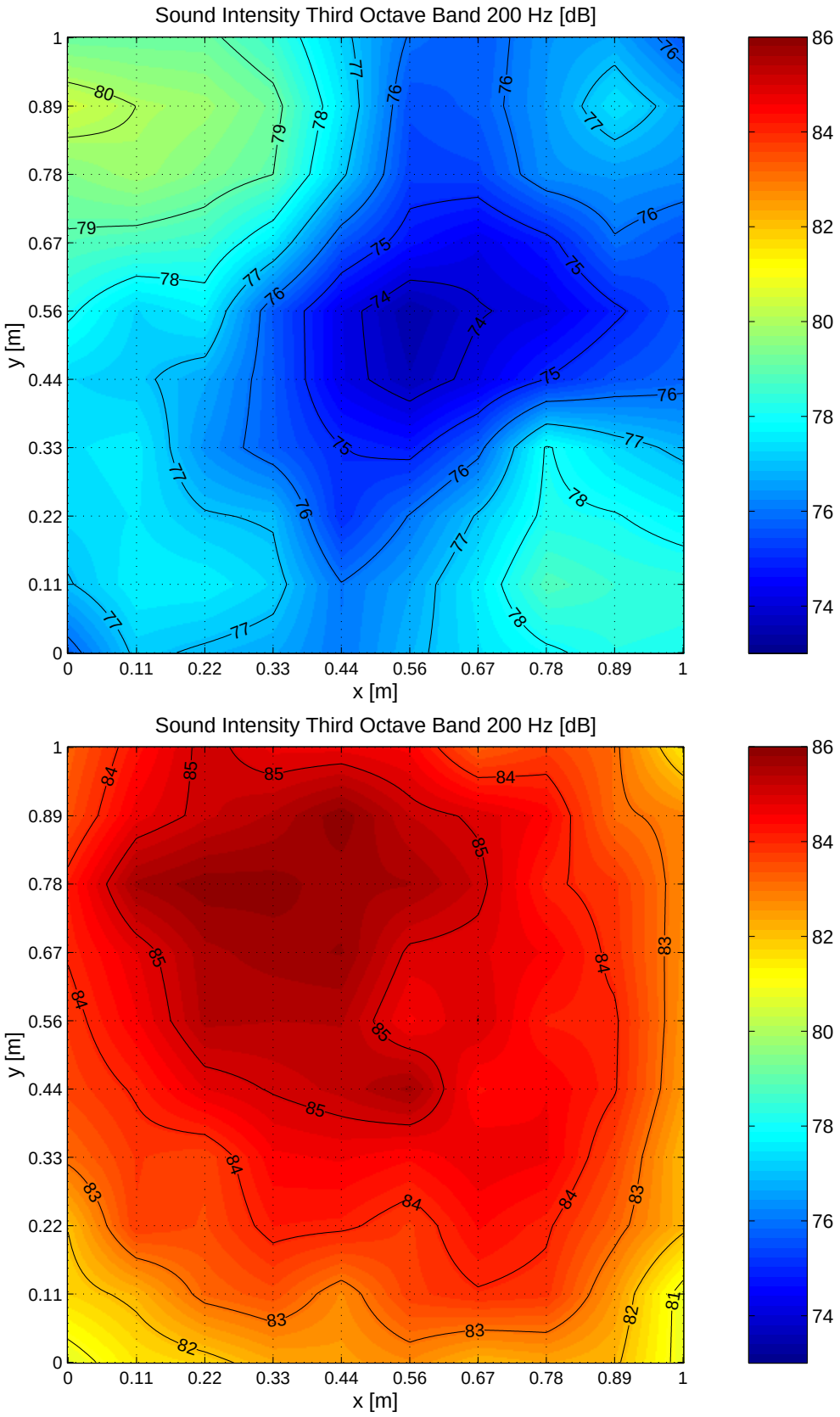

Figure C.17: Sound intensity level with (above) and without (below) ASAC control

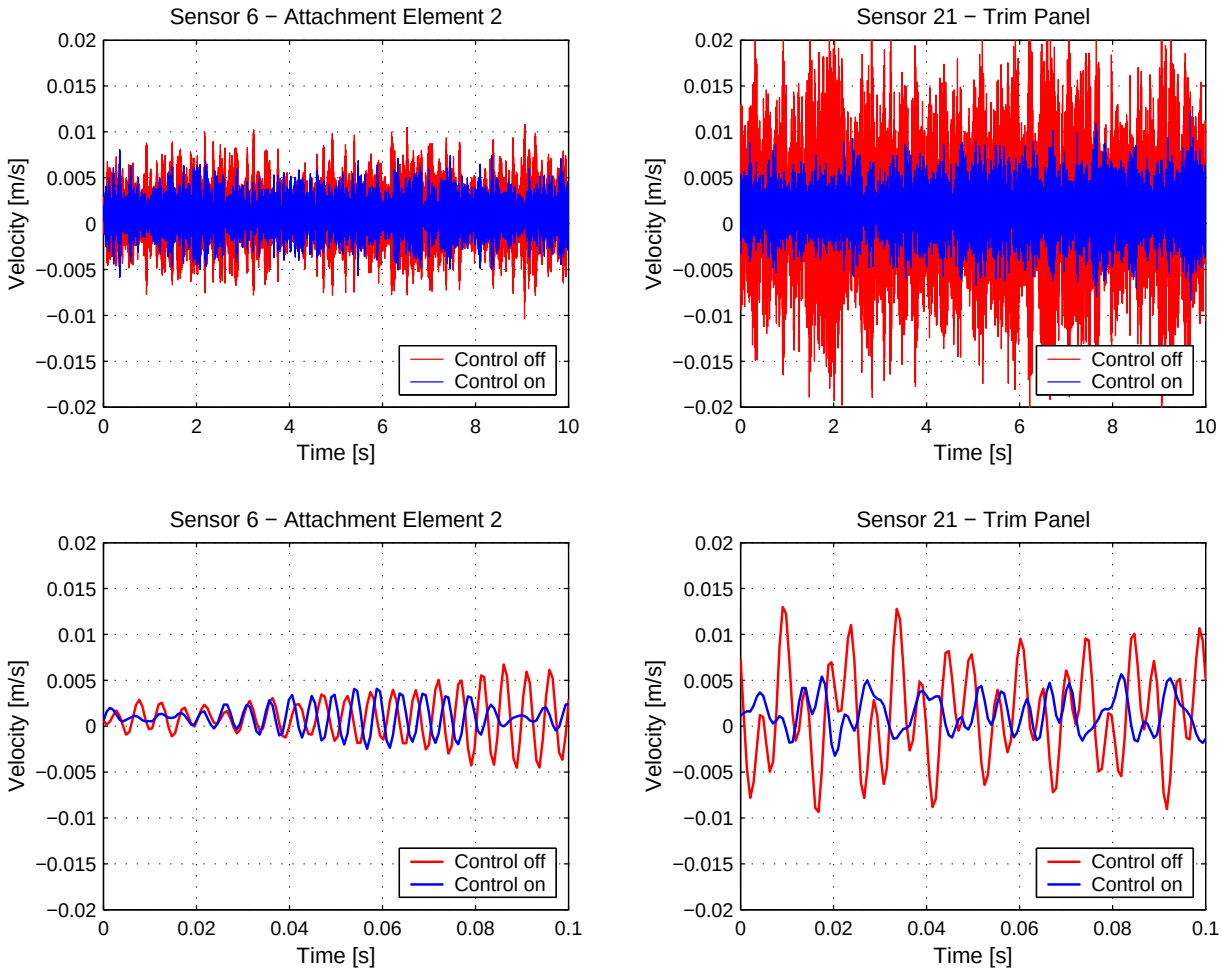

Figure C.18: Velocity measured by error sensor 6 and 21, with and without control

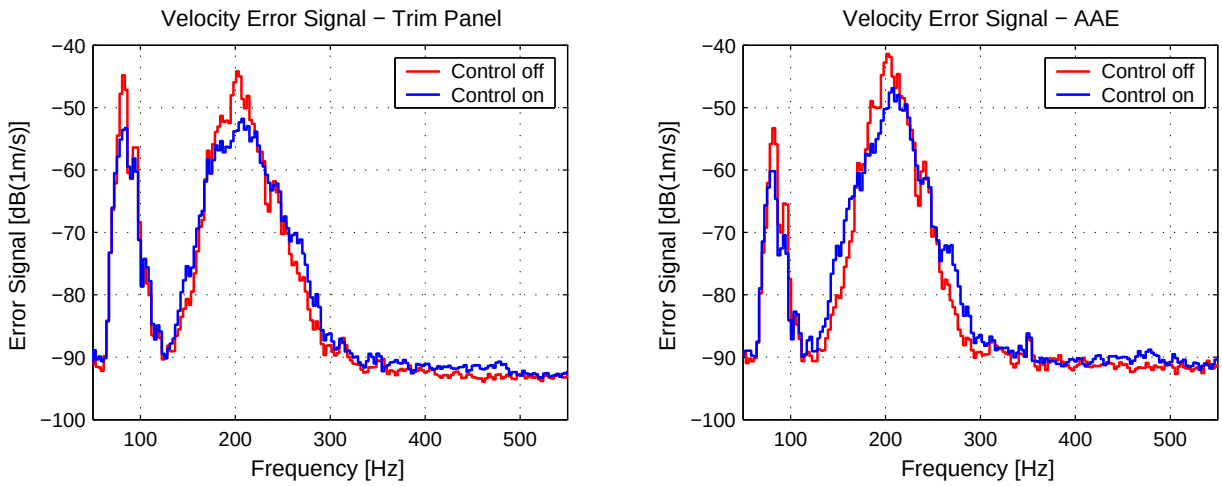

Figure C.19: Squared sum of error signals on trim panel and attachment elements

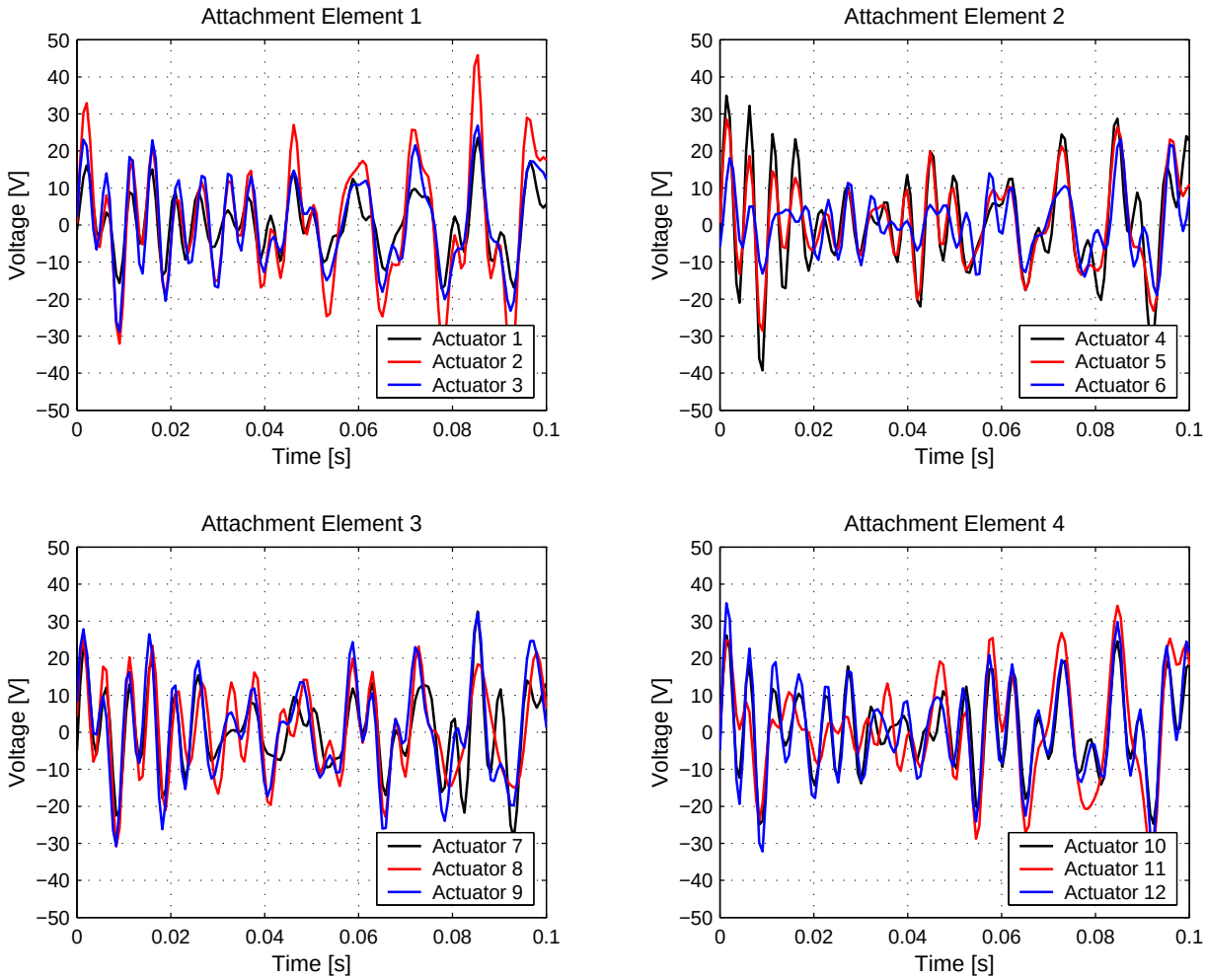

Figure C.20: Actuator voltage

Point Force Excitation - 80 and 199 Hz

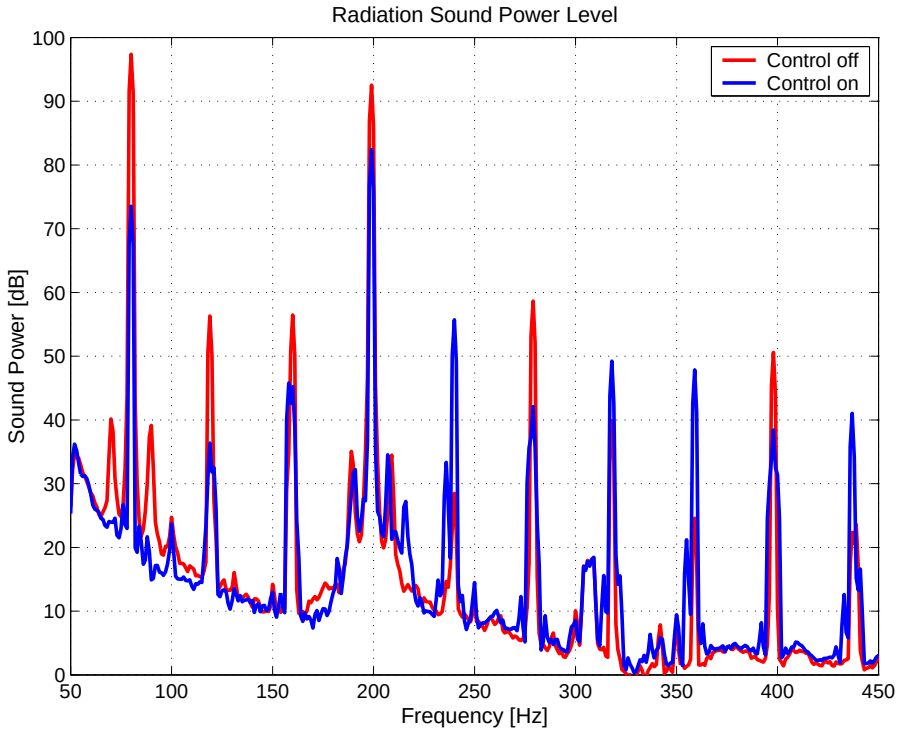

Figure C.21: Radiation sound power level

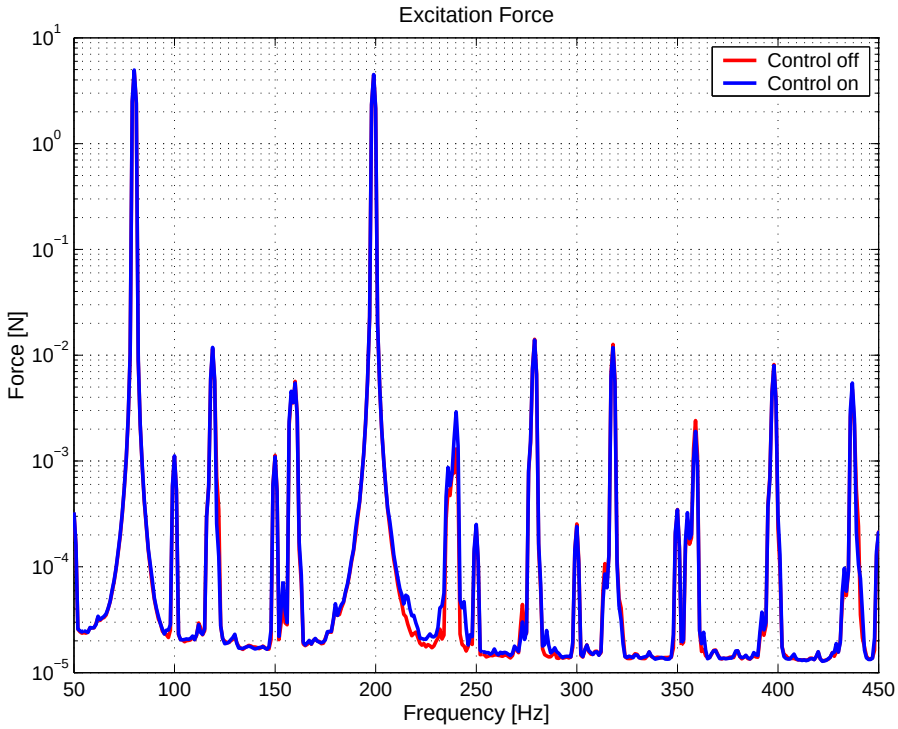

Figure C.22: Excitation force

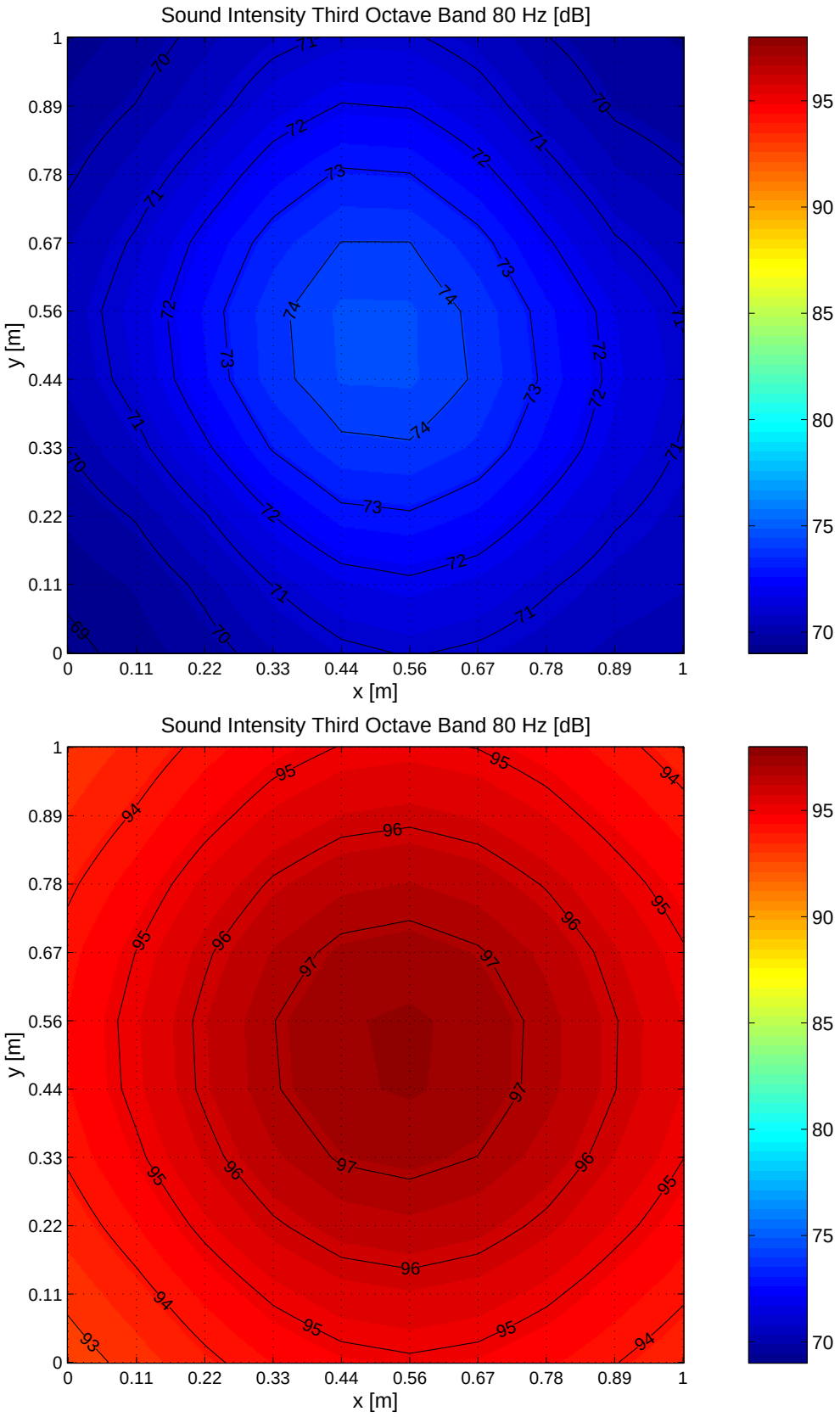

Figure C.23: Sound intensity level with (above) and without (below) ASAC control

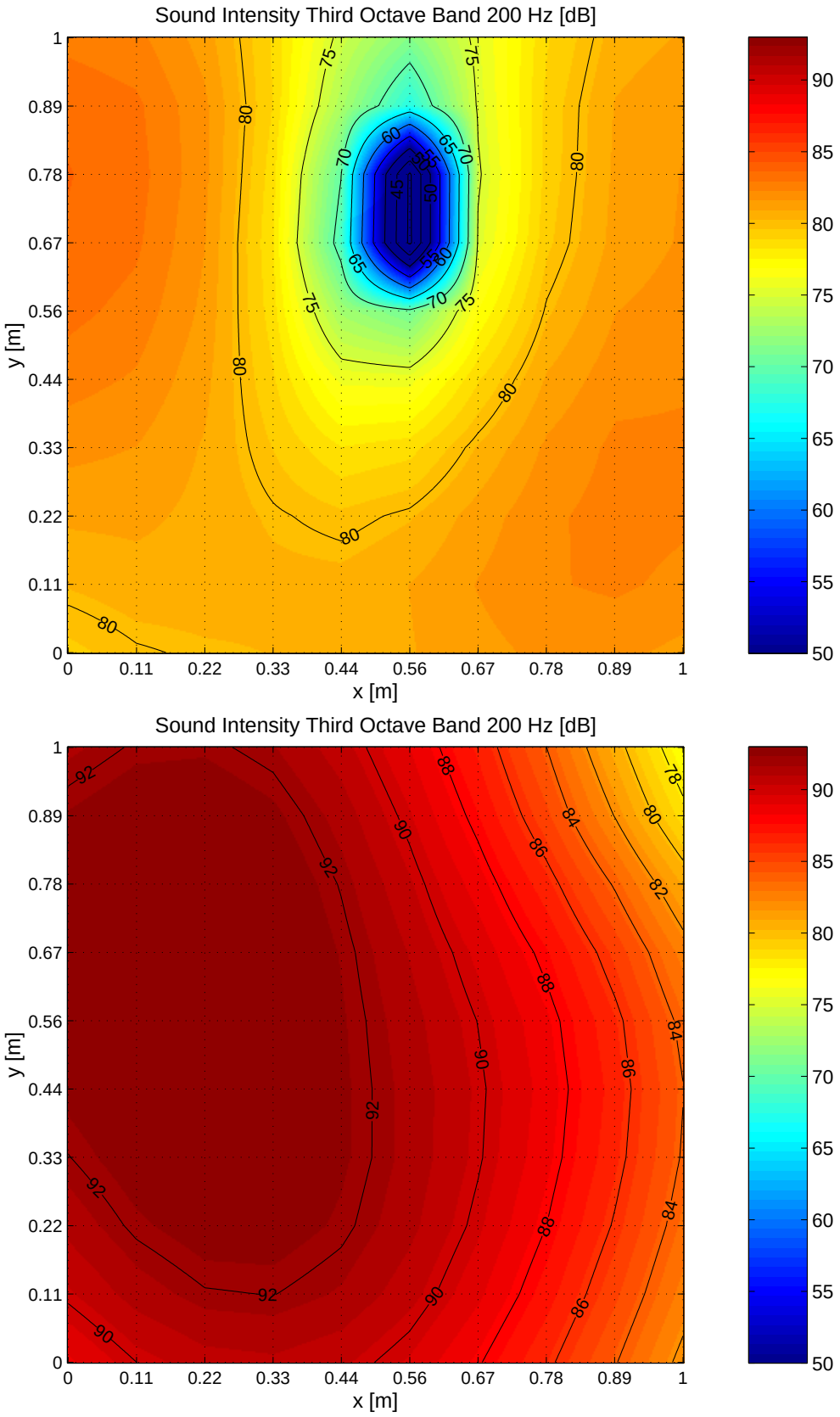

Figure C.24: Sound intensity level with (above) and without (below) ASAC control

Point Force Excitation - 284 Hz

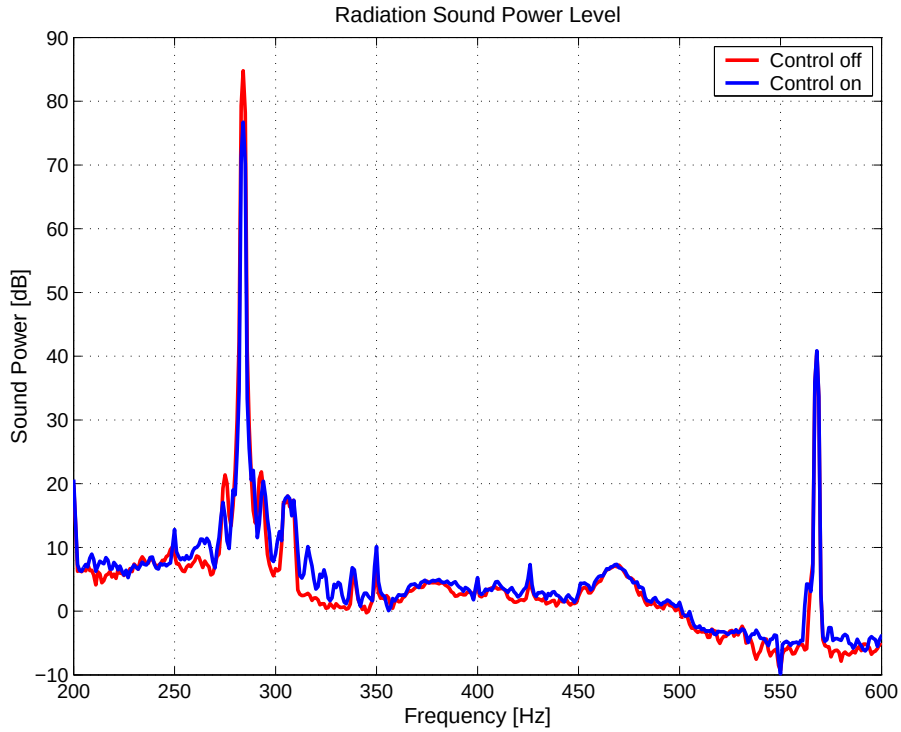

Figure C.25: Radiation sound power level

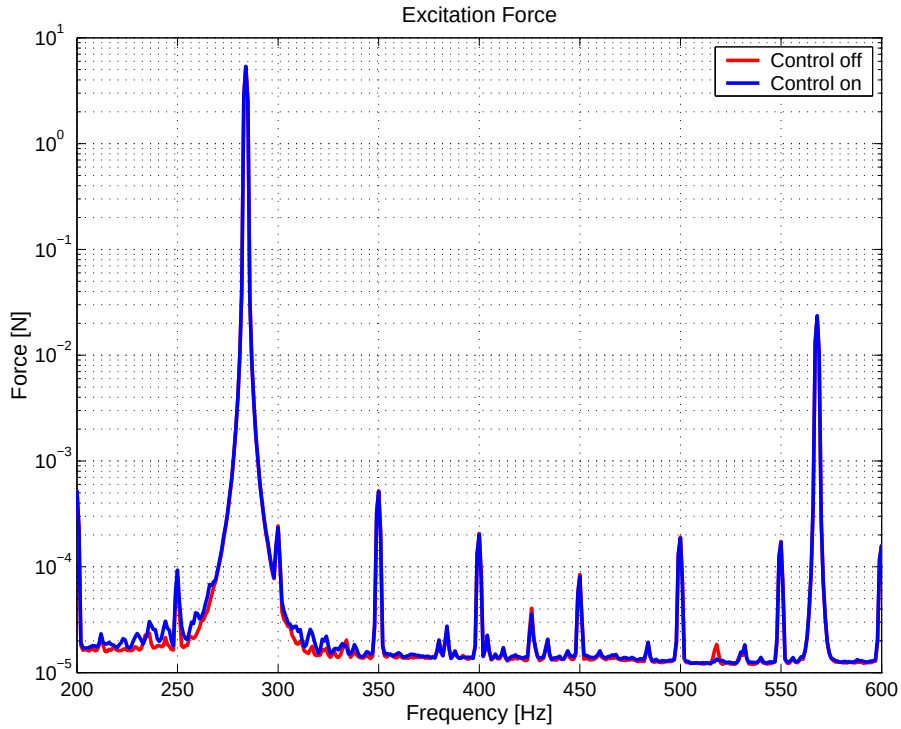

Figure C.26: Excitation force

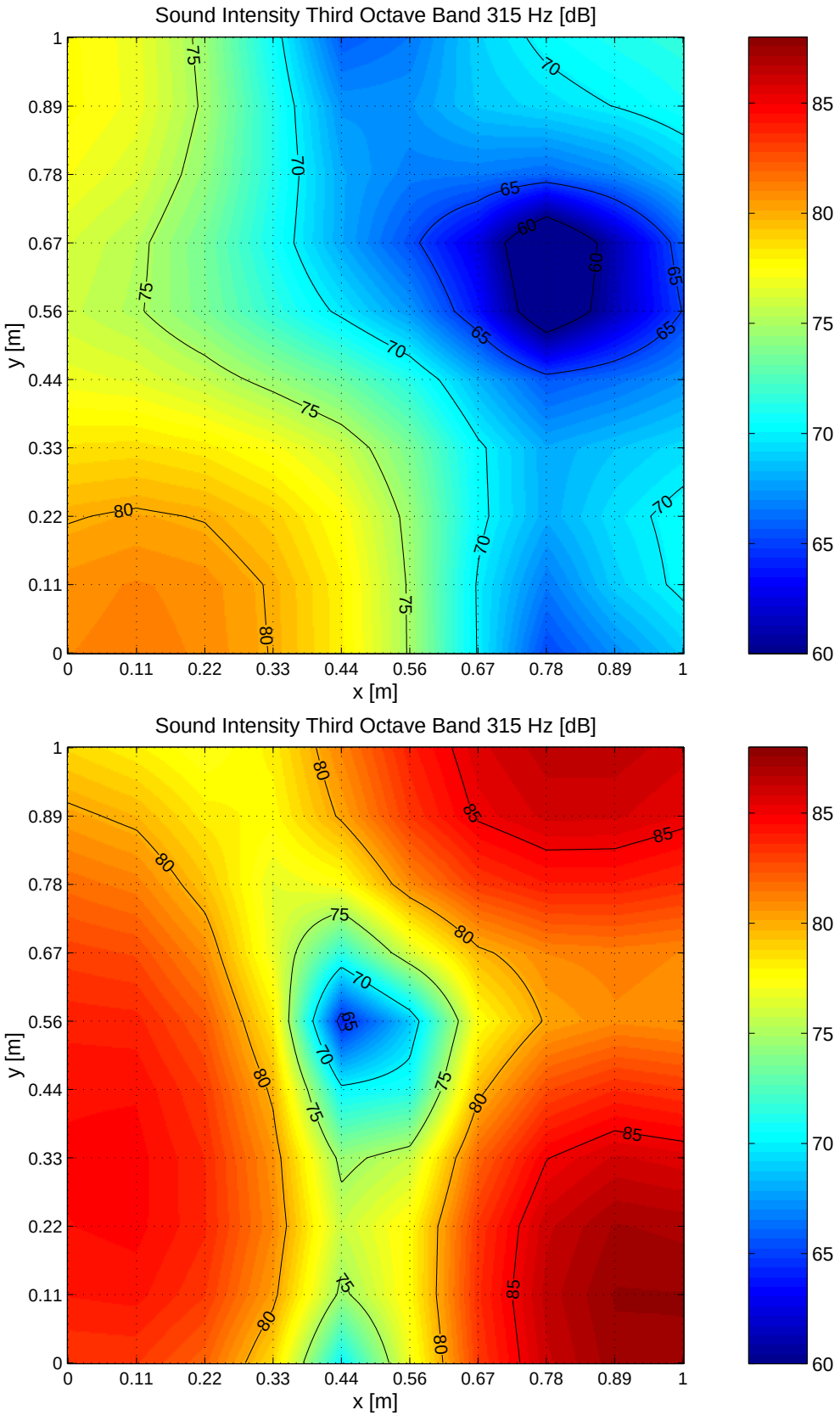

Figure C.27: Sound intensity level with (above) and without (below) ASAC control

Point Force Excitation - 702 Hz

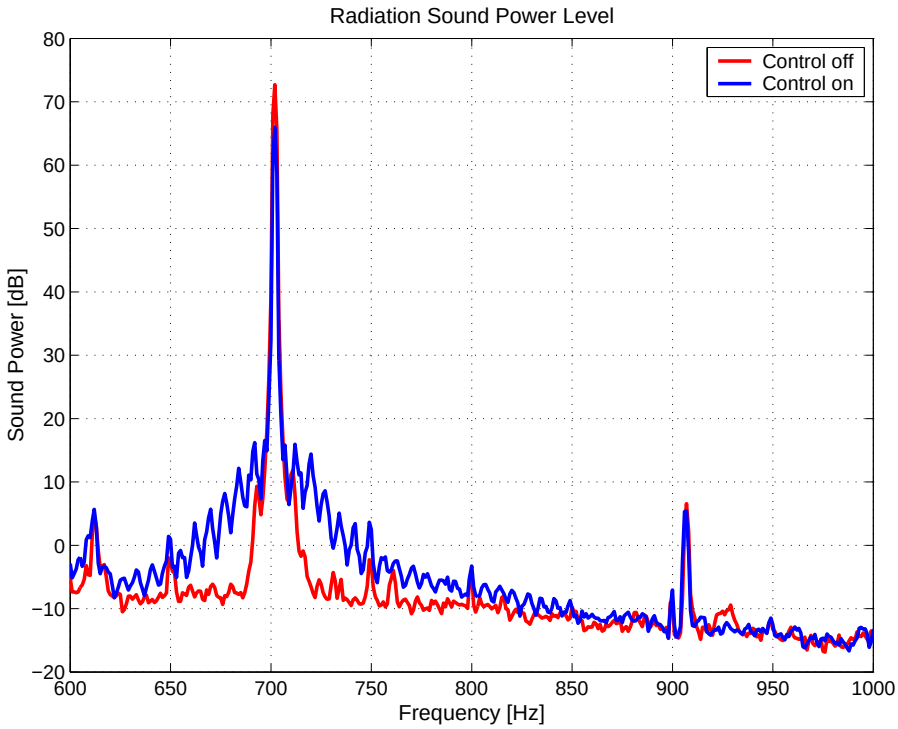

Figure C.28: Radiation sound power level

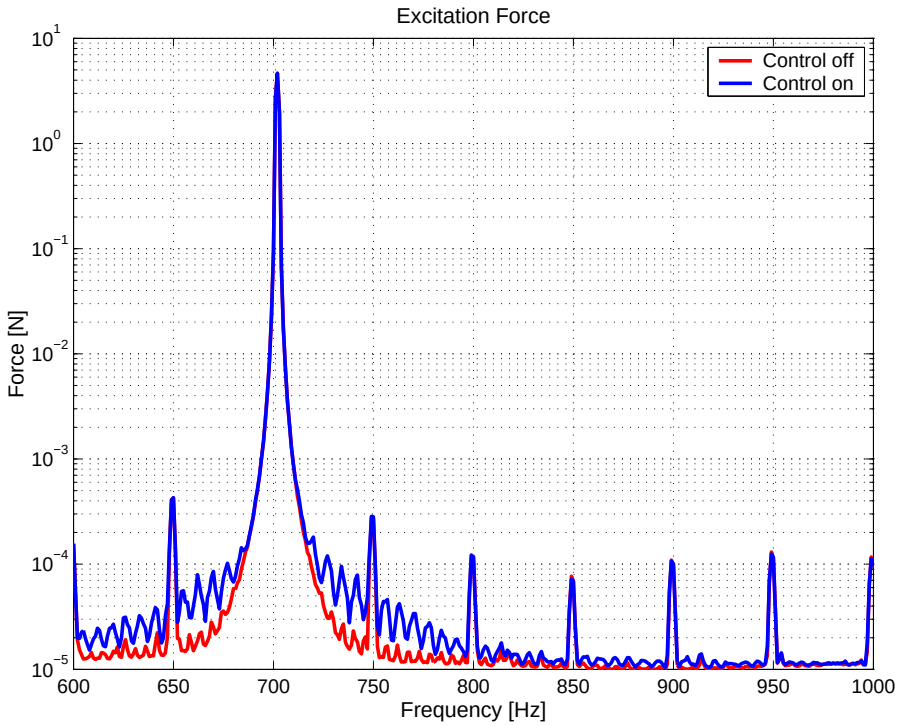

Figure C.29: Excitation force

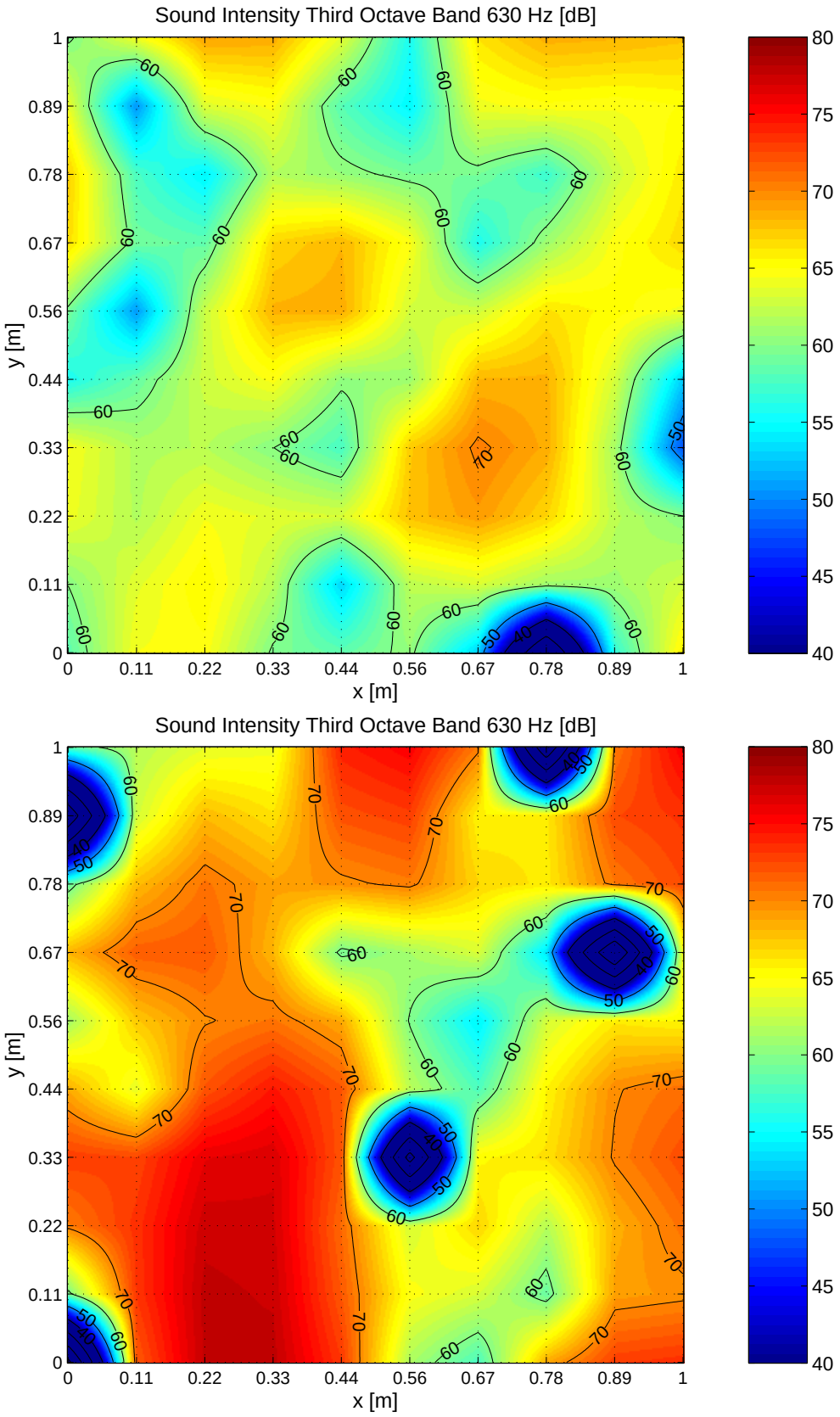

Figure C.30: Sound intensity level with (above) and without (below) ASAC control

Point Force Excitation - Broadband Excitation 80 Hz Third Octave Band

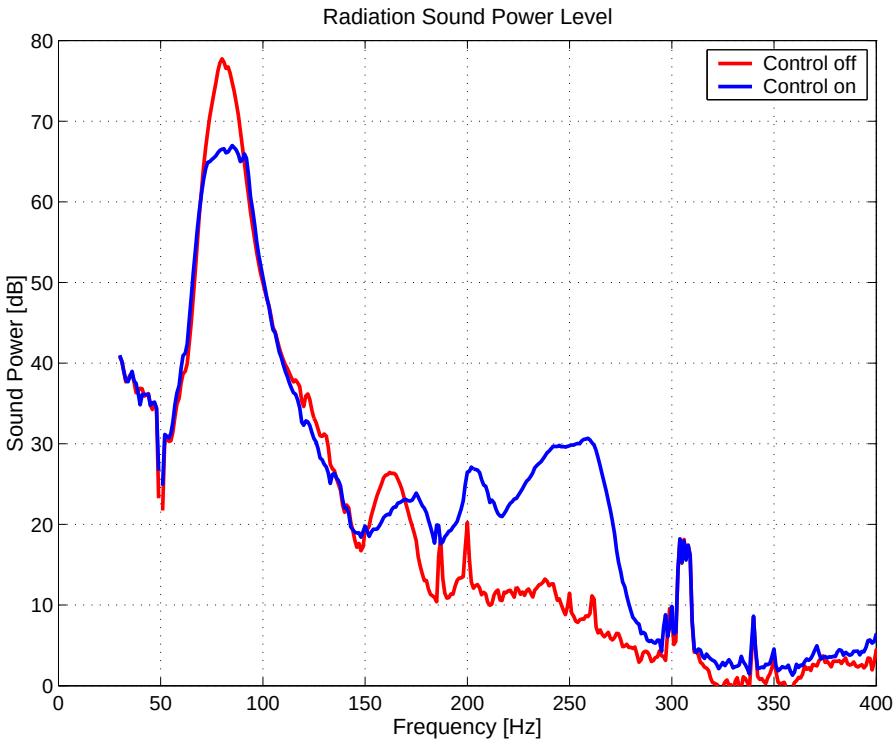

Figure C.31: Radiation sound power level

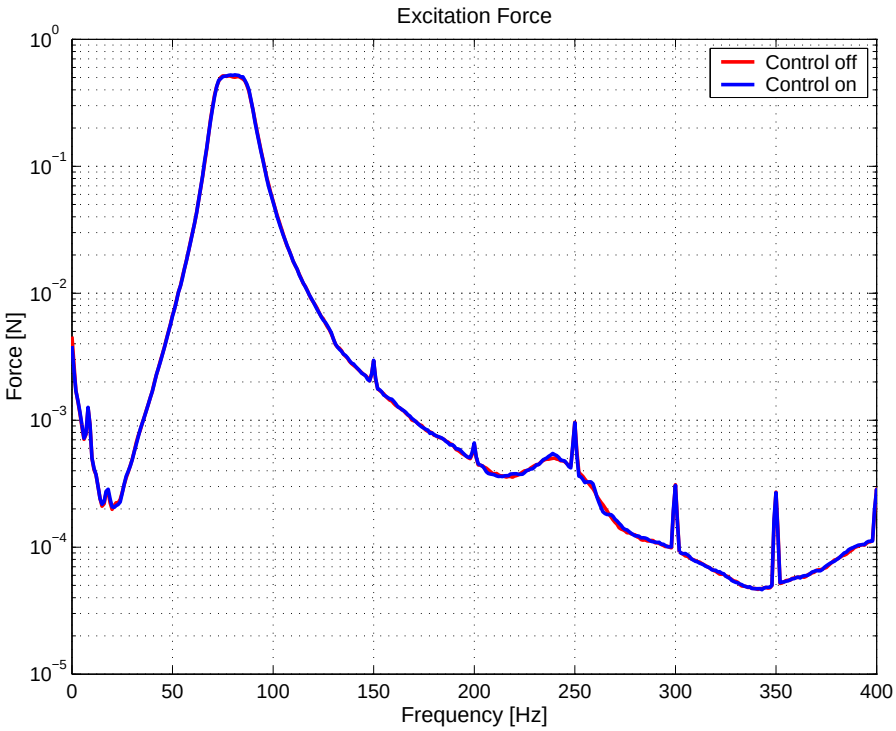

Figure C.32: Excitation force

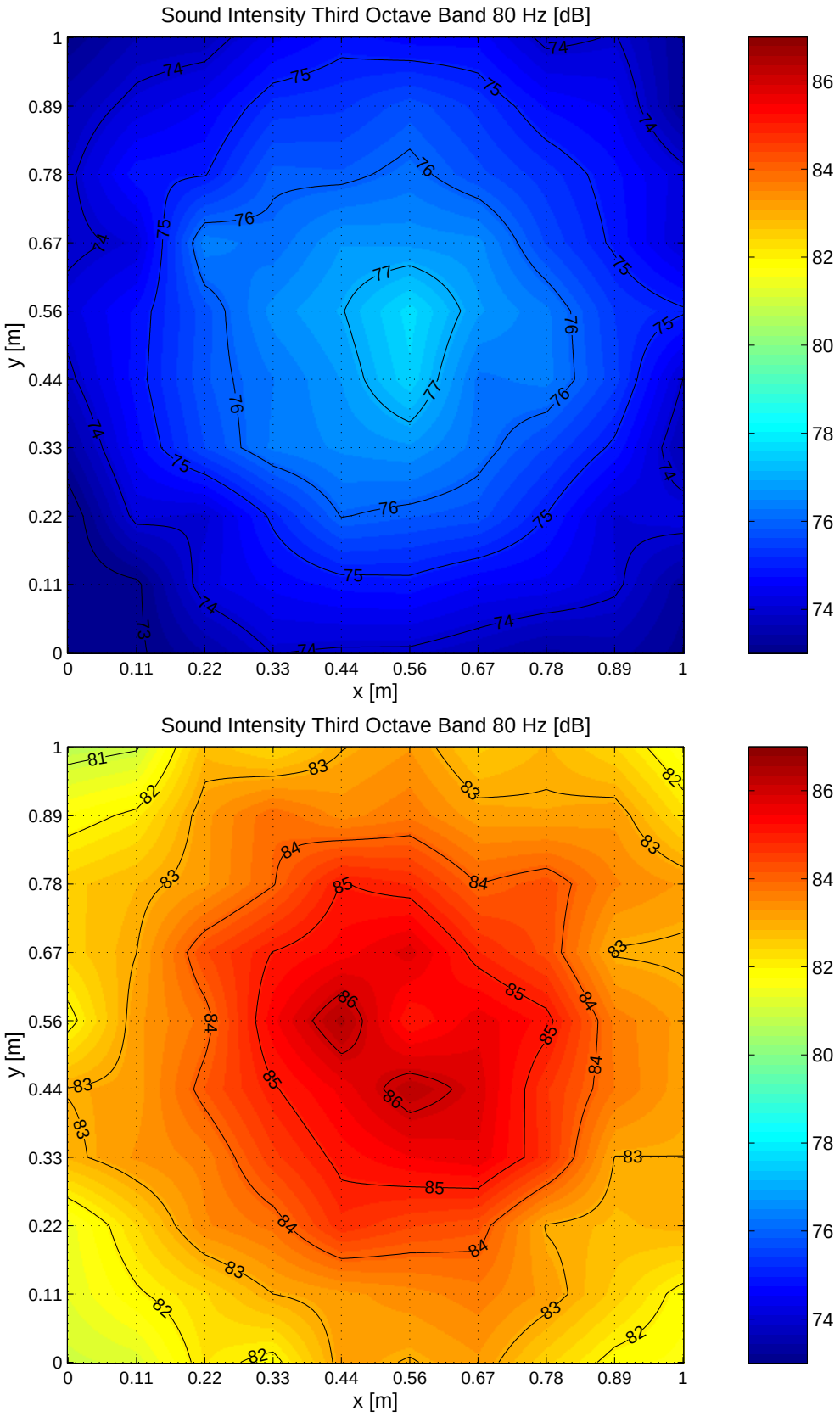

Figure C.33: Sound intensity level with (above) and without (below) ASAC control

Artificial Buzz-Saw Noise Excitation

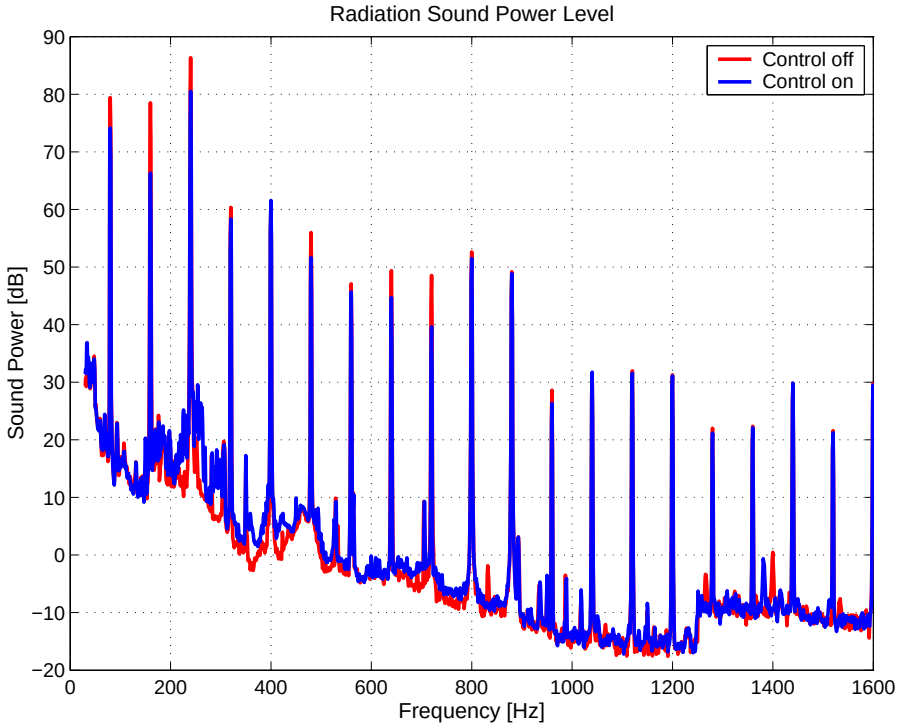

Figure C.34: Radiation sound power level

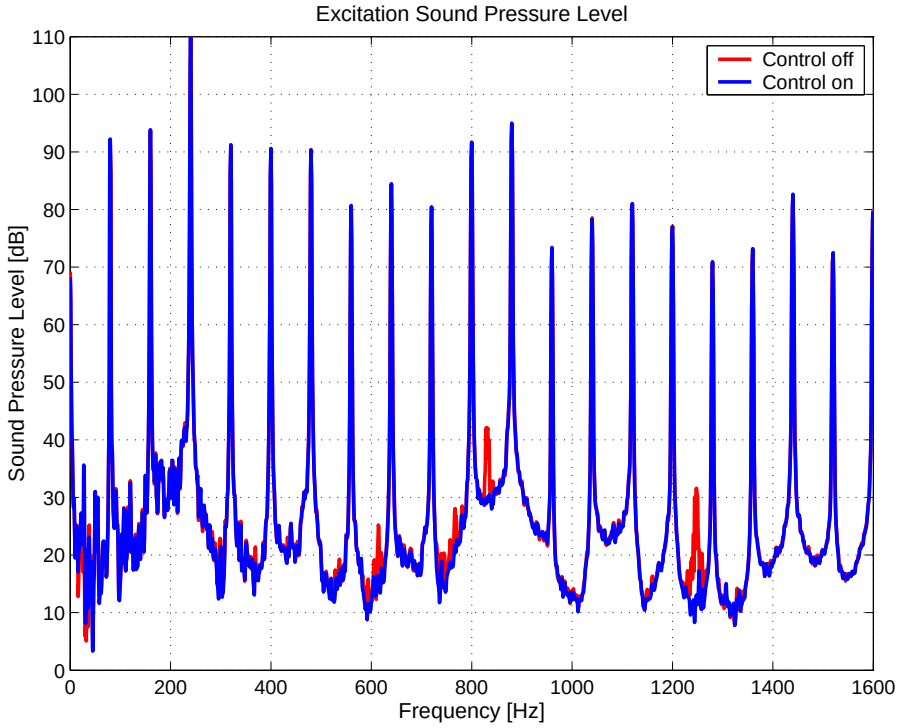

Figure C.35: Excitation sound pressure level

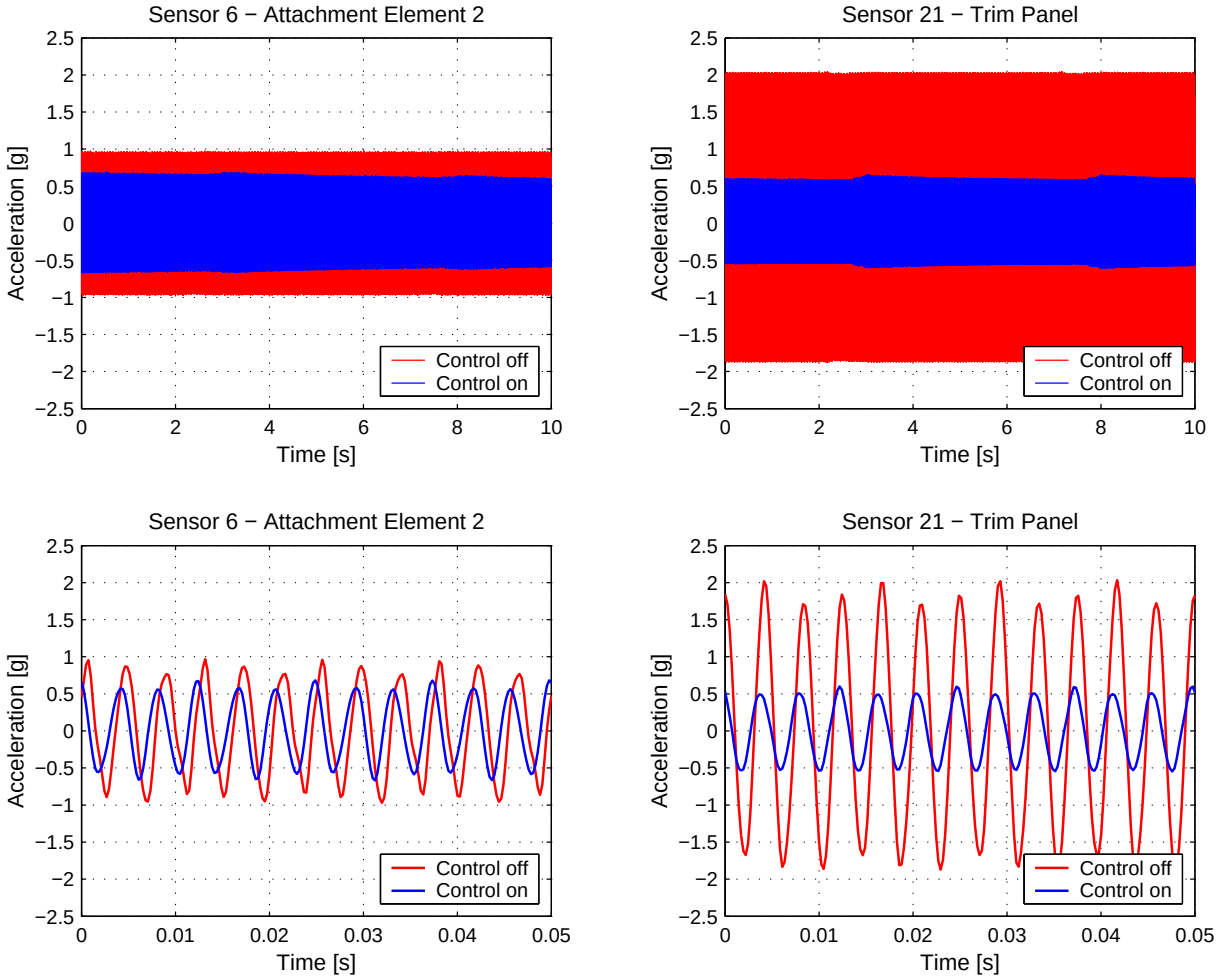

Figure C.36: Acceleration measured by error sensor 6 and 21, with and without control

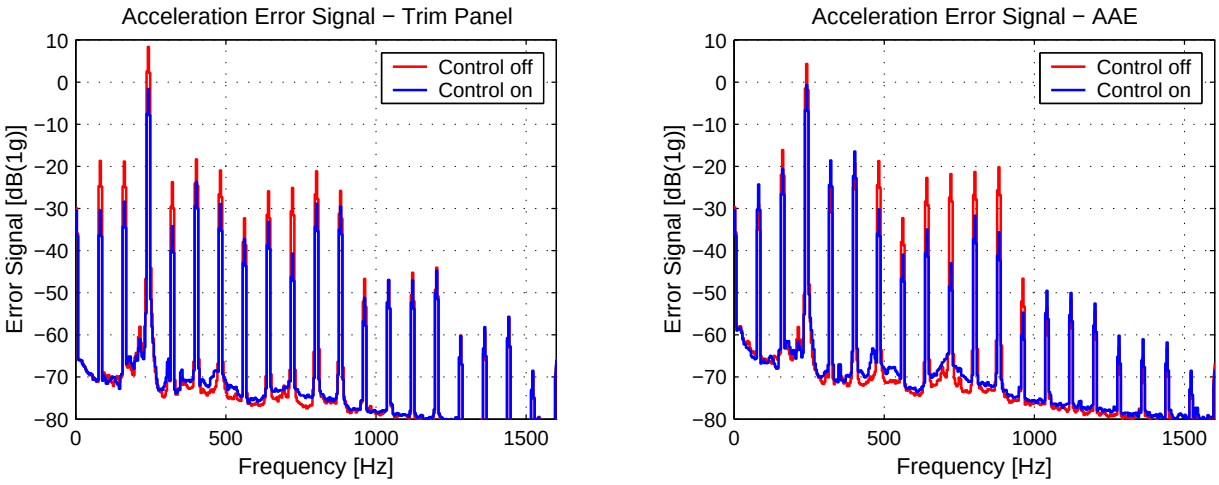

Figure C.37: Squared sum of error signals on trim panel and attachment elements

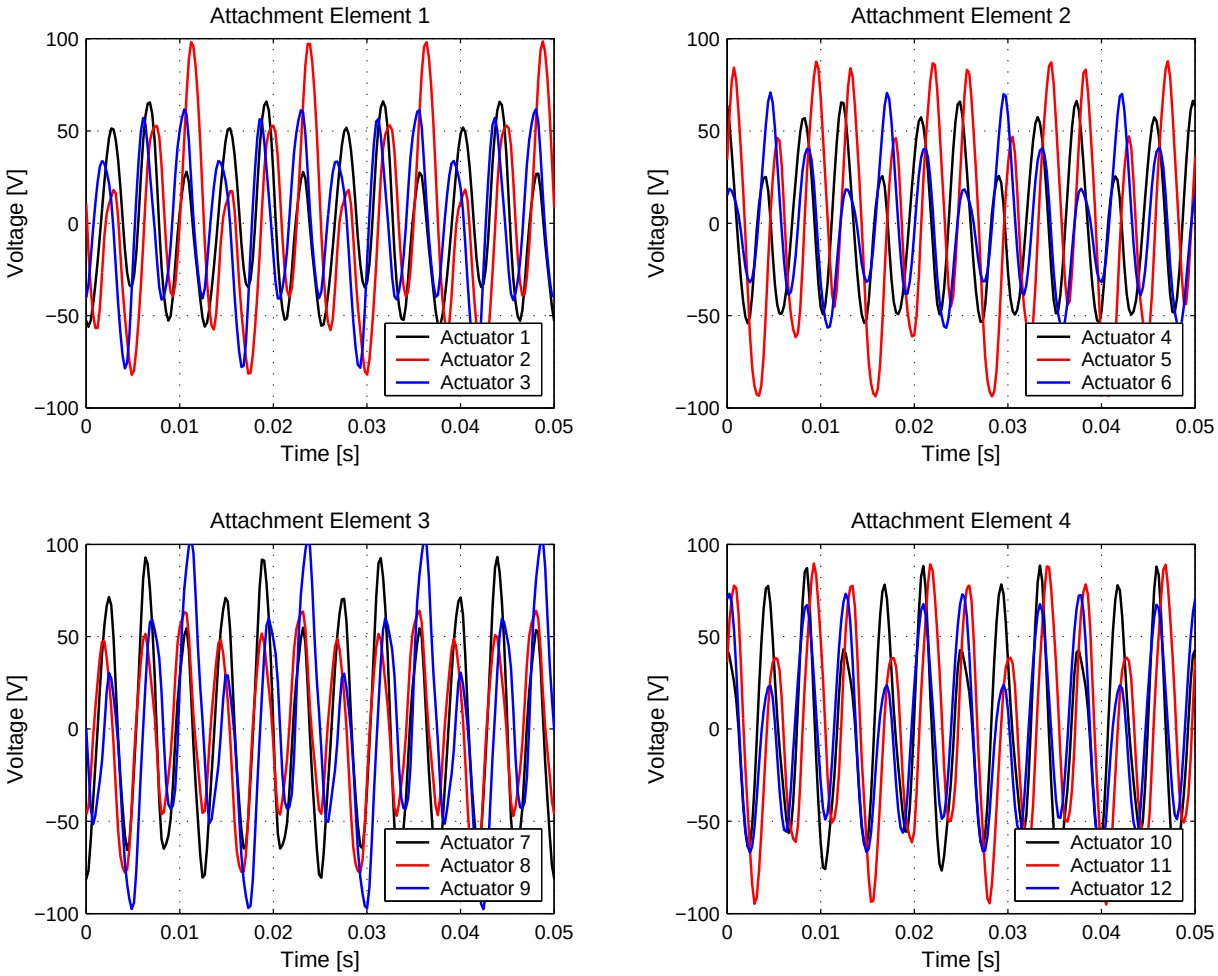

Figure C.38: Actuator voltage